Technische Universität Kaiserslautern

Fachbereich Chemie

SPIN AND ORBITAL MAGNETIC MOMENTS OF ISOLATED SINGLE MOLECULE MAGNETS AND TRANSITION METAL CLUSTERS

Am Fachbereich Chemie der Technischen Universität Kaiserslautern zur Erlangung des akademischen Grades "Doktor der Naturwissenschaften"

genehmigte

Dissertation
(D386)

vorgelegt von
Dipl.-Chem. Matthias Tombers

Betreuer: Prof. Dr. G. Niedner-Schatteburg

Tag der wissenschaftlichen Aussprache 06. August 2015
Technische Universität Kaiserslautern

Der experimentelle Teil der vorliegenden Arbeit wurde in der Zeit von April 2011 bis Mai 2015 im Fachbereich Chemie der Technischen Universität Kaiserslautern unter der Betreuung von Prof. Dr. G. Niedner-Schatteburg angefertigt.

Datum des Antrags der Eröffnung des Promotionsverfahrens: 03.06.2015

Promotionskommission:

Vorsitzender   Prof. Dr. S. Kubik

1. Berichterstatter   Prof. Dr. G. Niedner-Schatteburg

2. Berichterstatter   Prof. Dr. M. Gerhards

meinem Großvater

„Die Neugier steht immer an erster Stelle eines Problems,

das gelöst werden will.“

Galileo Galilei

Content

_____

_____

Abbreviations

XMCD	X-ray Magnetic Circular Dichroism
$[Fe_4Ln_2]$	I: $[Fe_4Ln_2(N_3)_6(N(C_2H_4OH)(C_2H_4O)_2)_4(C(CH_3)_3COO)_4]$ or II: $[Fe_4Ln_2O_2((CH_3)_3CCOO)_4(NO_3)_2(H_3C_3N(C_2H_4O)_2)_4]$
$[Fe_4Ln_2]^+$	I: $[Fe_4Ln_2(N_3)_6(N(C_2H_4OH)(C_2H_4O)_2)_4(C(CH_3)_3COO)_3CH_3CN]^+$ or II: $[Fe_4Ln_2O_2((CH_3)_3CCOO)_4(NO_3)(H_3C_3N(C_2H_4O)_2)_4CH_3CN]^+$
$[Mn_{12}ac]$	$[Mn_{12}O_{12}(CH_3COO)_{16}(H_2O)_4]$
$[Mn_{12}ac]^+$	$[Mn_{12}O_{12}(CH_3COO)_{15}(CH_3CN)]^+$
$\lvert\phi\rangle$	valence final state
$\lvert\iota\rangle$	initial core state
$<S_L>$	expectation value of the orbital angular momentum
$<S_J>$	expectation value of the total angular momentum
$<S_z>$	expectation value of the spin
$<T_z>$	expectation value of the spin magnetic dipole operator
μ^-	XA spectrum recorded with negative circularly polarized light; $q = -\hbar$
μ^+	XA spectrum recorded with positive circularly polarized light; $q = +\hbar$
μ_0	magnetic permeability of the free space
μ_0	XA spectrum recorded with linearly polarized light; $q = 0$
μ_B	Bohr magneton
μ_r	relative magnetic permeability of a given material
APPLE	Advanced Planar Polarized Light Emitter
B	magnetic flux density
BLYP	functional by Becke Lee Yang and Parr
D	axial zero-field splitting parameter
def2-TZVP	triple zeta basis set
DFT	Density Functional Theory
DMFT	Dynamical Mean Field Theory
E	rhombic zero-field splitting parameter
e	elementary charge
E_a	electron affinity
E_{mag}	magnetic dipolar interaction
ESI	ElectroSpray Ionization
FT-ICR	Fourier Transform Ion Cyclotron Resonance
GAMBIT	General Abstraction of Magnetic moments as BESSY by Ion Trapping
GGA	Generalized Gradient Approximation
g_J	Landé-factor of the total magnetic moment
g_L	Landé-factor of the orbital magnetic moment; $g_L = 1.0$
g_S	Landé-factor of the electron; $g_S = 2.0$
H	magnetic induction
H_{int}	interaction Hamiltonian
I_{hres}	X-ray absorption resonance intensity
I_P	ionization potential
J	total angular momentum, $J = L + S$
k	wave vector
L	total orbital angular momentum
lcp	left-handed circularly polarized light
LDA	Local Density Approximation

LVAP	Laser VAPorization
M	magnetization, transition matrix element
m_e	electron mass
m_L	orbital magnetic moment
$m_L^{(z)}$	projection of the orbital magnetic moment onto the quantization axis (magnetization)
m_S	spin magnetic moment
$m_S^{(z)}$	projection of the spin magnetic moment onto the quantization axis (magnetization)
m_{tot}	total magnetic moment
$m_{tot}^{(z)}$	projection of the total magnetic moment onto the quantization axis (magnetization)
n_h	number of holes in the final state / shell (= $4l_f$ + 2 - n)
p	electron momentum operator
PBE	Perdew-Burke-Ernzerhof
P_q^a	polarization dependent dipole operator
q	photon angular momentum
r	length operator
rcp	right-handed circularly polarized light
RF	radio frequency
$R_{n,l}(r)$	radial component of the wave function
S	total spin
SG	Stern-Gerlach
SMM	Single Molecule Magnet
SOC	Spin Orbit Coupling
T	temperature
TEY	Total Electron Yield
TFY	Total Fluorescence Yield
T_{if}	transition probability from an initial to a final state
TIY	Total Ion Yield
U	anisotropy barrier
XA	X-ray Absorption
$Y_{l,ml}$	angular part of the wave function, expressed in spherical harmonics
α_f	fine structure constant
α_N	cluster polarizabilities
γ	surface tension of a spherical droplet
ε	unit photon polarization operator
ε_{coh}	binding energy/atom (cohesive energy)
$\varepsilon_{i,f}$	energy of the initial and final state
η_{pol}	degree of circular polarization
Θ	paramagnetic Curie temperature
$\rho(\varepsilon_f)$	density of final states per unit energy
σ^-	left-handed circularly polarized light, q = -1
σ^+	right-handed circularly polarized light, q = +1
σ^{abs}	absorption cross section
χ	susceptibility
$\chi_{s, ms}$	spin part of the wave function
ω	photon frequency
ω_r	resonance frequency of a spherical metal cluster

1. INTRODUCTION

Since the first discovery of magnetism in form of so called lodstones (leading stone, or compass, 800 B.C.)[1] mankind is fascinated by the phenomenon of magnetism and magnetic attraction / repulsion. Over time many different kinds of magnetism have been discovered such as dia-, para-, ferro-, antiferro and ferri magnetism[2]. These different kinds of magnetism are based on a long range magnetic ordering of magnetic (spin) centers. They are typical forms of magnetism in bulk samples[3]. This has led to a vast amount of studies concerning the magnetic properties of bulk samples[4-7]. During the last decades the focus of the investigations of magnetism has switched from macroscopic (3D) bulk systems to systems with lower dimensionality. This lead to the discovery of other highly interesting magnetic properties such as superparamagnetism[8] and single molecule magnetism[9].

In 3D bulk systems a sample´s magnetism is dominated by the spin magnetic moment (e.g. in the bulk ferromagnets Fe, Co and Ni) as the orbital magnetic moment is mostly quenched in such systems due to orbital hybridization and symmetry reduction. In atomic samples on the other hand, the orbital component has a significant contribution to the total magnetic moment of the sample and can even exceed the spin component. A highly interesting topic is the investigation of the transition of magnetic properties from the spin dominated bulk case to the atomic case with high orbital contributions[10,11]. Superparamagnetic transition metal clusters provide for a perfect model system for such investigations[12-14]. In this work we use X-ray Magnetic Circular Dichroism (XMCD) to investigate iron (Fe_n^+, $7 \leq n \leq 17$), cobalt (Co_n^+, $8 \leq n \leq 22$) and nickel cluster (Ni_n^+, $7 \leq n \leq 17$) cations. The XMCD technique combined with the so called sum rule analysis[15,16] allows for an investigation of the magnetic moments of these clusters separated into their spin and orbital contributions. XMCD has proven a valuable tool in the investigations of spin and orbital magnetic moments of samples such as surfaces[17,18], thins films[19-21], deposited nanoparticles[22-28] or clusters[13,14,29-32] and adatoms[33-35]. Most recently this technique has been transferred into the gas phase[36-40]. Gas phase investigations enable a study of intrinsic magnetic moments without any influences of a surrounding bulk or matrix or a supporting substrate. Recording the intrinsic magnetic moments of those clusters separated into their spin and orbital contributions provides for invaluable insight into the fundamentals of magnetism. As the investigated transition metal clusters bridge the gap between

1. Introduction

the bulk and the atomic magnetic properties, we investigate the applicability of scaling laws for the spin and orbital magnetic moments between the bulk and atomic value.

Another highly interesting form of magnetism in samples with even further reduced dimensionality as transition metal clusters is the above mentioned single molecule magnetism[9,41]. Single Molecule Magnets (SMM) provide for a unique combination of magnetic properties on a molecular level which are not based on a long range magnetic ordering but are intrinsic properties of a sole molecule. They combine a large magnetic (spin) moment with a significant anisotropy barrier. This can be recorded in a magnetic hysteresis loop in the magnetic field dependent magnetization of the molecule[41]. In such a hysteresis loop another interesting property can be recorded, i.e. magnetic quantum tunneling[42]. The Mn_{12}-acetate[43] ($[Mn_{12}O_{12}(CH_3COO)_{16}(H_2O)_4]$, in short $[Mn_{12}ac]$) was the first molecule discovered to show such properties. It shows a high spin ground state (S = 10) and an anisotropy barrier of 50 cm^{-1}. Possible applications in high capacity data storage devices[44] and for quantum computing[45,46] of such SMMs have led to numerous investigations and attempts of creating better SMMs. One attempt is to combine 3d transition metals with a high spin ground state with 4f lanthanides providing a high magnetic anisotropy[47].

In the presented work, we investigate the archetypal $[Mn_{12}ac]$ single molecule magnet as well as SMMs combining iron and two different lanthanides ($[Fe_4Ln_2]$, Ln = Gd, Tb). We investigate these compounds with gas phase X-ray magnetic circular dichroism. This is the first attempt of a magnetic characterization of SMMs in the gas phase. XMCD spectra of single molecule magnets have been recorded before on bulk or deposited samples[48-56]. In such measurements the alteration of the intrinsic magnetic moments by a surrounding matrix or supporting substrate cannot be excluded. The gas phase XMCD technique provides us with the intrinsic magnetic properties of the investigated single molecule magnets. As SMMs are defined by their magnetic properties being intrinsic properties of a single molecule, we think that the investigation of SMMs as isolated molecules in the gas phase becomes inevitable.

In the case of the Mn_{12}-acetate we compare our results to spectra recorded on a bulk sample[57]. By this comparison we check for differences in the magnetic properties of $[Mn_{12}ac]$ as a bulk sample and an isolated molecule in the gas phase. With our measurements we aim to confirm the magnetic properties of $[Mn_{12}ac]$ recorded in the bulk phase to be intrinsic properties of the isolated molecule and to confirm $[Mn_{12}ac]$ as a SMM.

With our investigations on the $[Fe_4Ln_2]$ SMMs we try to exploit the theoretical potential of XMCD investigations on SMMs. Next to the possibility of recording the intrinsic spin and orbital contributions to the total magnetic moment, XMCD element selectivity allows for a separation of

these spin and orbital magnetic moments into the contributions from the containing elements (i.e. Fe and Ln = Gd, Tb). We check for an assumed antiferromagnetic coupling between the Fe atoms and the spin and orbital magnetic moments of the containing lanthanides. The containing lanthanide atoms present highly interesting spin and orbital contributions to the total magnetic moments. In the presented work we provide possible explanations and their plausibility, a detailed interpretation pending.

By our gas phase investigations using XMCD we gain insight into the basic components of magnetism in the highly interesting cases of superparamagnetic transition metal clusters and single molecule magnets.

[1]   Carus, L., DE RERUM NATURA, 1ST CENTURY BC REFERENCES ARE TO VV. 906 FF., IN THE TRANSLATION BY TH, Creech,(London, 1714). Pliny, quoted in W. Gilbert, De Magnete, trans.(Gilbert Club, London, 1900), rev. ed, 8.

[2]   Getzlaff, M. Fundamentals of magnetism; Springer Science & Business Media, 2007.

[3]   Stöhr, J.; Siegmann, H. C., MAGNETISM, Solid-State Sciences. Springer, Berlin, Heidelberg **2006**, 5.

[4]   Blundell, S. Magnetism in condensed matter; Oxford Univ. Press, 2001.

[5]   Crangle, J. Solid· State Magnetism; Springer Science & Business Media, 2012.

[6]   Mohn, P. Magnetism in the solid state: an introduction; Springer Science & Business Media, 2006; Vol. 134.

[7]   Martin, D. H.; Martin, D. H. Magnetism in solids; MIT Press Cambridge, MA, 1967.

[8]   Bean, C.; Livingston, J., SUPERPARAMAGNETISM, Journal of Applied Physics **1959**, 30, S120.

[9]   D. Gatteschi, R. S., J. Villain Molecular Nanomagnets; Oxford University Press: Oxford, 2006.

[10]   Jun, Y.-W.; Seo, J.-W.; Cheon, A., NANOSCALING LAWS OF MAGNETIC NANOPARTICLES AND THEIR APPLICABILITIES IN BIOMEDICAL SCIENCES, Accounts of Chemical Research **2008**, 41, 179.

[11]   Clusters of Atoms and Molecules; Haberland, H., Ed.; Springer, 1994.

[12]   Metal clusters at surfaces; Meiwes-Broer, K. H., Ed.; Springer, 2000.

[13]   Glaser, L.; Chen, K.; Fiedler, S.; Wellhöfer, M.; Wurth, W.; Martins, M., MAGNETIC PROPERTIES OF SMALL SIZE-SELECTED CO AND COPT CLUSTERS ON NI, Physical Review B **2012**, 86, 075435.

[14]   Wurth, W.; Martins, M., ELECTRONIC STRUCTURE AND MAGNETIC PROPERTIES OF SMALL DEPOSITED TRANSITION METAL CLUSTERS, Chem. Phys. Solid Surf. **2007**, 12, 471.

[15]   Carra, P.; Thole, B. T.; Altarelli, M.; Wang, X. D., X-RAY CIRCULAR-DICHROISM AND LOCAL MAGNETIC-FIELDS, Physical Review Letters **1993**, 70, 694.

[16]   Thole, B. T.; Carra, P.; Sette, F.; Vanderlaan, G., X-RAY CIRCULAR-DICHROISM AS A PROBE OF ORBITAL MAGNETIZATION, Physical Review Letters **1992**, 68, 1943.

[17]   Tischer, M.; Hjortstam, O.; Arvanitis, D.; Hunter Dunn, J.; May, F.; Baberschke, K.; Trygg, J.; Wills, J. M.; Johansson, B.; Eriksson, O., ENHANCEMENT OF ORBITAL MAGNETISM AT SURFACES: CO ON CU(100), Physical Review Letters **1995**, 75, 1602.

[18]   Baberschke, K., THE MAGNETISM OF NICKEL MONOLAYERS, Applied Physics A **1996**, 62, 417.

[19]   Chen, C. T.; Idzerda, Y. U.; Lin, H. J.; Smith, N. V.; Meigs, G.; Chaban, E.; Ho, G. H.; Pellegrin, E.; Sette, F., EXPERIMENTAL CONFIRMATION OF THE X-RAY MAGNETIC CIRCULAR DICHROISM SUM RULES FOR IRON AND COBALT, Physical Review Letters **1995**, 75, 152.

[20]   Bornemann, S.; Šipr, O.; Mankovsky, S.; Polesya, S.; Staunton, J. B.; Wurth, W.; Ebert, H.; Minár, J., TRENDS IN THE MAGNETIC PROPERTIES OF FE, CO, AND NI CLUSTERS AND MONOLAYERS ON IR(111), PT(111), AND AU(111), Physical Review B **2012**, 86, 104436.

[21]   Dhesi, S. S.; Dudzik, E.; Dürr, H. A.; Brookes, N. B.; van der Laan, G., *Correlation between L3 absorption satellite intensity and spin moment in ultrathin Ni films*, *Surface Science* **2000**, *454–456*, 930.

[22]   Baniodeh, A.; Mereacre, V.; Magnani, N.; Lan, Y.; Wolny, J. A.; Schuenemann, V.; Anson, C. E.; Powell, A. K., *Para versus meta ligand substituents as a means of directing magnetic anisotropy in Fe2Dy2 coordination clusters*, *Chem. Commun. (Cambridge, U. K.)* **2013**, *49*, 9666.

[23]   Bansmann, J.; Kleibert, A.; Getzlaff, M.; Rodriguez, A. F.; Nolting, F.; Boeglin, C.; Meiwes-Broer, K.-H., *Magnetism of 3d transition metal nanoparticles on surfaces probed with synchrotron radiation - from ensembles towards individual objects*, *Physica Status Solidi B-Basic Solid State Physics* **2010**, *247*, 1152.

[24]   Kleibert, A.; Passig, J.; Meiwes-Broer, K. H.; Getzlaff, M.; Bansmann, J., *Structure and magnetic moments of mass-filtered deposited nanoparticles*, *Journal of Applied Physics* **2007**, *101*, 114318.

[25]   Gambardella, P.; Rusponi, S.; Veronese, M.; Dhesi, S. S.; Grazioli, C.; Dallmeyer, A.; Cabria, I.; Zeller, R.; Dederichs, P. H.; Kern, K.; Carbone, C.; Brune, H., *Giant magnetic anisotropy of single cobalt atoms and nanoparticles*, *Science* **2003**, *300*, 1130.

[26]   Durr, H. A.; Dhesi, S. S.; Dudzik, E.; Knabben, D.; van der Laan, G.; Goedkoop, J. B.; Hillebrecht, F. U., *Spin and orbital magnetization in self-assembled Co clusters on Au(111)*, *Physical Review B* **1999**, *59*, R701.

[27]   Edmonds, K. W.; Binns, C.; Baker, S. H.; Thornton, S. C.; Norris, C.; Goedkoop, J. B.; Finazzi, M.; Brookes, N. B., *Doubling of the orbital magnetic moment in nanoscale Fe clusters*, *Physical Review B* **1999**, *60*, 472.

[28]   Pietzsch, O.; Kubetzka, A.; Bode, M.; Wiesendanger, R., *Spin-Polarized Scanning Tunneling Spectroscopy of Nanoscale Cobalt Islands on Cu(111)*, *Physical Review Letters* **2004**, *92*, 057202.

[29]   Lau, J. T.; Föhlisch, A.; Martins, M.; Nietubyc, R.; Reif, M.; Wurth, W., *Spin and orbital magnetic moments of deposited small iron clusters studied by x-ray magnetic circular dichroism spectroscopy*, *New Journal of Physics* **2002**, *4*, 98.

[30]   Lau, J. T.; Föhlisch, A.; Nietubyc̀, R.; Reif, M.; Wurth, W., *Size-Dependent Magnetism of Deposited Small Iron Clusters Studied by X-Ray Magnetic Circular Dichroism*, *Physical Review Letters* **2002**, *89*, 057201.

[31]   Fauth, K.; Hessler, M.; Batchelor, D.; Schutz, G., *Strong influence of defects on the electronic structure of Pt adatoms and clusters on graphite*, *Surface Science* **2003**, *529*, 397.

[32]   Ballentine, G.; Heßler, M.; Kinza, M.; Fauth, K., *Superparamagnetism in small Fe clusters on Cu(111)*, *The European Physical Journal D* **2007**, *45*, 535.

[33]   Eelbo, T.; Waśniowska, M.; Thakur, P.; Gyamfi, M.; Sachs, B.; Wehling, T. O.; Forti, S.; Starke, U.; Tieg, C.; Lichtenstein, A. I.; Wiesendanger, R., *Adatoms and Clusters of 3d Transition Metals on Graphene: Electronic and Magnetic Configurations*, *Physical Review Letters* **2013**, *110*, 136804.

[34]   Gambardella, P.; Dhesi, S. S.; Gardonio, S.; Grazioli, C.; Ohresser, P.; Carbone, C., *Localized magnetic states of Fe, Co, and Ni impurities on alkali metal films*, *Physical Review Letters* **2002**, *88*.

[35]   Brune, H.; Gambardella, P., *Magnetism of individual atoms adsorbed on surfaces*, *Surface Science* **2009**, *603*, 1812.

[36]   Peredkov, S.; Neeb, M.; Eberhardt, W.; Meyer, J.; Tombers, M.; Kampschulte, H.; Niedner-Schatteburg, G., *Spin and Orbital Magnetic Moments of Free Nanoparticles*, *Physical Review Letters* **2011**, *107*.

[37]   Peredkov, S.; Savci, A.; Peters, S.; Neeb, M.; Eberhardt, W.; Kampschulte, H.; Meyer, J.; Tombers, M.; Hofferberth, B.; Menges, F.; Niedner-Schatteburg, G., *X-ray absorption spectroscopy of mass-selected transition metal clusters using a cyclotron ion trap: An experimental setup for measuring XMCD spectra of free clusters*, *Journal of Electron Spectroscopy and Related Phenomena* **2011**, *184*, 113.

[38] Zamudio-Bayer, V.; Hirsch, K.; Langenberg, A.; Niemeyer, M.; Vogel, M.; Lawicki, A.; Terasaki, A.; Lau, J. T.; von Issendorff, B., *Maximum Spin Polarization in Chromium Dimer Cations as Demonstrated by X-ray Magnetic Circular Dichroism Spectroscopy*, *Angewandte Chemie (International ed. in English)* **2015**, *54*, 4498.

[39] Hirsch, K.; Zamudio-Bayer, V.; Langenberg, A.; Niemeyer, M.; Langbehn, B.; Moeller, T.; Terasaki, A.; von Issendorff, B.; Lau, J. T., *Magnetic Moments of Chromium-Doped Gold Clusters: The Anderson Impurity Model in Finite Systems*, *Physical Review Letters* **2015**, *114*.

[40] Langenberg, A.; Hirsch, K.; Lawicki, A.; Zamudio-Bayer, V.; Niemeyer, M.; Chmiela, P.; Langbehn, B.; Terasaki, A.; Issendorff, B. V.; Lau, J. T., *Spin and orbital magnetic moments of size-selected iron, cobalt, and nickel clusters*, *Physical Review B* **2014**, *90*.

[41] Christou, G.; Gatteschi, D.; Hendrickson, D. N.; Sessoli, R., *Single-molecule magnets*, *Mrs Bulletin* **2000**, *25*, 66.

[42] Gatteschi, D.; Sessoli, R., *Quantum tunneling of magnetization and related phenomena in molecular materials*, *Angewandte Chemie-International Edition* **2003**, *42*, 268.

[43] Lis, T., *Preparation, Structure, and Magnetic-Properties of a Dodecanuclear Mixed-Valence Manganese Carboxylate*, *Acta Crystallographica Section B-Structural Science* **1980**, *36*, 2042.

[44] Aromí, G.; Winpenny, R. E. *Single-molecule magnets and related phenomena*; Springer New York, 2006.

[45] Leuenberger, M. N.; Loss, D., *Quantum computing in molecular magnets*, *Nature* **2001**, *410*, 789.

[46] Aromí, G.; Aguila, D.; Gamez, P.; Luis, F.; Roubeau, O., *Design of magnetic coordination complexes for quantum computing*, *Chemical Society Reviews* **2012**, *41*, 537.

[47] Glaser, T., *Rational design of single-molecule magnets: a supramolecular approach*, *Chemical Communications* **2011**, *47*, 116.

[48] Mannini, M.; Pineider, F.; Sainctavit, P.; Danieli, C.; Otero, E.; Sciancalepore, C.; Talarico, A. M.; Arrio, M.-A.; Cornia, A.; Gatteschi, D.; Sessoli, R., *Magnetic memory of a single-molecule quantum magnet wired to a gold surface*, *Nat. Mater.* **2009**, *8*, 194.

[49] Mannini, M.; Pineider, F.; Sainctavit, P.; Joly, L.; Fraile-Rodríguez, A.; Arrio, M.-A.; Cartier dit Moulin, C.; Wernsdorfer, W.; Cornia, A.; Gatteschi, D.; Sessoli, R., *X-Ray Magnetic Circular Dichroism Picks out Single-Molecule Magnets Suitable for Nanodevices*, *Advanced Materials* **2009**, *21*, 167.

[50] Mannini, M.; Sainctavit, P.; Sessoli, R.; Cartier dit Moulin, C.; Pineider, F.; Arrio, M.-A.; Cornia, A.; Gatteschi, D., *XAS and XMCD Investigation of Mn12 Monolayers on Gold*, *Chemistry – A European Journal* **2008**, *14*, 7530.

[51] Dreiser, J.; Pedersen, K. S.; Birk, T.; Schau-Magnussen, M.; Piamonteze, C.; Rusponi, S.; Weyhermueller, T.; Brune, H.; Nolting, F.; Bendix, J., *X-ray Magnetic Circular Dichroism (XMCD) Study of a Methoxide-Bridged Dy-III-Cr-III Cluster Obtained by Fluoride Abstraction from cis-[(CrF₂)-F-III(phen)₂]⁺*, *Journal of Physical Chemistry A* **2012**, *116*, 7842.

[52] Dreiser, J.; Pedersen, K. S.; Piamonteze, C.; Rusponi, S.; Salman, Z.; Ali, M. E.; Schau-Magnussen, M.; Thuesen, C. A.; Piligkos, S.; Weihe, H.; Mutka, H.; Waldmann, O.; Oppeneer, P.; Bendix, J.; Nolting, F.; Brune, H., *Direct observation of a ferri-to-ferromagnetic transition in a fluoride-bridged 3d-4f molecular cluster*, *Chemical Science* **2012**, *3*, 1024.

[53] Ghigna, P.; Campana, A.; Lascialfari, A.; Caneschi, A.; Gatteschi, D.; Tagliaferri, A.; Borgatti, F., *X-ray magnetic-circular-dichroism spectra on the superparamagnetic transition-metal ion clusters Mn-12 and Fe-8*, *Physical Review B* **2001**, *64*.

[54] Ghigna, P.; Campana, A.; Lascialfari, A.; Caneschi, A.; Gatteschi, D.; Tagliaferri, A.; Borgatti, F., *X-ray magnetic-circular-dichroism spectra of the superparamagnetic transition-metal ion clusters Mn12 and Fe8. [Erratum to document cited in CA136:47067]*, *Phys. Rev. B: Condens. Matter Mater. Phys.* **2002**, *65*, 109903/1.

[55] Moroni, R.; Cartier, d. M. C.; Champion, G.; Arrio, M. A.; Sainctavit, P.; Verdaguer, M.; Gatteschi, D., *X-ray magnetic circular dichroism investigation of magnetic contributions from*

MN(III) AND MN(IV) IONS IN MN12-AC, Phys. Rev. B: Condens. Matter Mater. Phys. **2003**, *68*, 064407/1.

[56]   Corradini, V.; Ghirri, A.; Garlatti, E.; Biagi, R.; De Renzi, V.; del Pennino, U.; Bellini, V.; Carretta, S.; Santini, P.; Timco, G.; Winpenny, R. E. P.; Affronte, M., *MAGNETIC ANISOTROPY OF CR7NI SPIN CLUSTERS ON SURFACES*, *Advanced Functional Materials* **2012**, *22*, 3706.

[57]   Mannini, M.; Sainctavit, P.; Sessoli, R.; Moulin, C. C. D.; Pineider, F.; Arrio, M. A.; Cornia, A.; Gatteschi, D., *XAS AND XMCD INVESTIGATION OF MN-12 MONOLAYERS ON GOLD*, *Chemistry-a European Journal* **2008**, *14*, 7530.

2. THEORETICAL BACKGROUND

The following chapter contains a basic introduction into the theoretical background of magnetism and magnetic materials as well as X-ray absorption and X-ray magnetic circular dichroism as far as necessary to understand the presented studies. A brief introduction into magnetism and the basic characterization of magnetic materials is given. After presenting the basic concepts of magnetism, the special form of single molecule magnetism is addressed. As an introduction into the field, the basic theory of X-ray absorption spectroscopy is given before addressing the more complex issue of X-ray Magnetic Circular Dichroism (XMCD). The theoretical background chapter will be concluded by an introduction of the so called sum rule analysis of XMCD spectra.

2.1 Magnetism and magnetic materials

For a more detailed introduction into the basic concepts of magnetism and magnetic materials the reader is referred to the literature[1-3]. The shown introduction on magnetism and magnetic materials is based on the elaborations of M. Getzlaff[1].

Magnetic materials are defined by their response to an applied external magnetic field **H** which is called magnetic induction or magnetic flux density **B**. In vacuum, there is a linear relation between **B** and **H.**

$$\boldsymbol{B} = \mu_0 \boldsymbol{H} \quad (2.1)$$

μ_0:   magnetic permeability of the free space

Inside a given material, they may differ in direction and magnitude. This is due to the magnetization **M** of the material.

$$\boldsymbol{B} = \mu_0(\boldsymbol{H} + \boldsymbol{M}) \quad (2.2)$$

A materials magnetization is defined by its magnetic susceptibility χ if the magnetization is parallel to the external magnetic field (linear material)[1].

$$M = \chi H \quad \text{(2.3)}$$

In this case, we maintain a linear relation between **B** and **H**

$$B = \mu_0(1 + \chi)H \quad \text{(2.4a)}$$

$$= \mu_0\mu_r H \quad \text{(2.4b)}$$

with μ_r being the relative permeability of the material. In vacuum μ_r equals 1. In matter it is generally ≥ 1 and can range up to values of 100,000. χ serves for a rough classification of magnetic materials into three classes.

2.1.1 Diamagnetism

Diamagnetism is present in all materials and it is only relevant in the absence of collective magnetism or paramagnetism. In diamagnetic materials the external magnetic field **H** induces magnetic dipoles which orient antiparallel to the external field. Therefore the susceptibility of diamagnetic materials is negative.

$$\chi^{dia} = const. < 0 \text{ (2.5)}$$

Nearly all organic substances and also metals like Hg as well as superconductors below their critical temperatures show diamagnetic behavior.

2.1.2 Paramagnetism

Paramagnetic materials maintain permanent magnetic dipoles which orient in the external magnetic field **H**. The susceptibility of a paramagnetic material is characterized by:

$$\chi^{para} > 0 \quad \text{(2.6)}$$

$$\chi^{para} = \chi^{para}(T) \text{ (2.7)}$$

  T: temperature

The orientation of the permanent magnetic moments may be impaired by thermal fluctuations. The permanent magnetic moments can be of localized or itinerant nature which leads to a different temperature dependence of the resulting paramagnetism.

Electrons of partially filled inner shells of an atom cause localized moments. They can be found in 4f or 5f orbitals of rare earth metals and actinides. Paramagnetism based on these localized moments is called Langevin paramagnetism. The resulting susceptibility $\chi^{Langevin}$ is temperature dependent. At high temperatures it can be described by the Curie law[3]:

$$\chi^{Langevin}(T) = \frac{c}{T} \quad (2.8)$$

Itinerant moments result from nearly free electrons in the valence band which carry a permanent magnetic moment of 1 μ_B (μ_B = the Bohr magneton). This form of paramagnetism is called Pauli paramagnetism. The resulting susceptibility is nearly temperature independent:

$$\frac{\delta\chi^{Pauli}}{\delta T} \approx 0 \quad (2.9)$$

Due to their different origin, the magnitudes of χ for the two different types of paramagnetism are very different.

$$\chi^{Pauli} \ll \chi^{Langevin} \quad (2.10)$$

2.1.3 Collective magnetism

Collective magnetism results from exchange interactions between permanent magnetic moments within the material. The origin of this interaction can only be explained by quantum mechanics. The resulting susceptibility shows a much more complicated structure than for Pauli or Langevin paramagnetism.

$$\chi^{coll} = \chi^{coll}(T, \boldsymbol{H}, \text{"history"}) \quad (2.11)$$

Below a critical temperature (T^{crit}) materials showing collective magnetism present a spontaneous magnetization. This is due to an orientation of the permanent magnetic moments without the influence of an external magnetic field. Again, these permanent magnetic moments can be based on localized or itinerant magnetic moments. Collective magnetism can be divided into three subclasses.

2. Theoretical background

2.1.3.1 Ferromagnetism

In ferromagnetism the critical temperature (T^{crit}) is called Curie temperature T_C. For 0 K < T < T_C the permanent magnetic moments within the materials have a preferred orientation. For T = 0 K all magnetic moments are aligned parallel (Fig. 2.1a). If the ferromagnetism is based on itinerant magnetic moments it is called band or itinerant ferromagnetism (e.g. in Fe, Co, Ni). Above the Curie temperature T_C the material becomes paramagnetic.
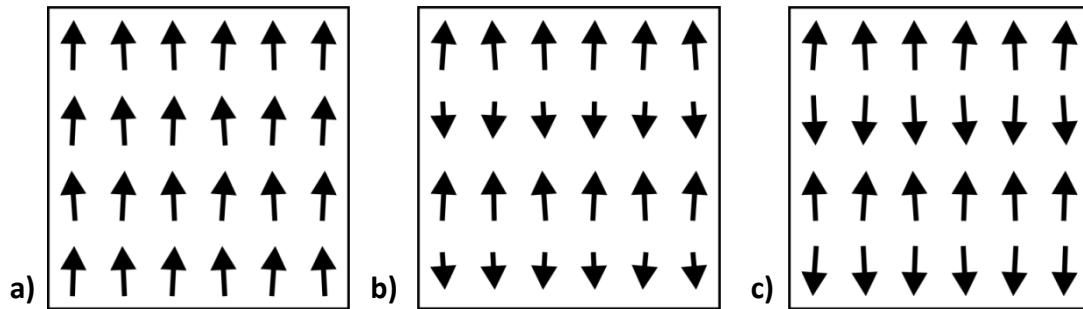
Figure 2.1[4] Spin orientations below the critical temperature (T^{crit}) for **(a)** a ferromagnet; **(b)** a ferrimagnet; **(c)** an antiferromagnet.

2.1.3.2 Ferrimagnetism

Ferrimagnetic materials are divided into at least two different sub lattices A and B. Both sub lattices present a different magnetization based on ferromagnetic spin alignment (Fig. 2.1b):

$$M_A \neq M_B \quad (2.12)$$

whereas

$$M = M_A + M_B \neq 0 \;\; \text{for} \;\; T < T_C \;(2.13)$$

with *M* being the total magnetization of the material. Above the Curie temperature T_C the material becomes paramagnetic.

2.1.3.3 Antiferromagnetism

A special case of ferrimagnetism is antiferromagnetism. In the case of antiferromagnetism the material is also divided into two sublattices with two different magnetizations. In the special case of antiferromagnetism, their magnetizations cancel each other out. With

$$|M_A| = |M_B| \neq 0 \;\; \text{for} \;\; T < T_C \quad (2.14)$$

and

$$M_A = -M_B \quad (2.15)$$

This leads to a total magnetization of the molecule:

$$M = M_A + M_B \equiv 0 \qquad (2.16)$$

The critical temperature in antiferromagnetism is called Néel temperature T_N. Above the Néel temperature the collective antiferromagnetism merges into paramagnetism with its characteristic behavior.

The temperature dependence of magnetic susceptibility can be seen in Fig. 2.2[1].
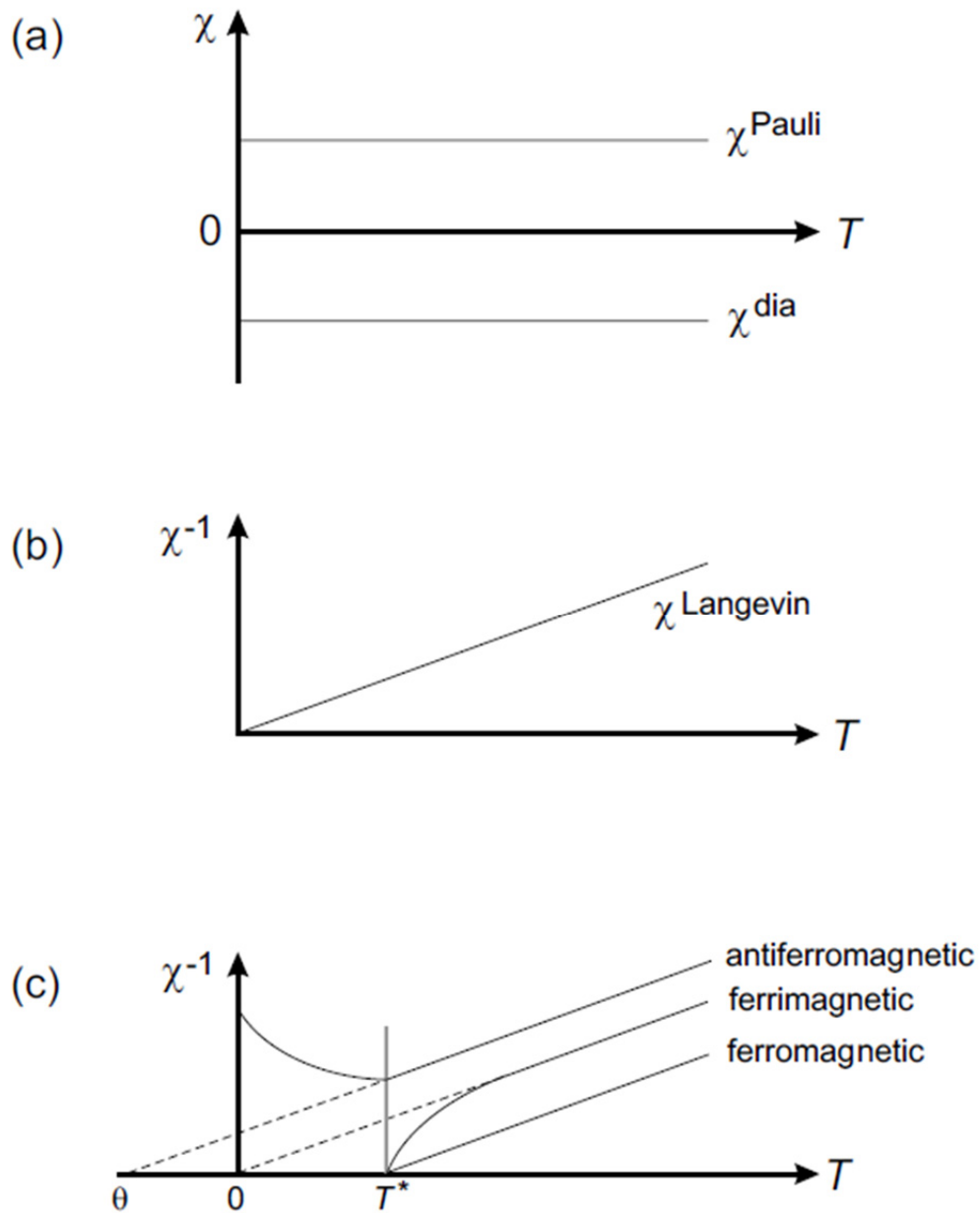
Figure 2.2[1] Temperature dependence of the magnetic susceptibility χ and inverse magnetic susceptibility χ^{-1} in the case of **(a)** diamagnetism and Pauli paramagnetism, **(b)** Langevin paramagnetism, **(c)** ferromagnetism, antiferromagnetism and ferrimagnetism with T^* being the critical temperature (T^{crit}) and Θ the paramagnetic Curie temperature.

2.1.4 Magnetic domains and superparamagnetism

For a detailed description of the origin of magnetic moments in transition metal clusters and the development of magnetic moments from the bulk to finite size systems, the reader is referred to the doctoral thesis of J. D. Meyer[4].

Within magnetic materials one has to consider the magnetic dipolar interaction between two spins next to their exchange interaction. The exchange interaction is about a thousand times stronger than the magnetic dipolar interaction but it declines much faster with the distance between two magnetic centers (r). The exchange interaction drops exponentially in r whereas the magnetic dipolar interaction drops to the inverse power of three (~ r^{-3}). Therefore the magnetic dipolar interaction dominates the long range ordering of the magnetic sample. This leads to a formation of so called magnetic domains which lower the magnetic dipolar energy stored within the system. Within such a magnetic domain the electron spins are ferromagnetically ordered. The orientations of the different domains differ from each other. At the fringes of the individual domains (domain walls) the total energy of the material is raised due to the reduction of exchange interaction. In larger systems this is compensated for by the long range dipolar interaction.

In very small magnetic materials such as transition metal clusters the short range magnetic ordering which is dominated by exchange interaction prevails. Due to the reduced system size the long range dipolar interaction can no longer compensate the energy loss due to the reduced exchange interaction at the domain walls. Therefore formation of different domains is omitted and only one single domain is formed. In this single domain all spins are coupled ferromagnetically. An ensemble of single domain particles is called superparamagnetic[5,6].

2.1.5 Temperature and magnetic field dependence of magnetizations

The application of an external magnetic field onto a sample leads to the alignment of the samples´ permanent or induced magnetic dipoles along the quantization axis (z). This quantization axis coincides with the axis of the external magnetic field. The degree of alignment (magnetization) of the samples´ magnetic dipoles and the respective magnetic moments depends on the temperature and the external magnetic field strength. The degree of alignment can be defined by the projection of the intrinsic magnetic moments onto the quantization axis. In the case of perfect alignment the projection equals the intrinsic magnetic moment. In the course of this work, intrinsic magnetic moments per atom will be labeled m_X (X = S, L, J (or tot) for spin, orbital and total magnetic moments). Their projections onto the quantization axis (z) will be labeled $m_X^{(z)}$. High magnetic field strengths lead to a better alignment. High temperatures decrease the alignment due to thermal randomization (Fig 2.3).
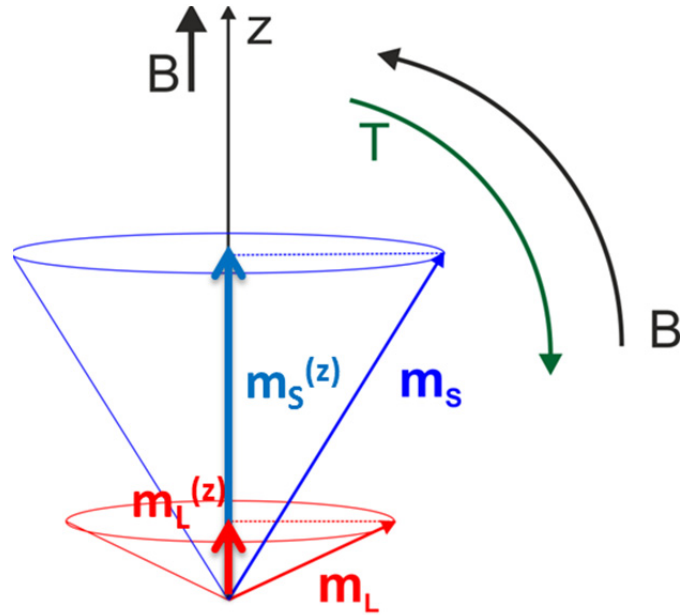
Figure 2.3 Schematic depiction of intrinsic spin (m_S) and orbital (m_L) magnetic moments and their projections (magnetizations) onto the quantization axis ($m_S^{(z)}$ and $m_L^{(z)}$). The influences of temperature and magnetic field strength on the allignment are indicated by the green and black arrows.

The Brillouin formula[2] describes this temperature and magnetic field strength dependence of the magnetization. The Brillouin function reads as:

$$m_J^{(z)} = g_J \mu_B J \left(\frac{2J+1}{2J} \coth \left(\frac{2J+1}{2J} \frac{\mu_B g_J J B}{k_B T} \right) - \frac{1}{2J} \coth \frac{1}{2J} \frac{\mu_B g_J J B}{k_B T} \right) \qquad (2.17a)$$

$$m_L^{(z)} = g_L \mu_B L \left(\frac{2L+1}{2L} \coth \left(\frac{2L+1}{2L} \frac{\mu_B g_L L B}{k_B T} \right) - \frac{1}{2L} \coth \frac{1}{2L} \frac{\mu_B g_L L B}{k_B T} \right) \qquad (2.17b)$$

$$m_S^{(z)} = g_S \mu_B S \left(\frac{2S+1}{2S} \coth \left(\frac{2S+1}{2S} \frac{\mu_B g_S S B}{k_B T} \right) - \frac{1}{2S} \coth \frac{1}{2S} \frac{\mu_B g_S S B}{k_B T} \right) \qquad (2.17c)$$

For X → ∞ the Brillouin function turns into the Langevin[2] function. With $m_X = g_x \mu_B X$ (X = J, S, L) it reads:

$$m_J^{(z)} = m_J \left(\coth \left(\frac{m_J B}{k_B T} \right) - \frac{k_B T}{m_J B} \right) \quad \text{(2.18a)}$$

$$m_L^{(z)} = m_L \left(\coth \left(\frac{m_L B}{k_B T} \right) - \frac{k_B T}{m_L B} \right) \quad \text{(2.18b)}$$

$$m_S^{(z)} = m_S \left(\coth \left(\frac{m_S B}{k_B T} \right) - \frac{k_B T}{m_S B} \right) \quad \text{(2.18c)}$$

$m_S^{(z)}, m_L^{(z)}, m_J^{(z)}$ projection (magnetization) of the intrinsic spin, orbital and total magnetic moments per atom onto the quantization axis

m_S, m_L, m_J intrinsic spin, orbital and total magnetic moments per atom

S, L, J   total spin, orbital and total angular momentum, J=L+S

g_S Landé-factor of the electron; g_S = 2.0

g_L Landé-factor of the orbital magnetic moment; g_L = 1.0

g_J Landé-factor of the total magnetic moment

B   magnetic field strength

T   temperature

If one can determine the magnetization of a given sample at a known temperature and magnetic field strength, the Brillouin / Langevin formula enable a scaling of these projections $m_X^{(z)}$ to a projection at 0 K and infinite field. Such a projection is equal to the intrinsic magnetic moment m_X. In the presented experiments the coupling between the spin (S) and orbital (L) angular momentum to the total angular momentum (J) exceeds the individual coupling of S and L to the external magnetic field[7-9]. Therefore a Brillouin / Langevin scaling of $m_J^{(z)}$ to m_J and no individual scaling of $m_S^{(z)}$ and $m_L^{(z)}$ is performed. We calculate the respective values for m_S and m_L from m_J by the $m_S^{(z)}$ to $m_L^{(z)}$ ratio before scaling.

2.2 Single molecule magnetism

For a detailed description of the exploration and quantum mechanical foundations of single molecule magnetism the reader is referred to the literature [10-13]. Here only a brief introduction into the origin of the main features of Single Molecule Magnets (SMM) is given.

Reduction of the system size to only one single molecule can give rise to a completely new form of magnetism. These recently discovered new kinds of magnets are called Single Molecule Magnets (SMM)[11]. They are defined by a high total spin ground state (S) combined with a magnetic anisotropy barrier below a critical temperature. This means that there is a preferred orientation of the spin within the molecule. The anisotropy is not based on a long range magnetic ordering as it is the case for most bulk samples showing magnetic anisotropy. It is an intrinsic property of the molecule itself. A pure spin is magnetically completely isotropic; therefor the anisotropy has to originate from contributions from the angular momentum or spin-spin dipolar interactions. The anisotropy can be phenomenologically described by the so called zero-field splitting and the zero field splitting parameters *D* and *E* according to the Hamiltonian:

$$\widehat{H} = DS_z^2 + E(S_x^2 - S_y^2) \quad \text{(2.19)}$$

Where $S_{x,y,z}$ are the x -,y -, and z - components of the total Spin S. The z − direction represents the quantization axis (e.g. an external magnetic field). The axial *D* and the rhombic *E* zero-field splitting parameters describe the symmetry of the zero-field splitting around the given magnetic center. *D* and *E* are zero for a cubic symmetry. For an axial symmetry only *E* is zero. The quotient of E/D is called rhombicity. A system with a given total spin S presents 2S + 1 sublevels of m_s ranging from - S < m_s < +S. Without an external magnetic field these sublevels are degenerate. The influence of an axial zero field splitting (*E* = 0) with *D* < 0 is shown in Fig. 2.4. The negative sign of the axial zero field splitting parameter is mandatory for SMM behavior. For D > 0 (easy-plane anisotropy) the m_s = 0 substate (m_s = ± ½ for a non-integer number of S) will be lowest in energy. Only if D < 0 (easy axis anisotropy) the m_s ± S states become the lowest in energy. This means that the alignment either parallel or antiparallel to the quantization axis (e.g. an external magnetic field) is lowest in energy. This leaves the system with two possibilities of m_s population (cf. double well potential, Fig. 2.4) which is the basis for single molecule magnetism. Without an external magnetic field both

possibilities are evenly populated (Fig. 2.4a). Switching on an external magnetic field stabilizes the m_s states parallel to the external field ($m_s < 0$) and destabilizes those antiparallel to the external magnetic field ($m_s > 0$, Fig. 2.4b).
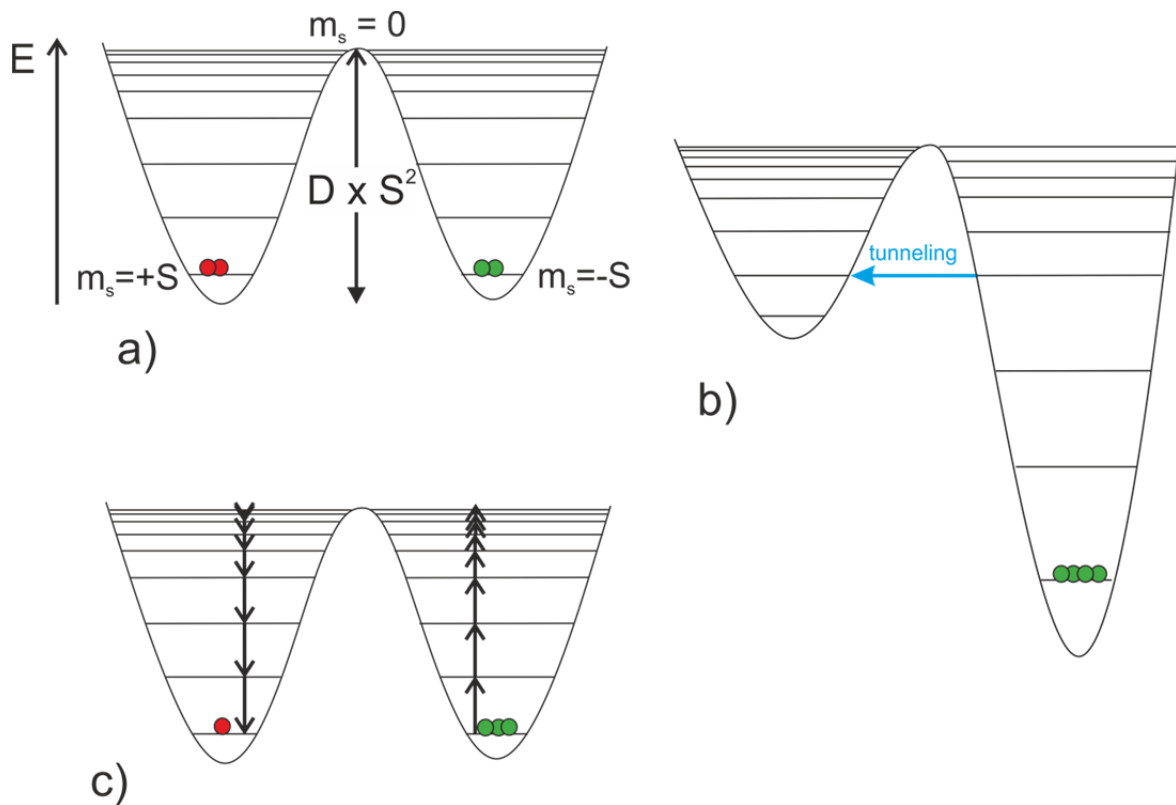
Figure 2.4 Schematic representation of the anisotropy barrier and the respective m_s state populations for a SMM with easy axis anisotropy in **(a)** no external magnetic field, **(b)** in presence of an external magnetic field and **(c)** after the application of an external magnetic field. The differences in energy (E) are given for a parallel ($m_s < 0$) and antiparallel ($m_S > 0$) alignment of the magnetic moments to the external magnetic field. The given possibility of resonant magnetization tunneling between degenerate states in the presence of an external magnetic field is indicated by the blue arrow.

The destabilized m_s states are depopulated and the stabilized m_s states are further populated. This leads to a magnetization of the sample as it can be seen in paramagnetic materials. After switching off the external magnetic field the displaced population (and therefore the magnetization) remains and can only return to the evenly distributed (non-magnetized) population by overcoming the anisotropy barrier (*U*) between the two wells (Fig. 2.4c). The anisotropy barrier U is given by:

$$U = DxS^2 \quad (2.20)$$

2. Theoretical background

This slow relaxation of the magnetization can be seen in a hysteresis loop in the magnetic field dependent magnetization of such molecules. In the hysteresis loop of SMMs (exemplified by the hysteresis loop of the Mn$_{12}$-acetate[14] SMM in Fig. 2.5[12]) one can find vertical steps. These steps originate from the so called resonant magnetization tunneling.
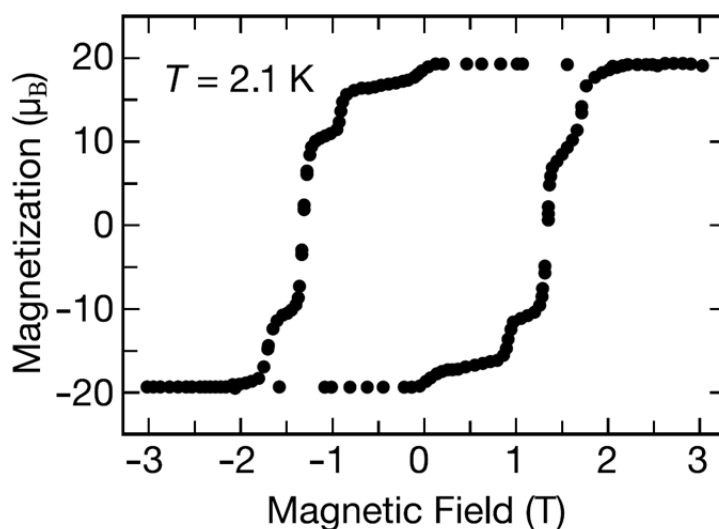
Figure 2.5[12] Magnetization versus magnetic field hysteresis loop for Mn$_{12}$-acetate. The data was recorded on a single crystal with the magnetic field applied along the tetragonal axis of the Mn$_{12}$-acetate molecules.

Resonant magnetic tunneling occurs at "critical" magnetic field strengths. In certain cases the distortion of the double well potential due to the external magnetic field reveals degenerate states in the two different wells. In these cases tunneling of the system from a $m_s < 0$ to a $m_s > 0$ state is possible. This tunneling significantly increases the reorganization from the magnetized to the non-magnetized population of m_s states. This very fast reorganization can be seen in the vertical sections of the hysteresis loop.

The combination of the given magnetic properties of the SMMs namely a high spin ground state combined with an anisotropy barrier that maintains the magnetization of the molecule even without an external magnetic field makes these molecules promising prospects for magnetic data storage devices on a molecular level[10] and for quantum computing[15,16].

2.3 X-ray absorption and X-ray Magnetic Circular Dichroism (XMCD)

The given introduction into X-ray absorption and X-ray magnetic circular dichroism is based on the elaborations of Stöhr and Siegmann[3].

2.3.1 X-ray absorption

Absorption of an X-ray photon can lead to the excitation of a core shell electron within a given atom. This excitation can be resonant or non-resonant. In the resonant case the photon is excited from a core shell state into an empty valence state of the atom. In the non-resonant case the electron is excited into continuum, which leads to an initial or further ionization of the system. In both cases the system is left with an empty core state (core hole). This core hole can be filled by electrons "dropping down" from higher occupied states. This filling of the core hole releases an amount of energy equal to the difference in energy between the core hole and the higher filled state. This energy can either be emitted as radiation (fluorescence) or it leads to the ejection of valence electrons into continuum. These electrons are called Auger electrons.

Further on, only the resonant absorption from an initial core state $|i\rangle$ to an empty valence state (final state $|f\rangle$) will be discussed in terms of a one electron picture and in terms of a first-order process. This means that the time dependent perturbation of the system by the X-rays´ electromagnetic field leads to an immediate excitation from the initial $|i\rangle$ into the final state $|f\rangle$ without crossing any intermediate states $|n\rangle$.
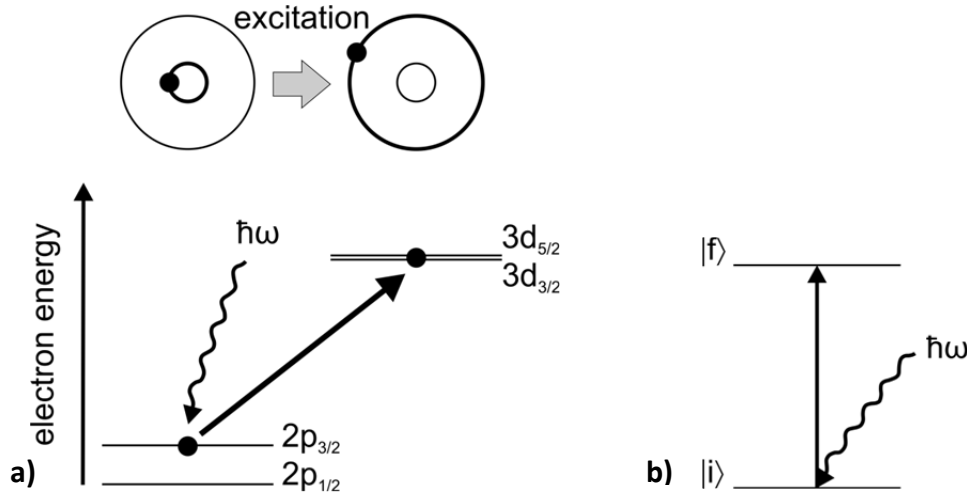
Figure 2.6[4] Depiction of the resonant $L_{2,3}$ edge absorption (2p → 3d) in a one electron picture. **(a)** An electron is resonantly excited by the absorption of an X-ray photon. The energy levels are labeled by their quantum numbers. **(b)** The core state is the initial state $|i\rangle$ and the valence state into which the electron is excited is the final state $|f\rangle$.

The transition probability from $|i\rangle$ to $|f\rangle$ (T_{if}) can be described by "Fermi's Golden Rule No. 2" including only the first order term as derived by Dirac[17].

$$T_{if} = \frac{2\pi}{\hbar} \left| \langle f | \hat{H}_{int} | i \rangle \right|^2 \delta(\varepsilon_i - \varepsilon_f) \rho(\varepsilon_f) \quad (2.21)$$

$\hat{H}_{int}$ interaction Hamiltonian
$\varepsilon_{i,f}$ energy of the initial and final state
$\rho(\varepsilon_f)$ density of final states per unit energy

The interaction Hamiltonian can be described as the product of the momentum operator $\boldsymbol{p}$ and the vector potential $\boldsymbol{A}$[18-21].

$$\hat{H}_{int} = \frac{e}{m_e} \boldsymbol{p} \cdot \boldsymbol{A} \quad (2.22)$$

e   elementary charge
m_e electron mass

The initial $|i\rangle$ and final $|f\rangle$ states and the resulting matrix elements contain an electronic and a photon part. After quantization of the electromagnetic field[22] and evaluation of the photon part, the relevant matrix elements can be written as a transition from an electronic initial $|a\rangle$ to an electronic final state $|b\rangle$.

$$M = \langle b | \boldsymbol{p} \cdot \boldsymbol{\epsilon} e^{i\boldsymbol{k} \cdot \boldsymbol{r}} | a \rangle \qquad \text{(2.23)}$$

M	transition matrix element
$\boldsymbol{p}$	electron momentum operator
$\boldsymbol{\varepsilon}$	unit photon polarization operator
$\boldsymbol{k}$	wave vector
$\boldsymbol{r}$	length operator

Applying the dipole approximation the $\boldsymbol{k}$ dependence is eliminated and $\boldsymbol{p}$ can be expressed in terms of the length operator $\boldsymbol{r}$.

$$M = \langle b | p \cdot \varepsilon (1 + ikr + \cdots) | a \rangle \cong \langle b | p \cdot \varepsilon | a \rangle = im_e \langle b | r \cdot \varepsilon | a \rangle \quad \text{(2.24)}$$

The dipole approximation presumes the X-ray wavelength to be much larger than the adsorbing atomic shell. This means the exiting electric field is constant over the atomic volume i.e.:

$$|r| \ll \frac{1}{|k|} = \frac{\lambda}{2\pi} \qquad \text{(2.25)}$$

The resulting absorption cross section σ^{abs} is given by:

$$\sigma^{abs} = 4\pi^2 \frac{e^2}{4\pi\varepsilon_0 \hbar c} \hbar\omega |\langle b | r \cdot \varepsilon | a \rangle|^2 \delta[\hbar\omega - (E_b - E_a)] \rho(E_b) \qquad \text{(2.26)}$$

2. Theoretical background

The energy integral over this cross section after volume normalization of $|a\rangle$ and $|b\rangle$ to unity gives the X-ray absorption resonance intensity I_{res}.

$$I_{res} = A|\langle b|\boldsymbol{\epsilon} \cdot \boldsymbol{r}|a\rangle|^2 \qquad (2.27)$$

with the proportionality factor A:

$$A = 4\pi^2 \alpha_f \hbar\omega \qquad (2.28)$$

and the fine structure constant α_f:

$$\alpha_f = \frac{e^2}{4\pi\varepsilon_0\hbar c} \qquad (2.29)$$

To implement cases of different photon polarization into the expression $\varepsilon \cdot r$ (eq. 2.24), one has to take into account the polarization dependent dipole operator P_α^q, where $\hbar q$ represents the angular momentum of the absorbed photon. For linear polarized light $q = 0$ and for circularly polarized light $q = \pm 1$, in short $q = \pm$. α indicates the X-ray incident direction in a Cartesian (x, y, z) coordinate system. With

$$P_\alpha^q = \varepsilon_a^q \cdot r = \varepsilon \cdot r \qquad (2.30)$$

follows

$$I_{res} = A|\langle b|\boldsymbol{\epsilon} \cdot \boldsymbol{r}|a\rangle|^2 = A\left|\langle b|\boldsymbol{\epsilon}_\alpha^q \cdot \boldsymbol{r}|a\rangle\right|^2 = A\left|\langle b|P_\alpha^q|a\rangle\right|^2 \qquad (2.31)$$

accordingly. P_α^q can be written in terms of spherical harmonics[23,24] or in terms of Racah´s spherical tensor operators[23].

To calculate the transition matrix elements one needs the wave functions of the initial $|a\rangle$ and final $|b\rangle$ electronic states. They can be described in the simplest way by the following expression:

$$R_{n,l}(r)Y_{l,m_l}\chi_{s,m_s} = \left|R_{n,l}(r); l, m_l, s, m_s\right\rangle \qquad (2.32)$$

$R_{n,l}(r)$	radial component of the wave function
$Y_{l,ml}$	angular part of the wave function, expressed in spherical harmonics
$\chi_{s,ms}$	spin part of the wave function
n, l, m_l, s, m_s	quantum numbers

Following this basic expression the wave function of the initial (core shell n, angular momentum c) state can be written as:

$$|a\rangle = |R_{n,c(r);c,m_c,s,m_s}\rangle \quad (2.33)$$

The final state (valence shell n´, angular momentum l) follows accordingly:

$$|b\rangle = |R_{n',c\ (r);l,m_l,s,m_s}\rangle \quad (2.34)$$

Now, the transition matrix elements can be calculated by:

$$\langle b|P_\alpha^q|a\rangle = \langle R_{n',l}(r); l, m_l, s, m_s'|P_\alpha^q|R_{n,c}(r); c, m_c, s, m_s\rangle \quad (2.35)$$

The transition matrix elements factor into a spin, radial and angular part:

$$\langle b|P_\alpha^q|a\rangle = \delta(m_s', m_s)\langle R_{n',l}(r)|r|R_{n,c}(r)\rangle \sum_{m_c,m_l,p} \left(e_{\alpha,p}^q \left\langle l, m_l \left|C_p^{(1)}\right|c, m_c\right\rangle\right)$$

$$= \quad \textit{spin} \qquad \textit{radial} \qquad\qquad \textit{angular} \qquad (2.36a,b)$$

The spin part remains completely unaffected by the dipole operator. Therefore the spin has to be preserved upon excitation. The angular part maintains the polarization dependence while the angle integrated transition strength is represented in the radial part of the wave function. Investigating the non-zero matrix elements of the expression given above, one can derive the following selection rules for X-ray excitation between states of the form $|n, l, m_l, s, m_s\rangle$:

- o   Δl = l' - l = ±1
- o Δm_l = m_l' - m_l = q =0, ±1
- o   Δs = s' - s = 0
- o Δm_s = m_s' - m_s = 0

2.3.2 Intensity sum rule for the charge

We define an orientation independent resonant X-ray absorption intensity (white line intensity)

$$\langle I \rangle = \tfrac{1}{3}\left(I_x^q + I_y^q + I_z^q\right) = \tfrac{1}{3}\left(I_\alpha^{-1} + I_\alpha^0 + I_\alpha^{+1}\right) \text{ (2.37)}$$

following the definition of an X-ray propagation (α) and polarization (*q*) dependent dipole operator P_α^q. It can be deduced in a nonmagnetic sample with higher than monoclinic symmetry by the average over three orthogonal measurements. This can involve either a sum over *q* or α. In the special case of a spherical symmetry on single measurements suffices.

For magnetic samples this white line intensity can be achieved analogically by using linear polarized light while performing an angular average. If one uses circular polarized light the sample has to be magnetically saturated with its orientation parallel and antiparallel to the X-ray propagation direction α summing over both intensities.

This orientation independent resonant X-ray absorption follows an important intensity sum rule (illustrated in figure 2.7):

"The angle-average intensity of the combined L$_3$ and L$_2$ resonances is directly proportional to the total number of d states above the Fermi level, i.e., the number of holes in the d band"[3]
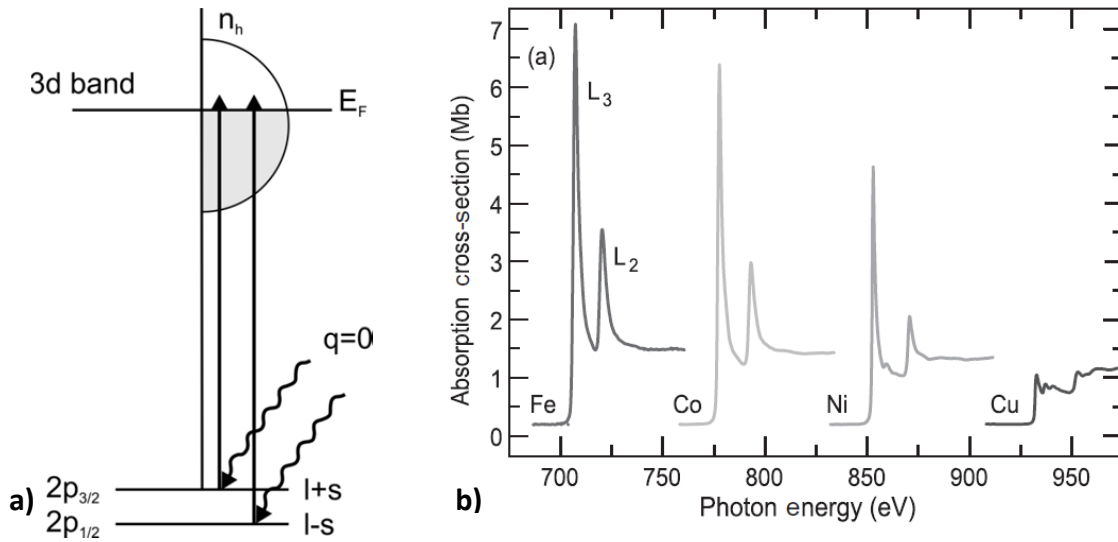
Figure 2.7[3,4] Illustration of the intensity sum rule by **(a)** a scheme of the absorption of linear polarized X-ray photons and **(b)** normalized $L_{2,3}$ edge X-ray absorption spectra of the 3d metals iron, cobalt, nickel and copper.
The absorption intensity drops with increasing number of 3d electrons, i.e. less holes in the valence band.

The "white line intensity" for a core (n, c) to valence (n´, L) transition with $c = L -1$ is proportional to the number of unoccupied states in the valence shell N_h.

$$\langle I \rangle = C \cdot N_h \quad (2.38)$$

with

$$C = AR^2 \frac{L}{3(2L+1)} \quad (2.39)$$

and

$$A = \frac{4\pi^2 \hbar \omega}{137} \quad (2.40)$$

and R is the radial matrix element for the $nc \rightarrow n´L$ transition.

2.3.3 XMCD and sum rule analysis

Following the intensity sum rule for the charge and using circular polarized X-ray photons, one can make the X-ray absorption "spin dependent". This enables a detection of a difference in X-ray absorption that is proportional to the "spin up" and "spin down" holes in the valence shell, i.e. the resulting magnetic moment.

The basis for this "spin dependent" X-ray absorption can be described by a simple two step model: In the first step the X-ray photon is absorbed by the spin-orbit split ground state (e.g. the $2p_{3/2}$ and the $2p_{1/2}$ levels for a 2p to 3d transition). Due to the spin orbit coupling in the initial state the angular momentum of the exciting X-ray photon is transferred in part to the spin of the excited electron. Thereby this electron becomes spin polarized. The spin polarization is opposite for the two core levels due to their opposite spin orbit coupling (*l + s* and *l - s*). The quantization axis of the excited electrons is identical to that of the photon angular momentum, i.e. parallel or antiparallel to the X-ray propagation direction.

In the second step the exchange split valence shell with an uneven population of "spin up" and "spin down holes" acts as a detector for the spin polarized photon electrons. The maximum difference in X-ray absorption can be detected if the "detector axis" (the spins of the valence shell) is aligned to the photon angular momentum / the X-ray propagation direction.
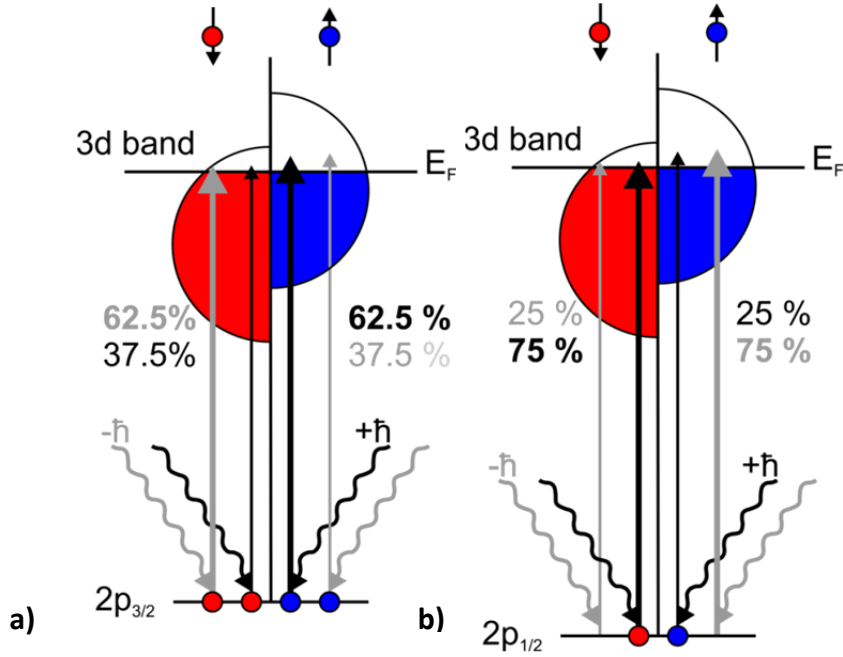
Figure 2.8[4] Relative transition probabilities for spin up (↑) and spin down (↓) electrons from the spin orbit split 2p levels, i.e. $2p_{3/2}$ **(a)** and $2p_{1/2}$ **(b)** level upon excitation with circularly polarized photons with q = ±1 (q = -1 = -ℏ = transition marked in grey and q = +1 = +ℏ = transitions marked in black)

Transition probabilities for the excitation of spin up or spin down electrons switch when the photon helicity is reversed. Positive (q = +1) circularly polarized light predominantly excites spin up electrons at the L_3 edge ($2p_{3/2} \rightarrow 3d$) and at the L_2 edge ($2p_{1/2} \rightarrow 3d$), it mostly excites spin down electrons. The situation is reversed for negative (q = -1) circularly polarized photons.

The relative excitation probabilities given in Fig. 2.9 can be derived from the transition matrix elements for an electronic transition from a ground state |a⟩ with a configuration $|c, m_c, m_s⟩$ to a final state |b⟩ with $|l, m_l, m_{s'}⟩$.[25,26]

$$\langle n', l, m_l | P_{(1)}^{+1} | n, c, m_c \rangle = \sqrt{\frac{(c+m_c+2)(c+m_c+1)}{2(2c+3)(2c+1)}} R \quad (2.41)$$

$$\langle n', l, m_l | P_{(1)}^{-1} | n, c, m_c \rangle = \sqrt{\frac{(c-m_c+2)(c-m_c+1)}{2(2c+3)(2c+1)}} R \quad (2.42)$$

n (n')   principal quantum number of the core (final) state
c (l)   orbital angular momentum quantum number of the core (final) state
m_C (m_l)   orbital magnetic quantum number of the core (final) state

d level $|m_l, m_s\rangle$ $|2,\downarrow\rangle$ $|0,\uparrow\rangle$ $|1,\uparrow\rangle$ $|1,\downarrow\rangle$

$\Delta l = +1$
$\Delta m_l = q = +1$
$\Delta m_s = 0$

60%   10%   15%   15%

$m_j = +1/2$ $\sqrt{2/3}|m_l = 1,\downarrow\rangle$ + $-1/\sqrt{3}|m_l = 0,\uparrow\rangle$ $-1/\sqrt{3}\,Y_{1,0}(\uparrow) + \sqrt{2/3}\,Y_{1,1}(\downarrow)$

$p_{1/2}$

$-\sqrt{2/3}|m_l = -1,\uparrow\rangle$ + $1/\sqrt{3}|m_l = 0,\downarrow\rangle$ $+1/\sqrt{3}\,Y_{1,0}(\downarrow) - \sqrt{2/3}\,Y_{1,-1}(\uparrow)$

a) $m_j = -1/2$

d level $|m_l, m_s\rangle$ $|0,\downarrow\rangle$ $|-2,\uparrow\rangle$ $|-1,\uparrow\rangle$ $|-1,\downarrow\rangle$

$\Delta l = +1$
$\Delta m_l = q = -1$
$\Delta m_s = 0$

10%   60%   15%   15%

$m_j = +1/2$ $\sqrt{2/3}|m_l = 1,\downarrow\rangle$ + $-1/\sqrt{3}|m_l = 0,\uparrow\rangle$ $-1/\sqrt{3}\,Y_{1,0}(\uparrow) + \sqrt{2/3}\,Y_{1,1}(\downarrow)$

$p_{1/2}$

$-\sqrt{2/3}|m_l = -1,\uparrow\rangle$ + $1/\sqrt{3}|m_l = 0,\downarrow\rangle$ $+1/\sqrt{3}\,Y_{1,0}(\downarrow) - \sqrt{2/3}\,Y_{1,-1}(\uparrow)$

b) $m_j = -1/2$
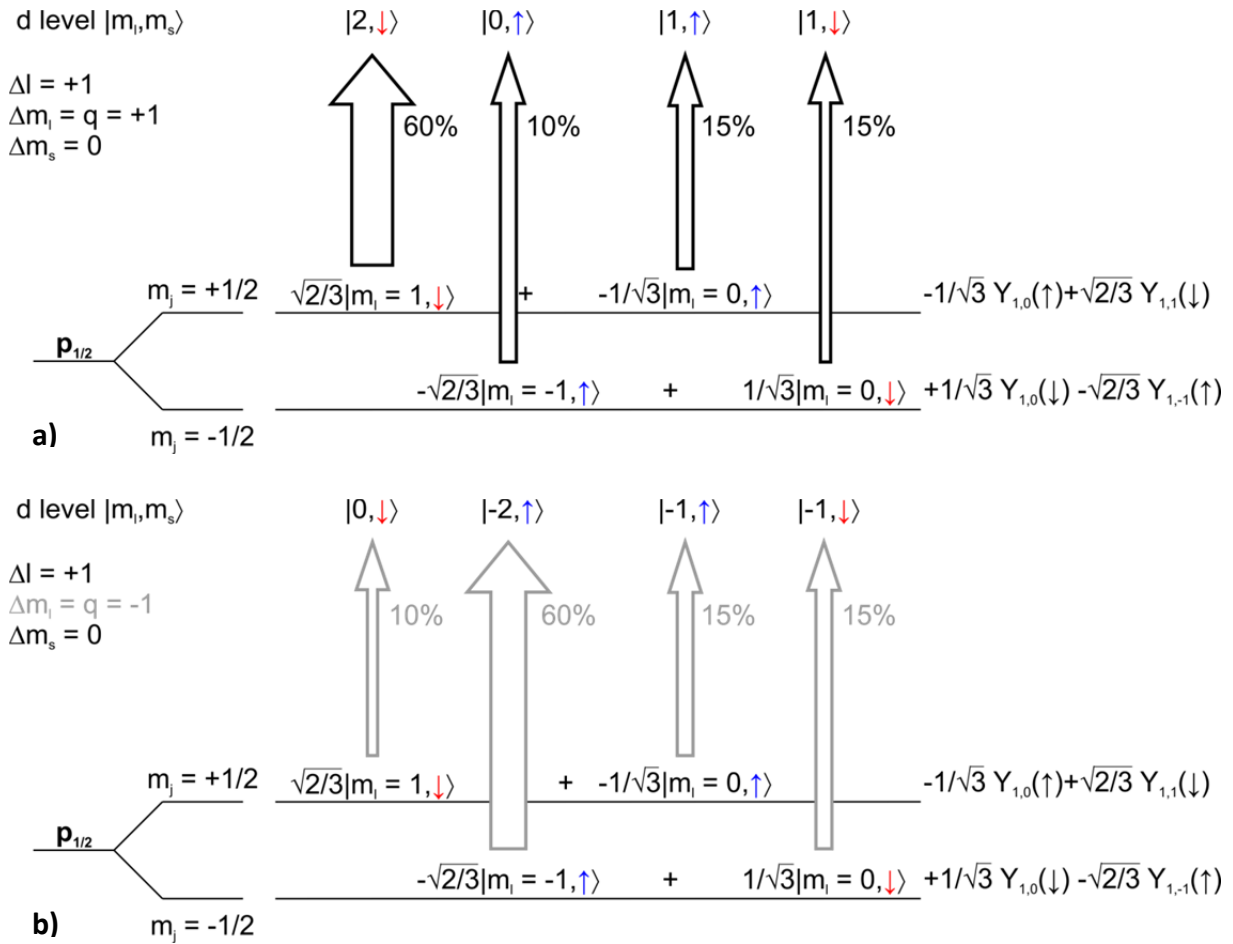
Figure 2.9[4] Transition probabilities from the different $m_j = \pm 1/2$ states (energetically identical) of the $p_{1/2}$ spin orbit split level into final d states in an LS coupling scheme (modified, from Ref. [27]). The statistical weights of the individual transitions are given for the absorption of either a photon with angular momentum **(a)** $q = +\hbar$ or **(b)** $q = -\hbar$. Thus, $\Delta m_l = +1$ for Fig. 2.9a and $\Delta m_l = -1$ for Fig. 2.9b. $\uparrow$ denotes spin up and $\downarrow$ spin down states. The representation of the electronic state in terms of spherical harmonics is given on the right.

Note that the photon angular momenta are not completely transferred to the photon spin. Part of the photon angular momentum is transferred to the electron angular momentum. This angular momentum of the excited electron is also "detected" by the valence shell if the valence shell possesses an angular momentum.
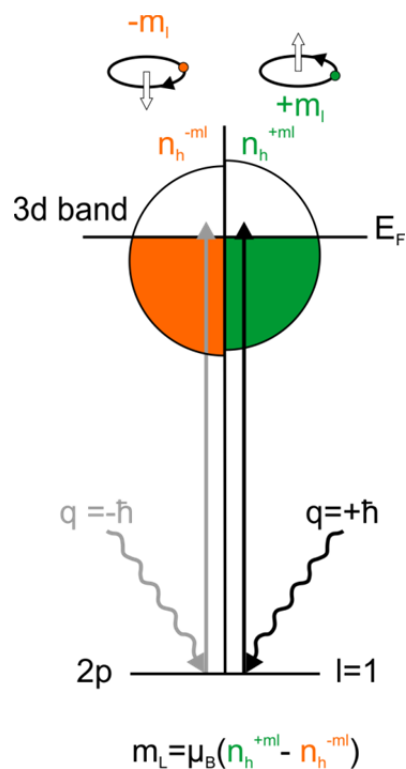
Figure 2.10[4] Probing of orbital angular momentum by XMCD spectroscopy. If the valence shell has an orbital angular momentum quantum number $l \neq 0$, a net orbital angular momentum can arise if the m_L states are not equally occupied.

Due to angular momentum conservation, after the absorption of a negative (q = -1) circularly polarized photon, only transitions with $\Delta m_l = -1$ are allowed. After the absorption of a positive (q = +1) circularly polarized photon, only transitions with $\Delta m_l = +1$ are allowed. Dipole allowed transitions following the dipole selection rules derived from Eq. 2.31a,b for a 2p to 3d transition are shown in Fig. 2.11.
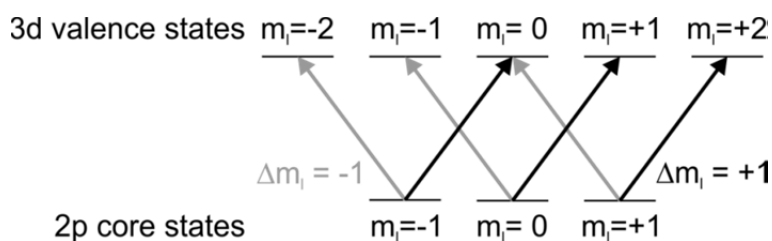
Figure 2.11[28] Sensitivity of the XMCD effect of orbital magnetism.

In summary, the excited electron carries the angular momentum of the absorbed X-ray photon as different spin and orbital momentum degrees of freedom, which can be detected by the magnetic

2. Theoretical background

valence shell. The detection becomes visible as a difference in X-ray absorption using left and right handed circular polarized light.

The spin and orbital contribution to the difference in X-ray absorption have been derived by Thole and Carra in the form of so called "sum rules"[29,30]. One important issue in their elaborate derivation was the elimination of the radial matrix elements by the use of the ratio of magnetic and nonmagnetic absorption profiles[31]. They have been validated for the $L_{3,2}$ edges by Chen et al.[32,33]. The sum rules derived by Thole and Carra read as:

$$\frac{-\left(\int_{j_+}\left(\mu^+(E)-\mu^-(E)\right)\cdot dE - b\int_{j_-}\left(\mu^+(E)-\mu^-(E)\right)\cdot dE\right)}{\int_{j_++j_-}\left(\mu^+(E)-\mu^-(E)+\mu^0(E)\right)\cdot dE} = \frac{c\langle S_z\rangle + d\langle T_z\rangle}{n_h} \quad (2.43a)$$

$$\frac{-\left(\int_{L_3}\left(\mu^+(E)-\mu^-(E)\right)\cdot dE - b\int_{L_2}\left(\mu^+(E)-\mu^-(E)\right)\cdot dE\right)}{\int_{L_2+L_3}\left(\mu^+(E)-\mu^-(E)+\mu^0(E)\right)\cdot dE} = \frac{c\langle S_z\rangle + d\langle T_z\rangle}{n_h} \quad (2.43b)$$

for the spin magnetic moment and

$$\frac{\int_{j_++j_-}\left(\mu^+(E)-\mu^-(E)\right)\cdot dE}{\int_{j_++j_-}\left(\mu^+(E)-\mu^-(E)+\mu^0(E)\right)\cdot dE} = a\frac{\langle L_z\rangle}{n_h} \quad (2.44a)$$

$$\frac{\int_{L_2+L_3}\left(\mu^+(E)-\mu^-(E)\right)\cdot dE}{\int_{L_2+L_3}\left(\mu^+(E)-\mu^-(E)+\mu^0(E)\right)\cdot dE} = a\frac{\langle L_z\rangle}{n_h} \quad (2.44b)$$

for the orbital magnetic moment with:

j_+, j_-	transitions from spin orbit split core levels
μ^+	XA spectrum recorded with positive circularly polarized light; q = +ℏ
μ^-	XA spectrum recorded with negative circularly polarized light; q = -ℏ
μ_0	XA spectrum recorded with linearly polarized light; q = 0
n_h	number of holes in the final state / shell (= $4l_f + 2 - n$)
a, b, c, d	sum rule related prefactors

$\langle S_z \rangle$ and $\langle L_z \rangle$ are the expectation values of the spin and orbital moments projected onto the quantization axis. The quantization axis coincides with the external magnetic field and the X-ray propagation direction. $\langle T_z \rangle$ is the expectation value for the magnetic dipole term. It describes a aspheric spin contribution in a non-cubic system. It treats a possible anisotropy in the spin distribution of the investigated sample. It corresponds to a spin asymmetry along the quantization axis. It may modulate the spin magnetic moment in a highly anisotropic medium by up to 20 %[34], and it would cancel by an angular average[35]. For X-ray absorption spectra given by a 3d to 4f transition the integration over the L$_{3,2}$ edges can be replaced by the M$_{5,4}$ edges.

l_f and l_i denote the orbital angular momentum of the initial and final state of the X-ray absorption. The dipole selection rule denotes $l_f = l_i \pm 1$. The orbital angular momenta of the initial and final state also define the prefactors *a*, *b* and *c*.

Table 2.1 Sum rule related prefactors

l_i	l_f	a	b	c	d
s: 0	p: 1	1	-	-	-
p: 1	d: 2	1/2	2	2/3	7/3
d: 2	f: 3	1/3	3/2	2/3	2

In usual measurements only the X-ray absorption for left and right handed circular polarized light is measured and the spectrum for linearly polarized light is not known. For samples with a cubic symmetry the sum rule´s denominator can be approximated by:

$$\mu^+(E) + \mu^-(E) + \mu^0(E) \approx \mu^+(E) + \mu^-(E) + \frac{\left(\mu^+(E) + \mu^-(E)\right)}{2}$$

$$= \frac{3}{2}\left(\mu^+(E) + \mu^-(E)\right) \quad (2.45)$$

Even for a non-cubic system the approximated integral does not differ significantly from the measured sum over all 3 photon polarizations.

The projection of the spin ($m_S^{(z)}$) and orbital ($m_L^{(z)}$) magnetic moments onto the quantization axis and the resulting projection of the total magnetic ($m_J^{(z)}$) moment can be derived from the

2. Theoretical background

expectation values $\langle S_z \rangle$ and $\langle L_z \rangle$ of the spin and orbital moments projected onto the quantization axis by the following relation:

$$m_L^{(z)} = -g_L \mu_B \langle L_z \rangle \quad (2.46)$$

$$m_S^{(z)} = -g_S \mu_B \langle S_z \rangle \quad (2.47)$$

$$m_J^{(z)} = m_L^{(z)} + m_S^{(z)} = -\mu_B(g_L\langle L_z \rangle + g_S\langle S_z \rangle)$$

$$= -\mu_B(\langle L_z \rangle + 2\langle S_z \rangle) = -\mu_B g_J \langle J_z \rangle \quad (2.48)$$

$m_S^{(z)}, m_L^{(z)}, m_J^{(z)}$	spin, orbital and total magnetic moment projected onto the quantization axis
$\langle S_z \rangle, \langle L_z \rangle, \langle J_z \rangle$	expectation value of the spin, orbital and total angular momentum projected onto the quantization axis
g_S	g-factor the electron spin; g = 2.0
g_L	g-factor of the orbital moment; g_L = 1.0
g_J	g-factor of the total magnetic moment
μ_B	Bohr magneton

Following these relations the equations 2.40 and 2.41 can be rewritten as following:

$$m_S^{(z)} = g_S \mu_B \frac{\left(\int_{L_3}\left(\mu^+(E)-\mu^-(E)\right)\cdot dE - b\int_{L_2}\left(\mu^+(E)-\mu^-(E)\right)\cdot dE\right)}{c\int_{L_2+L_3}(\mu^+(E)-\mu^-(E)+\mu^0(E))\cdot dE} n_h - g_S \mu_B \frac{d}{c}\langle T_z \rangle \quad (2.49)$$

$$m_L^{(z)} = -g_L \mu_B \frac{\int_{L_2+L_3}\left(\mu^+(E)-\mu^-(E)\right)\cdot dE}{a\int_{L_2+L_3}(\mu^+(E)-\mu^-(E)+\mu^0(E))\cdot dE} n_h \quad (2.50)$$

Note that the underlying two step model as well as the sum rules themselves imply important premises for their application:[31]

- The absorption into final states with reduced orbital moments (e.g. 2p → 4s) must be negligible as compared to the absorption for increased orbital moments (e.g. 2p → 3d).
- The radial matrix elements should not be varying as a function of the energy of the final state. This happens if final state electrons are less bound and more delocalized compared to final state excitations close to the absorption threshold.

- Relativistic corrections to the radial matrix elements should be negligible. Or, in other words, the radial matrix element should not be different for the $l_i + \frac{1}{2}$ and the $l_i - \frac{1}{2}$ excitation.
- The dipole approximation should be a good approximation, or higher terms in the expansion, like the quadrupolar transition, should have spectral weight less than the error bar.
- For the effective spin sum rule the $l_i + \frac{1}{2}$ and the $l_i - \frac{1}{2}$ excitation, for example. The L_3 and L_2 resonances must be separable in terms of energy. This includes spectral overlap and quantum mechanical mixing, that is a mixture of $l_i + \frac{1}{2}$ and $l_i - \frac{1}{2}$ excitation of the same energy induced by an additional interaction, for example, 2p – 3d Coulomb interaction.

2.4 References

[1]   Getzlaff, M. *Fundamentals of magnetism*; Springer Science & Business Media, 2007.

[2]   Stefanita, C. G. *Magnetism: Basics and Applications*; Springer, 2012.

[3]   Stöhr, J.; Siegmann, H. C., *MAGNETISM*, *Solid-State Sciences. Springer, Berlin, Heidelberg* **2006**, 5.

[4]   Meyer, J. D. *Spin and orbital contributions to the magnetic moment of isolated transition metal clusters and complexes*. Doctoral Thesis, **2014**.

[5]   Elmore, W., *THE MAGNETIZATION OF FERROMAGNETIC COLLOIDS*, *Physical Review* **1938**, *54*, 1092.

[6]   Bean, C.; Livingston, J., *SUPERPARAMAGNETISM*, *Journal of Applied Physics* **1959**, *30*, S120.

[7]   Langenberg, A.; Hirsch, K.; Lawicki, A.; Zamudio-Bayer, V.; Niemeyer, M.; Chmiela, P.; Langbehn, B.; Terasaki, A.; Issendorff, B. V.; Lau, J. T., *SPIN AND ORBITAL MAGNETIC MOMENTS OF SIZE-SELECTED IRON, COBALT, AND NICKEL CLUSTERS*, *Physical Review B* **2014**, *90*.

[8]   Niemeyer, M.; Hirsch, K.; Zamudio-Bayer, V.; Langenberg, A.; Vogel, M.; Kossick, M.; Ebrecht, C.; Egashira, K.; Terasaki, A.; Moller, T.; Issendorff, B. V.; Lau, J. T., *SPIN COUPLING AND ORBITAL ANGULAR MOMENTUM QUENCHING IN FREE IRON CLUSTERS*, *Physical Review Letters* **2012**, *108*.

[9]   Fauth, K.; Münzing, B., *UNTERDRÜCKTER IMPULS*, *Physik Journal* **2012**, *11*, 22.

[10]   Aromí, G.; Winpenny, R. E. *Single-molecule magnets and related phenomena*; Springer New York, 2006.

[11]   D. Gatteschi, R. S., J. Villain *Molecular Nanomagnets*; Oxford University Press: Oxford, 2006.

[12]   Christou, G.; Gatteschi, D.; Hendrickson, D. N.; Sessoli, R., *SINGLE-MOLECULE MAGNETS*, *Mrs Bulletin* **2000**, *25*, 66.

[13]   Glaser, T., *RATIONAL DESIGN OF SINGLE-MOLECULE MAGNETS: A SUPRAMOLECULAR APPROACH*, *Chemical Communications* **2011**, *47*, 116.

[14]   Lis, T., *PREPARATION, STRUCTURE, AND MAGNETIC-PROPERTIES OF A DODECANUCLEAR MIXED-VALENCE MANGANESE CARBOXYLATE*, *Acta Crystallographica Section B-Structural Science* **1980**, *36*, 2042.

[15]   Leuenberger, M. N.; Loss, D., *QUANTUM COMPUTING IN MOLECULAR MAGNETS*, *Nature* **2001**, *410*, 789.

[16]   Aromí, G.; Aguila, D.; Gamez, P.; Luis, F.; Roubeau, O., *DESIGN OF MAGNETIC COORDINATION COMPLEXES FOR QUANTUM COMPUTING*, *Chemical Society Reviews* **2012**, *41*, 537.

[17]   Dirac, P. A. "The quantum theory of the emission and absorption of radiation"; Proceedings of the Royal Society of London A: Mathematical, Physical and Engineering Sciences, 1927.

[18]   Messiah, A. QUANTUM MECHANICS. VOL. I, 1958.

[19]   Als-Nielsen, J.; McMorrow, D. *Elements of modern X-ray physics*; John Wiley & Sons, 2011.

[20]   Schiff, L. I., *QUANTUM MECHANICS, 3RD*, *New York: M cGraw-Hill* **1968**, 61.

[21]   Mandl, F.; Shaw, G. *Quantum field theory*; John Wiley & Sons, 2010.

[22]   Kramers, H. A.; Heisenberg, W., *ÜBER DIE STREUUNG VON STRAHLUNG DURCH ATOME*, *Zeitschrift für Physik A Hadrons and Nuclei* **1925**, *31*, 681.

[23]   Shore, B. W.; Menzel, D. H., *PRINCIPLES OF ATOMIC SPECTRA*, **1968**.

[24]   Cowan, R. D. *The theory of atomic structure and spectra*; Univ of California Press, 1981; Vol. 3.

[25]   Funk, T.; Deb, A.; George, S. J.; Wang, H.; Cramer, S. P., *X-RAY MAGNETIC CIRCULAR DICHROISM—A HIGH ENERGY PROBE OF MAGNETIC PROPERTIES*, *Coordination chemistry reviews* **2005**, *249*, 3.

[26]   Stöhr, J.; Wu, Y. X-ray magnetic circular dichroism: Basic concepts and theory for 3d transition metal atoms. In *New Directions in Research with Third-Generation Soft X-Ray Synchrotron Radiation Sources*; Springer, 1994; pp 221.

[27]   Schütz, G.; Goering, E.; Hermann, S. Synchrotron Radiation Techniques Based on X-ray Magnetic Circular Dichroism. In *Handbook of Magntism and Advanced Magnetic Matierals*; Kronmüller, H., Parkin, S., Eds.; John Wiley & Sons, Ltd., 2007; Vol. 3.

[28]   Lau, J. T. *Magnetische Eigenschaften kleiner massenseparierter Übergansgsmetallcluster*. Doctoral, Universität Hamburg, **2002**.

[29]   Carra, P.; Thole, B. T.; Altarelli, M.; Wang, X. D., *X-RAY CIRCULAR-DICHROISM AND LOCAL MAGNETIC-FIELDS*, *Physical Review Letters* **1993**, *70*, 694.

[30]   Thole, B. T.; Carra, P.; Sette, F.; Vanderlaan, G., *X-RAY CIRCULAR-DICHROISM AS A PROBE OF ORBITAL MAGNETIZATION*, *Physical Review Letters* **1992**, *68*, 1943.

[31]   Schütz, G.; Goering, E.; Stoll, H., *Synchrotron Radiation Techniques Based on X-ray Magnetic Circular Dichroism*, *Handbook of Magnetism and Advanced Magnetic Materials* **2007**.

[32]   Chen, C. T.; Idzerda, Y. U.; Lin, H. J.; Smith, N. V.; Meigs, G.; Chaban, E.; Ho, G. H.; Pellegrin, E.; Sette, F., *EXPERIMENTAL CONFIRMATION OF THE X-RAY MAGNETIC CIRCULAR-DICHROISM SUM-RULES FOR IRON AND COBALT*, *Physical Review Letters* **1995**, *75*, 152.

[33]   Chen, C.; Sette, F.; Ma, Y.; Modesti, S., *Soft-x-ray magnetic circular dichroism at the L 2, 3 edges of nickel*, *Physical Review B* **1990**, *42*, 7262.

[34]   Sipr, O.; Minar, J.; Ebert, H., *On the importance of the magnetic dipole term T_z in analyzing X-ray magnetic circular dichroism spectra of clusters*, *Europhysics Letters* **2009**, *87*, 67007.

[35]   Stöhr, J.; König, H., *Determination of Spin- and Orbital-Moment Anisotropies in Transition Metals by Angle-Dependent X-ray Magnetic Circular Dichroism*, *Physical Review Letters* **1995**, *75*, 3748.

- 36 -

3. EXPERIMENTAL METHODS

All data concerning spin and orbital magnetic moments of isolated transition metal clusters was obtained with the GAMBIT (General Abstraction of Magnetic moments at BESSY by Ion Trapping) setup. The investigated ions were produced in a home built Laser VAPorization (LVAP) cluster ion source[1,2]. A modified Fourier Transform Ion Cyclotron Resonance (FT-ICR) mass spectrometer served to record the presented polarization dependent X-ray absorption (XA) and respective X-ray Magnetic Circular Dichroism (XMCD) spectra. A detailed description of the performed modifications is given in the doctoral thesis of Heinrich Kampschulte[3] and in an earlier publication[4]. We recorded all spectra by Total Ion Yield (TIY) spectroscopy (cf. chapter 3.1). A detailed description of the data acquisition scheme constructed by S. Peredkov, J.D. Meyer and myself which is used for the measurements on isolated transition metal clusters is given in the doctoral thesis of J. D. Meyer[5].

The results on spin and orbital magnetic moments of isolated Single Molecule Magnets (SMM) were obtained using the NanoClusterTrap - setup operated by the group of T. Lau (Helmholtz Zentrum Berlin). We exchanged the otherwise equipped magnetron sputter source by a custom built ElectroSpray Ionization (ESI) source kindly provided by the group of T. Schlathölter (University of Groningen, The Netherlands).

3.1. Total Ion Yield (TIY) spectroscopy

Dealing with highly diluted samples in the gas phase, the application of the Beer - Lambert[6] law is not possible. Due to the very low sample density, the initial light intensity is not altered in a detectable magnitude after passing through the sample. In solid state physics the contradictory effect accurse. Here the sample density is often that high that the light will be completely absorbed, which also makes the determination of relative changes in the irradiated light impossible. Here Total Electron Yield (TEY)[7] and Total Fluorescence Yield (TFY)[7] spectroscopy serve to overcome this problem. Not the initial photon absorption but resulting effects e.g. electron emission (TEY) or fluorescence (TFY) after the excitation of a core electron are detected. These two techniques have become standard methods of recording X-ray absorption spectra in solid state physics[7,8]. Although these techniques themselves cannot be applied to gas phase samples, the general concept of looking

3. Experimental methods

for changes in the irradiated sample can. In the gas phase this action type spectroscopy is called Total Ion Yield (TIY) spectroscopy. For this technique the ion of interest is isolated, e.g. in an ion trap coupled to a mass spectrometer, and irradiated with the respective light. In our case we irradiate our samples with circularly polarized soft X-ray photons from an undulator beamline. Absorption of an X-ray photon (500 – 1300 eV) leads to the deposition of the photons energy within the sample (cf. chapter 2.3.1). In the gas phase this energy cannot be redistributed into a crystal lattice or a supporting substrate. After the X-ray absorption the isolated sample starts to fragment because of the high amount of energy deposited in the sample molecule by the X-ray photon. If the energy of the irradiated X-ray beam coincides with a resonant absorption within our sample, the absorption intensity will increase drastically. Subsequently, fragment production will increase. As the experiments are conducted within a mass spectrometer, charged fragments can be captured and the amount of fragments can be recorded as a function of X-ray energy. The amount of fragments as a function of photon energy then represents the X-ray absorption spectrum. This enables us to record polarization dependent X-ray absorption (XA) spectra of highly diluted samples in the gas phase[4,9-11].

3.2 The UE52-PGM beamline @ BESSY II

For the presented measurements both experiments (the GAMBIT setup and the NanoClusterTrap) were connected to the UE52-PGM beamline at the BESSY II synchrotron facility of the Helmholtz Zentrum Berlin. A detailed explanation of the creation of synchrotron radiation can be found in the literature[12]. Here, only a very brief introduction is given.

At the BESSY II synchrotron electrons are accelerated to relativistic energies of 1.7 GeV and then transferred into the storage ring. Within the storage ring, straight sections alternate with dipole magnets. The dipole magnets serve to bend the electron beam to form a circular beam path of the electrons. Passing through these dipole magnets, the stored electrons eject synchrotron radiation due to the radial acceleration within these dipoles. This ejected light from the dipole magnets can be monochromatized and used for X-ray experiments.

So called undulators present another way of creating more brilliant synchrotron radiation. They are located within the straight sections of the storage ring. Within an undulator, permanent magnets with alternating polarity serve to induce an oscillatory motion of the electrons passing through the undulator (Fig. 3.1). This oscillatory motion (acceleration) also induces X-ray emission from the electrons. If the radiation from different electrons within the undulator interferes constructively, highly brilliant X-ray radiation is emitted. The photon energy emitted from the undulator depends on

the gap between the permanent magnets within the undulator. This gap is variable to tune the undulator for the desired photon energy.
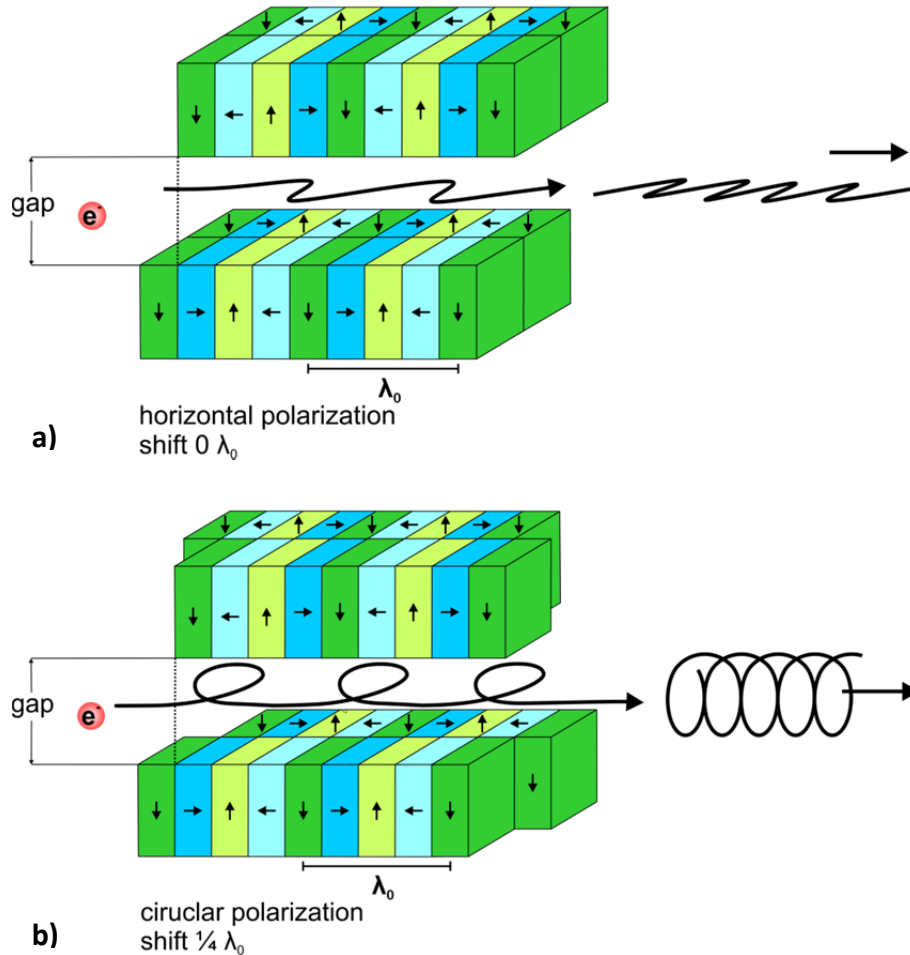
Figure 3.1[13] Positioning of the permanent magnets within an APPLE2 undulator (advanced planar polarized light emitter)[14-16] **(a)** setting of the permanent magnets for horizontal photon polarization **(b)** Setting of the permanent magnets for circular photon polarization.

The UE52 is an undulator beamline equipped with an APPLE2 (advanced planar polarized light emitter)[14-16] undulator. Such an undulator consists of 4 rows of permanent magnets of alternating polarization. They can be shifted independently from each other. The undulator can be set to either eject linear (horizontally or vertically) polarized light as well as circularly (left or right handed) polarized light, depending on the relative position of these permanent magnets (Fig. 3.1).

Figure 3.2 Picture of the APPLE2 undulator at the UE52 beamline at the BESSY II synchrotron facility.

After creation in the undulator the synchrotron radiation is monochromatized by a grating and transferred to the endstation through the beamline. The UE52 beamline provides 90 % circularly polarized soft X-rays in the energy region from 85 to 1600 eV and a photon flux of 10^{12} photons / s (Tab. 3.1).

Table 3.1 Specifications of the UE52-PGM undulator beamline at BESSY II[17]

energy range	85 - 1600 eV (soft X-ray regime)
resolving power at 400 eV	> 10000
polarization	variable
degree of polarization	90 %
photon flux (500 eV - 1000 eV)	$> 10^{12}$ photons / s
divergence	0.8 mrad x 0.2 mrad

Electron loss due to collisions of the electrons with the vacuum tube or residual gas is compensated for by constant injection of new electrons from the synchrotron into the storage ring. By this so called "top up" operation mode the current within the storage ring is kept at a constant 300 mA. The

electrons´ energy loss is compensated for by radio frequency (RF) excitation within 3 cavities spread over the storage ring.

3.3 The GAMBIT setup

3.3.1 Laser VAPorization (LVAP) cluster ion source

Within the GAMBIT setup the investigated cationic transition metal clusters are produced by a home built Laser VAPorization (LVAP) cluster ion source[18,19]. The major components of this source are a home built piezo electric valve[20], an expansion / interaction region and an expansion channel (Fig 3.3).
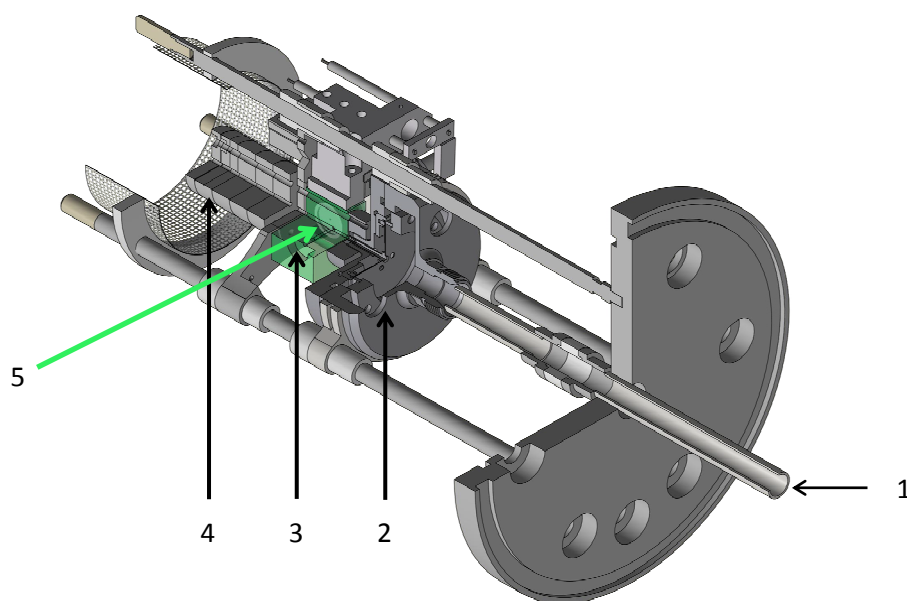
Figure 3.3[5,21] Schematic drawing of the LVAP source: (1) gas inlet (2) piezoelectric valve, (3) expansion / interaction region, (4) expansion channel, (5) laser light path

Within the interaction region, the second harmonic (532 nm) of a Nd:YAG (Innolas, Spitlight200, 20 Hz) laser is focused on a rotation foil comprising of the metal of interest. The thickness of this foil varies between 0.2 and 0.5 mm. The laser pulse creates a plasma at the surface of the rotating metal foil. This plasma contains neutral atoms as well as cationic and anionic species. The plasma is cooled by a transverse He gas pulse. A home built piezo electric valve creates this pulse. It operates with a

backing pressure of 10-20 bar, a repetition rate of 20 Hz to match the laser frequency and an opening time of approximately 40 µs. The gas pulse expands into a vacuum chamber with a pressure of about 5×10^{-7} mbar raising this pressure up to 2×10^{-4} mbar. The expanding gas cools down the atoms and ions created in the plasma and cluster formation starts. Cluster formation completes within the expansion channel. Clusters in the size range of 2 to 30 atoms per cluster are created. Variation of backing pressure, valve opening time and laser-valve-delay serves to influence the intensity maximum in the created cluster size distribution. The cluster charge state of choice is selected by applying according voltages to extract the ionic clusters from the source region.

The cobalt foil was purchased form Alfa Aesar (purity 99.95 %). Ion and Nickel foils were purchased as mono isotopic materials from Oak Ridge National Lab (Fe-56, purity 99.93 %; Ni-58, purity 99.61 %). The choice of mono isotopic materials is necessary to prevent signal reduction in the mass spectrometer due to intensity spreading over several peaks related to the different isotopes. CoAu and CoRh alloy clusters were created from alloy targets with a Co / Rh and Co / Au ratio of 90 / 10 mol % (HMW Hauner).

3.3.2 The FT-ICR mass spectrometer

The GAMBIT setup is a modified Fourier Transform Ion Cyclotron Resonance (FT-ICR) mass spectrometer. It is based on a commercially purchased Bruker Apex IV FT-ICR. Modifications present as an electrostatic quadrupole ion beam bender for multiple source attachments, the Laser Vaporization (LVAP) cluster ion source and a cryogenically cooled FT-ICR ion trap. The trap is of a Bruker Infinity Cell^{TM} design. In our experiments it serves as ion trap, mass separator and mass analyzer at once.

The FT-ICR ion trap is located in the high field region (B = 7 T) of a superconducting solenoid. The trap is connected to a two staged closed cycle He cryostat (Sumitomo SRDK-408S2, compressing unit W-71D) by copper plating. Shielding for radiative heating of the trap is achieved by two actively cooled and three passive shielding tubes. Three temperature sensors (LakeShore, Cernox^{TM}, calibrated from 4 - 325 K) distributed over the cryogenic setup monitor the temperature within the experimental setup.
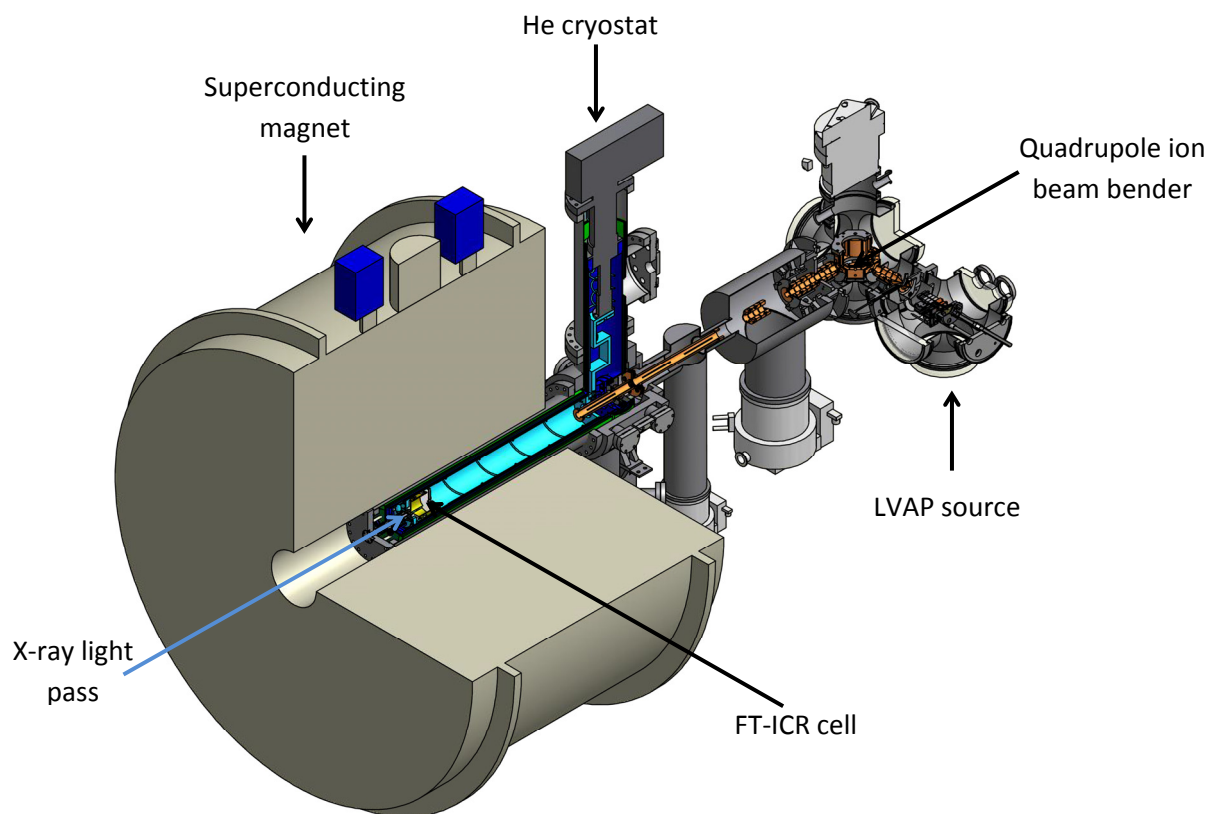
Figure 3.4[5,21] Schematic drawing of the GAMBIT setup, a modified FT-ICR mass spectrometer.

To record the polarization dependent X-ray absorption (XA) spectra, the ions are created in the LVAP ion source. The extracted ion beam is bent by 90° onto the magnetic field axis by the electrostatic quadrupole ion beam bender. Several electrostatic ion optics transfer the ions into the high field region of the superconducting magnet and into the ICR cell, within which the ions are stored. Mass selection of the ion of interest is achieved by radio frequency (RF) excitation of the unwanted ions to such a degree that they are ejected from the ICR cell. A helium gas pulse which passes the second stage of the He cryostat and is thermalized to the trap temperature ($\sim$ 20 K) is injected into the ICR cell. It raises the pressure within the UHV region cell from 5×10^{-10} to 1×10^{-6} mbar. This He gas pulse cools down the ions of interest to the pulse gas temperature of 20 K by collisional cooling. Before irradiation with the X-ray beam the system is allowed to pump down to a pressure of about 2×10^{-8} mbar by entering a pump down delay of 8 s. The X-ray beam from the UE52 undulator beamline enters the ICR cell collinear to the magnetic field from the back of the experiment. The stored and cooled ions are irradiated with the X-ray beam for 10 to 15 s. The XA spectra are recorded by Total Ion Yield (TIY) spectroscopy (cf. chapter 3.1). A detailed description of the setup is given in the

doctoral thesis of H. Kampschulte[3,4]. A detailed description of the data acquisition and the effects of collisional cooling are given in the doctoral thesis of J. D. Meyer[5].

3.3.3 Data treatment

During the investigations of transition metal clusters, "small" fragments dominate the fragmentation pattern in the mass spectra after X-ray excitation, i.e. monomers, dimers and trimers (M^+, M_2^+ and M_3^+). Note that the fragment intensity only makes up several percent of the intensity of the parent cluster investigated (Fig. 3.5). A data point in a single XA spectrum (raw spectrum) recorded by TIY spectroscopy comprises of the summed intensities of all accruing fragments in 2 FT-ICR mass spectra at a given photon energy[4]. These summed intensities are normalized by the photon flux derived from the synchrotron´s storage ring current and the intensity of the parent cluster. These raw spectra are recorded with an alternated use of left and right handed circular polarized X-rays. The spectra we use for the final analysis consist of a sum of 15 to 40 of these normalized raw spectra. We obtain the XMCD spectrum by subtracting the sum of XAS spectra taken with negative photon polarization from the sum of spectra taken with positive photon polarization. This XMCD spectrum is then analyzed in terms of sum rule analysis (cf. chapter 2.3.3)[22,23] The calculated projections of the spin ($m_S^{(z)}$) and orbital ($m_L^{(z)}$) magnetic moments at the given temperature (T = 20 K) and magnetic field (B = 7 T) are scaled to projection at 0 K by the Langevin formula (cf. chapter 2.1.5)[24]. The projection of the magnetic moments at 0 K coincide with the intrinsic spin (m_S) and orbital (m_L) magnetic moments. They are given in μ_B / atom if not denoted otherwise. The total magnetic moments per atom (m_{tot}) are calculated by the sum of m_S and m_L. A much more detailed description of the data treatment is given in the doctoral thesis of Dr. J. D. Meyer[5].
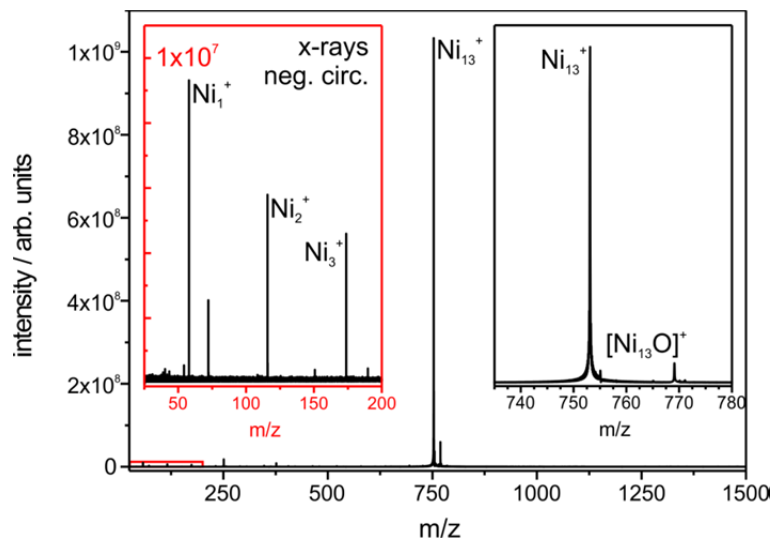
Figure 3.5[5] Mass spectrum of Ni_{13}^+ after isolation collisional cooling and exposure to negative circularly polarized X-rays. The photon energy was set to 853 eV, i.e. the L_3 edge, with a photon flux of about $2 \cdot 10^{12}$ photons / s (ring current = 280 mA).

3. Experimental methods

3.4. The NanoClusterTrap setup

The NanoClusterTrap setup used in the presented ESI-XMCD experiments was built by the groups of Thomas Möller, Bernd von Issendorff and Tobias Lau, operated by the group of Tobias Lau at the UE52 beamline at BESSY II. The 5 T superconducting magnet was provided by Akira Terasaki.

3.4.1 The ElectroSpray Ionization (ESI) source

Electrospray ionization mass spectrometry has become one of the most important "ionization" techniques in modern mass spectrometry[25-27]. The fundamentals of ESI ion formation can be found in the literature[28-31]. The importance of ESI in modern mass spectrometry was underlined by the bestowal of the Nobel-Prize to John Fenn who entitled his noble lecture "Wings for molecular elephants"[32]. Next to proteins with a very high mass to charge ratio[33-35] it is also very efficient in creating ionic species of smaller transition metal complexes[36-38] which will be investigated in the course of this study.

We use a home built ESI source kindly provided by the group of Thomas Schlathölter (University of Groningen, The Netherlands). It consists of a stainless steel spray needle, a stainless steel transfer capillary and a home built radio frequency (RF) ion funnel[39]. The spray needle is placed on an x, y ,z-translation stage outside the vacuum chamber. It is placed several millimeters in front of the transfer capillary and its position is optimized for maximum signal intensity. We apply a voltage of 3 – 3.5 kV between the spray tube and the transfer capillary to form the Taylor cone[40,41] for ESI ion formation. Best signal intensities are achieved by an off axis arrangement of the spray needle and the transfer capillary. In this case only the outer parts of the Taylor cone hit the transfer capillary. The created ions are transferred into vacuum through the transfer capillary. A constantly applied voltage of 11 V serves to heat the capillary. The transferred ions are captured by a home built radio frequency ion funnel. The ion funnel consists of 26 ion lenses with a declining inner diameter. It operates at a frequency of 100 kHz with a peak to peak amplitude of 350 mV. This alternating RF field is overlaid by a constant voltage declining from 120 V on the first ion lens to 25 V on ion lens 26. After the ion funnel the ions are transferred into the first hexapole ion guide of the NanoClusterTrap (cf. chapter 3.4.2)

We prepare all samples as a solution in acetonitrile (CH_3CN) with a concentration of ~ 1 x 10^{-3} mol/l. Hamilton^{TM} gas tight syringes (0.5 – 2.5 ml) placed in an automated syringe pump serve to inject the

sample solution into the spray needle through a peak capillary. Flow rates of the syringe pump vary between 50 and 200 µl/h. We use no purge or nebulizer gas in our ESI setup.

Cationic ions are created by replacing one negatively charged ligand (e.g., CH_3COO^- for $[Fe_4Ln_2]$ structure **I** and the Mn_{12}-acetate as well as NO_3^- for $[Fe_4Ln_2]$ (Ln = Gd, Tb) structure **II,** cf. chapter 5.3.2) with one neutral acetonitrile solvent molecule.

3.4.2 The NanoClusterTrap

The NanoClusterTrap is a custom built mass spectrometer to record Total Ion Yield (TIY) gas phase X-ray absorption spectra (XAS)[42-47] as well as X-ray Magnetic Circular Dichroism (XMCD)[10,48-51] spectra. Main components are: an ion source (magnetron sputter source or electro spray ionization (ESI)), a quadrupole mass filter, an electrostatic quadrupole ion beam bender, a liquid He cooled linear quadrupole ion trap and a reflectron time of flight mass spectrometer.
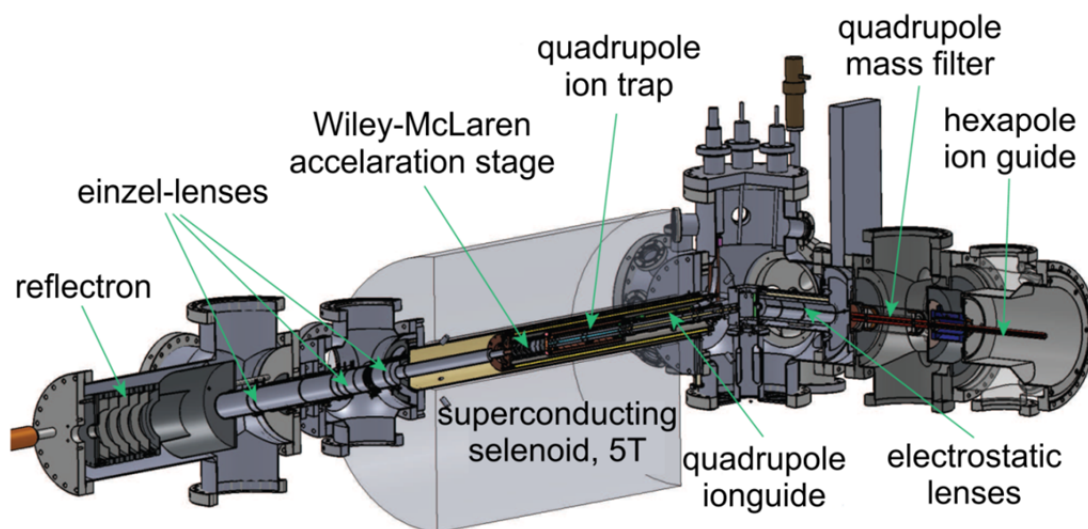
Figure 3.6[52] Schematic drawing of the NanoClusterTrap setup built by the groups of Thomas Möller, Bernd von Issendorff and Tobias Lau, operated by the group of Tobias Lau at the UE52 beamline at BESSY II. The 5 T superconducting magnet was provided by Akira Terasaki. The ion source is not shown in this figure.

For our experiments we used the ESI source for ion creation. After creation and transfer through a hexapole ion guide, the ion of interest is mass selected in a linear quadrupole mass filter (Extrel, 40 – 4000 amu). The mass selected ions are transported further through several electrostatic lenses into the electrostatic quadrupole ion beam bender which bends the ion beam by 90° onto the axis of the

3. Experimental methods

superconducting solenoid and the X-ray propagation direction. The electrostatic lenses prior to the electrostatic ion beam bender serve to compensate for ion losses induced by ion deflection due to the stray field of the superconducting solenoid. After the ion beam bender, a quadrupole ion guide transfers the ions into the linear quadrupole ion trap which is located within the high field region (5 T) of the surrounding superconducting solenoid. The trap is operated at frequencies between 2 and 4 MHz depending on the mass of the investigated ions. The ion trap is cooled by evaporative liquid He cooling down to temperatures < 4 K. A constant He backing pressure of 5×10^{-7} to 1×10^{-6} mbar within the vacuum chamber cools down the ions by collisional cooling. The ions thermalize at a slightly higher temperature of 10 to 15 K[10] due to "heating" of the ions by the radio frequency of the trap. The ions are constantly injected into the ion trap. From the ion trap the ions are ejected into the reflectron time of flight mass spectrometer with a frequency of about 100 Hz to record mass spectra. For the XA spectra recorded by TIY spectroscopy the ions are irradiated for 10 to 15 s at a set photon energy. The X-ray from the undulator beamline enters the setup through the electrostatic ion beam bender. The beam passes through the quadrupole ion guide, the quadrupole ion trap where it irradiates the stored ions and the time of flight mass spectrometer. Behind the reflection stage of the mass spectrometer it is detected by a GaAs-diode and its intensity is recorded for photon flux normalization of the recorded spectra. Spectra on the Fe absorption edges were taken with an exit slit width of 250 μm and a respective resolution of 500 meV at 711 eV. For spectra recorded at the lanthanide absorption edges the exit slit width was 500 μm with a respective spectral resolution of ~ 2.5 eV.

3.4.3 Data treatment

All reported spectra a measured by TIY spectroscopy (cf. chapter 3.1). The investigations on transition metal clusters by the GAMBIT experiment showed the formation of "small" fragments as the prevailing fragmentation behavior after X-ray irradiation. This is also the case for the investigations performed on Single Molecule Magnets (SMMs) with the NanoClusterTrap setup. For the Mn_{12}-acetate, $[MnO]^+$ and $[Mn_2O_3]^+$ are the dominant fragments. For the $[Fe_4Ln_2]$-type SMMs, $[FeO]^+$ is the dominating fragment. The fragment signal intensity only makes up several percent of the signal intensity of the investigated parent molecule. An unambiguous assignment of the fragments was not always possible because the calibration of the time of flight mass spectrometer was sacrificed for optimizing it for maximum fragment signal intensity. For a single data point in a raw spectrum "single shot spectra" of the time of flight mass spectrometer were added over 10-15 s with a frequency of 80-120 Hz at a given photon energy. We recorded spectra for left and right handed circularly polarized light in an alternating manner. For spectra taken on the Fe absorption

edges 3-5 of these raw spectra were added for both X-ray polarizations before further analysis. For spectra on the lanthanide absorption edges, these sums comprise of 6 to 15 raw spectra taken with left and right handed circularly polarized X-rays each. The higher amount of raw spectra summed up for spectra on the lanthanide absorption edges compensates for the lower signal to noise ratio in those raw spectra. This is due to the much lower photon flux of the UE52 beamline (about one order of magnitude) at the energy range of the lanthanide absorption edges compared to the iron absorption edges.
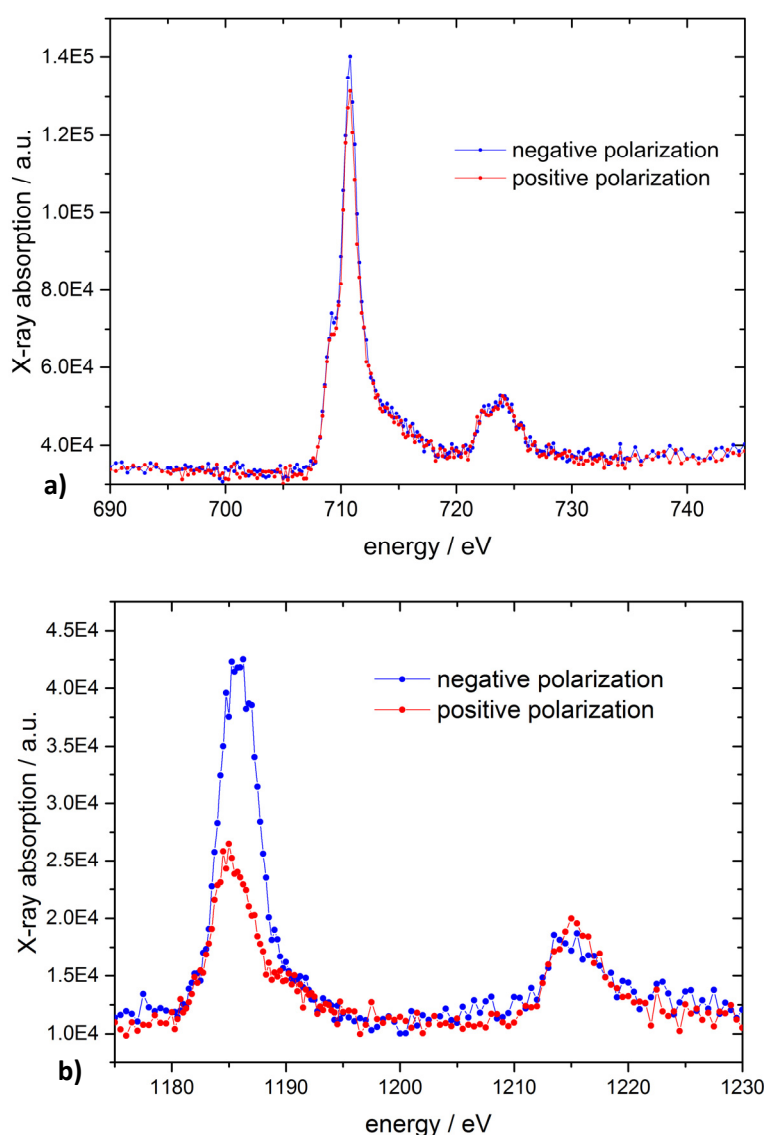
Figure 3.7 XA raw spectra recorded at the **(a)** Fe $L_{3,2}$ and **(b)** Gd $M_{5,4}$ absorption edges in the $[Fe_4Gd_2]^+$ single molecule magnet of structure type **II.**

Normalization of the raw spectra by scaling to a common maximum intensity prevents different contributions from the different raw spectra to the investigated sum.

Figure 3.8 Raw spectra **(a)** and normalized raw spectra **(b)** for the Gd $M_{5,4}$ absorption edges in the $[Fe_4Gd_2]^+$ single molecule magnet of structure type **II**. Shown spectra are taken with negative circular polarized X-rays and in consecutive runs.

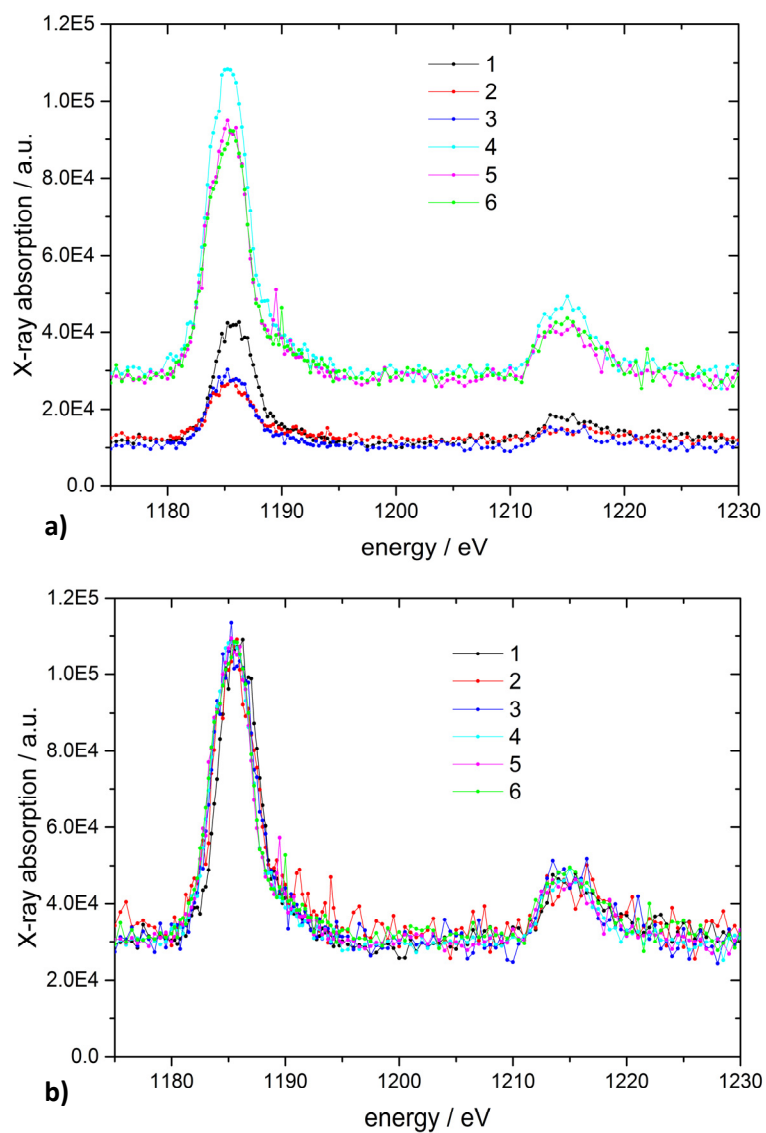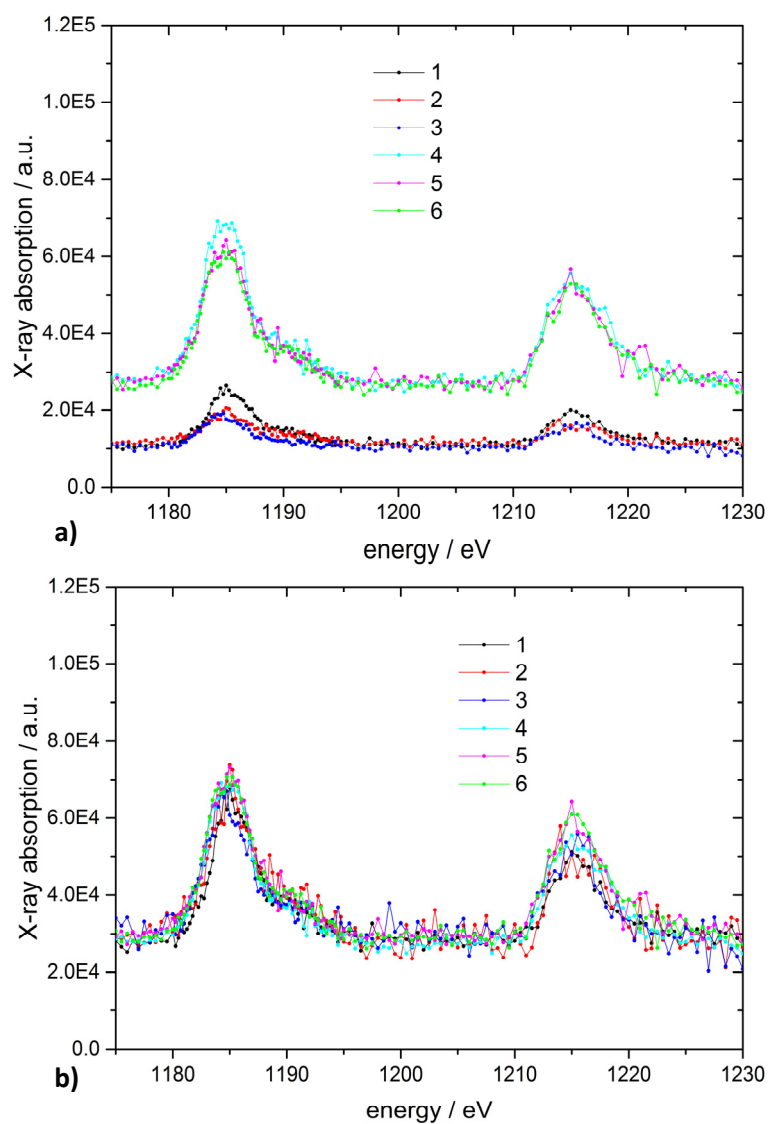**Figure 3.9** Raw spectra **(a)** and normalized raw spectra **(b)** for the Gd $M_{5,4}$ absorption edges in the $[Fe_4Gd_2]^+$ single molecule magnet of structure type **II**. Shown spectra are taken with positive circular polarized X-rays and in consecutive runs.

The resulting sum of the normalized raw spectra for both helicities is given in Fig. 3.10.

3. Experimental methods
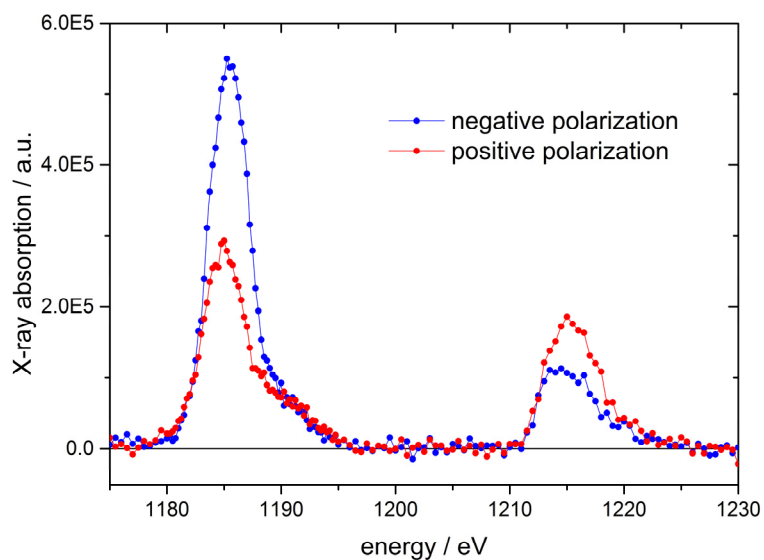
Figure 3.10 Sum of normalized raw spectra for negative and positive circular photon polarization for the [Fe$_4$Gd$_2$]$^+$ single molecule magnet of structure type **II.**

We analyzed these sums of spectra in terms of sum rule analysis (cf. section 2.3.3)[22,23]. The integrals given in the enumerator of Eq. 2.43 and 2.44 are represented in the integrated XMCD spectrum (Fig. 3.11) by the color coded areas and are labeled A and B**.**
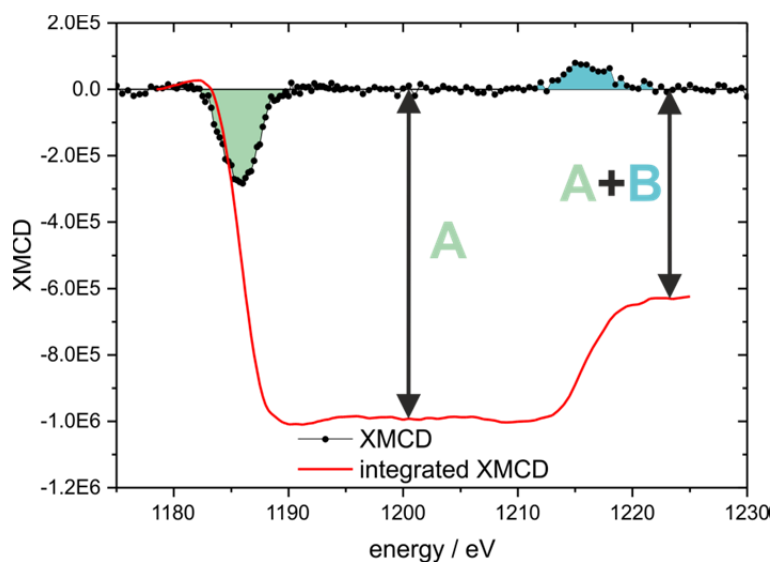
Figure 3.11 XMCD spectrum and its integral over both (M$_{5,4}$) absorption edges for the [Fe$_4$Gd$_2$]$^+$ single molecule magnet of structure type **II.** The integrals over the first and second absorption edge are color coded and named A and B.

Following the assumption made to derive the integral in the denominator of Eq. 2.43 and 2.44 by Eq. 2.45 it can be calculated from the sum of both spectra for the different photon helicities (Fig. 3.12). The resulting integral is named **C**.
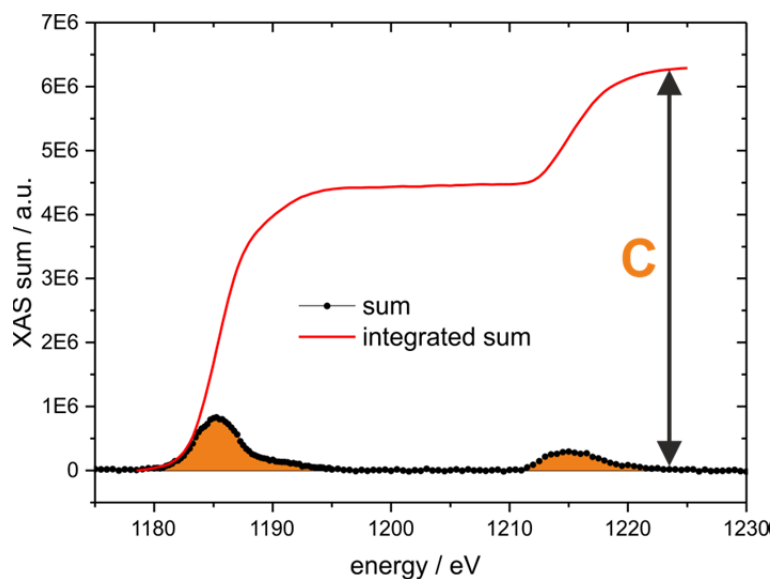
Figure 3.12 Integrated sum of both XA spectra for both photon helicities for the $[Fe_4Gd_2]^+$ single molecule magnet of structure type **II**. The integrated area over both absorption edges ($M_{5,4}$) is color coded and labeled **C**.

A subtraction of a non-resonant background absorption was performed before integrating the sum of X-ray absorption spectra (area **C**) in the case of the investigations on transition metal clusters.[4,5,9] Such a subtraction was not performed in the case of the $[Fe_4Ln_2]^+$ species. On the Ln $M_{5,4}$ absorption edges no non-resonant absorption is visible (Fig. 3.14). On the Fe $L_{3,2}$ absorption edges such a background is visible. For pure transition metal clusters, the non-resonant background absorption is only dependent on the transition metal itself. It can be subtracted by a simple 2 step function[4,5,9]. For the investigated $[Fe_4Ln_2]^+$ compounds the non-resonant background absorption is an overlay of non-resonant background absorptions of the containing elements Fe, C, N, O and H (cf. chapter 5.2.3). This makes an educated guess for a subtraction of the non-resonant background very difficult. Such an assumption would lead to an error in the calculated magnetizations that is equal or even larger than the error induced by omission of a non-resonant background subtraction. The omission of this background subtraction implies higher calculated magnetizations. We estimate this error to be less than 5 %.

Replacing the integrals in Eqs. 2.49 and 2.50 (chapter 2.3.3) by the above given color coded areas **A**, **B** and **C** they can be rewritten as:

3. Experimental methods

$$m_S^{(z)} = g_S \mu_B \frac{(A - bB)}{c \frac{3}{2} C} n_h - g_S \mu_B \frac{d}{c} \langle T_z \rangle \quad \text{(3.1)}$$

$$m_L^{(z)} = -g_L \mu_B \frac{A + B}{a \frac{3}{2} C} n_h \quad \text{(3.2)}$$

n_h	number of holes in the final state / shell $(= 4l_f + 2 - n)$
g_S	g-factor the electron spin; $g_S = 2.0$
g_L	g-factor of the orbital moment; $g_L = 1$
μ_B	Bohr magneton
a, b, c, d	sum rule related prefactors (cf. Tab. 2.1)

We extract the projections ($m_S^{(z)}$ and $m_L^{(z)}$) of the intrinsic spin (m_S) and orbital (m_L) magnetic moments by sum rule analysis. For the $[Fe_4Ln_2]^+$ compounds this was done on the Fe $L_{3,2}$ and the Ln $M_{5,4}$ edges. This was not done in the case of the Mn_{12}-acetate compound. For the absorption on the Mn $L_{3,2}$ absorption edges the premises for sum rule analysis given in chapter 2.2.3 are not fulfilled for the sum rule for the spin magnetic moment.

For the $[Fe_4Ln_2]^+$ species we assume the containing Fe^{3+} and Ln^{3+} ions to be in a $3d^5$ and $4f^n$ ($n = 7, 8$ for Gd, Tb) high spin state, respectively. Therefore we chose the number of unoccupied valence orbitals n_h to be $n_h = 5$ for Fe^{3+} and $n_h = 7$ and $n_h = 6$ for the Gd^{3+} and Tb^{3+} species, respectively.

We obtain the projection of the intrinsic spin ($m_S^{(z)}$) and orbital ($m_L^{(z)}$) magnetic moments onto the quantization axis. A scaling to the intrinsic magnetic moment by the Langevin formula (cf. chapter 2.1.5) was not performed in case of the $[Fe_4Ln_2]^+$ species. As described in chapter 2.1.5 for a Langevin scaling the total magnetic moment of the investigated $[Fe_4Ln_2]^+$ species has to be known. One has to know all contributions and the exact coupling of the several magnetic centers within the molecule to calculate this total magnetic moment. In the case of the investigated lanthanides, possible contributions to the total magnetic moments from partially occupied 3d states are not probed by our technique. These possible contributions and the exact coupling scheme of the partial magnetic moments is not known to us by now. Therefore Langevin correction is omitted in case of the investigations on single molecule magnets. The projections ($m_S^{(z)}$ and $m_L^{(z)}$) of the intrinsic spin (m_S) and orbital (m_L) magnetic moments onto the quantization axis at the given experimental conditions ($B = 5$ T and $T = 10 - 15$ K) are given in this work. These projections of the intrinsic spin and orbital magnetic moments onto the quantization axis are called magnetizations in the further course of this work.

For the investigations on isolated transition metal clusters, detailed description of the evaluation of the magnetic moments as well as the Langevin scaling of those moments is given in the doctoral thesis of J. D. Meyer[5].

3.5 References

[1]   Bondybey, V. E.; English, J. H., *LASER INDUCED FLUORESCENCE OF METAL CLUSTERS PRODUCED BY LASER VAPORIZATION: GAS PHASE SPECTRUM OF PB2*, *The Journal of Chemical Physics* **1981**, *74*, 6978.

[2]   Dietz, T. G.; Duncan, M. A.; Powers, D. E.; Smalley, R. E., *LASER PRODUCTION OF SUPERSONIC METAL CLUSTER BEAMS*, *The Journal of Chemical Physics* **1981**, *74*, 6511.

[3]   Kampschulte, H. *Entwicklung einer Tieftemperatur FT-ICR Zelle und ihre Charakterisierung mittels Reaktionskinetiken und Synchrotron-Spektroskopie*. Doctoral Thesis, **2010**.

[4]   Peredkov, S.; Savci, A.; Peters, S.; Neeb, M.; Eberhardt, W.; Kampschulte, H.; Meyer, J.; Tombers, M.; Hofferberth, B.; Menges, F.; Niedner-Schatteburg, G., *X-RAY ABSORPTION SPECTROSCOPY OF MASS-SELECTED TRANSITION METAL CLUSTERS USING A CYCLOTRON ION TRAP: AN EXPERIMENTAL SETUP FOR MEASURING XMCD SPECTRA OF FREE CLUSTERS*, *Journal of Electron Spectroscopy and Related Phenomena* **2011**, *184*, 113.

[5]   Meyer, J. D. *Spin and orbital contributions to the magnetic moment of isolated transition metal clusters and complexes*. Doctoral Thesis, **2014**.

[6]   Atkins, P.; De Paula, J. *Elements of physical chemistry*; Oxford University Press, 2012.

[7]   Schütz, G.; Goering, E.; Stoll, H., *SYNCHROTRON RADIATION TECHNIQUES BASED ON X-RAY MAGNETIC CIRCULAR DICHROISM*, *Handbook of Magnetism and Advanced Magnetic Materials* **2007**.

[8]   Stöhr, J.; Siegmann, H. C., *MAGNETISM*, *Solid-State Sciences. Springer, Berlin, Heidelberg* **2006**, 5.

[9]   Peredkov, S.; Neeb, M.; Eberhardt, W.; Meyer, J.; Tombers, M.; Kampschulte, H.; Niedner-Schatteburg, G., *SPIN AND ORBITAL MAGNETIC MOMENTS OF FREE NANOPARTICLES*, *Physical Review Letters* **2011**, *107*.

[10]   Langenberg, A.; Hirsch, K.; Lawicki, A.; Zamudio-Bayer, V.; Niemeyer, M.; Chmiela, P.; Langbehn, B.; Terasaki, A.; Issendorff, B. V.; Lau, J. T., *SPIN AND ORBITAL MAGNETIC MOMENTS OF SIZE-SELECTED IRON, COBALT, AND NICKEL CLUSTERS*, *Physical Review B* **2014**, *90*.

[11]   Niemeyer, M.; Hirsch, K.; Zamudio-Bayer, V.; Langenberg, A.; Vogel, M.; Kossick, M.; Ebrecht, C.; Egashira, K.; Terasaki, A.; Moller, T.; Issendorff, B. V.; Lau, J. T., *SPIN COUPLING AND ORBITAL ANGULAR MOMENTUM QUENCHING IN FREE IRON CLUSTERS*, *Physical Review Letters* **2012**, *108*, 057201.

[12]   Margaritondo, G., *A PRIMER IN SYNCHROTRON RADIATION: EVERYTHING YOU WANTED TO KNOW ABOUT SEX (SYNCHROTRON EMISSION OF X-RAYS) BUT WERE AFRAID TO ASK*, *Journal of synchrotron radiation* **1995**, *2*, 148.

[13]   Wende, H., *RECENT ADVANCES IN X-RAY ABSORPTION SPECTROSCOPY*, *Reports on Progress in Physics* **2004**, *67*, 2105.

[14]   Sasaki, S.; Kakuno, K.; Takada, T.; Shimada, T.; Yanagida, K.-i.; Miyahara, Y., *DESIGN OF A NEW TYPE OF PLANAR UNDULATOR FOR GENERATING VARIABLY POLARIZED RADIATION*, *Nuclear Instruments and Methods in Physics Research Section A: Accelerators, Spectrometers, Detectors and Associated Equipment* **1993**, *331*, 763.

[15]   Asano, H.; Takenaka, H.; Wakabayashi, T.; Fujii, T., *NUCLEAR INSTRUMENTS AND METHODS IN PHYSICS RESEARCH SECTION A: ACCELERATORS, SPECTROMETERS*, *Detectors and Associated Equipment* **2005**, *542*, 154.

3. Experimental methods

[16]   Bahrdt, J.; Frentrup, W.; Gaupp, A.; Scheer, M.; Gudat, W.; Ingold, G.; Sasaki, S., *A QUASI-PERIODIC HYBRID UNDULATOR AT BESSY II*, *Nuclear Instruments and Methods in Physics Research Section A: Accelerators, Spectrometers, Detectors and Associated Equipment* **2001**, *467*, 130.

[17]   https://www.helmholtz-berlin.de/pubbin/igama_output?modus=einzel&sprache=en&gid=1640&typoid=50740.

[18]   Berg, C.; Schindler, T.; Niednerschatteburg, G.; Bondybey, V. E., *REACTIONS OF SIMPLE HYDROCARBONS WITH NB_N^+ - CHEMISORPTION AND PHYSISORPTION ON IONIZED NIOBIUM CLUSTERS*, *Journal of Chemical Physics* **1995**, *102*, 4870.

[19]   Maruyama, S.; Anderson, L. R.; Smalley, R. E., *DIRECT INJECTION SUPERSONIC CLUSTER BEAM SOURCE FOR FT-ICR STUDIES OF CLUSTERS*, *Review of Scientific Instruments* **1990**, *61*, 3686.

[20]   Proch, D.; Trickl, T., *A HIGH-INTENSITY MULTI-PURPOSE PIEZOELECTRIC PULSED MOLECULAR BEAM SOURCE*, *Review of Scientific Instruments* **1989**, *60*, 713.

[21]   Heinrich Kampschulte, T. K. *Autodesc Inventor$^{(R)}$*

[22]   Carra, P.; Thole, B. T.; Altarelli, M.; Wang, X. D., *X-RAY CIRCULAR-DICHROISM AND LOCAL MAGNETIC-FIELDS*, *Physical Review Letters* **1993**, *70*, 694.

[23]   Thole, B. T.; Carra, P.; Sette, F.; Vanderlaan, G., *X-RAY CIRCULAR-DICHROISM AS A PROBE OF ORBITAL MAGNETIZATION*, *Physical Review Letters* **1992**, *68*, 1943.

[24]   Stefanita, C. G. *Magnetism: Basics and Applications*; Springer, 2012.

[25]   Rossi, D. T.; Sinz, M. *Mass spectrometry in drug discovery*; CRC Press, 2001.

[26]   Ardrey, R. E. *Liquid chromatography-mass spectrometry: an introduction*; John Wiley & Sons, 2003.

[27]   Schalley, C. A., *THE EXPANDING ROLE OF MASS SPECTROMETRY IN BIOTECHNOLOGY GARY SIUZDAK*, *Journal of the American Society for Mass Spectrometry* **2004**, *15*, 625.

[28]   Schalley, C. A.; Armentrout, P. B. *Modern mass spectrometry*; Springer Science & Business Media, 2003; Vol. 225.

[29]   Gross, J. H. *Mass spectrometry: a textbook*; Springer Science & Business Media, 2004.

[30]   Fenn, J. B.; Mann, M.; Meng, C. K.; Wong, S. F.; Whitehouse, C. M., *ELECTROSPRAY IONIZATION FOR MASS SPECTROMETRY OF LARGE BIOMOLECULES*, *Science* **1989**, *246*, 64.

[31]   Fenn, J. B.; Mann, M.; Meng, C. K.; Wong, S. F.; Whitehouse, C. M., *ELECTROSPRAY IONIZATION– PRINCIPLES AND PRACTICE*, *Mass Spectrometry Reviews* **1990**, *9*, 37.

[32]   Fenn, J. B., *ELECTROSPRAY WINGS FOR MOLECULAR ELEPHANTS (NOBEL LECTURE)*, *Angewandte Chemie International Edition* **2003**, *42*, 3871.

[33]   Schalley, C. A., *SUPRAMOLECULAR CHEMISTRY GOES GAS PHASE: THE MASS SPECTROMETRIC EXAMINATION OF NONCOVALENT INTERACTIONS IN HOST–GUEST CHEMISTRY AND MOLECULAR RECOGNITION*, *International Journal of Mass Spectrometry* **2000**, *194*, 11.

[34]   Cristoni, S.; Bernardi, L. R., *DEVELOPMENT OF NEW METHODOLOGIES FOR THE MASS SPECTROMETRY STUDY OF BIOORGANIC MACROMOLECULES*, *Mass spectrometry reviews* **2003**, *22*, 369.

[35]   Heck, A. J.; van den Heuvel, R. H., *INVESTIGATION OF INTACT PROTEIN COMPLEXES BY MASS SPECTROMETRY*, *Mass spectrometry reviews* **2004**, *23*, 368.

[36]   Menges, F. *Structure and Reactivity of Isolated Mononuclear and Oligonuclear Metal Complexes*. Doctoral Thesis, **2013**.

[37]   Colton, R.; D'Agostino, A.; Traeger, J. C., *ELECTROSPRAY MASS SPECTROMETRY APPLIED TO INORGANIC AND ORGANOMETALLIC CHEMISTRY*, *Mass Spectrometry Reviews* **1995**, *14*, 79.

[38]   Traeger, J. C., *ELECTROSPRAY MASS SPECTROMETRY OF ORGANOMETALLIC COMPOUNDS*, *International Journal of Mass Spectrometry* **2000**, *200*, 387.

[39]   Julian, R. R.; Mabbett, S. R.; Jarrold, M. F., *ION FUNNELS FOR THE MASSES: EXPERIMENTS AND SIMULATIONS WITH A SIMPLIFIED ION FUNNEL*, *Journal of the American Society for Mass Spectrometry* **2005**, *16*, 1708.

[40]   Higuera, F., *FLOW RATE AND ELECTRIC CURRENT EMITTED BY A TAYLOR CONE*, *Journal of Fluid Mechanics* **2003**, *484*, 303.

[41]   Wilm, M. S.; Mann, M., *ELECTROSPRAY AND TAYLOR-CONE THEORY, DOLE'S BEAM OF MACROMOLECULES AT LAST?*, *International Journal of Mass Spectrometry and Ion Processes* **1994**, *136*, 167.

[42] Hirsch, K.; Zamudio-Bayer, V.; Ameseder, F.; Langenberg, A.; Rittmann, J.; Vogel, M.; Moeller, T.; von Issendorff, B.; Lau, J. T., *2P X-RAY ABSORPTION OF FREE TRANSITION-METAL CATIONS ACROSS THE 3D TRANSITION ELEMENTS: CALCIUM THROUGH COPPER*, *Physical Review A* **2012**, *85*.

[43] Lau, J. T.; Vogel, M.; Langenberg, A.; Hirsch, K.; Rittmann, J.; Zamudio-Bayer, V.; Moeller, T.; von Issendorff, B., *HIGHEST OCCUPIED MOLECULAR ORBITAL-LOWEST UNOCCUPIED MOLECULAR ORBITAL GAPS OF DOPED SILICON CLUSTERS FROM CORE LEVEL SPECTROSCOPY*, *Journal of Chemical Physics* **2011**, *134*.

[44] Lau, J. T.; Hirsch, K.; Langenberg, A.; Probst, J.; Richter, R.; Rittmann, J.; Vogel, M.; Zamudio-Bayer, V.; Moeller, T.; von Issendorff, B., *LOCALIZED HIGH SPIN STATES IN TRANSITION-METAL DIMERS: X-RAY ABSORPTION SPECTROSCOPY STUDY*, *Physical Review B* **2009**, *79*.

[45] Lau, J. T.; Hirsch, K.; Klar, P.; Langenberg, A.; Lofink, F.; Richter, R.; Rittmann, J.; Vogel, M.; Zamudio-Bayer, V.; Moeller, T.; v. Issendorff, B., *X-RAY SPECTROSCOPY REVEALS HIGH SYMMETRY AND ELECTRONIC SHELL STRUCTURE OF TRANSITION-METAL-DOPED SILICON CLUSTERS*, *Physical Review A* **2009**, *79*.

[46] Hirsch, K.; Lau, J. T.; Klar, P.; Langenberg, A.; Probst, J.; Rittmann, J.; Vogel, M.; Zamudio-Bayer, V.; Moller, T.; von Issendorff, B., *X-RAY SPECTROSCOPY ON SIZE-SELECTED CLUSTERS IN AN ION TRAP: FROM THE MOLECULAR LIMIT TO BULK PROPERTIES*, *Journal of Physics B-Atomic Molecular and Optical Physics* **2009**, *42*.

[47] Lau, J. T.; Rittmann, J.; Zamudio-Bayer, V.; Vogel, M.; Hirsch, K.; Klar, P.; Lofink, F.; Moeller, T.; Von Issendorff, B., *SIZE DEPENDENCE OF L(2,3) BRANCHING RATIO AND 2P CORE-HOLE SCREENING IN X-RAY ABSORPTION OF METAL CLUSTERS*, *Physical Review Letters* **2008**, *101*.

[48] Zamudio-Bayer, V.; Hirsch, K.; Langenberg, A.; Niemeyer, M.; Vogel, M.; Lawicki, A.; Terasaki, A.; Lau, J. T.; von Issendorff, B., *MAXIMUM SPIN POLARIZATION IN CHROMIUM DIMER CATIONS AS DEMONSTRATED BY X-RAY MAGNETIC CIRCULAR DICHROISM SPECTROSCOPY*, *Angewandte Chemie (International ed. in English)* **2015**, *54*, 4498.

[49] Hirsch, K.; Zamudio-Bayer, V.; Langenberg, A.; Niemeyer, M.; Langbehn, B.; Moeller, T.; Terasaki, A.; von Issendorff, B.; Lau, J. T., *MAGNETIC MOMENTS OF CHROMIUM-DOPED GOLD CLUSTERS: THE ANDERSON IMPURITY MODEL IN FINITE SYSTEMS*, *Physical Review Letters* **2015**, *114*.

[50] Zamudio-Bayer, V.; Leppert, L.; Hirsch, K.; Langenberg, A.; Rittmann, J.; Kossick, M.; Vogel, M.; Richter, R.; Terasaki, A.; Moeller, T.; Issendorff, B. v.; Kuemmel, S.; Lau, J. T., *COORDINATION-DRIVEN MAGNETIC-TO-NONMAGNETIC TRANSITION IN MANGANESE-DOPED SILICON CLUSTERS*, *Physical Review B* **2013**, *88*.

[51] Niemeyer, M.; Hirsch, K.; Zamudio-Bayer, V.; Langenberg, A.; Vogel, M.; Kossick, M.; Ebrecht, C.; Egashira, K.; Terasaki, A.; Moller, T.; Issendorff, B. V.; Lau, J. T., *SPIN COUPLING AND ORBITAL ANGULAR MOMENTUM QUENCHING IN FREE IRON CLUSTERS*, *Physical Review Letters* **2012**, *108*.

[52] Langenberg, A. *Magnetische Momente freier, massenselektierter Eisen-, Cobalt-und Nickelcluster*, Doctoral thesis, 2013, Technische Unvierstät Berlin.

4. SPIN AND ORBITAL MAGNETIC MOMENTS OF PURE AND DOPED TRANSITION METAL CLUSTERS

In this chapter the results on gas phase XMCD investigation of isolated pure and doped transition metal clusters and the resulting spin and orbital contributions to their total magnetic moments are presented. The results are given, discussed, introduced and concluded in one published, one accepted and one submitted paper. Results and manuscripts arose in team work as contemporary. The contributions of myself to these presented manuscripts are stated prior to the respective manuscripts.

4. Spin and orbital magnetic moments of pure and doped transition metal clusters

4.1 Publication: "Spin and orbital magnetic moments of free nanoparticles"

The following work has been published at Physical Review Letters with the title: "Spin and orbital magnetic moments of free nanoparticles".

The experiments were performed by the experimental team consisting of S. Peredkov, J. D. Meyer and myself lead by M. Neeb at the Helmholtz Zentrum Berlin (BESSY II). W. Eberhard and G. Niedner-Schatteburg designed the used GAMBIT-Setup and were involved in the revision of the manuscript. H. Kampschulte designed the cryogenic part of the GAMBIT-Setup and performed the first test experiments. The data evaluation and the paper draft were done by S. Peredkov and J. D. Meyer. The shown results are also part of the doctoral thesis of J. D. Meyer.

The contributions of myself consisit in being a member of the experimental team which acquired the presented data and being involved in the data evaluation and revision of the manuscript.

Full reference to the publication:

Peredkov, S.; Neeb, M.; Eberhardt, W.; Meyer, J.; Tombers, M.; Kampschulte, H.; Niedner-Schatteburg, G., *Spin and orbital magnetic moments of free nanoparticles*, *Physical Review Letters* **2011**, *107*, 233401.

Spin and orbital magnetic moments of free nanoparticles

S. Peredkov,[1] M. Neeb,[2] W. Eberhardt,[1] J. Meyer,[3] M. Tombers,[3] H. Kampschulte,[3] and G. Niedner-Schatteburg[3]

[1]Institut für Optik und Atomare Physik, Technische Universität Berlin, Hardenbergstrasse 36, 10623 Berlin, Germany

[2]Helmholtz-Zentrum Berlin für Materialien und Energie, BESSY II, Albert-Einstein-Strasse 15, 12489 Berlin, Germany

[3]Fachbereich Chemie und Forschungszentrum OPTIMAS, TU Kaiserslautern, 67663 Kaiserslautern, Germany

4.1.1 Abstract

The determination of spin and orbital magnetic moments from the free atom to the bulk phase is an intriguing challenge for nanoscience, in particular, since most magnetic recording materials are based on nanostructures. We present temperature-dependent x-ray magnetic circular dichroism measurements of free Co clusters (N = 8 - 22) from which the intrinsic spin and orbital magnetic moments of non-interacting magnetic nanoparticles have been deduced. An exceptionally strong enhancement of the orbital moment is verified for free magnetic clusters which is 4 - 6 times larger than the bulk value. Our temperature-dependent measurements reveal that the spin orientation along the external magnetic field is nearly saturated at 20 K and 7 T, while the orbital orientation is clearly not.

4.1.2 Introduction

Free transition metal atoms possess large spin and orbital magnetic moments according to Hund's rules. Bulk formation, on the other hand, causes a substantial attenuation of the spin (m_S) and orbital (m_L) moments. The latter can even be completely quenched in macroscopic systems, as shown by x-ray magnetic circular dichroism (XMCD) measurements on ferromagnetic bulk samples [1, 2]. Thus, one of the main concerns of magnetism is to understand how magnetic properties change when going from the electronic structure of a single atom to the bulk, i.e., when orbital hybridization, geometry, symmetry breaking, electron delocalization, and band formation come into play. Mass-selected clusters are most suitable objects to follow the evolution of magnetism as a function of size.

4. Spin and orbital magnetic moments of pure and doped transition metal clusters

Total magnetic moments (m_{tot}) of free mass-selected clusters have been determined by ingenious Stern-Gerlach experiments [3–5]. However, spin and orbital magnetic moments of free magnetic particles like molecular magnets and clusters are experimentally unknown due to a lack of magnetosensitve experiments for probing an extremely dilute target density of some attomoles /cm^3. Since the orbital moments are influenced more strongly by orbital hybridization and electron delocalization, it is important to quantify them and to study their size and temperature dependence. Do m_S and m_L reveal the same size dependence, or do they vary independently? On which length scale does the orbital momentum get quenched, and when does the spin moment converge to the bulk value? Is there a monotonic size evolution, or do m_S and m_L exhibit a non-scalable size dependence? Do m_S and m_L exhibit the same temperature dependence? Considerable efforts have been invested for the calculation of spin and orbital magnetic moments of free clusters which still await experimental data for comparison and code refinement [6-8]. Large orbital moments are expected to cause a large magnetic anisotropy and thus might play a crucial role in the inherent orientation of magnetic moments along a preferred spatial coordinate of the cluster, an important prerequisite for being used as magnetic data storage material.

Atomic islands, wires, and nanoparticles as well as supported clusters have been explored by XMCD in order to determine size-dependent information and to study the dependence of magnetic moments and anisotropy on dimensionality [9-14]. Common to all these measurements is that the explored particles are in contact with a support material. Extrinsic effects on the magnetic properties are inevitably due to modifications of geometry, electronic structure, charge transfer, and hybridization with the support. Thus, the determination of the intrinsic moments of free magnetic particles is extremely important for both experiment and theory, as the data elucidate the influence of the support on the magnetic properties of application-relevant deposited clusters and, on the other hand, as the measured moments can be used as reference data for highly sophisticated calculations.

4.1.3 Results and discussion

Here we present XMCD data on free ''ferromagnetic'' nanoparticles which have been used to extract the intrinsic spin and orbital magnetic moments of small Co_N cluster ions as a function of the number of atoms N = 8 - 22. Note that Co_N clusters are expected to possess orbital moments that are higher than those of other itinerant ferromagnetic elements like Fe and Ni [7]. The total magnetic moment m_{tot}, which is given by the vector sum of m_S and m_L, is compared with the magnetic moments as obtained from prior Stern-Gerlach experiments [5, 15, 16]. Interestingly, our data are systematically higher than those of Refs. [5, 15] but are close to the magnetic moments of Ref. [16]. We might be

able to solve this apparent mismatch by using the different temperature dependence of spin and orbital moments as will be explained in the following.

In order to record XMCD spectra of free mass-selected clusters, a Fourier transform ion cyclotron resonance mass spectrometer has been combined with a soft-x-ray synchrotron beam line at BESSY. The experimental setup has been described in detail in Ref. [17] and Fig. S1[18]. Figure 1(a) shows L-edge absorption curves of Co_{12}^+ which have been taken at a buffer-gas equilibrated cluster temperature of 20 K using right- and left-handed circular polarization of the x-ray light. The L_3 and L_2 edges are clearly resolved. The XMCD signal $\int(\sigma^+ - \sigma^-)$ at the L_3 edge is very prominent, while it is much smaller at the L_2 edge [Fig.1(b)].
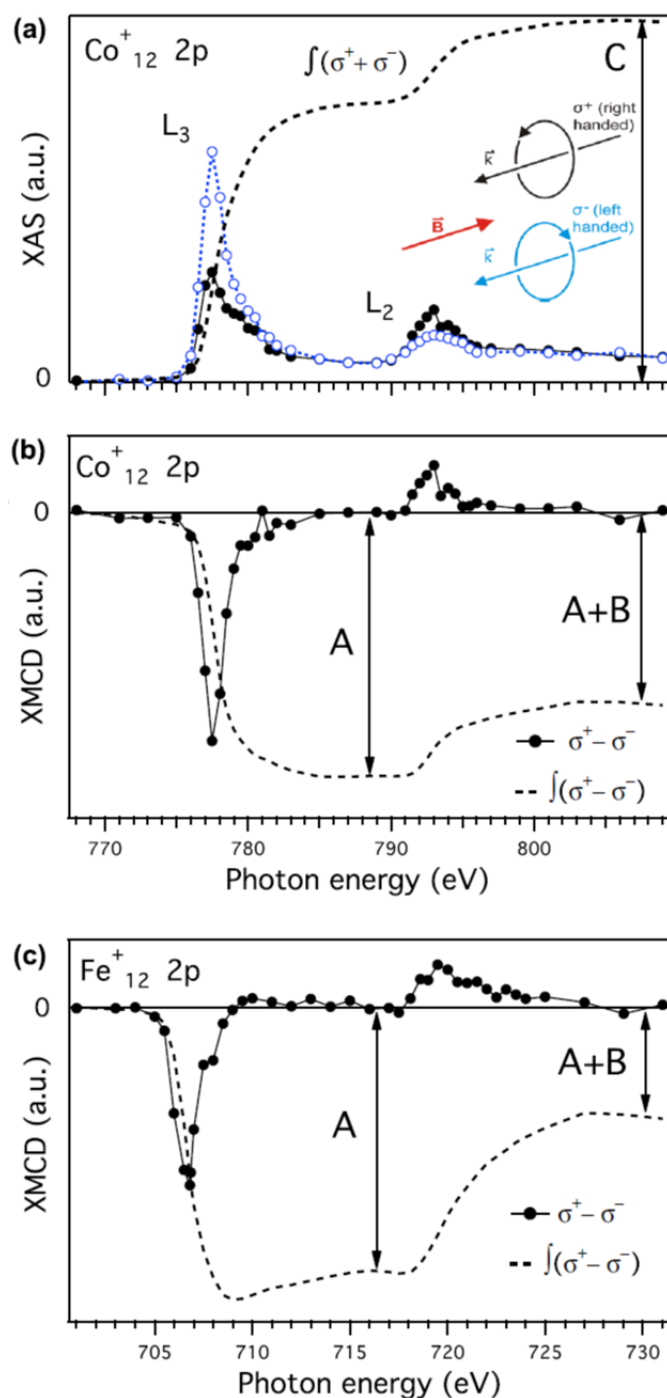
Figure 1 (a) Circularly polarized x-ray absorption spectra of Co_{12}^+ at the L edge. The spectrum recorded with negative polarization (σ^-) is shown by open circles and a dotted line (blue), that with positive polarization (σ^+) by filled dots and a full line (black). The relative orientation of polarization, light propagation (k), and magnetic field (B) is shown in the cartoon. The integration of the sum of both absorption curves is shown as a dashed line (C) which is used for calculation of the magnetic moments according to the magneto-optical sum rules. **(b)** The XMCD spectrum ($\sigma^+ - \sigma^-$) of Co_{12}^+ after subtracting the L-edge-jump intensity. A and B correspond to the area of the L_3 and L_2 dichroic intensity, respectively. The integration of the dichroic intensity is shown as a dashed line (A + B). Note that the large absolute value of

(A +B) exhibits a strong orbital moment. **(c)** L-edge XMCD spectrum of Fe_{12}^+ measured under the same conditions

Magneto-optical sum rules [19-21] have been used to extract the measured projection of the spin and orbital magnetic moments $m_S^{(z)}$ and $m_L^{(z)}$ [22]. The quantization axis z is defined by the direction of the applied magnetic trapping field. For a quantitative determination of spin and orbital magnetic moments, we used Eqs. (1) and (2) of the paper of Chen *et al.*[21]. Rewriting the formula of Ref. [21] by replacing A and B for the corresponding integrated XMCD signal $\int(\sigma^+ - \sigma^-)$ of the L_3 and L_2 edge, respectively, and C for the integral of the sum of the two helicity-dependent absorption curves $\int(\sigma^+ + \sigma^-)$ we obtain

$$m_L^{(z)} = -\frac{4(A+B)}{3C}n_h \tag{1}$$

$$m_S^{(z)} = -\frac{2(A-2B)}{C}n_h - 7T_z \tag{2}$$

$m_L^{(z)}$ and $m_S^{(z)}$ are given per atom in units of μ_B; n_h represents the number of 3d holes which has been set equal to the bulk value, $n_h = 2.5$ [21]. We use the bulk value instead of the atomic value ($n_h = 3$) in order to take an intra-atomic charge redistribution 4s $\longrightarrow$ 3d into account. This enables bonding between two adjacent Co atoms [23], as otherwise the $4s\sigma_g$ bond is compensated by an antibonding $4s\sigma_u$ orbital. $\langle T_z \rangle$ corresponds to the expectation value of the spin magnetic dipole operator for the spin quantization axis oriented along z [21, 24], which defines the asymmetry of the intra-atomic spin distribution. It is nonzero in anisotropic bonding environments due to the different number of spins in the unit cell along different crystallographic directions, but it vanishes when an angular average is performed [25, 26]. According to theory, the absolute value of $7T_z$ for systems with low dimensionality such as surfaces and deposited clusters can range up to 20% of the spin magnetic moment [24, 27]. In our study we are dealing with freely rotating particles which are not fixed in space. As T_z is a strongly directional value, we have good reasons to assume that T_z, which can adopt values of different sign, averages to a minimum value close to zero.

Applying the above sum rules, the analysis reveals that the measured orbital moments $m_L^{(z)}$ at 20 K and B = 7 T are clearly enhanced (2 - 4 times) with respect to the bulk [21], while the measured spin moments $m_S^{(z)}$ of the clusters (N = 8 - 22) are less strongly enhanced (< 1.4 times) as summarized in Table S2 [18]. Figure 1(c) exemplarily demonstrates that the enhancement of the orbital moment is not just seen for Co clusters but also for small Fe clusters [28]. The XMCD signal (A + B) is clearly larger than that of bulk iron, which almost vanishes [21]. The measured orbital moment $m_L^{(z)}$ amounts to 0.25 μ_B/atom compared to the bulk value of 0.085 μ_B/atom [21]. According to the

classical Langevin equation, which applies for single domain particles, the magnetization of small magnetic particles is expected to scale inversely with the temperature at a given B field [29-31]. Indeed, the measured moments $m_{L,S}^{(z)}$ show a striking temperature dependence as typical for superparamagnetic particles (Fig. 2). Our 7 T strong magnetic field substantially exceeds the Paschen-Back limit for atoms 1 T, and therefore orbital and spin angular momentum can be expected to decouple. This can be quantitatively rationalized by the relatively weak spin-orbit interaction energy of the itinerant 3d metals. The magnetic energy of Co_{11}^{+} is 1-2 meV /atom at a field strength of 7 T. This energy compares with the spin-orbit splitting of a few meV for the bulk as well as the magnetic anisotropy energy as calculated for the atoms of a Co monolayer [32, 33]. Based on these estimates and our observation of a change in the ratio $m_L^{(z)}/m_S^{(z)}$ with temperature, we apply the classical Langevin equation to fit the temperature dependence of spin and orbital moments separately. According to the Langevin function, the intrinsic magnetic orbital and spin moments m_L and m_S per atom in units of μ_B are given by

$$m_{L,S}^{(z)}(T) = m_{L,S}\left[\coth\left(\frac{Nm_{L,S}\mu_B B}{k_B T}\right) - \frac{k_B T}{Nm_{L,S}\mu_B B}\right] \tag{3}$$

$m_{L,S}^{(z)}$ are the temperature-dependent projected orbital and spin magnetic moments per atom in units of μ_B and N denotes the number of atoms in the cluster. As shown in Fig. 2, a least-squares fit has been used to fit the data $m_L^{(z)}(T)$ and $m_L^{(z)}(T)$ with the above Langevin functions using the intrinsic moments m_L and m_S as fitting parameters. No hints for freezing of the magnetization into a blocked state is observed down to 20 K in agreement with measurements on Co wires [9]. Moreover, Fig. 2 clearly shows that at 20 K the spin moment is much closer to its saturation limit than the smaller orbital moment. It is obvious that lower temperatures are necessary to saturate the orbital moment due to its smaller magnetic energy. In other words, the alignment of the orbital moment along the external field is weaker than the alignment of the larger spin moment. From this we conclude that spin and orbital moments are decoupled and interact separately with the external field analogous to the Paschen-Back effect in atoms [34].
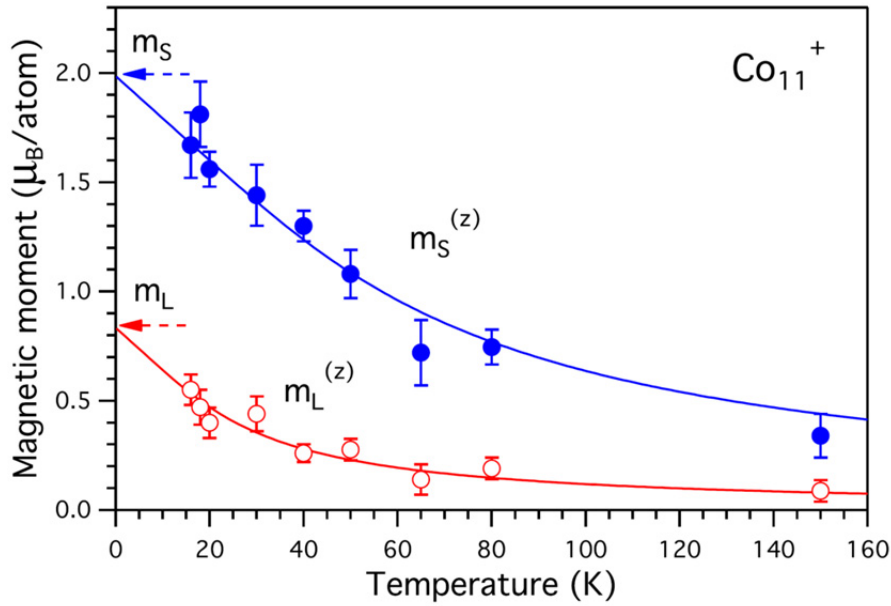
Figure 2 Measured spin and orbital magnetic moments ($m_{L,S}^{(z)}$) versus temperature of Co_{11}^+ . The line through the measured moments is a Langevin fit using B = 7 T.

Upon scaling $m_L^{(z)}$ (T) and $m_S^{(z)}$ to the saturation limit at T = 0 K, the measured moments $m_{L,S}^{(z)}(T = 20K)$ need to be corrected by 15 % and 70 %, respectively, to determine the intrinsic moments m_S and m_L . The corrections become larger the smaller the moments are, as the alignment along the magnetic field direction is thermally less stable. The Langevin-scaled intrinsic spin and orbital moments of the Co_N clusters are plotted in Fig. 3. The moments develop in a non-scalable manner from one cluster size to the next. Seemingly, the spin moment fluctuates more with cluster size N than the orbital moment. A convergence towards the bulk magnetic moments is not obvious up to clusters containing 22 atoms. The intrinsic spin moments of the clusters are in the range m_S = 2 - 2.7 μ_B per atom, while the orbital moments amount to m_L = 0.6 - 1 μ_B per atom. Thus the intrinsic orbital moments of the clusters are 4 - 6 times larger than the value of the solid, and the spin moments are enhanced by a factor of 1 - 2. Also, the intrinsic orbital moments of free clusters are enlarged with respect to small atomic islands formed on a crystalline platinum surface [35] as shown in Fig. 3.
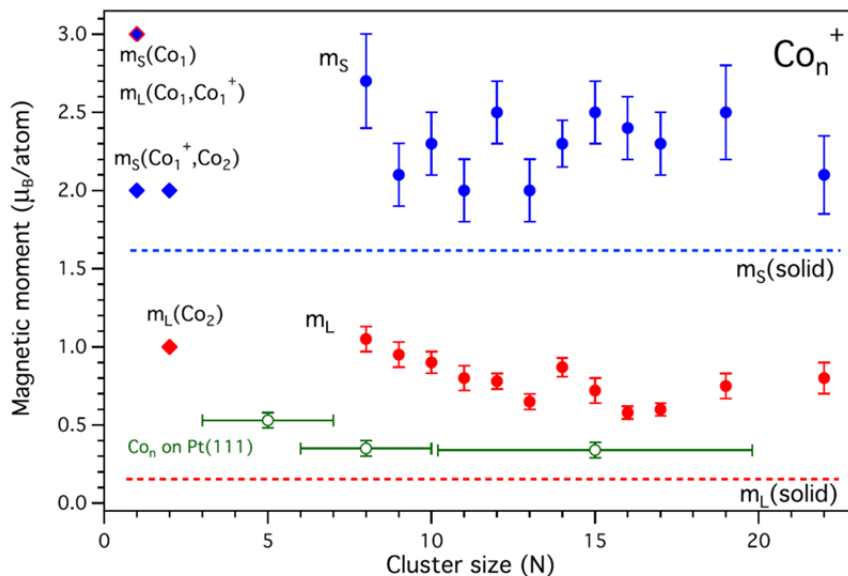
Figure 3 Magnetic moments as revealed from XMCD spectra using magneto-optical sum rule analysis. Filled symbols show the intrinsic spin (m_S , blue) and orbital magnetic moments (m_L , red) of the clusters after Langevin scaling of the measured moments ($m_S^{(z)}$, $m_L^{(z)}$) recorded at 20 K and 7 T. The error bar corresponds to the standard deviation from repeated measurements at 778 eV (cf. Fig. S1 [18]). Moments of Co bulk [21] (dotted line) and small atomic islands [35] (green full line) are indicated. Additionally, the corresponding moments of the atom (Co$_1$ ^{4}F; Co$_1^+$ ^{3}F) and dimer (Co$_2$ ^{5}Δ) are displayed.

The intrinsic orbital moment of a pentagonal bipyramid with a d-band filling of 2.5 (Co$_7$) has been calculated to be 0.7 μB/atom for magnetization along the equatorial C_2 axis [6] which comes close to our measured orbital moments. The orbital moment of the dimer m_L = 1 μB/atom, as approximated from Hund's rule for the ground state configuration ^{5}Δ [23, 36-38], is also similar to m_L of the clusters. However, the orbital moment of the atom (^{4}F [37], m_L = 3μB) is distinctly larger, which suggests a sudden drop of m_L from the atom to the dimer. Towards larger clusters, m_L further diminishes but rather smoothly. The moment of Co$_{13}^+$ represents a local minimum which might hint at a highly symmetric structure (I_h) of this cluster. The intrinsic spin moments of the clusters are somewhat higher than the calculated ones, which are in the range m_S = 1.9 - 2.1μB/atom for Co$_{2-20}$ [8], while they are smaller than this of the neutral atom (3 μB)[39]. Moreover, the XMCD measurements show that the ratio m_L /m_S of the clusters, which is independent of n$_h$, is 3 - 4 times higher than that of the solid (m_L /m_S = 0.1).
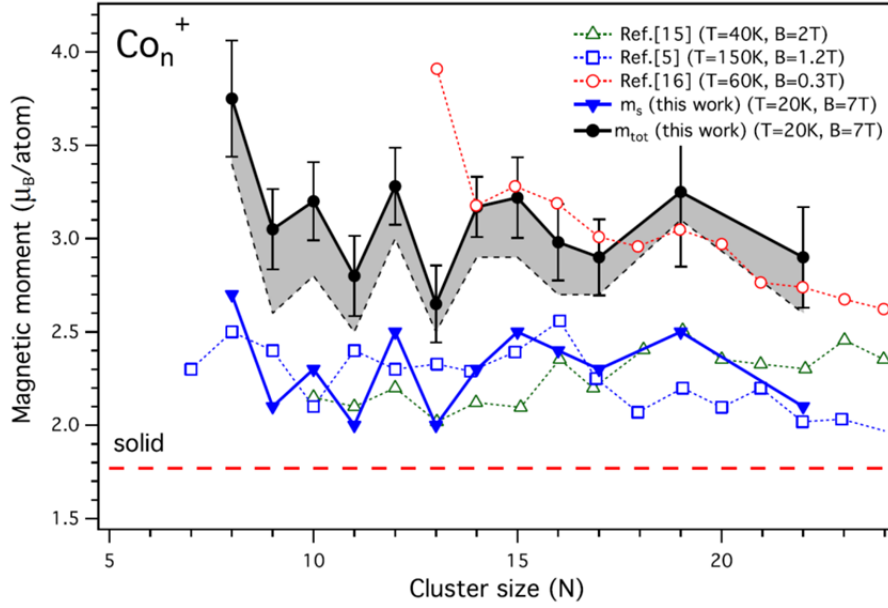
Figure 4 Total magnetic moments of Co_N^+ clusters as determined by XMCD (filled dots) in comparison with Stern-Gerlach results (open symbols) taken from Ref. [5, 15, 16]. The spin moments as revealed from XMCD are also shown (filled triangles) [The transition from fully coupled to decoupled moments changes gradually with the strength of the magnetic field. This affects the Langevin scaling of the measured moments which is indicated by the shaded region of the total moment. The boundaries for total coupling and decoupling are shown by the lower line (dotted) and upper line (bold). The intrinsic orbital moment (not shown) drops by 30 % - 40 % when coupled moments are considered while the spin moment hardly ever changes].

In Fig. 4, we compare the total magnetic moments $m_{tot} = m_S + m_L$ as revealed from our XMCD measurements with the results from earlier Stern-Gerlach experiments [5, 15, 16]. In these earlier experiments, the spatial deflection of neutral clusters in an inhomogeneous magnetic field is used as a measure of the total magnetic moment of the clusters. As the Stern-Gerlach data are analyzed by the Langevin model [5, 15, 16], the published data can directly be compared to the sum of our scaled moments. Two of the Stern-Gerlach series [5,15] show very similar results with magnetic moments ranging between 2 and 2.5 μ_B per atom, while another series exhibits much higher moments between 3 and 4 μ_B per atom [16]. Remarkably, the lower Stern-Gerlach data agree with the measured spin moments rather than with the sum of the spin and orbital moment. We therefore conclude that the magnetic moments of Refs. [5, 15] represent basically the spin moment, while the contribution of the orbital magnetic moment is relatively reduced. This might be explained as follows: The data of Xu *et al.* [15] and Knickelbein [5] have been measured with a magnetic field of 1.2 and 2 T, respectively. It is likely that under these field strengths spin and orbital moments interact rather independently with the external B field similar to our experiment. As established by our

temperature-dependent measurements (Fig. 2), the orbital moment is less aligned along the magnetic field direction than the larger spin moment. For example, the orbital contribution $m_L^{(z)}$ to the measured total magnetic moment is less than 15 % at 1 T and 40 K. The individual temperature dependence of spin and orbital moments must be compensated for by different scaling factors in order to deduce the intrinsic moments. Note that the weaker orbital moment must be scaled more than the larger spin moment (cf. Fig. S3 [18]). In our XMCD experiments, the measured moments are scaled individually according to separate Langevin fits of spin and orbital moments. In Stern-Gerlach experiments, however, such an individual scaling is not possible.

The data of Payne et al. [16] have been measured with a considerably lower magnetic field (0.2 - 0.3 T). Under these conditions, spin and orbital moments are most likely coupled by spin-orbit interaction and interact as a total moment with the external magnetic field. In this case, Langevin scaling of the total moment becomes appropriate. This might explain the rather good agreement of the temperature-scaled data of Payne et al. [16] with the sum of m_S and m_L as determined from our high-field XMCD measurements in which the uncoupled moments are scaled separately before summing up.

4.1.4 Conclusion

In summary, the present data demonstrate the importance of quantifying spin and orbital moments as a function of temperature in order to analyze the intrinsic magnetic properties of free ferromagnetic particles. A clear Langevin-type temperature dependence has been established for small Co clusters revealing a different temperature scaling of spin and orbital moments under high magnetic field conditions. The data demonstrate that the intrinsic orbital moments of small Co clusters are strongly enlarged by a factor of 4 - 6 in comparison to the bulk. The decomposition of the total moments into spin and orbital moments and their different temperature dependence might help to clarify diverging results of former Stern-Gerlach experiments. The analysis of spin and orbital magnetic moments of free clusters bears high potential for future investigation of application-relevant magnetic storage particles such as magnetic building block clusters, molecular magnets, and magnetic biomolecules.

4.1.5 References

[1]   G. Schütz, W. Wagner, W. Wilhelm, P. Kienle, R. Zeller, R. Frahm, and G. Materlik, Phys. Rev. Lett. **58**, 737 (1987).

[2]   J. Stöhr, J. Electron Spectrosc. Relat. Phenom. **75**, 253 (1995).

[3]   M.L. Billas, A. Chatelain, and W.A. de Heer, Science **265**, 1682 (1994).

[4]   S.E. Apsel, J.W. Emmert, J. Deng, and L.A. Bloomfield, Phys. Rev. Lett. **76**, 1441 (1996).

[5]   M.B. Knickelbein, J. Chem. Phys. **125**, 044308 (2006).

[6]   R. Guirado-Lopez, J. Dorantes-Davila, and G. Pastor, Phys. Rev. Lett. **90**, 226402 (2003).

[7]   B. Nonas, I. Cabria, R. Zeller, P. Dederichs, T. Huhne, and H. Ebert, Phys. Rev. Lett. **86**, 2146 (2001).

[8]   S. Datta, M. Kabir, S. Ganguly, B. Sanyal, T. Saha-Dasgupta, and A. Mookerjee, Phys. Rev. B **76**, 014429 (2007).

[9]   P. Gambardella, A. Dallmeyer, K. Maiti, M. Malagoli, W. Eberhardt, K. Kern, and C. Carbone, Nature (London) **416**, 301 (2002).

[10]   J.T. Lau, A. Föhlisch, R. Nietubyc, M. Reif, and W.Wurth, Phys. Rev. Lett. **89**, 057201 (2002).

[11]   J. Bansmann, A. Kleibert, M. Getzlaff, A. Rodriguez, F. Nolting, C. Boeglin, and K. Meiwes-Broer, Phys. Status Solidi B **247**, 1152 (2010).

[12]   K. Fauth, M. Heßler, D. Batchelor, and G. Schütz, Surf. Sci. **529**, 397 (2003).

[13]   H. Dürr, S. Dhesi, E. Dudzik, D. Knabben, G. van der Laan, J. Goedkop, and F. Hillebrecht, Phys. Rev. B **59**, R701 (1999).

[14]   H. Brune and P. Gambardella, Surf. Sci. **603**, 1812 (2009).

[15]   X. Xu, S. Yin, R. Moro, and W. de Heer, Phys. Rev. Lett. **95** , 237209 (2005)

[16]   F.W. Payne, W. Jiang, J.W. Emmert, J. Deng, and L.A. Bloomfield, Phys. Rev. B **75**, 094431 (2007).

[17]   S. Peredkov, A. Savci, S. Peters, M. Neeb, W. Eberhardt, H. Kampschulte, J. Meyer, M. Tombers, B. Hofferberth, F. Menges, and G. Niedner-Schatteburg, J. Electron. Spectrosc. Relat. Phenom. **184**, 113 (2011).

[18]   See Supplemental Material at
        http://link.aps.org/supplemental/10.1103/PhysRevLett.107.233401 for a description of the experimental setup (S1), a table showing measured and scaled magnetic moments (S2), and a graph showing scaling factors of magnetic moments as a function of temperature and different magnetic field strengths.

[19]   B. Thole, P. Carra, F. Sette, and G. van der Laan, Phys. Rev. Lett. **68**, 1943 (1992).

[20]   P. Carra, B. Thole, M. Altarelli, and X. Wang, Phys. Rev. Lett. **70**, 694 (1993).

[21]   C. Chen, Y. Idzerda, H.-J. Lin, N. Smith, G. Meigs, E. Chaban, G. Ho, E. Pellegrin, and F. Sette, Phys. Rev. Lett. **75**, 152 (1995).

[22]   By using the Langevin formalism, the intrinsic moments of superparamagnetic particles can be received from the measured moments.

[23]   G. Gutsev, S. Khanna, and P. Jena, Chem. Phys. Lett. **345**,481 (2001).

[24]   O. Sipr, J. Minar, and H. Ebert, Europhys. Lett. **87**, 67007 (2009).

[25]   J. Stöhr and R. Nakajima, IBM J. Res. Dev. **42**, 73 (1998).

[26]   J. Stöhr and H. König, Phys. Rev. Lett. **75**, 3748 (1995).

[27]   R. Wu and A. Freeman, Phys. Rev. Lett. **73**, 1994 (1994).

[28]   S. Palutke, I. Baev, M. Martins, W. Wurth, J. Meyer, M. Tombers, G. Niedner-Schatteburg, S. Peredkov, M. Neeb, and W. Eberhardt (to be published).

[29]   S. Khanna and S. Linderoth, Phys. Rev. Lett. **67**, 742 (1991).

[30]   J. Bucher, D. Douglass, and L. Bloomfield, Phys. Rev. Lett. **66**, 3052 (1991).

[31]   B. Reddy, S. Nayak, S. Khanna, B. Rao, and P. Jena, J. Phys. Chem. A **102**, 1748 (1998).

[32]   J. Stöhr, J. Magn. Magn. Mater. *200*, 470 (1999).

[33]   G. Daalderop, P. Kelly, and M. Schuurmanns, Phys. Rev. B **50**, 9989 (1994).

[34]   M. Knickelbein, J. Chem. Phys. **121**, 5281 (2004).

[35]   P. Gambardella, S. Rusponi, M. Veronese, S. Dhesi, C. Grazioli, A. Dallmeyer, I. Cabria, R. Zeller, P. Dederichs, K. Kern, C. Carbone, and H. Brune, Science **300**, 1130 (2003).

[36]   H. Wang, Y. Khait, and M. Hoffmann, Mol. Phys. **103**, 263 (2005).

[37]   F. Furche and J. Perdew, J. Chem. Phys. 124, 044103 (2006).

[38]   D. Hales and P. Armentrout, J. Cluster Sci. **1**, 127 (1990).

[39]   We assume that the extra charge does not much alter the magnetic moments of the ionized clusters, as the single hole is just a small fraction of the total number of valence electrons for $N \geq 8$ atoms (≥ 72 electrons)

4.1.6 Supplementary material to "Spin and orbital magnetic moments of free nanoparticles"

S.1 Experimental setup

The experimental setup has been described in detail in Ref. [1]. A Fourier-Transform-Ion-Cyclotron-Resonance (FT-ICR) mass spectrometer has been combined with a soft-X-ray undulator beamline at BESSY II (UE52-PGM). A Penning-like ICR cell serves both as an ion trap and a mass analyzer. A pulsed laser vaporization source is used for production of a Co-cluster ion beam. The strong (7 T) axial-symmetric magnetic field of the FT-ICR is used for radial confinement of the cluster ions. Axially the cluster ions are trapped by electric fields of ICR trap. The axial magnetic field is not only used for trapping but also for alignment of the magnetic moments. The magnetic field of the superconducting solenoid is directed parallel to the incoming photon beam for maximum XMCD intensity. Moreover, the ICR cell has been modified in order to cool it down cryogenically. This cooling device enables thermalization of the trapped clusters through multiple collisions with a pulsed inert buffer gas (e.g. He, $1 \cdot 10^{-6}$ mbar for a few seconds) resulting in cluster temperatures as low as 18 K. In order to record XMCD spectra circularly polarized X-ray radiation (photon flux $\approx 5 \cdot 10^{11}$ s^{-1}, polarization degree 90%) has been used which is provided by the UE52-PGM undulator beamline of the BESSY storage ring. Photon helicity-dependent L-edge absorption spectra of trapped Co-cluster ions have been recorded. Core-electron transitions are induced in the stored cluster ions by the absorption of an X-ray photon. Subsequent internal relaxation produces multiply-ionized mother ions and fragment ions which are individually recorded in the FT-ICR-detection mode. The total fragment signal intensity is proportional to the X-ray absorption probability. The spectra are normalized to the mother cluster intensity and photon flux. We assume that a variation of the trapped cluster density after each refill is the main source of error. This density variation is caused by pulse-to-pulse fluctuations cluster beam. Repeated measurements at the energy of the L_3-peak maximum were done several times during recording of X-ray absorption spectra (XAS). The two standard deviation ($\pm 2\sigma$) from the repeated measurements is considered as the experimental error of XA spectra.

4. Spin and orbital magnetic moments of pure and doped transition metal clusters

S.2 Magnetic moments of Co$_N$ clusters

Table SI. Magnetic moments of Co$_N$ clusters: $m_L^{(z)}$ and $m_S^{(z)}$ are the measured orbital and spin magnetic moments calculated with equations (1) and (2) in assumption T$_z$ = 0 and n$_h$ = 2.5. m_L and m_S are the corresponding separately Langevin scaled intrinsic moments. m_{tot} corresponds to the total magnetic moments. Co-bulk (hcp): m_L = 0.15 µB/atom; m_S = 1.62 µ$_B$/atom Ref. [2]

Cluster size Co$_N$	Measured moment T = 20 K, B = 7 T		Intrinsic moment		
	$m_L^{(z)}$	$m_S^{(z)}$	m_L	m_S	m_{tot}
8	0.6 ± 0.08	2.3 ± 0.25	1.0	2.7	3.7
9	0.52 ±0.07	1.7 ± 0.2	0.95	2.1	3.1
10	0.5 ±0.07	1.9 ± 0.2	0.9	2.1	3.2
11	0.47 ±0.07	1.7 ± 0.15	0.8	2.0	2.8
12	0.47 ± 0.07	2.15 ± 0.2	0.78	2.5	3.3
13	0.37 ± 0.05	1.7 ± 0.2	0.65	2.0	2.7
14	0.6 ± 0.06	2.0 ± 0.15	0.85	2.3	3.2
15	0.47 ± 0.08	2.2 ± 0.15	0.7	2.45	3.2
16	0.36 ± 0.04	2.2 ± 0.2	0.6	2.4	3.0
17	0.38 ± 0.04	2.1 ± 0.2	0.6	2.3	2.9
19	0.54 ± 0.06	2.3 ± 0.3	0.75	2.5	3.3
22 (T = 30 K)	0.5 ± 0.07	1.8 ± 0.25	0.7	2.2	2.9

S.3 Langevin scaling factors
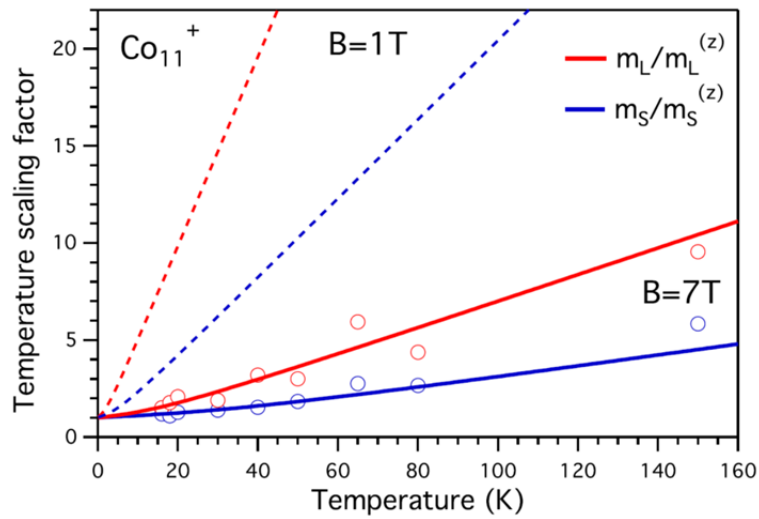
Figure S1. Langevin-scaling of the spin and orbital moment in case of decoupled moments. Note that the temperature scaling factor is larger for the smaller orbital moment than the spin moment. The XMCD measurements have been carried out at 7 T (full line). The corresponding date points of Co_{11}^+ are shown as open circles. For example, at 1 T (broken lines) the scaling disparity would become very prominent. This disparity also changes with temperature

[1]   S. Peredkov, A. Savci, S. Peters, M. Neeb, W. Eberhardt, H. Kampschulte, J. Meyer, M. Tombers, B. Hofferberth, F. Menges, and G. Niedner-Schatteburg, J. Electron Spectrosc.and Relat. Phenom. **184**, 113 (2011).

[2]   C. Chen, Y. Idzerda, H.-J. Lin, N. Smith, G. Meigs, E. Chaban, G. Ho, E. Pellegrin, and F. Sette, Phys. Rev. Lett. **75**, 152 (1995).

4.2 Publication: "The spin and orbital contributions to the total magnetic moments of free Fe, Co and Ni clusters"

An initial version of the presented draft named "The spin and orbital contributions to the total magnetic moments of free Fe, Co and Ni clusters" was submitted to the Journal of Chemical Physics. This initial version is part of the doctoral thesis of J. D. Meyer. After receiving the reviewers´ comments, G. Niedner-Schatteburg and myself reviewed and modified the initial draft extensively. The reviewed and re-submitted version of the paper is given below.

The experiments were performed by the experimental team consisting of S. Peredkov, J. D. Meyer, S. Palutke and myself lead by M. Neeb at the Helmholtz Zentrum Berlin (BESSY II). W. Eberhard, M. Martins, W. Wurth and G. Niedner-Schatteburg designed the used GAMBIT-Setup and were involved in the revision of the manuscript. The date evaluation and the initial paper draft were done by S. Peredkov and J. D. Meyer.

The contributions of myself to the presented manuscript consist in being part of the experimental team which acquired the presented date, being involved in the data evaluation and reviewing the manuscript extensively after receiving the reviewers comments.

The spin and orbital contributions to the total magnetic moments

of free Fe, Co and Ni clusters

Jennifer Meyer[&], Matthias Tombers, Christoph van Wüllen, Gereon Niedner-Schatteburg

Fachbereich Chemie and Forschungszentrum OPTIMAS,

Technische Universität Kaiserslautern, 67663 Kaiserslautern, Germany

Sergey Peredkov[§], Wolfgang Eberhardt

Institut für Optik und Atomare Physik, Technische Universität Berlin, Hardenbergstrasse 36, 10623

Berlin, Germany and DESY-CFEL, Notkestr. 85, 22607 Hamburg, Germany

Matthias Neeb

Helmholtz-Zentrum für Materialien und Energie, BESSY II, Albert-Einstein-Strasse 15,

12489 Berlin, Germany

Steffen Palutke, Michael Martins, Wilfried Wurth

Institut für Experimentalphysik, Universität Hamburg, Luruper Chausee 149, 22761 Hamburg,

Germany

[&]Present address: Institut für Ionenphysik und Angewandte Physik, Universität Innsbruck, Innsbruck,
Austria; [§] Present address: Max-Planck-Institut für Chemische Energiekonversion, Stiftstr. 34-36, D-
45470, Mülheim an der Ruhr, Germany

4.2.1 Abstract

We present size dependent spin and orbital magnetic moments of cobalt (Co_n^+, $8 \leq n \leq 22$), iron
(Fe_n^+, $7 \leq n \leq 17$) and nickel (Ni_n^+, $7 \leq n \leq 17$) cluster cations as obtained by X-ray Magnetic Circular
Dichroism (XMCD) spectroscopy of isolated clusters in the gas phase. The spin and orbital magnetic
moments range between the corresponding atomic and bulk values in all three cases. We compare
our findings to previous XMCD data, Stern-Gerlach data and computational results. We discuss the
application of scaling laws to the size dependent evolution of the spin and orbital magnetic moment
per atom in the clusters. We find a spin scaling law "per cluster diameter", $\sim n^{-1/3}$, that interpolates
between known atomic and bulk values. In remarkable contrast, the orbital moments do likewise
only if the atomic asymptote is exempt. A concept of "primary" and "secondary" (induced) orbital
moments is invoked for interpretation.

4. Spin and orbital magnetic moments of pure and doped transition metal clusters

4.2.2 Introduction

The discussion of magnetic phenomena in homogeneous samples of bulk materials focuses on the dominant exchange coupling of pseudospins which localize at atomic centers. The concomitant orbital angular moments of individual electrons quench in the bulk due to orbital hybridization and symmetry reduction. Some orbital angular moments however persist in part. This gives rise to the adjustable bulk g-factors by e.g. 4 - 10 % (Tab. 1) corrections to the spin only g-factor (2.0) in the case of ferromagnetic 3d bulk metals. In the free atoms or ions of those metals, however, the spin and the orbital moments possess values of equal magnitude, e.g. the orbital moment of a free nickel atom even exceeds its spin moment. A change in system size obviously induces a change in the electronic structure which may manifest in a change of magnetic properties.

The evolution of magnetism with sample size and its application has been at the scientific focus for some time[1, 2]. Size selected clusters became favorable objects to follow such evolution[3-5]. Suitable gas phase isolation experiments aim at the determination of intrinsic magnetic moments without the interference of either a supporting surface or of any other environment[6]. Stern-Gerlach experiments serve to determine the total magnetic moments of isolated transition metal clusters in the gas phase as shown by de Heer *et al.*[7] and others[8-11]. These experiments revealed enhanced magnetic moments compared to the bulk attributed to an enhanced contribution of the orbital magnetic moment. However, Stern-Gerlach experiments (see chapter 3.4.) conceptually lack the capability to separate the magnetic moment into its spin and orbital contributions. Moreover, the *ab initio* description of the orbital magnetic moment is still a challenge, despite the ongoing progress in the field (see chapter 3.5.).[12] Problems arise from the highly correlated nature of the magnetic materials.

X-ray magnetic circular dichroism (XMCD) spectroscopy has proven instrumental to elucidate the spin and orbital contributions to total magnetic moments of bulk samples [13-15]. Enhanced orbital moments were found in low-dimensional samples, e.g. thin films [16, 17], nano structures[18, 19], deposited clusters[4, 20, 21] or adatoms[22, 23]. Recently, it became feasible to conduct XMCD spectroscopy of highly diluted samples in the gas phase[24-26]. Accordingly, It was expected to find an enhancement with respect to the bulk of orbital magnetic moments in isolated clusters. Indeed, the findings of both contemporary gas phase experimental setups[24-26] have revealed orbital magnetic moments of clusters that are quenched with respect to the atomic values, but enhanced with respect to the bulk. The differences in the spin magnetic moments are less pronounced.

Table 1: magnetic moments of the atom, cluster and bulk for iron, cobalt and nickel in comparison with spin orbit coupling constants (SOC) for the atom / ion and g-factors for the bulk

	Magnetic moment [μ_B/atom]			Landé g-factor	g' factor[§]	g-factor	SOC[*] constant [cm^{-1}]
	orbit	spin	total				
Fe$_1$ [a] ^{5}D [Ar]4s^{2}3d^6	2	4	6	1.50			-104[i]
Fe$_1^+$ [a] ^{6}D [Ar]4s^{1}3d^6	2	5	7	1.71			-86[j]
Fe$_n^+$ [b]	0.24	2.82	3.07	1.85		2.18	
Fe (bcc, bulk)[c]	0.083	1.98	2.063		1.92[e]	2.09[h]	
Co$_1$ ^{4}F [Ar]4s^{2}3d^7	3	3	6	1.33			-181[k]
Co$_1^+$ ^{3}F [Ar]4s^{0}3d^8	3	2	5	1.40			-238[l]
Co$_n^+$	0.55	2.28	2.83	1.68		2.49	
Co (hcp, bulk)[c]	0.153	1.55	1.703		1.84[f]	2.25[h]	
Ni$_1$ ^{3}F [Ar]4s^{2}3d^8	3	2	5	1.25			-333[m]
Ni$_1^+$ ^{2}D [Ar]4s^{0}3d^9	2	1	3	1.33			-603[j]
Ni$_n^+$	0.33	1.42	1.75	1.68		2.49	
Ni (fcc, bulk)[d]	0.06	0.6	0.66		1.84[g]	2.18[h]	

[a] magnetic moments for atoms and cations calc. according to Hund's rules

[b] average moments of the measured size range of Fe$_n^+$, Co$_n^+$ & Ni$_n^+$, this work

[c] magnetic moments from Ref. [14]

[d] magnetic moments from Ref. [49, 50]

[§] magnetomechanical ratio g': [e] Ref. [95]; [f] Ref. [96], [g] Ref. [97];

[h] taken from Ref. [7]

[*] spin orbit coupling (SOC) constants extracted by Landé interval rule form experimental values:

[i] Ref. [98, 99]; [j] Ref. [99, 100]; [k] Ref. [99, 101], [l] Ref. [99, 102]; [m] Ref. [99, 103]

relationship between the differnt g-factors and g' is given in the Appendix.

A question arising when investigating cluster properties is the following: Does every atom count as in the so called "non-scalable" size regime, or will a trend be followed from the bulk to the atomic

value. For large cluster sizes the properties follow a scaling law which interpolates between the bulk and the atomic value (Tab. 1). Once, the "non-scalable" size regime is reached individual fluctuations are superimposed onto the general trend. There may be noticeable changes in the recorded magnetic moments if one adds or subtracts an atom to a given cluster. Electronic and / or geometric shell closures might occur as well[12]. Therefore, we analyzed the cluster size dependence of spin and orbital magnetic moments for conceivable scaling laws. We have found that the general trend of the spin and orbital magnetic moments each follow a different scaling law which was not to be expected. Individual cluster sizes reveal magnetic moments that are enhanced or diminished with respect to the scaling law values. These are the non-scalable fluctuations that superimpose. Implications of this behavior will be discussed in the final section.

The paper is organized as follows: We introduce the applied and novel combination of experimental techniques and explain the XMCD data evaluation scheme. Subsequently, we present the recorded XMCD data and discuss the obtained spin and orbital moments of iron, cobalt and nickel cluster cations. Next, we compare our total magnetic moments to prior data from Stern-Gerlach experiments, and we compare to spin only moments by computations. A dedicated chapter on concepts of scaling laws precedes our final conclusions. We collect extra material in two appendices and in supplementary material.

4.2.3 Experimental methods and data evaluation scheme

4.2.3.1 The experimental setup for XMCD data recording

The experimental setup ("GAMBIT") consists of a modified Fourier Transform - Ion Cyclotron Resonance - mass spectrometer (FT-ICR; Apex IV, Bruker Daltonics) which was coupled to a soft X-ray undulator beamline at the Helmholtz-Zentrum Berlin / BESSY II (UE52-PGM) as described before [24, 27]. A cryogenic cooling of the ICR cell to 20 K is enabled through an extensive modification of the ICR cell housing. Metal clusters on choice are generated by a custom laser vaporization - cluster ion source[28, 29]. This source utilizes a Q-switched Nd:YAG laser (532 nm, 20 Hz) which is focussed onto the metal target to ablate atomic matter into a short transverse helium gas pulse which yields clusters by swift aggregation. A homebuilt piezo electric valve provides for the gas pulse[30]. Mono isotopic target materials were used in the case of iron (Oak Ridge National Laboratory, Fe-56, 99.93%) and nickel (Oak Ridge National Laboratory, Ni-58, 99.61%) in order to avoid multi isotopic dilution of the signal intensity. The cluster ion beam is transferred into the ICR cell which serves as ion trap as well as mass analyzer. The desired cluster size is selected, isolated and buffer gas cooled

to an appropriately low temperature (T ≤ 20 K). The superconducting magnet (B = 7 T) of the FT-ICR aligns the magnetic moments of the cluster ions. X-ray absorption spectra were measured in Total Ion Yield (TIY), i.e. the trapped cluster ions are exposed to the X-ray beam and the subsequent fragmentation is measured. We recorded fragmentation mass spectra while tuning the photon energy. By summation of all fragment intensities and subsequent normalization to the X-ray photon flux and to the parent cluster intensity, we obtain an integrated and normalized fragmentation spectrum that is equivalent to a relative X-ray Absorption Spectrum (XAS). We obtained L-edge XMCD spectra by subtraction of XAS for both photon helicities (left- and right-handed polarization, lcp and rcp; 90 % polarization at beamline UE52-PGM), cf. the example of Ni_7^+ in Fig.1. Clearly resolved dichroic effects are visible at both the L_2 and the L_3 edge. We obtained XMCD spectra for cobalt, iron and nickel cluster cations in the size range of seven to twenty atoms per cluster. We account for the finite degree of X-ray polarization throughout the further data evaluation.
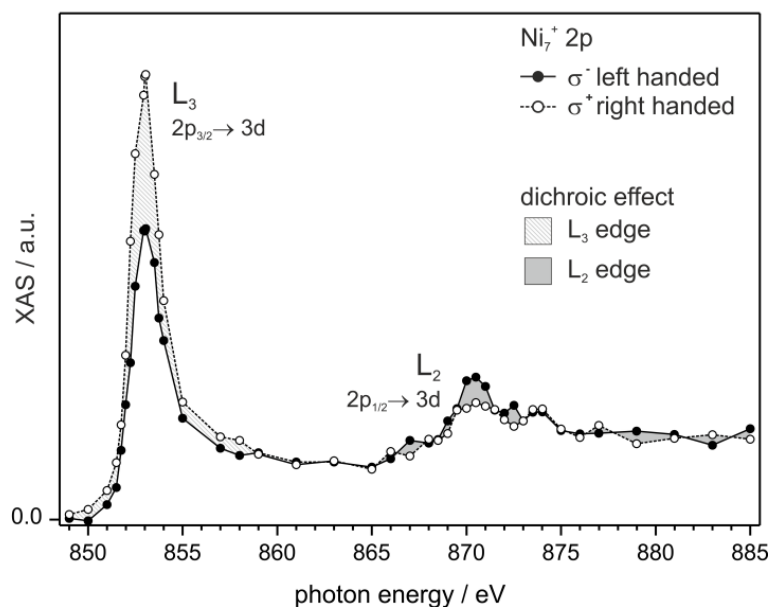

Figure 1 Polarization dependent x-ray absorption spectra for Ni_{12}^+ at the $L_{2,3}$ edge. The spectra were recorded with negative (open symbols) and positive (filled symbols) circular photon polarization with the propagation direction of the x-ray beam parallel to the magnetic field axis. Shaded areas indicate the x-ray magnetic circular dichroism (XMCD) effects for the L_2 and L_3 edge. Spin and orbital magnetic moments are extracted following the procedure outlined by Chen *et al.*[14]

4.2.3.2 The XMCD data evaluation scheme

The projections of the clusters' spin and orbital magnetic moments upon the quantization axis are extracted from the spectra by magneto optical sum rule analysis[14, 31, 32]. The z axis, as quantization axis, coincides with the magnetic field axis of the ICR magnet. The magnetic field axis is collinear with the propagation direction of the X-ray beam. We obtain the numerical values of the z components of spin- and orbital moments, $m_S^{(z)}$ and $m_L^{(z)}$[14] in units of μ_B, by the customized sum rule evaluation formulas:

$$m_L^{(z)} = \left[-\frac{4(A+B)}{3C} n_h \right] / \eta_{pol} \qquad (1)$$

$$m_S^{(z)} = \left[-\frac{2(A-2B)}{C} n_h - 7\langle T_z \rangle \right] / \eta_{pol} \qquad (2)$$

The parameters **A** and **B** represent the integrated dichroic effects ($\sigma^+ - \sigma^-$) at the L_2 and L_3 absorption edges of the experimental spectra (Fig. 1). **C** is the corresponding value of the isotropic spectrum which is approximated by the sum of spectra of both polarizations ($\sigma^+ + \sigma^-$), corrected for non-resonant background absorption[14]. $\langle T_z \rangle$ is the anisotropic dipole term, and n_h is the number of unoccupied 3d valence states ("3d holes"). The finite degree of circular polarization η_{pol} (in present case: 90%) necessitates the application of an according linear correction.

There are clear relations amongst the number of 3d holes n_h, the number of unpaired electrons $5 - |5 - n_h|$, the total spin $S = \frac{1}{2} (5 - |5 - n_h|)$, and the spin magnetic moments per atom $m_S = (5 - |5 - n_h|) \mu_B$. The $4s^2 3d^x$ configurations of Fe, Co, and Ni atoms (x = 6, 7, 8) thus determine via n_h = 4, 3, and 2 their spin magnetic moments m_S = 4 μ_B, 3 μ_B, and 2 μ_B. In the bulk phase, the diffuse 4s atomic orbitals form a broad conduction band, whereas the compact 3d orbitals are less overlapping and form a narrower valence band. As a result, the conduction (4s) band is more or less half-filled and the spins are paired to a large extend. The 3d population is then substantially increased. The value of 3d holes n_h/atom reduce in the bulk with respect to atomic samples. Possible issues on the determination of bulk n_h values have been discussed before[33]. Currently accepted values of bulk phase 3d holes per atom are n_h^{bulk} = 3.4[34, 35] for iron, n_h^{bulk} = 2.5[14] for cobalt, and n_h^{bulk} = 1.45[36, 37] for nickel. Most recently an independent study[26] elaborately concluded in $n_h(Fe)$ = 3.3±0.2, $n_h(Co)$ = 2.5±0.2, and $n_h(Ni)$ = 1.3±0.2. Both sets of values agree within stated uncertainties to better than 3%. For the purpose of the current study, we chose to utilize the former set of n_h data.

Small clusters are single domain particles[38, 39] which can be considered to behave super paramagnetic[40-42]. The magnitudes of XMCD spin magnetic moments per atom m_S are expected

to range around the superparamagnetic prediction of $m_s^{(sp)} = n_e^{(u)} s \, g_e \, \mu_B = n_h^{bulk} \mu_B$, where $n_e^{(u)}$ is the number of unpaired electrons per atom, and s and g_e indicate the electron spin and its gyromagnetic ratio. The latter equality holds in the case of elements with more than half filled valence sub shells. Deviations of the recorded XMCD spin magnetic moments from the predicted $m_s^{(sp)}$ values indicate electronic rearrangement within the clusters with respect to the corresponding bulk material. The documentation of recorded XMCD spin magnetic moments (Fig.2) includes the above cited n_h values for ease of comparison.

The anisotropic dipole term in Eq. (2), $\langle T_z \rangle$, treats a possible anisotropy in the spin distribution of the investigated sample. It corresponds to a spin asymmetry along the quantization axis. It may modulate the spin magnetic moment in a highly anisotropic medium up to 20 % [43], and it would cancel by an angular average [44]. A previous XMCD experiment has verified the absence of linear dichroism in an iron cluster, i.e. Fe_{10}^+, when stored as isolated ions within an ion trap[26]. This provides for an experimental verification that $\langle T_z \rangle$ is small enough to allow for a decoupling of the spin magnetic moment from the clusters nuclear framework. Thus, at the current field strength (7 Tesla) the magnetic moments of the cluster may align (see below) while the cluster body - its framework of nuclei - is able to rotate freely. At any time their nuclear orientation is random. In the following we approximate $\langle T_z \rangle \approx 0$. The opposite case, $\langle T_z \rangle \gg 0$, would imply that magnetic moments do not rotate independently of the cluster nuclear framework. Then the magnetic crystalline anisotropy energy would exceed the thermal rotational energy. The magnetic moments would lock to the cluster frame below a critical blocking temperature, in short a locked moment behavior.

The projection of quantized magnetic moments upon a quantization axis obeys the Brillouin function $f_{Br}(T, B)$ in dependence of sample temperature T and external magnetic field strength B[45]. It is well approximated by the classical Langevin function $f_{La}(T, B)$[9, 41, 46, 47]. Thus, the projections of the magnetic moments onto the quantization axis are functions of cluster temperature and applied magnetic field. The intrinsic spin magnetic moments m_S and the intrinsic orbital magnetic moments m_L derive from their measured projections $m_S^{(z)}$ and $m_L^{(z)}$. The intrinsic magnetic moments would correspond to a sample magnetization at 0 Kelvin and infinite magnetic field. In the present case of 3d metal clusters, the experimental conditions ($T_{cluster} = 20$ K and $B_{external} = 7$ T) indicate Russel-Saunders (LS) coupling, and it is the total magnetic moment which aligns to the external magnetic field[25]. Note, that our previous study has considered both LS coupled and Paschen-Back decoupled magnetic moments[24].

Deriving the spin and orbital magnetic moments by sum rule analysis is known to imply a systematical error of $\pm\, 5 - 10$ %[48]. Further uncertainty enters by the choice of n_H, by the choice of

the integration regions and by the subtraction of non-resonant background. Some minor uncertainty arises through the indirect knowledge of cluster temperature which enters into the Langevin scaling. We estimate these parameters to add another ± 5 % uncertainty. In total we derive an uncertainty of our spin and orbital magnetic moments of ± 15 % (1 σ standard deviation).

4.2.4 Results and discussion

The spin and orbital magnetic moments of small iron, cobalt and nickel cluster cations, Fe_n^+, Co_n^+, and Ni_n^+, were measured under the same experimental conditions as our previously published data on some cobalt clusters[24].

4.2.4.1 Magnetic moments of iron clusters by XMCD

We investigated iron cluster cations Fe_n^+ in the size range from $7 \leq n \leq 16$ and $n = 18$ atoms per cluster. The spin magnetic moments range from 2.13±0.3 to 3.48±0.47 μ_B/atom, and the orbital magnetic moments range from 0.45±0.07 to 0.12±0.02 μ_B/atom (Fig. 2). Spin as well as orbital magnetic moments are enhanced with respect to the bulk values (Fe, bcc) of m_S = 1.98 μB/atom and m_L = 0.083 μB/atom[14]. This enhancement of spin magnetic moments (factor 1.1 to 1.8) is smaller than that of the orbital magnetic moments (factor 1.5 to 4.0). Both the spin as well as the orbital magnetic moments of the clusters are significantly quenched with respect to their atomic values (cf. Tab.1).
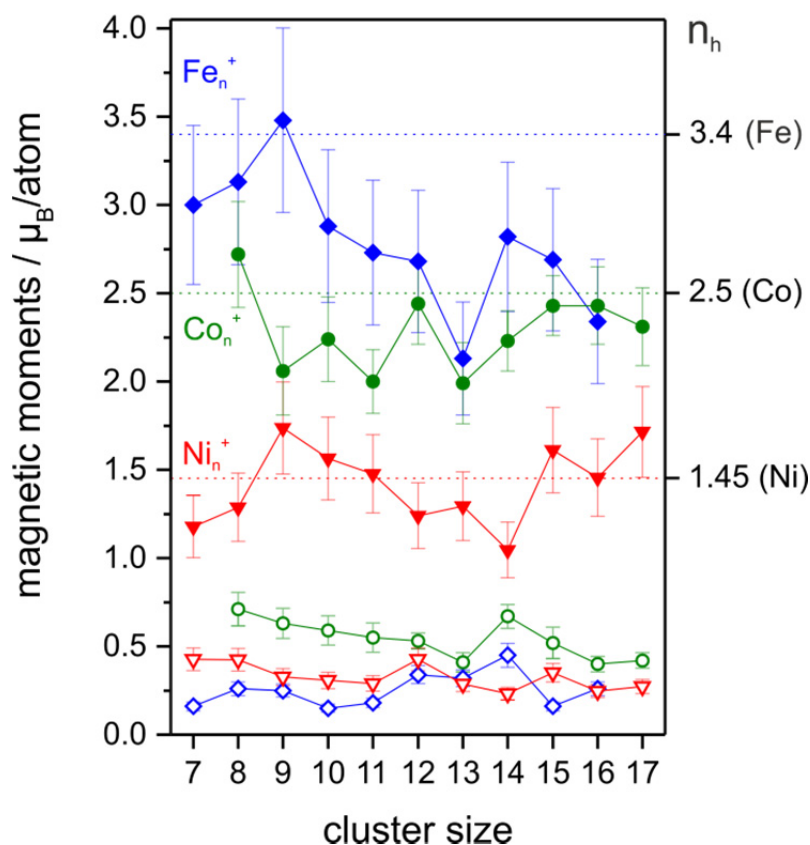
Figure 2 Spin (filled symbols) and orbital (open symbols) magnetic moments of iron Fe_n^+ (diamonds), cobalt Co_n^+ (circles) and nickel Ni_n^+ (triangles) cluster cations. Dashed lines indicate the number of 3d holes as used in the evaluation of the spin and orbital magnetic moments (see 4.2.3.2 XMCD data evaluation scheme).

The cluster size dependent absolute variations of spin moments in iron clusters are larger than those of the orbital moments, relative variations are comparable. Our spin magnetic moment of Fe_{13}^+ (2.13±0.3 μ_B/atom) is the smallest of all those measured, in agreement with Lau *et al.* [25] who found an interpretation in terms of an antiferromagnetic coupling in conjunction with icosahedral geometric shell closure in the case of this particular cluster size. Our spin magnetic moments of Co_{15}^+ and of Co_{16}^+ (2.7±0.4 and 2.30±0.35) are smaller than those reported by Lau *et al.* (3.7±0.5 and 3.7±0.5). The recorded deviations of both data sets range slightly beyond the combined uncertainties. For sure these deviations are minor as compared to the significant reduction of spin magnetic moment in Fe_{13}^+, where both data sets agree well.

Our experimental spin magnetic moments of Fe_n^+ clusters are on the average lower by 10 % than the average of the previously reported ones[25]. This difference is not explained by the different choice of n_h values which by themselves differ by 3% (cf. exptl. section).

4. Spin and orbital magnetic moments of pure and doped transition metal clusters

The orbital magnetic moments of our present study agree very well with those of Lau *et al.*[25] in the case of nine cluster sizes (Fig. S2). In two cases the agreement is inferior: Our value for Fe_{14}^{+} (0.45±0.07 μ_B/atom) is higher than theirs (0.14±0.35 μ_B/atom) while their value for Fe_9^{+} (0.6±0.35 μ_B/atom) is higher than ours (0.25±0.04 μ_B/atom). In all cases, however, there is agreement within combined 1σ uncertainties.

4.2.4.2 Magnetic moments of cobalt clusters by XMCD

We have determined spin and orbital contributions to total magnetic moments of isolated cobalt clusters (Co_n^{+}, 8 ≤ n ≤ 17 and n = 19, 22) by the XMCD technique before[24], and there has been an independent study on a limited cluster size range (n = 10 – 15)[26]. Here we report on a novel data set that originates from a re-evaluation of our previous experimental recordings. In all cases our new and previous XMCD spectra agree reproducibly well to within less than 10% deviation.

The current spin magnetic moments of the clusters are larger than the bulk value by approximately 1 μ_B per atom (cf. Tab.1). Our spin magnetic moments are lower than those of Lau *et al.*[26] with a minimum deviation of 1% for Co_{15}^{+} and a maximum deviation of 20 % for Co_{13}^{+} (Fig. 2; n = 19, 22 in Tab. S3a,b and Fig. S2; see also Figs. 3 and 4). Except for the Co_{13}^{+} cluster, spin magnetic moments agree within combined experimental uncertainties.

The orbital magnetic moments reveal almost constant values of about 0.55 ± 0.05 μ_B/atom. Note, that the present experiments cover a wider range of cluster sizes than [26]. The orbital moments vary between 0.4 - 0.7 μ_B/atom within our investigated cluster size range. This corresponds to a quenching of the atomic value of 3 μ_B, or to an enhancement by a factor of 2 - 4 of the bulk value (m_L (Co, hcp) = 0.153 μ_B / atom [14]).

4.2.4.3 Magnetic moments of nickel clusters by XMCD

By virtue of the present study, we achieve an extension in size range with respect to previously published XMCD data on the spin and orbital magnetic moments of nickel clusters Ni_n^{+} (n = 10 - 15) [26]. Our XMCD data set covers the extended range of n = 7 - 17. We find very good agreement of both data sets within the overlapping size range, the previous spin magnetic moments being 10 to 20 % lower than our new values, which falls within the combined uncertainties.

We find considerable fluctuations of spin magnetic moments throughout our investigated size range: They range from 1.05±0.1 μ_B/atom for Ni_{14}^{+} to 1.74±0.2 μ_B/atom for Ni_9^{+}. They are quenched with respect to those of isolated atoms (2 μ_B/atom in Ni $[Ar]4s^2 3d^8$, ^3F), and they are enhanced with respect to those of the bulk (Ni (fcc), 0.6 µB/atom[49, 50]).

There is very good agreement of the present nickel data set with the previously published data[26] on the magnitudes of the orbital magnetic moments within the overlapping cluster size range (cf. Fig. S2 in the supplement). Cluster size dependent variations are minor (+/- 25 %), and smooth.

The orbital magnetic moments of small nickel cluster cations ($7 \leq Ni_n^+ \leq 17$) range from 0.25 - 0.43 μ_B/atom, and they are enhanced with respect to those of the bulk (Ni (fcc), 0.06 μ_B/atom[49, 50]). They are quenched with respect to those of isolated atoms (3 μ_B/atom in Ni [Ar]$4s^2 3d^8$ ^{3}F). The orbital moment of Ni_{12}^+ is enhanced by 0.14 μ_B/atom with respect to the neighboring cluster sizes (cf Fig. 2).

Both of our data sets, on the spin magnetic moments of cobalt and iron clusters, provide for slightly smaller values than those of Lau et al.. Our data on the spin magnetic moments of nickel clusters, however, reveal slightly larger values than those of Lau et al. as discussed above. Neither of both experiments suffered from major variation of experimental parameters. Thus it is conclusive to interpret the recorded small differences as within statistical variations. We thus conclude on a verification of spin and orbital magnetic moments through two independent studies (present and previous) which have revealed values that mostly agree within combined error bars. The magnitudes of these magnetic moments thereby become known and confirmed entities that may compare to related cluster properties as obtained by other methods.

4.2.4.4 XMCD data on cationic clusters and Stern-Gerlach data on neutral clusters

Gas phase XMCD experiments determine partial magnetic moments of cationic clusters; Stern-Gerlach (SG) experiments determine total magnetic moments (SG moments) of neutral clusters. Partial XMCD moments due to spin and orbital contributions add up to total magnetic moments (XMCD moments). Current gas phase XMCD experiments take place on samples after in situ equilibration by buffer gas cryo cooling; SG experiments utilize supersonic expansion for irreversible cooling down to estimated temperatures. Current gas phase XMCD experiments utilize homogeneous magnetic fields of 5-7 Tesla; SG experiments have utilized inhomogeneous magnetic fields of 1-2 Tesla. Gas phase XMCD allows for orientation and relaxation of magnetic moments of the cluster samples on the time scale of multiple seconds in the presence of cold collision partners; previous SG experiments work on the microsecond time scale through relaxation of magnetic moments without collision partners. In summary, it is not obvious that magnetic measurements by the XMCD scheme and by the SG scheme compare well and would lead to identical data. (Fig. 3a,b,c).

The charge state of a cluster makes the less of a difference, the larger the cluster is. The positive charge of e.g. a Fe_8^+, Co_8^+, or Ni_8^+ cluster increases by one the enumerator and decreases by one the

4. Spin and orbital magnetic moments of pure and doped transition metal clusters

denominator in the ratio of unoccupied to occupied valence states (3d,4s) with respect to that of neutral clusters: 32/64, 24/72 or 16/80 (neutral) to 33/63, 25/71 or 17/79 (cationic), respectively. By virtue of the prevailing cases of more than half filled valence shells, the cationic clusters should bear total spin magnetic moments that should be larger by 1 μ_B than those of neutral clusters. Per cluster atom this dilutes to small enhancements of 1/n μ_B , e.g. in the case of n=8 the cationic charge makes up for an increase of 0.125 µB/atom in spin magnetic moment per atom. The ratio of vacant to occupied states (holes to electrons within the valence shell) increases through charging by mere 2% in Fe_{20}^+ while it increases considerably by 7.6% in Ni_8^+. We thus anticipate, that cationic charge has little influence on magnetic moments (and geometry) of large iron clusters and probably some influence on small nickel clusters. The case of charges in cobalt clusters is intermediate. These estimates require consideration when comparing XMCD data and SG data with each other.

The magnitudes of total magnetic moments of cationic cobalt clusters by XMCD range amongst the considerable scatter of currently available Stern-Gerlach data[7, 51-54]. The total magnetic moments deduced from the XMCD experiments are larger than the SG moments of de Heer *et al.*[7, 51, 54] and of Knickelbein *et al.*[53], and they are lower than those of Bloomfield *et al.* [52].

The total magnetic moments of the iron cluster cations by our current XMCD experiments reveal comparable magnitudes as obtained on neutral clusters by prior Stern-Gerlach experiments[7, 51, 55] for sizes n ≥ 13 (Fig. 3a). Our XMCD data of smaller clusters reveal little to no increase in magnitude (≤ 20%) while the SG moments of the sole available experiment jump in magnitude by a factor of two. This finding seems questionable to us – the more so as all but these data reveal a common trend of moderate variations by size.

Note, that the exceptionally low XMCD moments of Fe_{13}^+ coincides with an exceptionally low SG moment of Fe_{13} - nicely supporting the antiferromagnetic coupling scheme within an icosahedral closed shell geometry[25] as discussed above and before.

The total magnetic moments of the neutral clusters (by Stern-Gerlach) and of cluster cations (by XMCD) of cobalt and iron show pronounced minima for the same cluster sizes, e.g. for Fe_{13}^+[25, 51, 55]. Our absolute values of the total magnetic moments by XMCD for cobalt and iron cluster cations are comparable to the values of neutral clusters by Stern-Gerlach experiments. Our total magnetic moment of the cationic nickel clusters by XMCD are larger by 40 to 60 % than those of neutral nickel clusters by Stern-Gerlach[9-11]. Note, that the pattern of cluster size dependent variations in cationic nickel clusters resembles that of neutral nickel clusters but shifted by one atom – in contrast to the cases of cobalt and iron clusters where the significant reduction of total magnetic moments at n = 13 prevails for cations and neutrals alike. In the case of small nickel clusters the charge state seems to

influence magnetic moments significantly, whereas an according influence is not evident in the case of cobalt and iron clusters – much in line with the above discussed estimation.
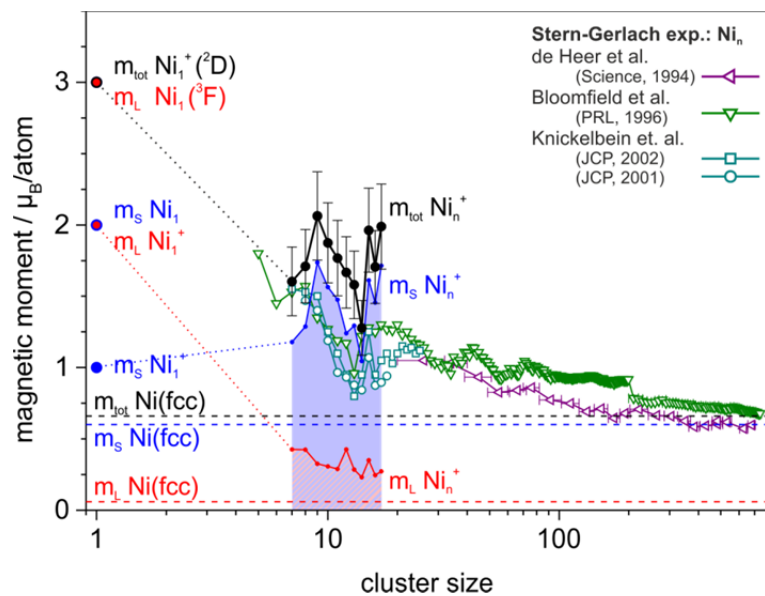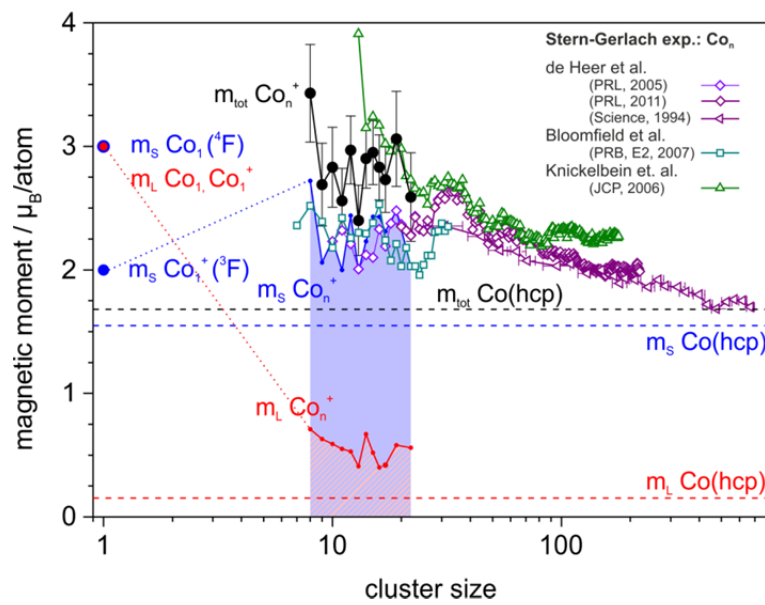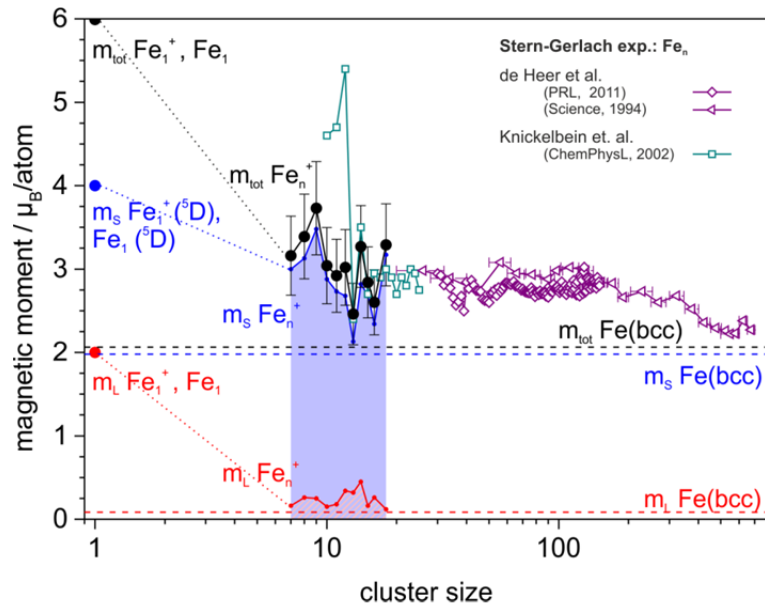
Figure 3 Total Magnetic moments (filled circles) determined by XMCD experiments in comparison with Stern-Gerlach results (open symbols).**(a) Fe_n^+, (b) Co_n^+, (c) Ni_n^+.** Shaded areas indicate the spin (solid, blue) and orbital (hatched, red) magnetic moments. Dashed lines display the magnetic moments of the respective bulk material (Fe & Co[14], Ni[49, 50]). The magnetic moments of the free atom and cation were calculated according to Hund's rules. Stern-Gerlach results were taken from Ref. [7, 51, 55] for Fe_n^+, from Ref. [7, 51-54] for Co_n^+ and from Ref. [7, 9-11] for Ni_n^+. For Ref. [51] the magnetic moments for the assigned high spin states are plotted and for Ref. [52] the experimental series denoted E2 is plotted. The Stern-Gerlach experiments investigated a wide cluster size range of up to several hundred atoms per clusters. The magnetic moment does not smoothly approach the bulk value with increasing cluster size but shows an oscillatory behavior. These oscillations are due to electronic and / or geometric shell closures and are superimposed onto the general trend[12]. Our narrow size range does not allow us to detect these oscillations.

Beyond the range of our present XMCD experiments some of the Stern-Gerlach experiments have revealed repetitive oscillations in total magnetic moments of large clusters. These were interpreted convincingly in terms of a modulation by electronic and / or geometric shell closures [7, 12, 56, 57].

4.2.4.5 XMCD data in the light of previous computations

Density functional theory served to obtain predictions for the spin magnetic moments of neutral iron clusters[58-65] and of cationic iron clusters[33, 58, 66, 67], of neutral cobalt clusters[59, 64, 67-75] and of cationic cobalt clusters[67-69, 76], of neutral nickel clusters [47, 59, 64, 67, 68, 77-80] and of cationic nickel clusters[67, 68, 77]. The predicted spin moments of the cationic clusters are smaller than the previous spin magnetic moments by XMCD experiments[26]. The found deviation was attributed to conceptual problems of approximate exchange-correlation functionals in describing highly correlated 3d electrons.

The published DFT predictions of spin magnetic moments of Fe_n^+ clusters in the size range from $7 \leq n \leq 20$[58, 66] with a focus on Fe_{13}^+[33, 68, 81] agree with the XMCD moments of the present study except on Fe_9^+ (XMCD expt. yields a larger spin magnetic moments) and Fe_{13}^+, Fe_{16}^+ (XMCD expt. yields a smaller spin magnetic moment), cf. Fig. S4 in the supplementary material. The exceptionally low spin magnetic moment found for Fe_{13}^+ has been interpreted in terms of an antiferromagnetic coupling of the center atom to its 12 surrounding surface atoms in an icosahedral geometry[25] with an ongoing controversy of its origin[33, 81] prevailing. Our present XMCD spin magnetic moment of Fe_{13}^+ falls low by 0.5 μ_B/atom with respect to $Fe_{12,14}^+$ and thereby lends support to the idea of antiferromagnetic coupling in icosahedral geometry. The cited controversy could be solved in the future by application of the so far not yet applied broken symmetry approach to DFT calculations[82, 83].

4. Spin and orbital magnetic moments of pure and doped transition metal clusters

The published DFT predictions of spin magnetic moments of Co_n^+ clusters in the size range from $2 \leq n \leq 30$[68] [69, 76] are lower than the XMCD moments of the present study except on $Co_{9,11,13}^+$ where perfect agreement is found, cf. Fig. S5 in the supplementary material.

DFT treatments of Ni_{12} and Ni_{12}^+ conclude on icosahedral structures and yield predicted spin magnetic moments of $8\,\mu_B$ ($0.67\mu_B$/atom) and $9\,\mu_B$ ($0.75\,\mu_B$/atom), respectively[68], which is significantly lower than the experimental value of $1.24\pm0.2\,\mu_B$/atom. The same study obtained for the cationic cluster Ni_{13}^+ two almost degenerate lowest energy isomers with spin magnetic moments of $0.69\,\mu_B$/atom and $0.85\,\mu_B$/atom, which is significantly smaller than the present spin magnetic moment by XMCD experiments of $1.3\pm0.2\,\mu B$/atom. Another study covered an extended cluster size range for Ni_n^+ with $n \leq 30$[77] and obtained spin magnetic moments that are about $0.3\,\mu_B$/atom lower than those of the present XMCD experiments. The Ni_7^+ cluster constitutes an exception where the XMCD value of spin magnetic moment ($1.2\,\mu_B$/atom) agrees perfectly with the value from the above DFT study[77] and with those of another one[67] . Both studies conclude on a capped octahedron structure of Ni_7^+.

In conclusion the present and previous XMCD experiments confirm the above theoretical predictions on quenching/ enhancement of spin magnetic moments in small iron, cobalt and nickel clusters with respect to atoms/the bulk. XMCD experiments and two dedicated model calculations[57, 66] agree that the orbital magnetic moments in small iron and nickel clusters will be larger than the bulk values[57, 66]. The particles' finite size leads to a reduced coordination number at the surface, such that the 3d electrons are more localized and therefore retain more of an orbital moment than the bulk does – much in line with previous discussion of magnetism in ultrathin films[84]. There will be size dependent shell closures modulating the actual values of the spin and orbital magnetic moments, superimposed on general trends[7, 12, 56, 57]. The following discussion shall neglect such shell effects and elucidate the underlying, more general size dependent trends.

4.2.5 Scaling laws of the spin and orbital contributions to magnetic moments of Fe_n^+, Co_n^+, and Ni_n^+ clusters?

Within the investigated size range, the obtained spin and orbital moments vary little. The values of the total magnetic moments fall within the range of those of previous investigations. Nevertheless, it pays to re-approach the data once more from a broad perspective. If clusters indeed interface between atom and bulk, and if they truly bridge the gap in-between, one would expect a scaling of their properties by size. Such a scaling should interpolate between bulk properties and atomic properties and it should follow predictable trends when scaling from bulk to clusters. Reducing sizes further, one anticipates strongly size dependent and non-monotonous jumps in cluster features (as predicted and observed often before), which has led to the coinage of the term of

a "non-scalable" size regime[85, 86]. Note, however, that the scalability of properties is not obsolete. Instead, "magic cluster size" related variations superimpose onto the prevailing scaling laws. (see Tab. 2 for various common scaling laws). In the present case of magnetic moments $m(n)$ and their individual contributions $m_x(n)$; $x = S, L$, conceivable scaling laws would read as follows:

$$m_x(n) = a_x + b_x\, n^{y_x} \qquad (3)$$

Note, that these magnetic moments $m_x(n)$ refer to intensive values[87], i.e. the magnetic moments are normalized "per atom". The parameters to determine are: the reference values a_S and a_L, the scaling factors b_S and b_L and the scaling powers y_S and y_L. The available experimental data of $n = 7 - 17$ would allow for a fit of these parameters – in principle. The concomitant uncertainties would render such a limited-size-range-fit meaningless, however. It is mandatory to consider the asymptotic limits and to evaluate physical models (Table 2).

Table 2 Various cluster properties and scaling laws - N refers to the number of particles or atoms per molecule or cluster

cluster property				proportional to
surface tension of a spherical droplet	γ	$1/R^2$	=	$N^{-1/2}$
ratio of surface to bulk atoms in a spherical particle	N_S / N_V	$1/R$	=	$N^{-1/3}$
binding energy/atom (cohesive energy) [104-106]	ε_{coh}			$N^{-1/3}$
ionization potential [107, 108]	I_P			$N^{-1/3}$
electron affinity [107, 109]	E_a			$N^{-1/3}$
resonance frequency of a spherical metal cluster [110-112]	ω_r	$1/R^3$	=	N^{-1}
autoionization resonance energy of Hg clusters [113-115]	δ_n			N^{-1}
average energy level spacing [116]	ΔE			N^{-1}
magnetic dipolar interaction [117]	E_{mag}			N^{-1}
cluster polarisabilities [112]	α_N	R^3		N

4. Spin and orbital magnetic moments of pure and doped transition metal clusters

Assuming a cluster of n spherical atoms in dense packing and with total diameter L,[88] the cluster volume V_c scales to a good approximation as $V_c \sim n \sim L^3$. The number of surface atoms n_s goes by the surface area, $n_s \sim L^2$. The fraction of surface atoms n_S/n scales as $\frac{n_S}{n} \sim L^{-1} \sim n^{-1/3}$. This fraction of surface atoms may be a taken as a quantitative measure for the mixing in of atomic like magnetic properties, justified by the lower coordination of the surface atoms. Accordingly, $y_x = -1/3$, and an interpolation from the atomic case (all surface) to the bulk case (all volume) may read as

$$m_x(n) = a_x + b_x\, n^{-\frac{1}{3}} \qquad\qquad \text{(4a)}$$

In a second step, it may be assumed that: $a_x = m_x(\infty)$ and $b_x = m_x(\infty) - m_x(1)$ would serve as valid/appropriate choices for the reference values a_x and scaling factors b_x:

$$m_x(n) = m_x(\infty) + \frac{m_x(1) - m_x(\infty)}{n^{1/3}} \qquad \text{(4b)}$$

Such a choice may look obvious at first sight. It is not forcing, however, and it takes verification. In any case, one needs to consider independently the spin and orbital contributions ($x = S, L$) to the magnetic moments of the Fe_n^+, Co_n^+ and Ni_n^+ clusters. This takes to verify six sets of parameters (a_x, b_x, y_x), which gives 18 values in total.
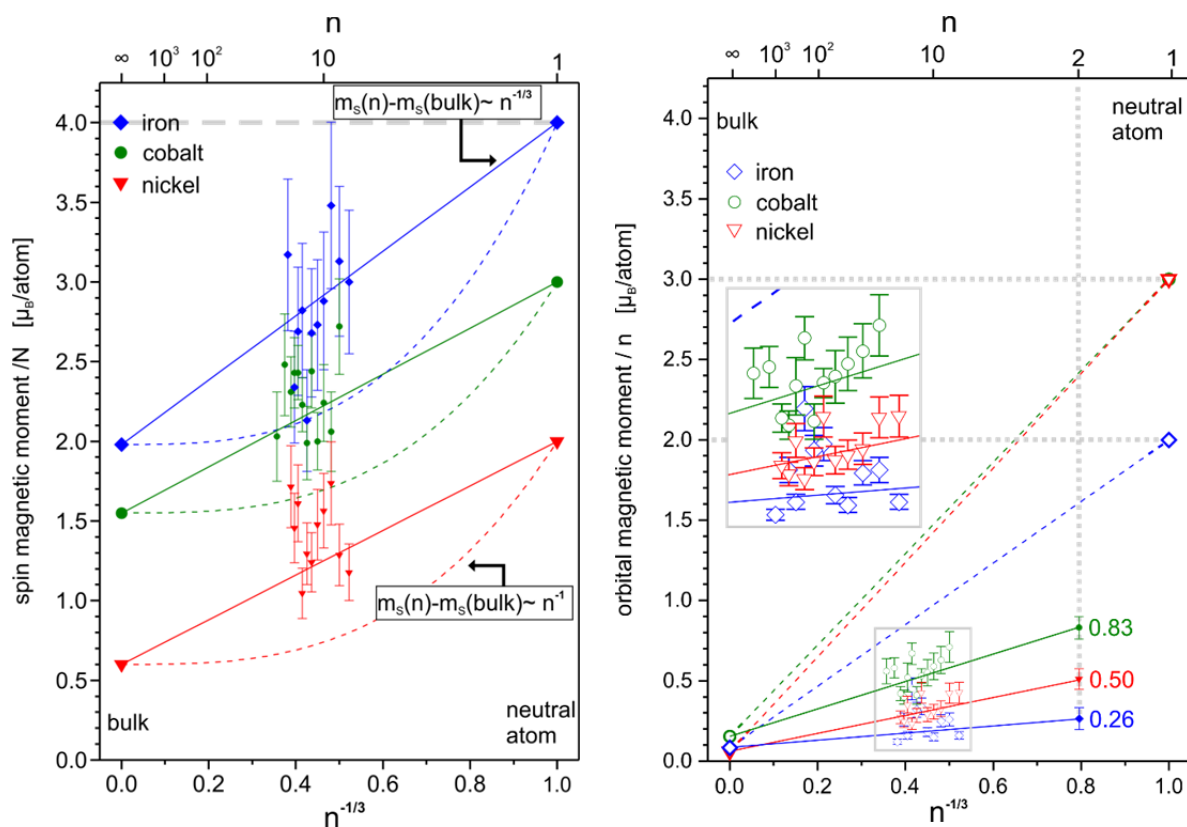
Figure 4 Spin (left) and orbital (right) magnetic moments of size selected clusters in comparison to conceivable trends that would interpolate between bulk metals and neutral atoms. Note, that the recorded spin moments seem to follow an $n^{-1/3}$ scaling. Orbital moments of n = 2 clusters ($n^{-1/3} = 0.794$, solid symbols) are tentative predictions from the $n^{-1/3}$ fits of experimental bulk and cluster data as displayed, with atomic values exempt from the fit.

Figs. 4a and 4b visualize an attempt to compare the recorded spin and orbital magnetic moments of the Fe_n^+, Co_n^+ and Ni_n^+ clusters to conceivable scaling laws. The x-axes of diagrams are chosen as $n^{-1/3}$ (namely: $y_x = -1/3$) which makes any accordingly scaling data set resemble a straight line. Note, that alternative scaling laws may be visualized by nonlinear curves as was done e.g. between the same asymptotes in Fig. 4a by dashed lines for the case of $y_S = -1$ (which corresponds to a scaling "per cluster volume").

Spin moments.

It is gratifying to realize that the recorded cluster data of spin magnetic moments (data points in Fig. 4a) come close to the conceived scaling law in the three cases of Fe_n^+ (blue diamonds), Co_n^+ (green circles) and Ni_n^+ (red triangles). In particular, the scaling "per diameter" ($y_S = -1/3$) reproduces the experimental data on spin contributions quite well. It would be inappropriate to

4. Spin and orbital magnetic moments of pure and doped transition metal clusters

consider an alternative scaling law "per cluster volume" ($y_S = -1$). An intermediate case of scaling "per surface area" ($y_S = -1/2$) is obviously not suitable either.

We conclude from this scaling law that the average spin magnetic moment per atom seems to follow the surface area of the cluster (normalized to the cluster volume). In a first try of an explanation we can follow the argumentation that rationalizes the enhanced spin magnetic moment at surfaces and of thin films. The reduced coordination number at surfaces leads to a stronger localization of the electron wave function and thus to a narrower band width which in turn leads to a higher density of states at surface atoms[42, 84, 89]. This leads to an enhanced spin magnetic moment at surfaces. As our measurement averages over all coordination sites (surface and volume), enhanced spin moments at surface sites will lead to an enhancement with respect to the bulk of the average spin magnetic moment per atom in clusters. This leads to a scaling by 1 over area per volume which appears as $n^{-1/3}$ - as observed. This might explain why the surface area is important. Individual size effects – few of which we find in our present data - should be superimposed onto the scaling law. If the investigated size range was to be extended towards larger and/or smaller clusters, the scaling trend should become more pronounced.

It remains to discuss whether the choice of the spin reference value $a_S = m_S(\infty)$ and of the spin scaling factor $b_x = m_S(1) - m_S(\infty)$ according to eq. (4b) is appropriate. The onset of complex (multi – domain) magnetic phases, which are characteristic for the bulk sample, is far beyond the size of the clusters investigated in this and other studies. Thus, single domain bulk spin moments might seem a more appropriate choice for the spin reference value a_S. However, the cited values (cf. Table 2.) stem from bulk XMCD studies which were conducted at saturation field strength where the magnetization of all domains was flipped into easy axis alignment with respect to the applied external field. Under such conditions the recording of bulk magnetization values may yield single domain like values which in turn suite for comparison to super paramagnetic clusters.

For the atom, the increased spin moment is not due to unpaired 4s electrons but a consequence of a completely filled 4s orbital, which causes an additional hole in the 3d shell. This feature is already absent if one goes to a diatomic molecule. Thus, for different reasons, surface and isolated atoms have an increased spin moment, and the difference between large clusters and the bulk is not too large. Note that in the case of nickel, the solid line seems to be too low. Maybe this is caused by a particularly small value of the spin moment per atom for the bulk.

Orbital moments.

There are remarkably different findings in the cases of the orbital magnetic moments (Fig. 4b) of Fe_n^+ (blue diamonds), Co_n^+ (green circles) and Ni_n^+ (red triangles). For sure, they are not explained by a

"per diameter" scaling as given by eq. (4b) (dashed lines in Fig. 4b).The found cluster values are quite small (< 0.6 μ_B/atom). They range close to the quenched asymptotic bulk values, and they are far below the atomic values. Those unquenched atomic orbital moments (of first order or primary nature) arise exclusively from orbitally degenerate ground states (where both clockwise and counterclockwise rotations are equally possible). Clustering lifts symmetry related degeneracies, and arbitrary degeneracies are unlikely – those would be lifted by a Jahn-Teller distortion. Henceforth, primary orbital moments of clusters necessarily vanish, they are completely quenched. If one "switches on" the spin-orbit coupling for a system of non-degenerate orbitals, small orbital moments are induced by mixing in exited states. We like to call those orbital moments "second order" or "secondary". The same mechanism is responsible for the shift of the g value in transition metal complexes, which is well known to result from an interplay of spin-orbit coupling and the local environment (crystal field). It is therefore reasonable to assume that coordination geometries and orbital occupancies interdepend. A change from bulk to surface coordination thus changes orbital occupancies in the affected atom(s). We therefore state that the fraction of surface atoms may serve as a measure for the cluster size related change in orbital moments, in accordance with eq. (4a), $y_L = -1/3$. The choice of reference value is obvious, as well, $a_L = m_L(\infty)$. As of the orbital scaling factor b_L , an *a priori* choice is not possible. Instead, we take the recorded $m_L(n)$ values to perform a linear fit (of b_L) to eq. (4a). The results of such fits are indicated in Fig. 4b by solid lines which quite convincingly reproduce the observed orbital values. It would be decisive to obtain experimental data for the clusters n = 2 and n = 3. Predicted values for the case of n=2 are indicated in the figure (Fig. 4b, solid symbols).

Surface layers of transition metals are known to show an enhanced orbital moment compared to the bulk phase[17]. This has been attributed before to the fact that atoms have a lower coordination number than bulk atoms and the 3d states are more localized than in the solid[13, 90, 91]. Hence, surface atoms are said to retain more angular orbital momentum than their bulk counterparts. Our present findings on isolated clusters are fully in line with this line of arguments. The orbital moment per transition metal atom should thus follow the ratio of surface atoms-to-bulk atoms (eq. 4a). It might follow that the general geometry of the clusters influences the orbital moment more strongly than the spin magnetic moment, i.e. the coordination environment, number of nearest neighbors and bond lengths, etc.. Exceptionally high or low orbital magnetic moments may appear for certain cluster geometries which have an open structure (high orbital magnetic moment) or a high symmetry (small orbital magnetic moment). In the case of the orbital magnetic moment, one might see a significant change if the geometrical motif changes e.g. from icosahedral to bulk like. Future experiments might cover an extended size range to elucidate such a transition in crystalline structure.

4. Spin and orbital magnetic moments of pure and doped transition metal clusters

Validation of scaling law

It is a general question of concern whether a continuous scaling of magnetic cluster properties amongst atomic and bulk values is to be expected in the first place. Discontinuous (phase) transitions are well conceivable. At present, we are able to phrase a "robust" finding of the present study *without* stating any scaling: Spin and orbit contributions of iron, cobalt and nickel clusters comprising 10 - 20 atoms are closer to bulk than to atomic values. The relative quenching of orbital moments in cluster is higher than that of the spin moments. A definite interpretation of the found scaling laws is pending and will need further support form theory.

Current interpretation discuss spin and orbital moments of ground state atomic configurations, $4s^2 3d^x$ as asymptotes of scaling laws. It is conceivable to consider instead the spin and orbital moments of metastable $4s^1 3d^{x+1}$ atomic configurations which closer resemble bulk type bonding. When doing so, the found spin moment scaling would diminish. Our conclusions on two types of orbital moments would not alter. We thus refrain from elaborating further into this direction.

4.2.6 Summary and outlook

We have investigated the spin and orbital magnetic moments of small iron (Fe_n^+, $7 \leq n \leq 18$), cobalt (Co_n^+, $8 \leq n \leq 17$, 19, 22) and nickel (Ni_n^+, $7 \leq n \leq 17$) clusters. In all cases investigated the spin magnetic moments, the orbital magnetic moments, and the total magnetic moments are enhanced with respect to the corresponding values of the bulk material, and quenched with respect to the atomic values.

The current spin magnetic moments by XMCD of Fe_n^+ are lower by 10% than those of a recent, independent XMCD experiment[25]. The current spin magnetic moments by XMCD of Co_n^+ are lower by 10% than previous XMCD values[26]. The current spin magnetic moments by XMCD of Ni_n^+ are larger by 10 to 20% than previous XMCD values[25]. In all three cases deviations are within combined uncertainties or slightly beyond. The orbital magnetic moments of Fe_n^+, Co_n^+ and Ni_n^+ are smaller by a factor of 2.5 to 20 than the spin magnetic moments, current and previous XMCD data well agreeing. The current investigation thus provides for an independent verification of the spin and orbital contributions of magnetic moments in cationic iron, cobalt and nickel clusters by the XMCD technique, and it extends the size ranges of studied cobalt and nickel clusters with respect to the previous studies.

The total magnetic moments of Fe_n^+ and Co_n^+ clusters by XMCD range above and below those of Fe_n and Co_n clusters by various Stern-Gerlach studies. The total magnetic moments of Ni_n^+ clusters by XMCD range above those of Ni_n clusters by three Stern-Gerlach studies. In all three cases the XMCD values of spin magnetic moments come closer to the recorded total magnetic moments by Stern-Gerlach. Reduced moments at n=13 in iron coincide in XMCD and SG studies. The reduced total magnetic moment of Ni_{14}^+ by XMCD stays in contrast to a reduced magnetic moment in Ni_{13}^+ by SG. A balancing of unpaired d - electrons versus vacancies suggests that cluster charge (cationic or neutral) matters in small nickel clusters while it is of less influence in large iron clusters.

Contemporary DFT calculations conclude on spin magnetic moments of Fe_n^+ ($7 \leq n \leq 20$) in line with the present XMCD values but low with respect to previous XMCD data. Computations of Co_n^+ ($n \leq 30$) and of Ni_n^+ ($n \leq 30$) seem to underestimate the spin magnetic moments by XMCD of the present study and of the previous studies. It is possible that conceptual problems prevail in approximate exchange-correlation functionals. There are few predictions of orbital magnetic moments through pertubative spin orbit coupling calculations which yield reasonable values in cases of small iron and nickel clusters. It is emphasized that broken symmetry DFT calculations are desperately needed in order to verify possible or even likely antiferromagnetic couplings. Furthermore, our present findings call for verification through future ab initio calculations that take spin orbit coupling explicitly into account.

We devise scaling laws that interpret the recorded spin and orbital magnetic moments in terms of surface effects which leads to $n^{-1/3}$ size dependencies in both cases. The spin magnetic moments interpolate between atomic and bulk values. The orbital magnetic moments interpolate between dimer and bulk values, with the atomic value exempt. We find a rationalization by recalling the very nature of "primary" atomic orbital moments and "secondary" spin-orbit-coupling induced orbital moments in clusters, the former being quenched in aggregates through loss of symmetry and concomitant loss of orbital degeneracies.

The presented results and compilation of the actual state of research in spin and orbital contributions to total magnetic moments in isolated clusters of ferromagnetic 3d elements provides a solid base to face standing challenges: The appropriate computational treatment of induced orbital magnetic moments; the elucidation by future experiments of the interplay of spin state in clusters and adsorbates on clusters; the unravelling of electronic and magnetic couplings of bulk surfaces to deposited clusters; the intrinsic magnetism in non-stoichiometric sub-oxides in clusters of ferromagnetic metals; the spin and orbital contributions of magnetic moments in alloy clusters; the systematic investigation of magnetic anisotropy and its influence on sum rule analysis; and many more questions to address in the future.

4. Spin and orbital magnetic moments of pure and doped transition metal clusters

Acknowledgements

Appendix 1: On gyromagnetic ratios

The magneto mechanical ratio g' can be deduced from gyromagnetic experiments by the Einstein-de Haas effect[92] (rotation induced by change of the magnetization). g' differs from the g factor determined by Ferromagnetic resonance (FMR) experiments. The definition of g' includes J_{tot} and thus a contribution of the orbital angular momentum J_{orbit} (L). The definition of g, on the other hand, only includes the spin angular momentum J_{spin} (= S)[93, 94]. The value of the free electron, i.e. the spin only value, is equal to two for g and g' (neglecting QED corrections). However, the deviation due to the orbital angular momentum results in g > 2 and g' < 2.

$$g' = \frac{2m_e}{e} \frac{M}{J_{tot}} = \frac{2m_e}{e} \frac{M}{J_{spin} + J_{orbit}}$$

$$g = \frac{2m_e}{e} \frac{M}{J_{spin}}$$

$$\frac{g'}{g} = \frac{J_{spin}}{J_{spin} + J_{orbit}} = \frac{S}{S + L}$$

Appendix 2: From a Taylor Expansion to Scaling Laws

Any steady differentiable function $f(x)$ may be defined through a Taylor expansion around a given point x_0:

$$f(x) = f(x_0) + \sum_{n=1}^{\infty} \frac{1}{n!} \left(\frac{df(x)}{dx^n} \Big|_{x=x_0} \right) (x - x_0)^n \qquad (A1)$$

Regarding a cluster size dependent entity $m(n)$ as a smoothly varying function of a continuous variable n, one may conceive an according expansion of $m(n)$ by orders of j and around a cluster size n_0:

$$m(n) = m(n_0) + \sum_{j=1}^{\infty} \frac{1}{j!} \left(\frac{dm(n)}{dn^j} \Big|_{n=n_0} \right) (n - n_0)^j \qquad (A2)$$

Physical effects often cause cluster size dependencies to run by some power y of n, $m(n) \sim const. + n^y$ (cf. Table 2). Such simple cases justify a truncation of the Taylor expansion at $j_{max} = y$ if $y > 0$.

In cases of inverse power dependencies, $y < 0$, however, an according Taylor expansion would require exceedingly many terms in order to achieve an accurate description of $m(n)$. It becomes advantageous to invoke a more appropriate transformation of the independent variable than the prior mapping $x \leftrightarrow n$. Instead, it is conceivable to apply $x \leftrightarrow n^y = \frac{1}{n^{|y|}}$. This yields:

$$m(n) = m(n_0) + \sum_{j=1}^{\infty} \frac{1}{j!} \left(\frac{dm(n)}{d(n^y)^j} \Big|_{n=n_0} \right) (n^y - n_0{}^y)^j \qquad (A3)$$

4. Spin and orbital magnetic moments of pure and doped transition metal clusters

Approximation to first order, $j_{max} = 1$, leads towards formulation of known scaling laws while choice of $n_0 = \infty$ helps to simplify:

$$m(n) = m(\infty) + \left(\frac{dm(n)}{d(n^y)}\bigg|_{n=\infty}\right)n^y = m(\infty) + c_\infty n^y \qquad (A4)$$

The significance of $m(\infty) = m_{bulk}$ is obvious. The slope coefficient c_∞ takes interpretation. As of now it is defined as a local entity at $n = \infty$. In case of the above first order approximation by a single power term n^y it is constant and does not vary by n. This allows to interpret:

$$c_\infty = \frac{dm(n)}{d(n^y)}\bigg|_{n=\infty} = \frac{\Delta m(n)}{\Delta(n^y)} = -\big(m(\infty) - m(1)\big) \qquad (A5)$$

Note, that the denominator $\Delta(n^y)$ has conveniently reduced with $y < 0$ and choice of interval $\Delta n = [\infty, 1]$ to $\Delta(n^y) = -1$. The resulting scaling law then reads (with $m(1) = m_{atom}$):

$$m(n) = m_{bulk} - \frac{m_{bulk} - m_{atom}}{n^{|y|}} \qquad (A6)$$

Alternate choices of interval Δn for evaluation of slope coefficient c_{n_0} leads to according, but slightly more complicated formulas. E.g. a choice of $\Delta n = [\infty, 2]$ would yield:

$$m(n) = m_{bulk} - 2^{|y|}\frac{m_{bulk} - m(2)}{n^{|y|}} \qquad (A6)$$

(Include here the prior cluster surface to volume arguments). With $y = -1/3$ the scaling law of spin contributions to cluster magnetic moments ($\Delta n = [\infty, 1]$) becomes:

$$m_S(n) = m_{S,bulk} - \frac{m_{S,bulk} - m_{S,atom}}{\sqrt[3]{n}} \qquad (A7)$$

Accordingly, the scaling law for orbital contributions to cluster magnetic moments within the reduced size interval ($\Delta n = [\infty, 2]$) becomes:

$$m_L(n) = m_{L,bulk} - \frac{m_{L,bulk} - m_{L,dimer}}{\sqrt[3]{n/2}} \qquad (A8)$$

Both laws may be combined to a joint law for total magnetic moments:

$$m_{tot}(n) = m_S(n) + m_L(n)$$
$$= m_{tot,bulk} - \frac{\big(m_{S,bulk} - m_{S,atom}\big) + \sqrt[3]{2}\big(m_{L,bulk} - m_{L,dimer}\big)}{\sqrt[3]{n}} \qquad (A7)$$

4.2.7 References

[1]   Y.-W. Jun, J.-W. Seo, and A. Cheon, Acc. Chem. Res. **41**, 179 (2008).
[2]   H. Haberland, *Clusters of Atoms and Molecules* (Springer, 1994).
[3]   K. H. Meiwes-Broer, *Metal clusters at surfaces* (Springer, 2000).
[4]   L. Glaser, K. Chen, S. Fiedler, M. Wellhöfer, W. Wurth, and M. Martins, Phys. Rev. B **86**, 075435(2012).
[5]   W. Wurth, and M. Martins, Chem. Phys. Solid Surf. **12**, 471 (2007).
[6]   E. Antonsson, H. Bresch, R. Lewinski, B. Wassermann, T. Leisner, C. Graf, B. Langer, and E. Rühl, Chem. Phys. Lett. **559**, 1 (2013).
[7]   I. M. L. Billas, A. Châtelain, and W. A. de Heer, Science **265**, 1682 (1994).
[8]   Y. Z. Wu, B. Sinkovic, C. Won, J. Zhu, Y. Zhao, and Z. Q. Qiu, Phys. Rev. B **85**, 134436 (2012).
[9]   M. B. Knickelbein, J. Chem. Phys. **116**, 9703 (2002).
[10]   M. B. Knickelbein, J. Chem. Phys. **115**, 1983 (2001).
[11]   S. E. Apsel, J. W. Emmert, J. Deng, and L. A. Bloomfield, Phys. Rev. Lett. **76**, 1441 (1996).
[12]   J. A. Alonso, Chem. Rev. **100**, 637 (2000).
[13]   J. Stöhr, J. Electron. Spectrosc. Relat. Phenom. **75**, 253 (1995).
[14]   C. T. Chen, Y. U. Idzerda, H. J. Lin, N. V. Smith, G. Meigs, E. Chaban, G. H. Ho, E. Pellegrin, and F. Sette, Phys. Rev. Lett. **75**, 152 (1995).
[15]   G. Schütz, W. Wagner, W. Wilhelm, P. Kienle, R. Zeller, R. Frahm, and G. Materlik, Phys. Rev. Lett. **58**, 737 (1987).
[16]   P. Gambardella, S. Rusponi, M. Veronese, S. S. Dhesi, C. Grazioli, A. Dallmeyer, I. Cabria, R. Zeller, P. H. Dederichs, K. Kern, C. Carbone, and H. Brune, Science **300**, 1130 (2003).
[17]   S. S. Dhesi, H. A. Dürr, G. van der Laan, E. Dudzik, and N. B. Brookes, Phys. Rev. B **60**, 12852 (1999).
[18]   P. Gambardella, A. Dallmeyer, K. Maiti, M. C. Malagoli, W. Eberhardt, K. Kern, and C. Carbone, Nature **416**, 301 (2002).
[19]   J. Bansmann, A. Kleibert, M. Getzlaff, A. F. Rodriguez, F. Nolting, C. Boeglin, and K.-H. Meiwes-Broer, Physica Status Solidi B-Basic Solid State Physics **247**, 1152 (2010).
[20]   J. T. Lau, A. Föhlisch, R. Nietubyc̀, M. Reif, and W. Wurth, Phys. Rev. Lett. **89**, 057201 (2002).
[21]   K. Chen, S. Fiedler, I. Baev, T. Beeck, W. Wurth, and M. Martins, New J. Phys. **14**, 123005 (2012).
[22]   H. Brune, and P. Gambardella, Surf. Sci. **603**, 1812 (2009).
[23]   T. Eelbo, M. Waśniowska, P. Thakur, M. Gyamfi, B. Sachs, T. O. Wehling, S. Forti, U. Starke, C. Tieg, A. I. Lichtenstein, and R. Wiesendanger, Phys. Rev. Lett. **110**, 136804 (2013).
[24]   S. Peredkov, M. Neeb, W. Eberhardt, J. Meyer, M. Tombers, H. Kampschulte, and G. Niedner-Schatteburg, Phys. Rev. Lett. **107**, 233401 (2011).
[25]   M. Niemeyer, K. Hirsch, V. Zamudio-Bayer, A. Langenberg, M. Vogel, M. Kossick, C. Ebrecht, K. Egashira, A. Terasaki, T. Möller, B. v. Issendorff, and J. T. Lau, Phys. Rev. Lett. **108**, 057201 (2012).
[26]   A. Langenberg, K. Hirsch, A. Lawicki, V. Zamudio-Bayer, M. Niemeyer, P. Chmiela, B. Langbehn,
        A. Terasaki, B. V. Issendorff, and J. T. Lau, Phys. Rev. B **90**, 184420, (2014).
[27]   S. Peredkov, A. Savci, S. Peters, M. Neeb, W. Eberhardt, H. Kampschulte, J. Meyer, M. Tombers, B. Hofferberth, F. Menges, and G. Niedner-Schatteburg, J. Electron. Spectrosc. Relat. Phenom. **184**, 113 (2011).
[28]   C. Berg, T. Schindler, G. Niedner-Schatteburg, and V. E. Bondybey, J. Chem. Phys. **102**, 4870 (1995).
[29]   S. Maruyama, L. R. Anderson, and R. E. Smalley, Rev. Sci. Instrum. **61**, 3686 (1990).
[30]   D. Proch, and T. Trickl, Rev. Sci. Instrum. **60**, 713 (1989).
[31]   P. Carra, B. T. Thole, M. Altarelli, and X. Wang, Phys. Rev. Lett. **70**, 694 (1993).
[32]   B. T. Thole, P. Carra, F. Sette, and G. Vanderlaan, Phys. Rev. Lett. **68**, 1943 (1992).
[33]   P. G. Alvarado-Leyva, F. Aguilera-Granja, L. C. Balbas, and A. Vega, PCCP **15**, 14458 (2013).

4. Spin and orbital magnetic moments of pure and doped transition metal clusters

[34]   O. Sipr, and H. Ebert, Phys. Rev. B **72**, 134406 (2005).

[35]   R. Wu, and A. J. Freeman, Phys. Rev. Lett. **73**, 1994 (1994).

[36]   P. Srivastava, F. Wilhelm, A. Ney, M. Farle, H. Wende, N. Haack, G. Ceballos, and K. Baberschke,
Phys. Rev. B **58**, 5701 (1998).

[37]   P. Srivastava, N. Haack, H. Wende, R. Chauvistré, and K. Baberschke, Phys. Rev. B **56**, R4398 (1997).

[38]   N. W. Ashcroft, and N. D. Mermin, *Festkörperphysik* (Oldenbourg Verlag München, 2013), 4th edn.

[39]   J. Stöhr, Siegmann, H. C., *Magnetism - From Fundamentals to Nanoscale Dynamics* (Springer, 2006), Springer Series in Solid-State Sciences, 152.

[40]   W. C. Elmore, Phys. Rev. **54**, 1092 (1938).

[41]   S. N. Khanna, and S. Linderoth, Phys. Rev. Lett. **67**, 742 (1991).

[42]   H. Brune, and P. Gambardella, (CRC Press, 2014), pp. 447.

[43]   O. Sipr, J. Minar, and H. Ebert, Europhys. Lett. **87**, 67007 (2009).

[44]   J. Stöhr, and H. König, Phys. Rev. Lett. **75**, 3748 (1995).

[45]   C. G. Stefanita, *Magnetism: Basics and Applications* (Springer, 2012).

[46]   J. P. Bucher, D. C. Douglass, and L. A. Bloomfield, Phys. Rev. Lett. **66**, 3052 (1991).

[47]   B. V. Reddy, S. K. Nayak, S. N. Khanna, B. K. Rao, and P. Jena, J. Phys. Chem. A **102**, 1748 (1998).

[48]   G. van der Laan, Journal of Synchrotron Radiation **6**, 694 (1999).

[49]   C. T. Chen, N. V. Smith, and F. Sette, Phys. Rev. B **43**, 6785 (1991).

[50]   J. Vogel, and M. Sacchi, Phys. Rev. B **49**, 3230 (1994).

[51]   X. Xu, S. Yin, R. Moro, A. Liang, J. Bowlan, and W. A. de Heer, Phys. Rev. Lett. **107**, 057203 (2011).

[52]   F. W. Payne, W. Jiang, J. W. Emmert, J. Deng, and L. A. Bloomfield, Phys. Rev. B **75**, 094431 (2007).

[53]   M. B. Knickelbein, J. Chem. Phys. **125**, 044308 (2006).

[54]   X. S. Xu, S. Y. Yin, R. Moro, and W. A. de Heer, Phys. Rev. Lett. **95**, 237209 (2005).

[55]   M. B. Knickelbein, Chem. Phys. Lett. **353**, 221 (2002).

[56]   P. J. Jensen, and K. H. Bennemann, Zeitschrift Fur Physik D-Atoms Molecules and Clusters **35**, 273 (1995).

[57]   R. A. Guirado-Lopez, J. Dorantes-Davila, and G. M. Pastor, Phys. Rev. Lett. **90**, (2003).

[58]   G. L. Gutsev, C. A. Weatherford, P. Jena, E. Johnson, and B. R. Ramachandran, J. Phys. Chem. A **116**, 10218 (2012).

[59]   A. N. Andriotis, and M. Menon, Phys. Rev. B **57**, 10069 (1998).

[60]   C. Köhler, G. Seifert, and T. Frauenheim, Chem. Phys. **309**, 23 (2005).

[61]   O. Diéguez, M. Alemany, C. Rey, P. Ordejón, and L. Gallego, Phys. Rev. B **63**, 205407 (2001).

[62]   P. Bobadova-Parvanova, K. Jackson, S. Srinivas, M. Horoi, C. Köhler, and G. Seifert, J. Chem. Phys. **116**, 3576 (2002).

[63]   K. Takahashi, S. Isobe, and S. Ohnuki, Appl. Phys. Lett. **102**, 113108 (2013).

[64]   J. Guevara, F. Parisi, A. M. Llois, and M. Weissmann, Phys. Rev. B **55**, 13283 (1997).

[65]   D. Roy, R. Robles, and S. Khanna, J. Chem. Phys. **132**, 194305 (2010).

[66]   H. K. Yuan, H. Chen, A. L. Kuang, C. L. Tian, and J. Z. Wang, J. Chem. Phys. **139**, 034314 (2013).

[67]   G. Guzmán-Ramírez, P. Salvador, J. Robles, A. Vega, and F. Aguilera-Granja, Theor. Chem. Acc. **132**, 1 (2012).

[68]   G. L. Gutsev, C. W. Weatherford, K. G. Belay, B. R. Ramachandran, and P. Jena, J. Chem. Phys. **138**, 164303 (2013).

[69]   M. Pérez, F. Muñoz, J. Mejía-López, and G. Martínez, J. Nanopart. Res. **14**, 1 (2012).

[70]   S. Datta, M. Kabir, S. Ganguly, B. Sanyal, T. Saha-Dasgupta, and A. Mookerjee, Phys. Rev. B **76**, 014429 (2007).

[71]   J. Rodríguez-López, F. Aguilera-Granja, K. Michaelian, and A. Vega, Phys. Rev. B **67**, 174413 (2003).

[72]   Q.-M. Ma, Z. Xie, J. Wang, Y. Liu, and Y.-C. Li, Phys. Lett. A **358**, 289 (2006).

[73]   C. Dong, and X. Gong, Phys. Rev. B **78**, 020409 (2008).

[74]   F. Aguilera-Granja, A. Vega, and L. C. Balbás, Chem. Phys. **415**, 106 (2013).

[75]   J. H. Mokkath, J. Magn. Magn. Mater. **349**, 109 (2014).

[76]   G. Martínez, E. Tangarife, M. Pérez, and J. Mejía-López, J. Phys.: Condens. Matter **25**, 216003 (2013).

[77]   W. Song, W.-C. Lu, C. Z. Wang, and K. M. Ho, Computational and Theoretical Chemistry **978**, 41 (2011).

[78]   F. Aguilera-Granja, S. Bouarab, M. López, A. Vega, J. Montejano-Carrizales, M. Iniguez, and J. Alonso, Phys. Rev. B **57**, 12469 (1998).

[79]   F. Reuse, and S. Khanna, Chem. Phys. Lett. **234**, 77 (1995).

[80]   Q. Lu, Q. Luo, L. Chen, and J. Wan, Europ. Phys. J. D **61**, 389 (2011).

[81]   M. Wu, A. K. Kandalam, G. L. Gutsev, and P. Jena, Phys. Rev. B **86**, 174410 (2012).

[82]   E. M. Kessler, S. Schmitt, and C. van Wüllen, J. Chem. Phys. **139**, 184110 (2013).

[83]   C. van Wüllen, J. Phys. Chem. A **113**, 11535 (2009).

[84]   C. A. F. Vaz, J. A. C. Bland, and G. Lauhoff, Rep. Prog. Phys. **71**, 056501 (2008).

[85]   I. Rips, and J. Jortner, J. Chem. Phys. **97**, 536 (1992).

[86]   H. Haberland, K. Kleinermanns, and F. Träger, in *Lehrbuch der Experimentalphysik Band 5 – Gase, Nanosysteme, Flüssigkeiten* (Walter de Gruyter, 2006), p. 819.

[87]   P. Atkins, and J. de Paula, *Elements of Physical Chemistry* (W. H. Freeman and Company, Oxford, 2005), 4th edn., p. 9.

[88]   It might seem confusing at first sight to define continuously varying cluster entities (diameter, volume) by relating them to a discrete number of building blocks (atoms). This is straight forward and valid to a very good approximation as long as dense packing dominates. Sometimes, such approximation is labeled as a "liquid drop model".

[89]   S. Blügel, in *Lecture Notes Magnetism goes Nano: Elctron Correlations, Spin Transport, Molecular Magnetism* (Forschungszentrum Jülich in der Helmholtz-Gemeinschaft, 2005).

[90]   J. Stöhr, J. Magn. Magn. Mater. **200**, 470 (1999).

[91]   M. Tischer, O. Hjortstam, D. Arvanitis, J. Hunter Dunn, F. May, K. Baberschke, J. Trygg, J. M. Wills, B. Johansson, and O. Eriksson, Phys. Rev. Lett. **75**, 1602 (1995).

[92]   A. Einsten, and W. J. de Haas, Verhandlungen Deutsch Physikalische Gesellschaft **17**, 152 (1915).

[93]   C. Kittel, Phys. Rev. **76**, 743 (1949).

[94]   T. M. Wallis, J. Moreland, and P. Kabos, Appl. Phys. Lett. **89**, 122502 (2006).

[95]   G. G. Scott, and H. W. Sturner, Phys. Rev. **184**, 490 (1969).

[96]   G. G. Scott, Phys. Rev. **148**, 525 (1966).

[97]   G. G. Scott, and R. A. Reck, Phys. Rev. B **8**, 233 (1973).

[98]   G. Nave, Johansson, S., Learner, R. C. M., Thorne, A. P. Brault, J. W., Astrophys. J. Supplement Series **94**, 221 (1994).

[99]   NIST ASD Team, in *National Institute of Standards and Technology, Gaithersburg, MD*2013).

[100]   G. Nave, Johansson, S., Astrophysical Journal Supplement Series **204**, 1 (2013).

[101]   J. Sugar, Corliss, C, Journal of Physical and Chemistry Reference Data **14**, 1 (1985).

[102]   J. C. Pickering, Raassen, A. J. J., Uylings, P. H. M., Johansson, S. , Astrophys. J. Supplement Series **117**, 216 (1998).

[103]   L. Ulf, W. B. James, and P. T. Anne, Phys. Scr. **47**, 628 (1993).

[104]   A. Kohn, F. Weigend, and R. Ahlrichs, PCCP **3**, 711 (2001).

[105]   T. Bachels, and R. Schäfer, Chem. Phys. Lett. **324**, 365 (2000).

[106]   F. Baletto, and R. Ferrando, Reviews of Modern Physics **77**, 371 (2005).

[107]   G. Wrigge, M. A. Hoffmann, and B. v. Issendorff, Phys. Rev. A **65**, 063201 (2002).

[108]   M. B. Knickelbein, and S. Yang, J. Chem. Phys. **93**, 5760 (1990).

[109]   G. Wrigge, M. Astruc Hoffmann, B. Issendorff, and H. Haberland, Europ. Phys. J. D **24**, 23 (2003).

[110]   W. A. de Heer, Reviews of Modern Physics **65**, 611 (1993).

[111]   M. M. Alvarez, J. T. Khoury, T. G. Schaaff, M. N. Shafigullin, I. Vezmar, and R. L. Whetten, J. Phys. Chem. B **101**, 3706 (1997).

[112]   W. A. de Heer, in *Metal clusters at surfaces*, edited by K.-H. Meiwes-Broer (Springer, 2000).

[113]   C. Brechignac, M. Broyer, P. Cahuzac, G. Delacretaz, P. Labastie, and L. Wöste, Chem. Phys. Lett. **120**, 559 (1985).

[114]   C. Bréchignac, M. Broyer, P. Cahuzac, G. Delacretaz, P. Labastie, J. P. Wolf, and L. Wöste, Phys. Rev. Lett. **60**, 275 (1988).

[115]   G. M. Pastor, and K. H. Bennemann, in *Clusters of Atoms and Molecules*, edited by H. Haberland (Springer, 1994).

[116]   M. R. Harrison, and P. P. Edwards, in *The metallic and non-metallic states of matter*, edited by P. P. Edwards, and C. N. R. Rao (Francis & Taylor London, 1985).

[117]   M. Getzlaff, *Fundamentals of Magnetism* (Springer, 2008).

4.2.8 Supplementary material to "The spin and orbit contributions to the total magnetic moments of free Fe, Co and Ni clusters"

Content

Table S3a Comparison of experimental and theoretical spin magnetic moments in μ_B/atom

Table S3b Comparison of experimental orbital magnetic moments in μ_B/atom

Figure S1 Spin and orbital magnetic moments of size selected clusters in comparison to conceivable trends that would interpolate between bulk metals and cationic atoms

Figure S2 Comparison of spin and orbital magnetic moments for Fe_n^+, Co_n^+ and Ni_n^+ clusters from this study and data obtained by Lau *et al.*

Figure S3 Theoretical data on the spin magnetic moments of Fe clusters.

Figure S4 Theoretical data on the spin magnetic moments of Co clusters.

Figure S5 Theoretical data on the spin magnetic moments of Ni clusters.

4. Spin and orbital magnetic moments of pure and doped transition metal clusters

Table S3a Comparison of experimental and theoretical spin magnetic moments in μ_B/atom

	Exp[a]	Theo[b]	Exp[c]		Exp[a]	Exp[d]		Exp[a]	Exp[d]
Fe_7^+	3.0±0.45	3.29	3.1±0.45				Ni_7^+	1.2±0.20	
Fe_8^+	3.1±0.50	3.13	3.2±0.45	Co_8^+	2.7±0.30		Ni_8^+	1.3±0.20	
Fe_9^+	3.5±0.50	3.00	2.8±0.40	Co_9^+	2.0±0.25		Ni_9^+	1.7±0.25	
Fe_{10}^+	2.9±0.40	2.90	3.4±0.45	Co_{10}^+	2.2±0.25	2.48±0.09	Ni_{10}^+	1.6±0.20	1.2±0.08
Fe_{11}^+	2.7±0.40	2.82	3.3±0.40	Co_{11}^+	2.0±0.20	2.37±0.14	Ni_{11}^+	1.5±0.20	1.3±0.15
Fe_{12}^+	2.7±0.40	3.08	3.4±0.50	Co_{12}^+	2.4±0.20	2.61±0.19	Ni_{12}^+	1.2±0.20	1.05±0.23
Fe_{13}^+	2.1±0.30	2.69	2.45±0.40	Co_{13}^+	2.0±0.20	2.41±0.14	Ni_{13}^+	1.3±0.20	1.18±0.14
Fe_{14}^+	2.8±0.40	3.07	3.50±0.50	Co_{14}^+	2.2±0.20	2.52±0.19	Ni_{14}^+	1.0±0.15	1.03±0.15
Fe_{15}^+	2.7±0.40	3.13	3.7±0.50	Co_{15}^+	2.5±0.20	2.47±0.19	Ni_{15}^+	1.6±0.25	1.25±0.15
Fe_{16}^+	2.3±0.35	3.19	3.7±0.50	Co_{16}^+	2.5±0.20		Ni_{16}^+	1.5±0.20	
				Co_{17}^+	2.3±0.20		Ni_{17}^+	1.7±0.25	
Fe_{18}^+	3.2±0.50	3.17	3.5±0.50						
				Co_{19}^+	2.5±0.30				
				Co_{22}^+	2.0±0.30				

[a] this work; [b] see Ref. [58]; [c] see Ref. [25] [d] see Ref. [26]

Table S3b Comparison of experimental orbital magnetic moments in μ_B/atom

	Exp[a]	Exp[b]		Exp[a]	Exp[d]		Exp[a]	Exp[d]
Fe_7^+	0.16±0.02	0.30±0.35				Ni_7^+	0.43±0.06	
Fe_8^+	0.26±0.04	0.28±0.35	Co_8^+	0.71±0.10		Ni_8^+	0.42±0.06	
Fe_9^+	0.25±0.04	0.60±0.35	Co_9^+	0.63±0.09		Ni_9^+	0.33±0.05	
Fe_{10}^+	0.15±0.02	0.21±0.35	Co_{10}^+	0.59±0.08	0.59±0.03	Ni_{10}^+	0.31±0.05	0.39±0.04
Fe_{11}^+	0.18±0.03	0.29±0.35	Co_{11}^+	0.55±0.08	0.68±0.05	Ni_{11}^+	0.29±0.04	0.30±0.06
Fe_{12}^+	0.34±0.05	0.09±0.35	Co_{12}^+	0.53±0.05	0.67±0.05	Ni_{12}^+	0.43±0.06	0.41±0.08
Fe_{13}^+	0.32±0.05	0.20±0.25	Co_{13}^+	0.41±0.06	0.62±0.03	Ni_{13}^+	0.29±0.04	0.28±0.06
Fe_{14}^+	0.45±0.07	0.14±0.35	Co_{14}^+	0.67±0.07	0.54±0.04	Ni_{14}^+	0.23±0.04	0.29±0.04
Fe_{15}^+	0.16±0.02	0.19±0.40	Co_{15}^+	0.52±0.09	0.36±0.04	Ni_{15}^+	0.35±0.05	0.20±0.03
Fe_{16}^+	0.26±0.04	0.13±0.40	Co_{16}^+	0.40±0.04		Ni_{16}^+	0.25±0.04	
			Co_{17}^+	0.42±0.04		Ni_{17}^+	0.27±0.04	
Fe_{18}^+	0.12±0.02	0.13±0.35						
			Co_{19}^+	0.58±0.06				
			Co_{22}^+	0.56±0.08				

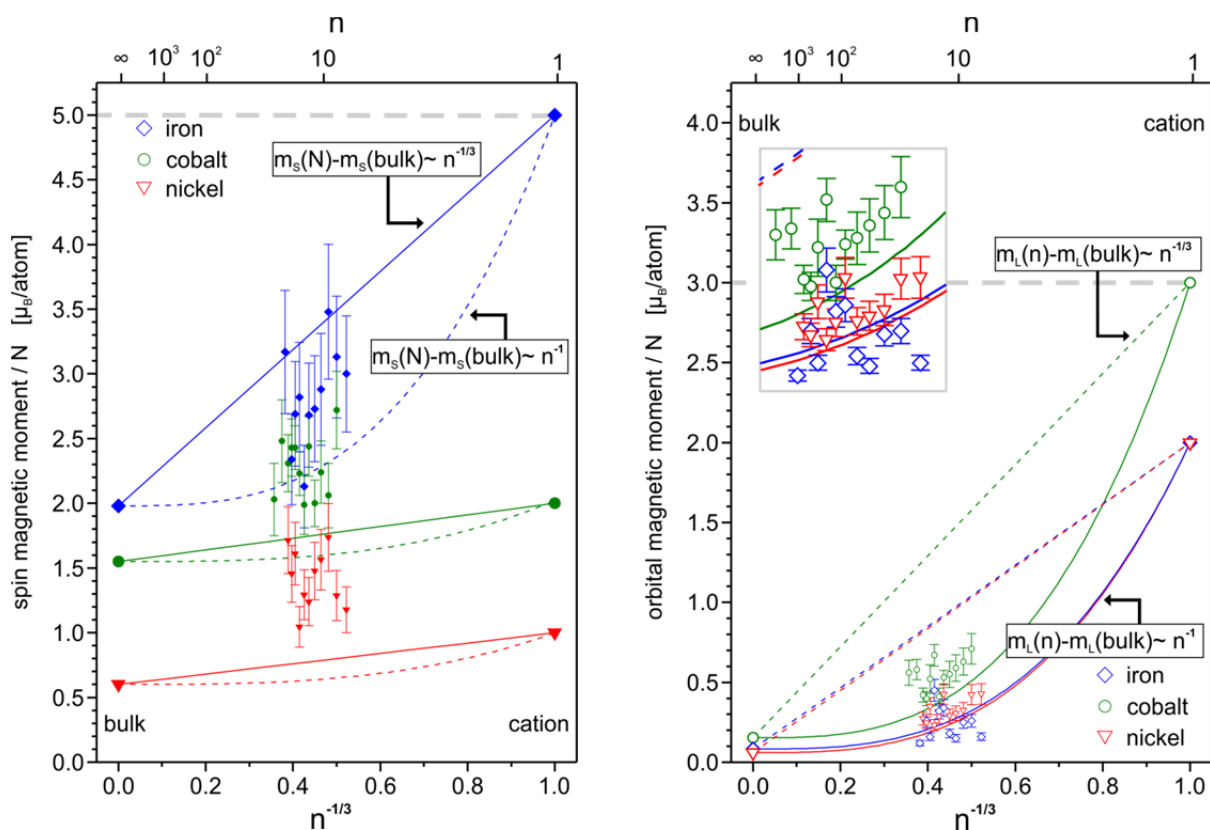[a] this work; [b] see Ref. [25]; [d] see Ref. [26]

Figure S1 Spin (left) and orbital (right) magnetic moments of size selected clusters in comparison to conceivable trends that would interpolate between bulk metals and cationic atoms. Note, that these trends do agree much less with the recorded XMCD data as the trends depicted in Figs. 4a and 4b, where neutral atoms serve as reference points instead.
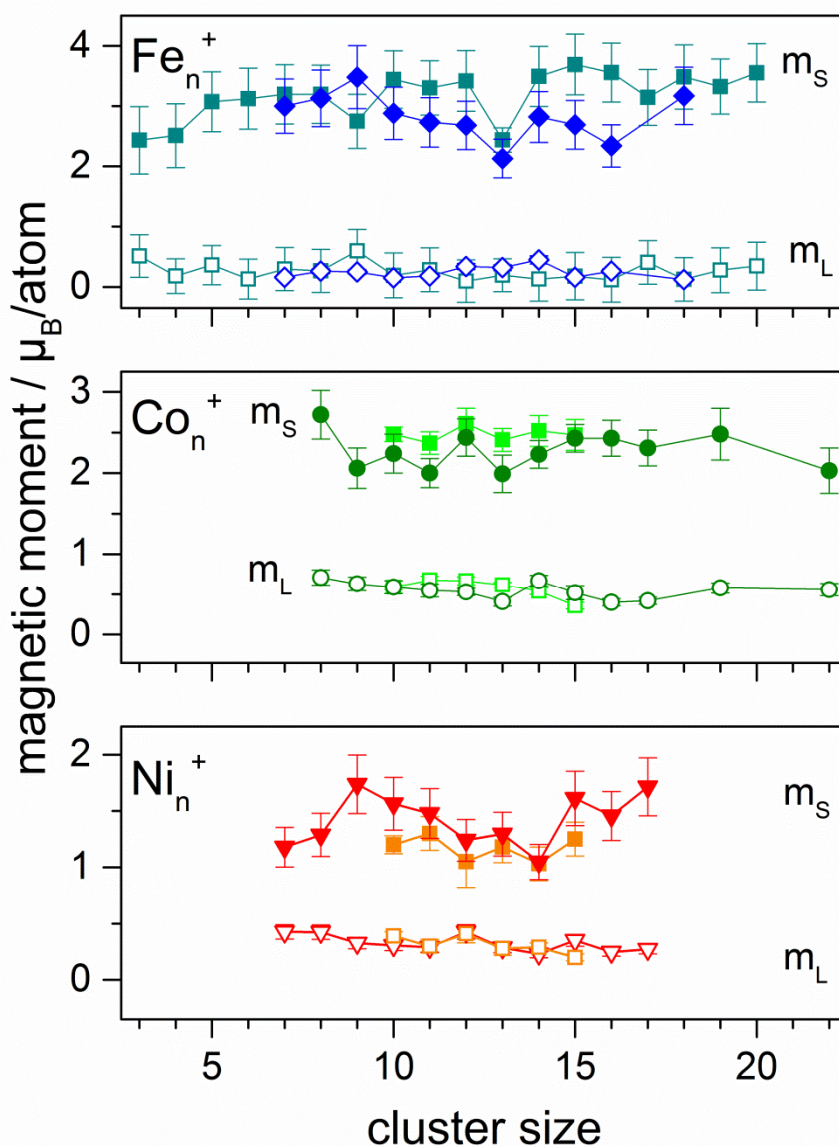
Figure S2 Comparison of spin and orbital magnetic moments for Fe_n^+ (top), Co_n^+ (middle) and Ni_n^+ (bottom) clusters from this study and data obtained by Lau *et al.*[25, 26] (squares in all three panels). The orbital magnetic moments are represented by open and the spin magnetic moments by filled symbols. The found magnetic moments agree well with each other within the error bars of both experiments. Our spin magnetic moments are systematically lower for iron and cobalt clusters and systematically larger for nickel clusters. Within combined uncertainties the results by the two experimental setups agree well with each other.
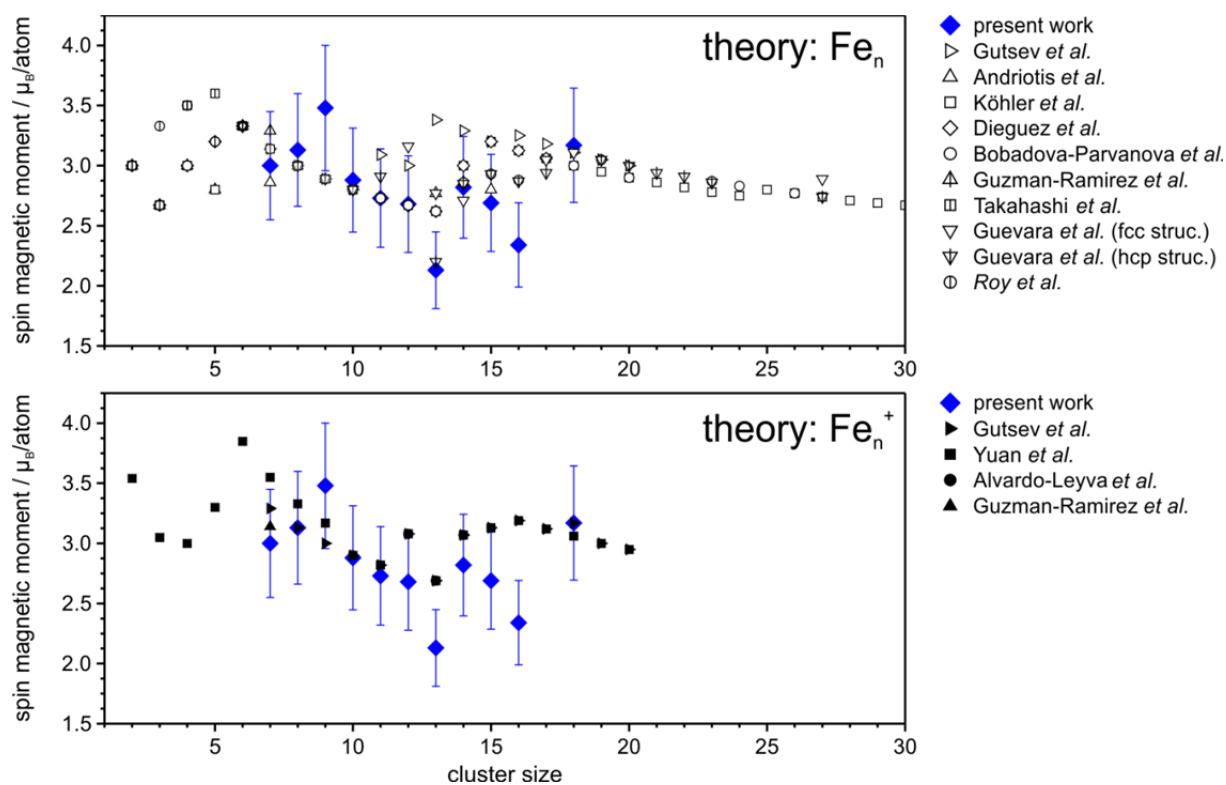
Figure S3 Theoretical data on the spin magnetic moments of Fe clusters.

For neutral Fe clusters: Gutsev et al. see [68]; Andriotis et al. see [59]; Köhler et al. see [60]; Dieguez et al. see [61]; Bobadova-Parvanova et al. see [62]; Guzman-Ramirez et al. see [67]; Takahashi et al. see [63]; Guevara et al. see [64]; Roy et al. see [65]; **For cationic iron clusters:** Gutsev et al. see [58]; Yuan et al. see [66]; Alvardo-Leyva et al. see [33]; Guzman-Ramirez et al. see [67];
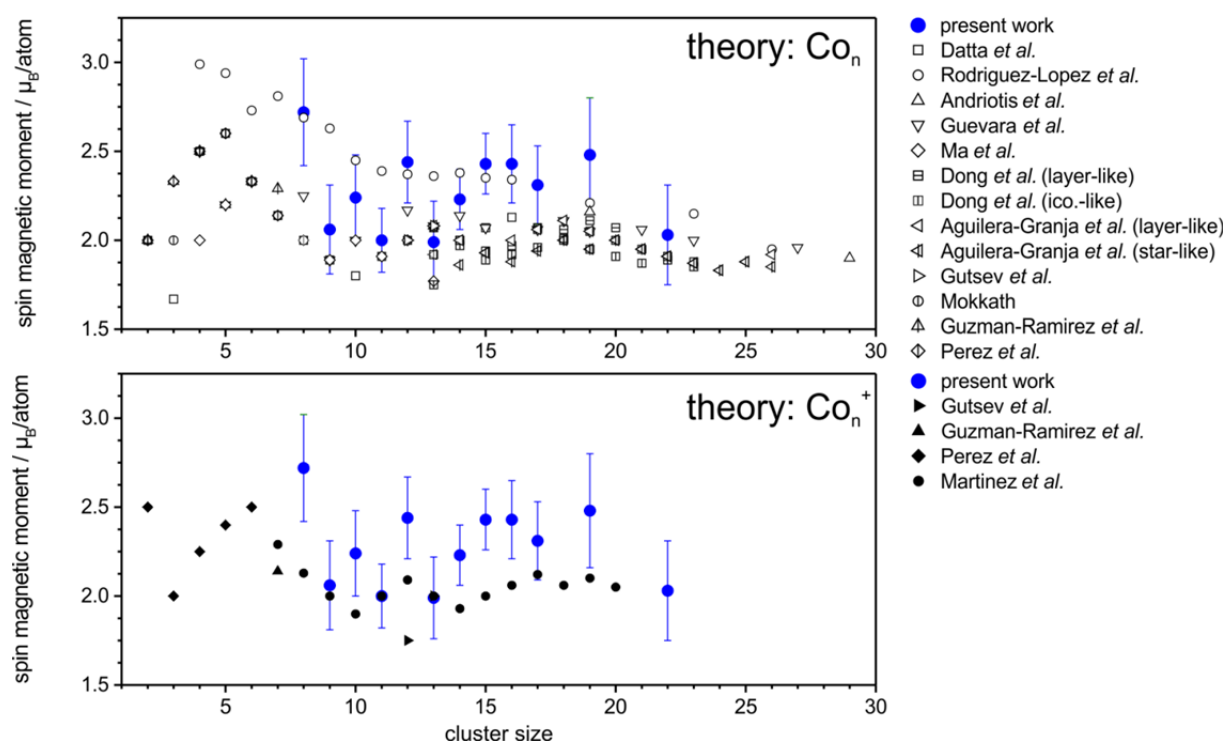
Figure S4 Theoretical data on the spin magnetic moments of Co clusters.
For neutral Co clusters: Datta et al. see [70]; Rodriquez-Lopez et al. see [71]; Andriotis et al. see [59]; Guevara et al. see [64]; Ma et al. see [72]; Dong et al. see [73]; Aguilera-Granja et al. see [74]; Gutsev et al. see [68]; Mokkath et al see [75]; Guzman-Ramirez et al. see [67]; Perez et al. see [69]; **For cationic Co clusters:** Gutsev et al. see [68]; Guzman-Ramirez et al. see [67]; Perez et al. see [69]; Martinez et al. see [76]
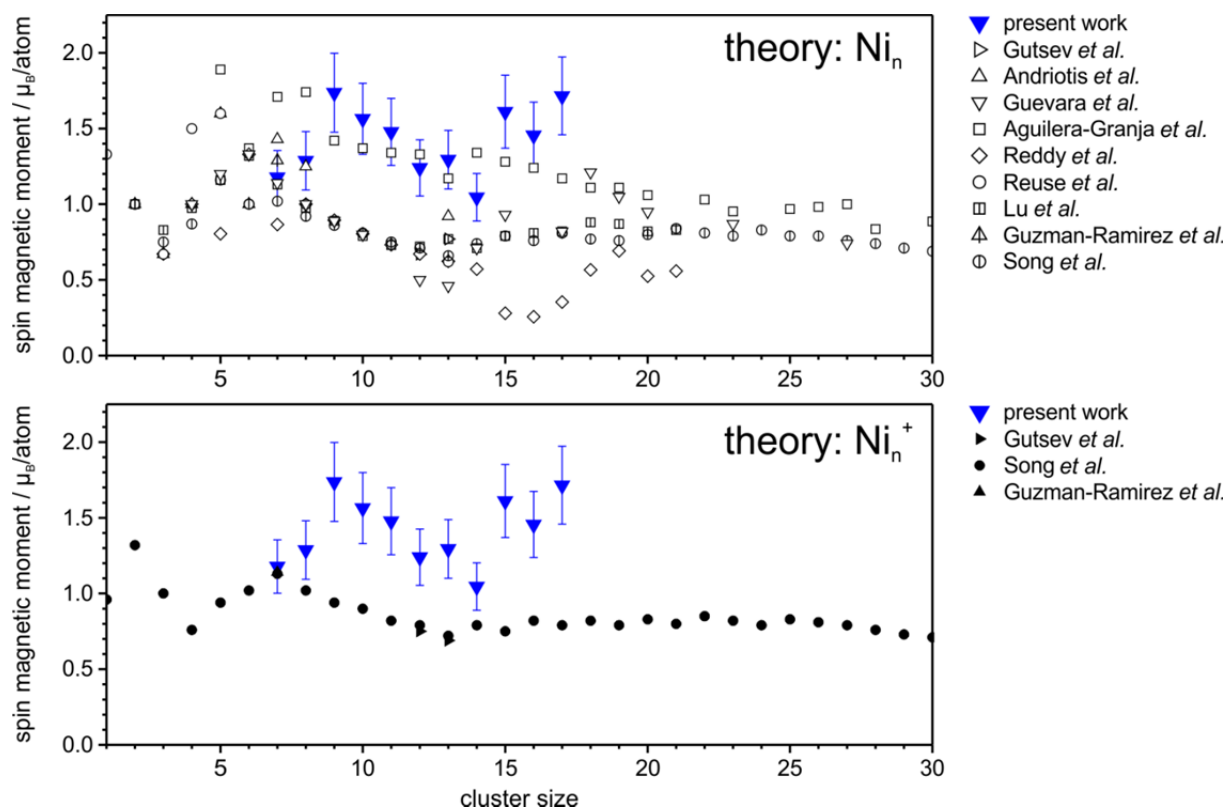
Figure S5 Theoretical data on the spin magnetic moments of Ni clusters.
For neutral Ni clusters: Gutsev et al. see [68]; Andriotis et al. see [59]; Guevara et al. see [64]; Aguilera-Granja et al. see [78]; Reddy et al. see [47]; Reuse et al. see [79]; Lu et al. see [80]; Guzman-Ramirez et al. see [67]; Song et al. see [77]; **For cationic Ni clusters:** Gutsev et al. see [68]; Song et al. see [77]; Guzman-Ramirez et al. see [67]

4.3 Publication: "Orbit and spin resolved magnetic properties of size selected [Co$_n$Rh]$^+$ and [Co$_n$Au]$^+$ nanoalloy clusters"

The presented draft named "Orbit and spin resolved magnetic properties of size selected [Co$_n$Rh]$^+$ and [Co$_n$Au]$^+$ nanoalloy clusters" was put together by D. Dieleman and the group of A. Kirilyuk at the University of Nijmegen, The Netherlands. It has been accepted for puplication at Physical Chemistry Chemical Physics (DOI: 10.1039/c5cp01923k). The presented results are also part of the doctoral thesis of D. Dieleman. The experiments were performed by the experimental team consisting of S. Peredkov, J. D. Meyer, J. Jalink, D. Dieleman and myself lead by M. Neeb at the Helmholtz Zentrum Berlin (BESSY II). W. Eberhard and G. Niedner-Schatteburg designed the used GAMBIT-Setup and were involved in the revision of the manuscript. The data evaluation was done by D. Dieleman and myself. The DFT computations were done in the group of A. Kirilyuk.

PCCP

PAPER

Orbit and spin resolved magnetic properties of size selected [Co$_n$Rh]$^+$ and [Co$_n$Au]$^+$ nanoalloy clusters

Dennis Dieleman,*[a] Matthias Tombers,[b] Lars Peters,[a] Jennifer Meyer,[b] Sergey Peredkov,[c] Jeroen Jalink,[a] Matthias Neeb,[d] Wolfgang Eberhardt,[e] Theo Rasing,[a] Gereon Niedner-Schatteburg[b] and Andrei Kirilyuk[a]

Bi-metallic nanoalloys of mixed 3d–4d or 3d–5d elements are promising candidates for technological applications. The large magnetic moment of the 3d materials in combination with a high spin–orbit coupling of the 4d or 5d materials give rise to a material with a large magnetic moment and a strong magnetic anisotropy, making them ideally suitable in for example magnetic storage devices. Especially for clusters, which already have a higher magnetic moment compared to the bulk, these alloys can profit from the cooperative role of alloying and size reduction in order to obtain magnetically stable materials with a large magnetic moment. Here, the influence of doping of small cobalt clusters on the spin and orbital magnetic moment has been studied for the cations [Co$_{8-14}$Au]$^+$ and [Co$_{10-14}$Rh]$^+$. Compared to the undoped pure cobalt [Co$_N$]$^+$ clusters we find a significant increase in the spin moment for specific Co$_{N-1}$Au$^+$ clusters and a very strong increase in the orbital moment for some Co$_{N-1}$Rh$^+$ clusters, with more than doubling for Co$_{12}$Rh$^+$. This result shows that substitutional doping of a 3d metal with even just one atom of a 4d or 5d metal can lead to dramatic changes in both spin and orbital moment, opening up the route to novel applications.

1 Introduction

The study of finite size effects on magnetism has been an active research theme for years. It is widely known that reducing the dimensionality of a system gives rise to a generally much higher magnetic moment than in the bulk system.[1,2] This is attributed to a reduced coordination number of the surface atoms for the smaller system, leading to less quenching of the magnetic moment. This increase of the magnetic moment is experimentally observed for the smallest possible systems, namely clusters consisting only out of a few atoms. Initially this was measured using Stern–Gerlach deflection, where only the total magnetic moment is resolved,[3] but recently also using X-ray Magnetic Circular

Dichroism (XMCD), which is sensitive to the spin and orbital magnetic moments.[4,5]

Not only does this enhancement of the magnetic moment occur for the 3d materials that are ferromagnetic in the bulk (Fe, Co, Ni).[3–5] It is even shown that 4d or 5d systems, which are non-magnetic in the bulk, can show a substantial magnetic moment when they are reduced in size. This is true for example in 4d rhodium clusters.[6,7] It has also been shown that alloying 3d and 4d metals can induce a magnetic moment on the 4d atoms. For CoRh this is observed experimentally (in the bulk,[8] for clusters on a Xe matrix[9] and for chemically prepared nanoparticles in a polymer matrix[10–12]). Also there has been a certain amount of theoretical work for CoRh, some of which included spin–orbit coupling (SOC)[10,11,13–15] but most without.[16–21] The reason that most work does not fully include SOC is that modern calculations still have difficulties properly accounting for the degree of quenching of orbital moments. However, the inclusion of SOC is important for comparison with the observed effects in this work. Specifically it is necessary in order to obtain values for the orbital magnetic moments in calculations.

We have studied the spin and orbit resolved magnetic moments of small ($8 \leq N \leq 14$) cobalt clusters doped with either one rhodium or one gold atom using XMCD on the L-edge of

[a] Radboud University Nijmegen, Institute for Molecules and Materials, Heyendaalseweg 135, 6525 AJ Nijmegen, The Netherlands.
E-mail: d.dieleman@science.ru.nl
[b] Fachbereich Chemie und Forschungszentrum OPTIMAS, TU Kaiserslautern, 67663 Kaiserslautern, Germany
[c] Max-Planck-Institut für Chemische Energiekonversion, Stiftstr. 34-36, D-45470, Mülheim an der Ruhr, Germany
[d] Helmholtz-Zentrum Berlin für Materialien und Energie, BESSY II, Albert-Einstein-Strasse 15, 12489 Berlin, Germany
[e] Inst. für Optics and Atomic Physics IOAP, TU-Berlin, Strasse des 17. Juni 135, 10623 Berlin, Germany

cobalt. We directly compare with the undoped cobalt clusters measured earlier,[4] this enables us to isolate the specific change that alloying introduces on the magnetic properties. We observe in certain cases dramatic changes in both the spin and orbital moments upon doping the cobalt clusters. In the case of going from Co_{13}^+ to $Co_{12}Rh^+$ the orbital moment for example increases with more than 150%, indicating that even the substitution of one atom can have enormous consequences.

2 Experimental details

The experimental setup that we used is described in detail by Peredkov *et al.*[4,22] In short we used X-ray Magnetic Circular Dichroism (XMCD) at the L_2 and L_3 absorption edge of cobalt to probe the magnetization in a spin and orbit resolved fashion.

2.1 Setup

Clusters are produced using pulsed laser vaporisation of a rotating thin foil which has a composition of either $Co_{90}Rh_{10}$ or $Co_{90}Au_{10}$. The ablation laser is a Nd:YAG-laser which is frequency doubled to emit at 532 nm with a repetition rate of 20 Hz and an energy per pulse of about 10 mJ. A piezo-valve pulses ($\approx 40~\mu s$) a helium carrier gas jet at a backing pressure of ≈ 15 bar into the source chamber. The Nd:YAG laser ablates atoms from the target foil into this helium pulse, which then condense into clusters of different charges and with a broad mass distribution. This cluster–helium mixture is then guided through a skimmer and through ion-optics in a manner that in our case only selects the positively charged cation clusters. Subsequently the clusters are steered by 90° by an electrostatic quadrupole deflector and guided *via* ion-optics into a Fourier-Transform Ion Cyclotron Resonance (FT-ICR) ion trap. This FT-ICR serves multiple purposes of ion-trapping, mass selection, X-ray interaction region and mass detection. For these purposes the trapping cell is placed in a superconducting magnet which generates a homogeneous field of 7 T at the interaction region. The direction of the magnetic field is parallel to the initial cluster propagation and anti-parallel to the incoming X-ray beam. The ion trap is filled with around 20 clusters packages generated by 20 shots of the Nd:YAG laser and the unwanted masses are subsequently ejected. Once mass selection is achieved, a cryogenic He pulse is allowed to interact with the clusters. Through collisional cooling the clusters will achieve a thermal equilibrium at about 20 K. All experiments were performed at the GAMBIT setup at the UE52-PGM beamline at Helmholtz-Zentrum Berlin.

2.2 XMCD spectroscopy on clusters

In bulk materials the interaction of X-rays with samples can directly be monitored by looking at the change that the propagating light undergoes by for example being absorbed by a target. For free clusters in the gas phase this is not possible due to the low density of the clusters which produce thus no observable change in the intensity of the X-rays upon absorption by the clusters. Therefore we need to employ an action-spectroscopy technique. In our case this means we look at the generated product
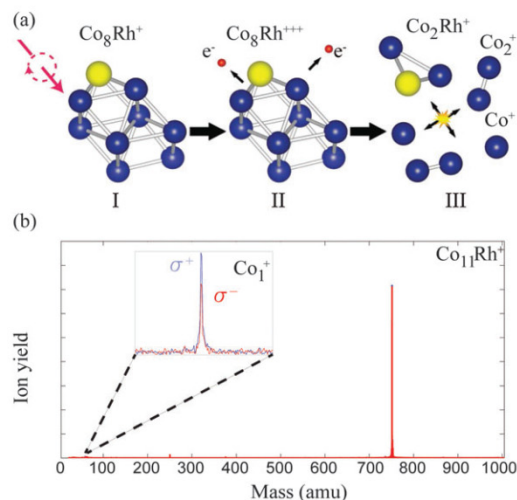

Fig. 1 The action spectroscopy method used to obtain the XMCD signal. (a-I) First a cation is allowed to interact with the X-ray, depending on the XMCD resonance conditions this will excite a 2p electron towards the 3d band, leaving a hole behind in the 2p shell. With Auger decay this hole will be filled up with an intermediate electron, releasing energy in the process. (a-II) This energy can trigger an avalanche of more electrons being excited, subsequently leading to ejections of electrons, leaving the cation more unstable. (a-III) This instability leads to the explosion or fragmentation of the cluster. (b) The fragments can be detected in the mass spectrum and counted as function of X-ray energy to give a X-ray absorption spectrum (XAS), see Fig. 2.

ions after the interaction with the X-ray beam, as detailed in Fig. 1. By counting the obtained fragments as a function of the X-ray energy and polarization we can reconstruct the X-ray absorption spectra (XAS). From these XAS we extract the integral parameters A, B and C as shown in Fig. 2 and calculate the spin and orbital magnetization using the Sum rules:[23]

$$m_{\rm orb} = -\frac{4(A + B)}{3C}n_{\rm h} \tag{1}$$

$$m_{\rm spin} = -\frac{2(A - 2B)}{C}n_{\rm h} - 7\langle T_z \rangle \tag{2}$$

with $n_{\rm h}$ the number of holes per cobalt atom in the d-shell and $\langle T_z \rangle$ the anisotropic magnetic dipole term. In principle $\langle T_z \rangle$ can have a large contribution in bulk crystals.[24] However, since the term is angle dependent, it averages out for randomly oriented samples like clusters. This is justified in detail in a study by Langenberg *et al.*[25] where they measured the XAS for transition metal clusters at different external magnetic fields B. The magnetic field will align the magnetic moment of the clusters to a certain degree, which, depending on the value of $\langle T_z \rangle$ can change the X-ray absorption spectra. However, they find no change in the line shape of the XAS for different magnetic fields, which indicates the absence of natural linear dichroism and thus $\langle T_z \rangle$ can be approximated to be zero. We take $n_{\rm h} = 2.5$ holes per atom as measured for pure cobalt clusters.[25]
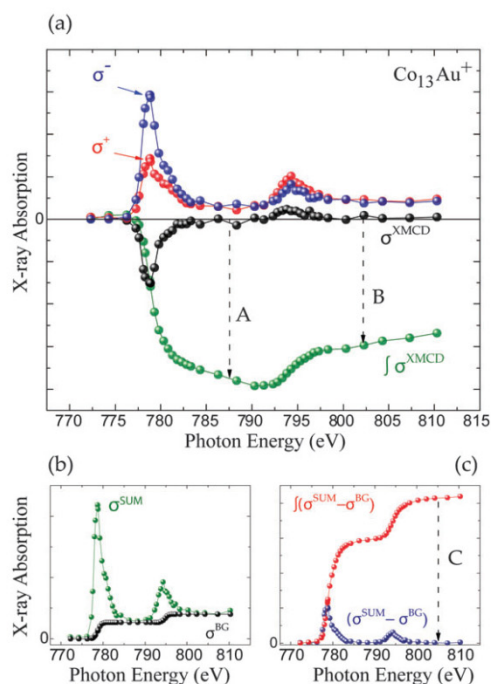
2 | *Phys. Chem. Chem. Phys.*, 2015, **00**, 1–7

This journal is © the Owner Societies 2015

Fig. 2 Exemplary XMCD traces for $Co_{13}Au^+$. Top panel (a): the ion yield as function of the photon energy for positive σ^+ (red) and negative σ^- (blue) circular polarization. The XMCD trace (black) is obtained by subtracting $\sigma^{XMCD} = \sigma^+ - \sigma^-$. The integral over the XMCD signal is plotted in green. Panel (b): the sum signal of both polarizations $\sigma^{SUM} = \sigma^+ + \sigma^-$ (green) and the background function σ^{BG} (black). (c) The sum signal with the background subtracted (blue) and the integral hereof (red). The quantities A, B and C are defined as indicated in the figures.

Fig. 3 All XMCD traces for the Co_nRh (top) and Co_nAu (down) clusters.

3 Results

All measured XMCD spectra are plotted in Fig. 3. All of the spectra clearly show the two resonant transitions, on both the L_3 and L_2 edge. Some features can be pointed out specifically. For Co_nRh it can clearly be seen that the XMCD signal on the L_2 edge around 795 eV is changing strongly with cluster size. Especially for $Co_{12}Rh$ the XMCD signal at the L_2 edge almost disappears. Using the sum rules (2) it can be understood that relatively speaking, the lower the L_2 dichroism signal is, the lower (more negative) B will be, indicating an increased orbital moment for this cluster.

The main results are shown in Fig. 4. Here our obtained results are compared with the magnetic moments of the pure cobalt clusters from Peredkov et al.[4] The results are already temperature corrected using the Langevin function. To compare with the results from Peredkov et al., as was also done before,[25] we have reanalysed their data in a way that does not assume a decoupling of the spin and orbital moments, contrary to their original interpretation. From the figure it becomes clear that not all clusters show a significant deviation from their undoped counterpart. Also, doping with either Rh or Au does not always systematically increase or decrease and μ_{spin}. For example, whereas
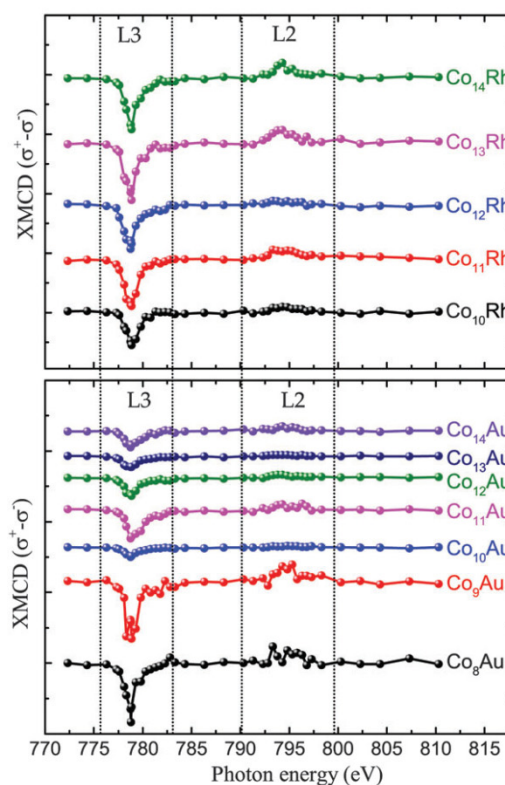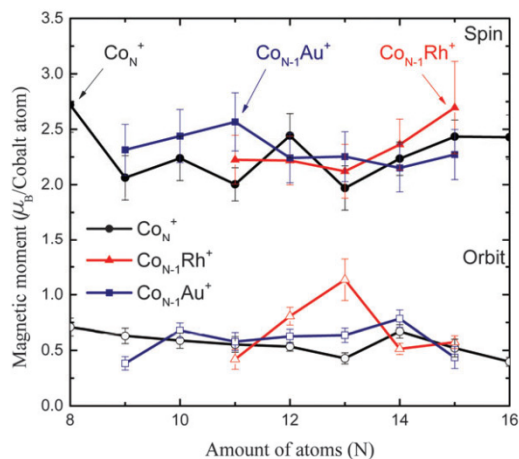

Fig. 4 The Langevin scaled spin (full symbols) and orbital (empty symbols) magnetic moments of Co_NRh^+ (red triangles) and Co_NAu^+ (blue squares), assuming $n_h = 2.5$. Also plotted are the results obtained for pure cobalt clusters obtained by Peredkov et al.[4] using the same setup as this work (black circles).

for Co_8Au^+ the gold atom introduces a decrease of μ_{orb}, for $Co_{12}Au^+$ the gold doping slightly increases μ_{orb}. The influence of doping is

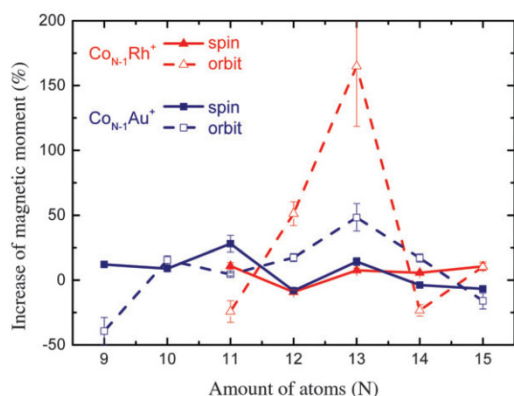Fig. 5 Percentile increase of the magnetic moments compared to the pure Co clusters measured by Peredkov et al.[4]

Fig. 6 Difference between the XAS and XMCD spectra between Co_{13} from Peredkov et al. and $Co_{12}Rh$ from this work. We have given both σ^+ and σ^- spectra an artificial offset to better distinguish the different traces in the graph. The offset is the same for both Co_{13} and $Co_{12}Rh$.

thus strongly dependent on the cluster size. It therefore becomes necessary to consider each individual cluster size.

9 atoms. For a cluster with 9 atoms, we will compare Co_9^+ and Co_8Au^+. Peredkov et al. found for the spin and orbital moments respectively $\mu_{spin} = 2.06$ μ_B per atom and $\mu_{orb} = 0.62$ μ_B per atom. When we replace one cobalt atom with gold, we obtain Co_8Au^+ and we measure a slight increase of the spin moment to $\mu_{spin} = 2.31 \pm 0.23$ μ_B per atom but a significant decrease of 39% in the orbital moment to $\mu_{orb} = 0.38 \pm 0.06$ μ_B per atom as can be seen also in Fig. 5. The decrease in the orbital moment for this size is remarkable, since in general when looking at different sizes of Co_NAu_M alloys it is found that both the orbital moments as well as the magnetic anisotropy increase with gold doping.[26,27]

10 atoms. For Co_9Au^+, as can be seen in Fig. 5, both the spin and orbital moments seem to be slightly increased compared to the Co_{10}^+ cluster, but the error bars (Fig. 4) of both individual measurements overlap. As is the case for most transition metal clusters, there have so far not been any calculations done for the Co_{10} cluster having spin–orbit coupling fully included, nor has the gold doped Co_9Au been calculated.

11 atoms. $Co_{10}Au^+$ has an almost unchanged orbital moment compared to Co_{11}^+ but a significant increase of 28% in μ_B per cobalt atom for the spin moment. The situation is opposite for $Co_{10}Rh^+$, where the spin moment overlaps with Co_{11}^+ but the orbital moment is decreased by 24%.

12 atoms. While for $Co_{10}Au^+$ the spin moment was enhanced, for $Co_{11}Au^+$ the spin moment drops sharply down to the undoped value within the error bars. Also the orbital moment remains almost the same compared to the undoped value.

For $Co_{11}Rh^+$ the spin moment overlaps with $Co_{11}Au^+$ but the orbital moment is significantly enhanced, with 51% compared to Co_{12}^+, starting an increase of orbital moment which will have it's maximum for $Co_{12}Rh^+$. It is not clear where this strong increase of the orbital moment comes from. We will discuss possible reasons later on, in the context of an even stronger increase for $Co_{12}Rh^+$. Also for this size there have been no calculations with spin–orbit coupling fully included to compare with.

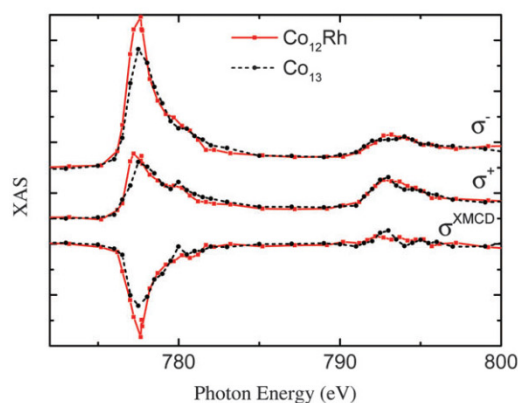**13 atoms.** Clusters with 13 atoms have been intensively studied.[29–31] For $Co_{12}Au^+$ we find an increase in the orbital moment of about 48% while the spin moment does not significantly change. In the case of rhodium, for $Co_{12}Rh^+$ the spin moment also does not change significantly, however the orbital moment changes drastically. We find an increase of 164% compared to Co_{13}^+. This is also visualized later in Fig. 8, where the ratio μ_{orb}/μ_{spin} is plotted. The average value is around 0.25 for most clusters but is highly increased to more than 0.5 for $Co_{12}Rh^+$.

We can see this difference already originate in the XAS spectra as visualized in Fig. 6. This most visible change is that the σ^- of the L_3 edge is much lower for Co_{13} than for $Co_{12}Rh$. This gives a larger XMCD signal for this edge as indicated in the graph. For the positive XAS the difference is less pronounced. This in combination with an already low XMCD signal on the L_2 edge, as pointed out before, indicates a high orbital moment.

In Fig. 7 some geometries of Co_{13} and $Co_{12}Rh$ are depicted. The icosahedron geometry for Co_{13} is found from density function theory (DFT) calculations that we did[28] using the RevTPSS functional without spin–orbit coupling fully included. The found geometries are subsequently compared with experimental data using vibrational spectroscopy in order to determine the geometrical ground
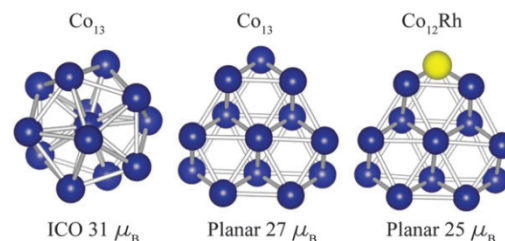

Fig. 7 Geometry of the Co_{13} cluster as calculated in our group by Jalink et al.[28] (left and middle) compared with $Co_{12}Rh$ as calculated by Aguilera-Granja et al.[21] (right).

4 | *Phys. Chem. Chem. Phys.,* 2015, **00**, 1–7

This journal is © the Owner Societies 2015

state. We are aware that theoretical studies exist that find a preference for a hexagonal growth pattern in Co clusters,[32] and specifically a slight preference for hexagonal geometry for Co$_{13}$[33] but in those studies there has been no comparison with experimental data. The geometry for Co$_{12}$Rh is taken with permission from Aguilera-Granja et al.,[21] calculated using the PBE form of GGA, without calculating the orbital magnetic moments.

When we consider the absolute increase of orbital moment per atom, from 0.43 ± 0.05 μ_B per atom to 1.14 ± 0.19 μ_B per atom, taking the error bars into account this would give a minimum increase of 0.47 μ_B per atom. This strong increase in orbital moment can either be attributed to a polarization of the Co atoms surrounding the dopant Rh atom or to a dopant induced geometry change.

14 atoms. Compared to Co$_{14}^+$ the Au doped Co$_{13}$Au$^+$ shows minimal, non-significant changes in both the spin and the orbital moment. Only the Rh doped cluster shows for this size a small change, the orbit moment drops slightly, by 17% compared to the pure cobalt cluster, while the spin moment remains within error bars unchanged. No calculations have been done for these clusters.

15 atoms. The largest cluster size that we have measured has 15 atoms. Here for both the Rh and Au doping the orbital and spin moment stay, within error bars, the same as the undoped case. It is to be expected that the influence of one doping atom will decrease with increasing cluster size, as the cluster will be less perturbed if just one of many atoms is replaced. To support this assumption however, more measurements have to be done, either by going to heavier clusters or increasing the doping per cluster size. Also for this size there have been no calculations for the doped clusters.

3.1 Comparison with previous XMCD experiments

As stated before, we consider the ranges of [Co$_{8-14}$Au]$^+$ and [Co$_{10-14}$Rh]$^+$, always attaching one single dopant atom to a cobalt cluster. Recently, Langenberg et al. remeasured XMCD data for pure Co clusters.[25] They found that the spin moments they obtain are larger than the spin moments obtained for the same clusters by Peredkov et al. In fact, their range of spin moments is closer to our results for Co$_N$Au$^+$ clusters. However, as also pointed out before,[25] the orbit/spin ratio is a more reliable way of comparing data because this will cancel out possible errors in for example the degree of circular polarization and the number of occupied 3d states. In Fig. 8 it is shown that the μ_{orb}/μ_{spin} ratio obtained by Peredkov et al. and Langenberg et al. are comparable. Is has to be noted that since our results are measured using the same experimental setup as Peredkov et al.[4] used, our results can be directly compared to their measurements for pure cobalt clusters even when the results from Langenberg et al. do not match completely.

3.2 How can doping influence the magnetic properties?

As briefly discussed later, theory cannot yet give a full explanation of the magnetic properties in small transition metal clusters. We are therefore forced to form models based on more qualitative arguments.
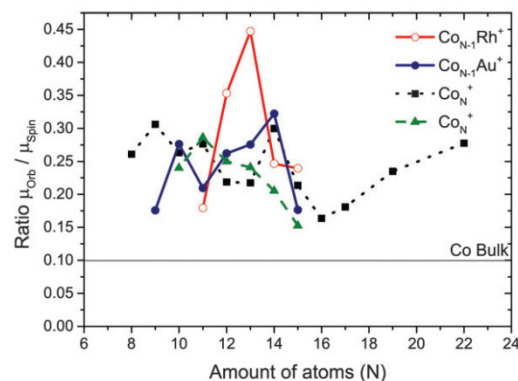

Fig. 8 The ratio of the orbital and spin magnetic moment μ_{orb}/μ_{spin} compared with Peredkov et al.[4] (black squares) and Langenberg et al.[25] (green triangles).

In general the magnetic moment of a doped material can change in three ways. First, the dopant atom can have a very high magnetic moment, which it can either intrinsically posses, or it can be polarized by the parent atoms. Second, the dopant may be a source of magnetic polarization on the neighbouring parent atoms. This it can do by hybridization with the parent orbitals, which can either lead to a different orbital moment or to a change in the spin moment. Third, the dopant can energetically favour a different ground state isomer geometry, which can lead to different magnetic properties.

The first option, the magnetic moment on the dopant atoms itself has been studied for example by Harp et al.[8] Here they discuss doping a bulk transition metal with a different transition metal. They note that the magnetic polarization on the impurity atoms depends on its d-band occupation number. When the occupation number of the dopant is the same or higher than the parent material, it generally polarizes ferromagnetically and when it's lower, it will normally polarize anti-ferromagnetically. In our case we study the parent material cobalt, with the same d-band occupation number as the dopant rhodium, hence rhodium is expected to magnetize ferromagnetically in a cobalt environment. For gold the situation is similar.

In particular this ferromagnetic coupling of the dopant is calculated by Aguilera-Granja et al.[21] They find for Co$_{12}$Rh an induced spin moment on the Rh atom of 1.09 μ_B per atom while for Rh$_{13}$ a spin moment of 0.69 μ_B per atom is found. This shows that the magnetic polarization increases when the Rh atom is in a Co environment. In our measurements we cannot say anything about the polarization of the Rh atom since we just probe the L-edge of the cobalt atoms, providing exclusively information about the magnetic properties around these atoms.

Possible origins for the strong increase in the orbital moment for substitutional doping with Rh have thus to be found in an induced magnetic polarization on the Co atoms or in a possible geometry change. For the latter it is known[19] that the strong spin–orbit coupling in the 4d and 5d metals can influence the geometry of the system. Since orbital quenching is a purely geometric effect, a

This journal is © the Owner Societies 2015

Phys. Chem. Chem. Phys., 2015, **00**, 1–7 | **5**

drastic change in geometry could in principle lead to a dramatic enhancement of the orbital moment. An induced magnetic polarization of the 3d atoms by a 4d or 5d material has been observed before in both experiment and calculations.[14,27] Proposed mechanisms for this can be found in hybridization of the 3d Co bands with the dopant 4d/5d bands as well as in the increased MAE at the interface between the Co and Rh/Co atoms.

4 Theoretical models

So far for $Co_{12}Rh$, to the best of our knowledge, only Aguilera *et al.* have calculated this cluster, see Fig. 7. For $Co_{12}Rh$ Aguilera *et al.* find a spin moment of 1.92 μ_B per atom,[21] and for Co_{13} μ_{spin} = 2.08 μ_B per atom, which is thus a small decrease in the spin moment when doped with Rh. These spin magnetic moments are comparable to our measured moments of 2.12 μ_B per atom for $Co_{12}Rh^+$ and 2.25 μ_B per atom for $Co_{12}Au^+$. The orbital moments were unfortunately not calculated by Alguilera *et al.*

In an attempt to reproduce the giant increase in the orbital moment when going from Co_{13}^+ to $Co_{12}Rh^+$ we have performed calculations using various approaches. Starting points for these calculations were the non spin–orbital coupled density function theory (DFT)[34,35] calculations that we have performed earlier for a range of cobalt clusters[28] and which are compared with their experimentally obtained vibrational spectra in order to confirm their ground state geometry. We have calculated the orbital and spin moments using both the generalized gradient approximation (GGA) functional defined by Perdew–Burke–Ernzerhof (PBE)[36] and the GGA + U method. DFT in its GGA form is derived in the limit of a nearly uniform electron gas, which usually works well for itinerant electron systems. However, for electrons with a more localized character, *i.e.* strongly correlated electrons, the electron–electron interaction is not properly described by GGA. We have tried to treat electron correlations on a higher level, *i.e. via* the GGA + U method. This method treats on-site Coulomb interactions within the static mean field approximation. One would thus expect that the description of the orbital moment improves in GGA + U with respect to plain GGA.

We found however that both GGA and GGA + U approaches cannot produce orbital moments comparable with the experiment. Both methods underestimate the experimental values. See for a full discussion our upcoming publication.[37] In short, most likely the reason for this underestimation is related to the way how electron correlation effects are taken into account. Broadly speaking when looking in terms of energy ordering, Hund's first rule treats the spin moments on a larger energy scale than the second rule, which is related to the orbital moment. The smaller the differences in energy become, the more important it becomes to properly take effects like electron correlation into account as the introduced error will be more important. This also means that if the electron correlation for a certain cluster size increases, the calculations will be less accurate. This can possibly also explain the discrepancies that we observed. In the future it would thus be highly interesting to see whether a more sophisticated method like DFT in combination with the dynamical mean field theory (LDA + DMFT)[38] would be able to produce orbital moments in agreement with experiment.

5 Conclusions

In conclusion, we have measured the orbital and spin magnetic moments of cobalt clusters which are substitutionally doped with either a rhodium or a gold atom. Comparing with pure cobalt clusters the spin and orbital moments are either increased or decreased in a way that is very dependent on the specific cluster size, no general trend can be extracted. For some sizes the changes are very extreme, for example in $Co_{12}Rh^+$ the orbital moment more than doubles compared to the pure cobalt clusters. The origins hereof remain to be clarified. In case of the $Co_{12}Rh^+$ cluster we propose that only a change of geometry or electronic structure compared to the pure Co_{13}^+ cluster can explain the strong increase. This transition could be brought about by the strong spin–orbit coupling present in the Rh atom. In the future our next step will be to compare these experimental results with the computationally expensive LDA + DMFT method.

Acknowledgements

References

1 Y.-W. Jun, J.-W. Seo and J. Cheon, *Acc. Chem. Res.*, 2008, **41**, 179–189.

2 H. Haberland, *Clusters of Atoms and Molecules*, Springer Berlin Heidelberg, Berlin, Heidelberg, 1994, vol. 52, p. 422.

3 I. M. Billas, A. Châtelain and W. A. de Heer, *Science*, 1994, **265**, 1682–1684.

4 S. Peredkov, M. Neeb, W. Eberhardt, J. Meyer, M. Tombers, H. Kampschulte and G. Niedner-Schatteburg, *Phys. Rev. Lett.*, 2011, **107**, 233401.

5 M. Niemeyer, K. Hirsch, V. Zamudio-Bayer, A. Langenberg, M. Vogel, M. Kossick, C. Ebrecht, K. Egashira, A. Terasaki, T. Möller, B. v. Issendorff and J. T. Lau, *Phys. Rev. Lett.*, 2012, **108**, 057201.

6 A. Cox, J. Louderback, S. Apsel and L. Bloomfield, *Phys. Rev. B: Condens. Matter Mater. Phys.*, 1994, **49**, 12295–12298.

7 A. Cox, J. Louderback and L. Bloomfield, *Phys. Rev. Lett.*, 1993, **71**, 923–926.

8 G. Harp, S. Parkin, W. O'Brien and B. Tonner, *Phys. Rev. B: Condens. Matter Mater. Phys.*, 1995, **51**, 37–40.

6 | *Phys. Chem. Chem. Phys.*, 2015, **00**, 1–7

This journal is © the Owner Societies 2015

9 V. Sessi, K. Kuhnke, J. Zhang, J. Honolka, K. Kern, C. Tieg, O. Šipr, J. Minár and H. Ebert, *Phys. Rev. B: Condens. Matter Mater. Phys.*, 2010, **82**, 184413.

10 M. Muñoz Navia, J. Dorantes-Dávila, D. Zitoun, C. Amiens, B. Chaudret, M.-J. Casanove, P. Lecante, N. Jaouen, A. Rogalev, M. Respaud and G. M. Pastor, *Faraday Discuss.*, 2008, **138**, 181.

11 M. Muñoz-Navia, J. Dorantes-Dávila, D. Zitoun, C. Amiens, N. Jaouen, A. Rogalev, M. Respaud and G. M. Pastor, *Appl. Phys. Lett.*, 2009, **95**, 233107.

12 D. Zitoun, M. Respaud, M.-C. Fromen, M. Casanove, P. Lecante, C. Amiens and B. Chaudret, *Phys. Rev. Lett.*, 2002, **89**, 037203.

13 H. K. Yuan, H. Chen, A. L. Kuang, B. Wu and J. Z. Wang, *J. Phys. Chem. A*, 2012, **116**, 11673–11684.

14 M. Muñoz Navia, J. Dorantes-Dávila and G. M. Pastor, *J. Phys.: Condens. Matter*, 2004, **16**, S2251–S2256.

15 M. Muñoz Navia, J. Dorantes-Dávila, M. Respaud and G. M. Pastor, *Eur. Phys. J. D*, 2009, **52**, 171–174.

16 S. Dennler, J. Morillo and G. Pastor, *Surf. Sci.*, 2003, **532–535**, 334–340.

17 S. Dennler, J. Morillo and G. M. Pastor, *J. Phys.: Condens. Matter*, 2004, **16**, S2263–S2272.

18 L. E. Daz-Sánchez, J. Dorantes-Dávila and G. M. Pastor, *Phys. Rev. B: Condens. Matter Mater. Phys.*, 2013, **88**, 134423.

19 E. Berlanga-Ramrez, F. Aguilera-Granja, J. Montejano-Carrizales, A. Daz-Ortiz, K. Michaelian and A. Vega, *Phys. B*, 2004, **354**, 278–281.

20 J. Lv, X. Bai, J.-F. Jia, X.-H. Xu and H.-S. Wu, *Phys. B*, 2012, **407**, 14–21.

21 F. Aguilera-Granja, R. C. Longo, L. J. Gallego and A. Vega, *J. Chem. Phys.*, 2010, **132**, 184507.

22 S. Peredkov, A. Savci, S. Peters, M. Neeb, W. Eberhardt, H. Kampschulte, J. Meyer, M. Tombers, B. Hofferberth, F. Menges and G. Niedner-Schatteburg, *J. Electron Spectrosc. Relat. Phenom.*, 2011, **184**, 113–118.

23 C. Chen, Y. Idzerda, H. Lin and N. Smith, *Phys. Rev. Lett.*, 1995, **75**, 152–155.

24 R. Wu and A. Freeman, *Phys. Rev. Lett.*, 1994, **73**, 1994–1997.

25 A. Langenberg, K. Hirsch, A. Ławicki, V. Zamudio-Bayer, M. Niemeyer, P. Chmiela, B. Langbehn, A. Terasaki, B. v. Issendorff and J. T. Lau, *Phys. Rev. B: Condens. Matter Mater. Phys.*, 2014, **90**, 184420.

26 F. Luis, J. Bartolomé, F. Bartolomé, M. J. Martínez, L. M. García, F. Petroff, C. Deranlot, F. Wilhelm and A. Rogalev, *J. Appl. Phys.*, 2006, **99**, 08G705.

27 J. Bartolomé, L. Garca, F. Bartolomé, F. Luis, R. López-Ruiz, F. Petroff, C. Deranlot, F. Wilhelm, A. Rogalev, P. Bencok, N. Brookes, L. Ruiz and J. González-Calbet, *Phys. Rev. B: Condens. Matter Mater. Phys.*, 2008, **77**, 184420.

28 J. Jalink, J. M. Bakker, D. Dieleman, D. Kiawi, T. Rasing and A. Kirilyuk, 2015, submitted.

29 J. Montejano-Carrizales, F. Aguilera-Granja, C. Goyhenex, V. Pierron-Bohnes and J. Morán-López, *J. Magn. Magn. Mater.*, 2014, **355**, 215–224.

30 B. Reddy, S. Khanna and B. Dunlap, *Phys. Rev. Lett.*, 1993, **70**, 3323–3326.

31 F. Aguilera-Granja, A. Garca-Fuente and A. Vega, *Phys. Rev. B: Condens. Matter Mater. Phys.*, 2008, **78**, 134425.

32 S. Datta, M. Kabir and T. Saha-Dasgupta, *Phys. Rev. B: Condens. Matter Mater. Phys.*, 2011, **84**, 075429.

33 S. Datta, M. Kabir, S. Ganguly, B. Sanyal, T. Saha-Dasgupta and A. Mookerjee, *Phys. Rev. B: Condens. Matter Mater. Phys.*, 2007, **76**, 014429.

34 P. Hohenberg and W. Kohn, *Phys. Rev.*, 1964, **136**, B864–B871.

35 W. Kohn and L. Sham, *Phys. Rev.*, 1965, **140**, A1133–A1138.

36 J. Perdew, K. Burke and M. Ernzerhof, *Phys. Rev. Lett.*, 1996, **77**, 3865–3868.

37 L. Peters, D. Dieleman and A. Kirilyuk, to be submitted.

38 S. Chadov, J. Minár, M. I. Katsnelson, H. Ebert, D. Ködderitzsch and A. I. Lichtenstein, *EPL*, 2008, **22**, 62–63.

This journal is © the Owner Societies 2015

Phys. Chem. Chem. Phys., 2015, **00**, 1–7 | 7

- 127 -

5. SPIN AND ORBITAL MAGNETIC MOMENTS OF ISOLATED SINGLE MOLECULE MAGNETS (SMMs)

In this chapter I present the results on gas phase XMCD investigations on isolated Single Molecule Magnets (SMMs) and the resulting spin and orbital contributions to their total magnetic moments. The results are introduced, discussed and concluded in two paper drafts. My contributions to the presented manuscripts are stated prior to the respective manuscripts.

5.1 Paper draft: "Single molecule magnetism in isolation – X-ray magnetic circular dichroism (XMCD) spectroscopy of gaseous [Mn$_{12}$ac]$^{+}$"

The following paper draft named "Single molecule magnetism in isolation – X-ray magnetic circular dichroism (XMCD) spectroscopy of gaseous [Mn$_{12}$ac]$^{+}$" was prepared to be published as a communication in a slightly shorter version. The experiments were performed by the experimental team consisting of J. D. Meyer, J. Meyer, A. Lawicki and myself lead by T. Lau at the Helmholtz Zentrum Berlin (BESSY II). The data evaluation was done by myself supported by V. Zamudio-Bayer. The computations were performed by E. Kessler under the supervision of C. van Wüllen. The initial paper draft was put together by myself.

5. Spin and orbital magnetic moments of isolated Single Molecule Magnets

Single molecule magnetism in isolation

–

X-ray magnetic circular dichroism (XMCD) spectroscopy

of gaseous [Mn$_{12}$ac]$^+$

Matthias Tombers[a], Jennifer Meyer[c], Jonathan Meyer[a], Arkadiuz Lawicki[b], Vicente Zamudio-Bayer[b], Tobias Lau[b], Eva Kessler[a], Christoph van Wüllen[a] and Gereon Niedner-Schatteburg[a]

(a) Fachbereich Chemie and Forschungszentrum OPTIMAS, Technische Universität Kaiserslautern, 67663 Kaiserslautern, Germany

(b) Helmholtz Zentrum Berlin für Materialien und Energie, BESSY II, Albert-Einstein-Straße 15, 12489 Berlin, Germany

(c) Institut für Ionenphysik und Angewandte Physik, Universität Innsbruck, A-6020 Innsbruck, Austria

5.1.1 Abstract

We present the first gas phase investigations of an isolated Single Molecule Magnet (SMM) by X-ray Magnetic Circular Dichroism (XMCD) spectroscopy. We investigate the archetypal Mn$_{12}$-acetate [Mn$_{12}$ac] SMM as a cationic species [Mn$_{12}$ac]$^+$ in the gas phase. Our measurements access the intrinsic magnetic properties of this compound void of effects resulting from bulk formation or surface deposition. Our technique enables us to characterize the [Mn$_{12}$ac]$^+$ complex as a real SMM, i.e. as an isolated molecule in the gas phase. By comparison to an XMCD spectrum of a bulk sample, we elucidate the influence of bulk formation on the magnetic properties of the SMM. Furthermore, we check for the influence of ion formation on the magnetic properties of the SMM by broken symmetry calculations.

5. Spin and orbital magnetic moments of isolated Single Molecule Magnets

5.1.2 Introduction

Single Molecule Magnets (SMMs) provide for a promising route towards novel magnetic materials of use in future high density data storage devices[1] and for quantum computing[2-5]. They combine a high magnetic moment with a slow relaxation of the magnetization by virtue of a significant magnetic anisotropy barrier. These are intrinsic properties of a sole molecule and do not result from any long range magnetic bulk ordering. Such a combination leads to an appreciable hysteresis as detected in bulk samples[6]. The most prominent SMM is the $[Mn_{12}O_{12}(CH_3COO)_{16}(H_2O)_4]$ complex[7] - in short $[Mn_{12}ac]$. It shows a high spin magnetic ground state (S = 10) and a magnetic anisotropy barrier of 50 cm^{-1}[8,9]. This makes it not only the first, but still one of the best SMMs.

The effect of X-ray Magnetic Circular Dichroism (XMCD) has proven to be a valuable tool in the investigation of magnetic properties of bulk samples[10-12], thin films[13], nano particles[14] and deposited transition metal clusters[15,16]. It has also proven useful in the study of bulk and surface deposited $[Mn_{12}ac]$ and related derivatives[17-19]. The intrinsic magnetic properties of SMMs are potentially affected by their environment, such as supporting surface or embedding matrix[19]. Such environmental effects are strong in cases of supported clusters[20]. It is an open question whether SMMs are equally affected by crystal packing effects of the bulk. Investigations of bulk and surface deposited $[Mn_{12}ac]$ and related derivatives[17-19] were not possible to quantify the electronic coupling of spin sample and environment in an unambiguous manner. An unconditional caveat sticks to any statement on intrinsic properties of such spin samples.

We have investigated the intrinsic magnetic moments of isolated transition metal clusters before by transferring the XMCD technique into the gas phase[21,22]. In the presented work, we transfer this gas phase XMCD technique to isolated SMMs. We aim to elucidate the intrinsic magnetic properties of the isolated $[Mn_{12}ac]$ and by comparison to previous studies we investigate the influences of bulk formation and surface deposition onto the magnetic properties.

5.1.3 Experimental and computational methods

We used the combination of an ElectroSpray Ionization source (ESI) with the NanoClusterTrap operated at the UE52-PGM beamline at the BESSY II (Helmholtz Zentrum Berlin) synchrotron facility to record the X-ray Absorption (XA) spectra presented in this work. The NanoClusterTrap has proven suitable to record XMCD spectra of isolated species in the gas phase during the investigation of magnetic moments of isolated transition metal clusters[21]. A detailed description of the setup is

given elsewhere[23]. In brief, after creation in the electrospray ion source the investigated species ($[Mn_{12}O_{12}(CH_3COO)_{15}(CH_3CN)]^+$, in short $[Mn_{12}ac]^+$) gets mass selected in a quadrupole mass filter and is transferred into a linear liquid helium cooled quadrupole ion trap. The investigated ion is formed by replacing a negatively charged acetate ligand with a neutral acetonitrile solvent molecule. Please note that the four waters of crystallization cannot be observed in the gas phase mass spectrum. The used ion trap is located inside the high field region of a superconducting solenoid (5 T) to align the magnetic moments of the investigated ions to the light pass of the X-ray beam. This alignment is mandatory for the latter XMCD experiments. Inside the trap the ions are cooled down to temperatures of ~ 15 K[24] by collisional cooling to reduce temperature induced orientation randomization of the magnetic moments. The cooled ions are irradiated with circularly polarized X-ray radiation from the UE52-PGM beamline. After irradiation the ions start to fragment. An in line reflectron time of flight mass spectrometer serves to record the resulting mass spectra. With this Total Ion Yield (TIY) action spectroscopy we gain X-ray absorption spectra by recording the amount of fragment ions as a function of X-ray energy. The spectra were recorded with a spectral resolution of 370 meV at 643 eV and an increment size of 200 meV.

All density functional theory (DFT) calculations were performed using the TURBOMOLE 6.5 package[25,26]. We used the BLYP[27,28] functional for the neutral species and the PBE0[29] functional for the cationic species. In all cases, the def2-TZVP[30,31] basis set with the D3 dispersion correction[32] was used. For BLYP calculations, the resolution of identity (RI-J) approximation[33] was applied. We investigated different high and low spin states with broken symmetry configurations (ferromagnetic and antiferromagnetic coupling between the Mn[III] ring and the Mn[IV] core). This was done for the neutral [Mn$_{12}$ac] and the cationic $[Mn_{12}ac]^+$ species. Full structural relaxation was allowed for every given species. The presented molecules represent the found energetic minimum structures / spin configurations for the neutral [Mn$_{12}$ac] and the cationic $[Mn_{12}ac]^+$.

5.1.4 Results and discussion

We recorded X-ray Absorption Spectra (XAS) of gaseous $[Mn_{12}ac]^+$ utilizing left and right handed circularly polarized photons (lcp and rcp). There is a distinct dichroic effect at both recorded edges (Manganese L_2 and L_3 resonances due to $2p_{1/2} \rightarrow 3d$ and $2p_{3/2} \rightarrow 3d$ transitions), cf. Fig. 1. We attribute this XMCD effect to the orientation of a persistent magnetic moment in $[Mn_{12}ac]^+$ by the external magnetic field of the superconducting solenoid. This magnetic moment does not arise from any surface, bulk or packing effects.
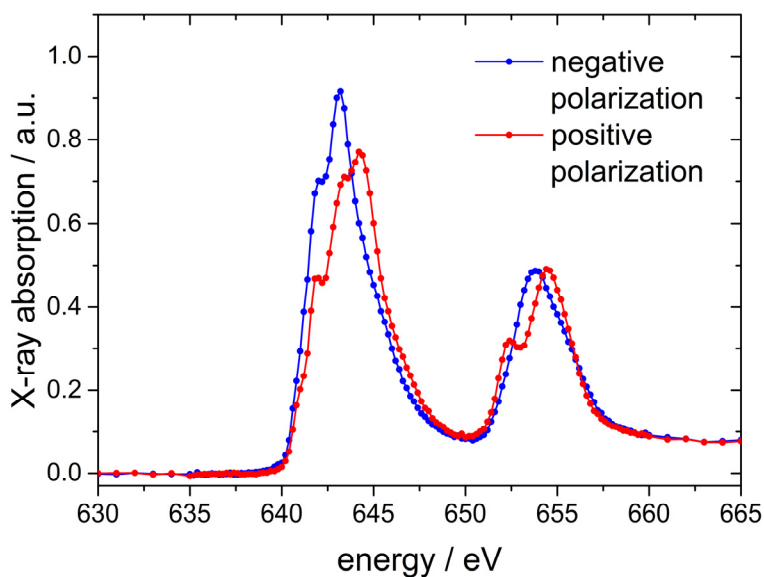
Figure 1: Gas phase X-ray absorption spectra at the Mn L_3 and L_2 absorption edge of $[Mn_{12}ac]^+$ recorded with negative (blue) and positive (red) circularly polarized X-ray radiation.

A so called XMCD spectrum, which is the difference of rcp and lcp XAS, clearly reveals subtle details (Fig. 2). Sum rule analysis[34,35] provided us with intrinsic spin and orbital contributions to the total magnetic moment when investigating transition metal clusters[22,24]. For Mn absorption edges this is not possible (especially in case of the spin sum rule) because in the early 3d series, the spin-orbit splitting of the $L_{3,2}$ edges is not large enough to prevent their mixing, caused by Coulomb interactions in the final state. This makes the application of sum rule analysis futile as it would present to much systematic error. Instead, we compare our gas phase XMCD spectrum to the results of XMCD investigations on a $[Mn_{12}ac]$ bulk sample by Sessoli et al.[17]. Our spectrum has been shifted in energy by -2.2 eV and scaled by a factor of 0.61 to overlap the maximum positive dichroic signal at the L_3 edge for better comparability and to compensate for possible energy shifts in the beamlines of both experiments. In their work the authors concluded that the molecular structure and especially the oxidation states and the resulting magnetic moments of the Mn_{12}-complex are not altered by the bulk sample preparation. We find an outermost good agreement of our gas phase spectrum with their bulk phase spectrum and therefore agree with the previous statement. Referencing to their prior XMCD studies[17], we join the prior identification of contributions of Mn^{III} and Mn^{IV} species. The combination of features from both oxidation states makes up for the complicated XMCD pattern.
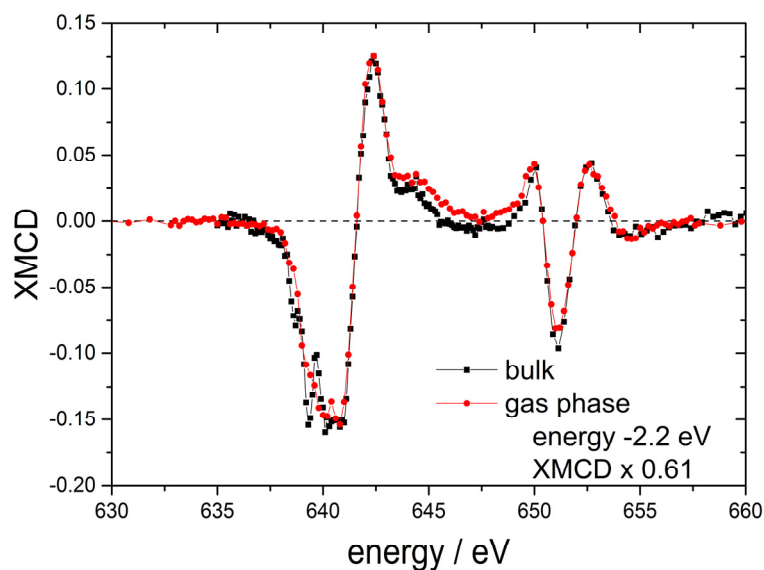
Figure 2: XMCD spectrum of [Mn$_{12}$ac] bulk samples by Mannini et al. (black squares) and the gas phase XMCD of this work (red circles) of [Mn$_{12}$ac]$^+$. The gas phase XMCD has been shifted by -2.2 eV and scaled by a factor of 0.61 to overlap the maximum positive dichroic signal for better comparability.

There is a sole difference amongst the bulk and our gas phase XMCD spectrum of [Mn$_{12}$ac]$^+$ which is beyond uncertainties. The bulk phase XMCD spectrum reveals a distinct negative peak and an anti-peak at 638 eV and 639 eV, respectively. Our gas phase spectrum shows neither. Prior bulk phase XMCD spectra of Mn^{II} complexes are dominated by a peak at 638 eV[17]. Possible reduction of Mn^{III} to Mn^{II} through radiation damage is discussed in all references on X-ray investigations of [Mn$_{12}$ac] in a bulk sample or on surfaces. We conclude: Although extensive efforts have been made to avoid radiation damage there is a very small contribution from reduction of Mn^{III} atoms to Mn^{II} in the bulk phase experiments. Our rarefied gas phase samples of [Mn$_{12}$ac]$^+$ continuously exchange while stored in our ion trap, such that radiation damage neither occurs nor accumulates. Note, that the seemingly significant radiation damage in the bulk is actually a small one. It becomes noticeable only by virtue of the strong and sharply peaked Mn^{II} contribution at 638 eV. In reference spectra of pure Mn^{II} and Mn^{III} samples[19], this sharply peaked Mn^{II} contribution at 638 eV is three to four times higher than the contribution from Mn^{III}.

Most certainly, differences in the XMCD spectrum might also arise from a different alignment of the magnetic moments to external magnetic field. The contributions to the total magnetic moment from the manganese atoms in different oxidation states have been derived by comparison to calculated spectra. This has been done for crystal field multiplet calculations[10] and simulations of the XA and XMCD spectra from spectra taken from reference compounds containing only Mn^{III} and Mn^{IV}

atoms[17]. Both approaches showed that omitting contributions from Mn^{II} species the minimum at the low energy end of the dichroic signal is dominated by the contribution of the Mn^{III} atoms. Furthermore, the crystal field multiplet calculations showed that the intensity of this minimum contributed by the Mn^{III} atom is highly dependent on the alignment of their magnetic moments to the external magnetic field assuming a tetragonal ligand field (D_{4h}). It reaches its maximum contribution for a parallel alignment of the magnetic moment to the external magnetic field and reduces up to only one third of its original value for orientations different from a parallel alignment. The Mn^{IV} contributions revealed indifferent to the alignment to the external magnetic field assuming an octahedral (O_h) ligand field. If we now compare our experimental conditions (B = 5 T; T ~ 15 K) to those of the bulk phase experiment (B = 4 T; T = 1.5 K) we find that the experimental conditions in the bulk phase in principal should lead to a better alignment of the magnetic moments to the external magnetic field. The Brillouin function[36] predicts an alignment of 99 % for the bulk and 82 % for the gas phase magnetic field and temperature conditions (assuming J = S = 10). This would be the case if the bulk molecules in [$Mn_{12}ac$] could orientate freely within the bulk structure, as the magnetic moment is coupled to the molecules structure. The bulk phase spectra are taken from crystals mortared into graphite powder. Therefor the resulting XMCD spectrum is an average over all possible orientations of the [$Mn_{12}ac$] molecules to the external magnetic field. This is confirmed by the comparison of the general intensities of the dichroic effects in the bulk and gas phase spectra. The overall intensity in the dichroic spectrum for the bulk sample is only about 60 % of the intensity in our studies although the Brillouin function predicts a better alignment for the conditions in the bulk experiment. This average over the [$Mn_{12}ac$] alignment was also assumed in the crystal field multiplett calculations. The resulting simulation did not show a comparable feature at the low energy end of the spectrum as it is present in the experimental data of the bulk studies. We therefore conclude that the difference in the dichroic spectra is not due to a better alignment of the Mn_{12} in the bulk sample and stick to our interpretation involving possible radiation damage in the bulk phase experiment.

5.1.5 Computations

In our gas phase measurements we investigate a modification of the very [$Mn_{12}ac$] complex. An anionic acetate ligand is swapped for a neutral acetonitrile solvent molecule to form an ionic species necessary for mass spectrometric investigations. Our XMCD spectrum thus characterizes the cationic [$Mn_{12}O_{12}(CH_3COO)_{15}CH_3CN]^+$, ([$Mn_{12}ac]^+$) species. The outermost important question is how much of an influence this modification exerts on the spin structure of the [$Mn_{12}ac$] core within the complexes. We address this question by density functional theory (DFT) broken symmetry calculations on the

neutral [Mn$_{12}$ac] and the cationic [Mn$_{12}$ac]$^+$ to estimate the changes in the magnetic properties by ion formation.

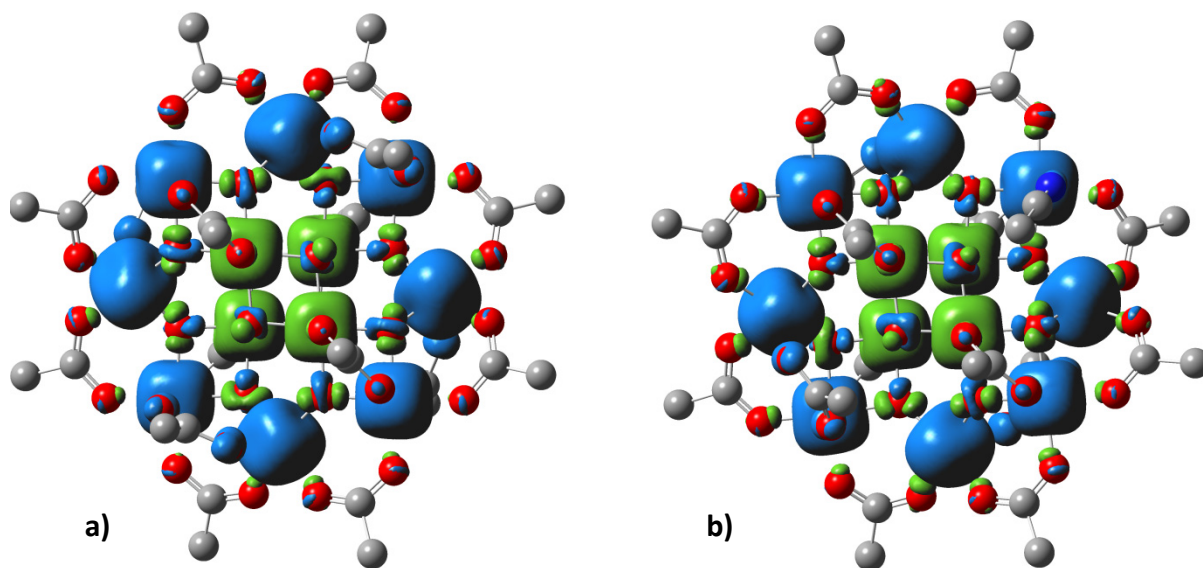**Figure 3:** Spin density plots of α (blue) and β (green) spin densities in **(a)** [Mn$_{12}$O$_{12}$(CH$_3$COO)$_{16}$] and **(b)** [Mn$_{12}$O$_{12}$(CH$_3$COO)$_{15}$(CH$_3$CN)]$^+$ by broken symmetry − DFT calculations (DFT; **(a)** BLYP, **(b)** PBE0; def2-TZVP)

For both species our preliminary calculations reveal equal α and β spin distributions (Fig. 3) to form the energetic minimum. Seemingly, there is little to no variation in the spin densities by the choice of functional. In both calculations the spin density on the outer acetate ligands is very low. This finding already hints towards the conclusion that the acetate ligands and respectively a swapping of such an acetate ligand with an acetonitrile molecule should have little to no effect on the magnetic structure of the complex. Both calculations resemble the antiferromagnetic coupling between the outer Mn^{III} and the inner Mn^{IV} species which gives rise to the total spin ground state of S = 10[37]. The given antiferromagnetic coupling maintains unaltered after ion formation. Comparison of the different Mn - Mn and Mn - O bond length affirms this statement (cf. Tab. S1). An altered coupling between the containing Mn and O atoms would reflect in significant changes in the respective bond length. This is not the case in our presented calculations. In our calculations the maximum divergence in Mn - Mn bond lengths are < 0.08 Å. The differences in Mn - O distances which are very important factors in the Mn - O superexchange coupling are even lower (< 0.05 Å). We therefore conclude that the ion formation has little to no effect on the magnetic properties of the [Mn$_{12}$ac]$^+$ core and the presented magnetic properties can be seen as intrinsic properties of the [Mn$_{12}$ac] SMM.

5.1.6 Conclusion

We have confirmed the single molecule magnet behavior of the investigated Mn$_{12}$-acetate complex by X-ray magnetic circular dichroism spectroscopy in the gas phase. Our experiment is the first to record the intrinsic magnetic properties of the Mn$_{12}$-acetate SMM as our experimental approach is void of possible influences of substrates and / or surrounding materials. Our results agree well with investigations on bulk samples[10]. We conclude that bulk sample preparation has only little to no influence on the magnetic properties of this species in contrast to severe changes of the magnetic properties recorded after surface deposition[17]. In comparison to our gas phase results the bulk phase spectrum showed very small signs of radiation damage. In our measurements we exclude radiation damage by continuous exchange of sample in our ion trap. We checked for possible alteration of the investigated magnetic properties by ion formation necessary for our mass spectrometry based investigations. Broken symmetry DFT calculations reveal that this ion formation has little to no influence on the magnetic structure of the [Mn$_{12}$ac] SMM´s core. We think that we have added a valuable tool to the investigation of intrinsic magnetic properties of single molecule magnets by transferring our XMCD investigations into the gas phase. We aim to expand our gas phase XMCD investigations to other SMMs to gain better insight into the basic components of this highly interesting phenomenon and to aid in the development and improvement of new SMMs.

5.1.7 References

[1]   Aromí, G.; Winpenny, R. E. *Single-molecule magnets and related phenomena*; Springer New York, 2006.

[2]   Leuenberger, M. N.; Loss, D., *QUANTUM COMPUTING IN MOLECULAR MAGNETS*, *Nature* **2001**, *410*, 789.

[3]   Aromí, G.; Aguila, D.; Gamez, P.; Luis, F.; Roubeau, O., *DESIGN OF MAGNETIC COORDINATION COMPLEXES FOR QUANTUM COMPUTING*, *Chemical Society Reviews* **2012**, *41*, 537.

[4]   Raman, K. V.; Kamerbeek, A. M.; Mukherjee, A.; Atodiresei, N.; Sen, T. K.; Lazic, P.; Caciuc, V.; Michel, R.; Stalke, D.; Mandal, S. K.; Blugel, S.; Munzenberg, M.; Moodera, J. S., *INTERFACE-ENGINEERED TEMPLATES FOR MOLECULAR SPIN MEMORY DEVICES*, *Nature* **2013**, *493*, 509.

[5]   Mannini, M.; Pineider, F.; Sainctavit, P.; Danieli, C.; Otero, E.; Sciancalepore, C.; Talarico, A. M.; Arrio, M.-A.; Cornia, A.; Gatteschi, D.; Sessoli, R., *MAGNETIC MEMORY OF A SINGLE-MOLECULE QUANTUM MAGNET WIRED TO A GOLD SURFACE*, *Nat Mater* **2009**, *8*, 194.

[6]   D. Gatteschi, R. S., J. Villain *Molecular Nanomagnets*; Oxford University Press: Oxford, 2006.

[7]   Lis, T., *PREPARATION, STRUCTURE, AND MAGNETIC-PROPERTIES OF A DODECANUCLEAR MIXED-VALENCE MANGANESE CARBOXYLATE*, *Acta Crystallographica Section B-Structural Science* **1980**, *36*, 2042.

[8]   Caneschi, A.; Gatteschi, D.; Sessoli, R.; Barra, A. L.; Brunel, L. C.; Guillot, M., *ALTERNATING-CURRENT SUSCEPTIBILITY, HIGH-FIELD MAGNETIZATION, AND MILLIMETER BAND EPR EVIDENCE FOR A GROUND S = 10 STATE IN MN12O12(CH3COO)16(H2O)4 .2CH3COOH.4H2O*, *Journal of the American Chemical Society* **1991**, *113*, 5873.

[9]   Glaser, T., *RATIONAL DESIGN OF SINGLE-MOLECULE MAGNETS: A SUPRAMOLECULAR APPROACH*, *Chemical Communications* **2011**, *47*, 116.

[10]   Moroni, R.; Moulin, C. C. D.; Champion, G.; Arrio, M. A.; Sainctavit, P.; Verdaguer, M.; Gatteschi, D., *X-RAY MAGNETIC CIRCULAR DICHROISM INVESTIGATION OF MAGNETIC CONTRIBUTIONS FROM MN(III) AND MN(IV) IONS IN MN12-AC*, *Physical Review B* **2003**, *68*.

[11]   Chen, C. T.; Idzerda, Y. U.; Lin, H. J.; Smith, N. V.; Meigs, G.; Chaban, E.; Ho, G. H.; Pellegrin, E.; Sette, F., *EXPERIMENTAL CONFIRMATION OF THE X-RAY MAGNETIC CIRCULAR-DICHROISM SUM-RULES FOR IRON AND COBALT*, *Physical Review Letters* **1995**, *75*, 152.

[12]   Schutz, G.; Wagner, W.; Wilhelm, W.; Kienle, P.; Zeller, R.; Frahm, R.; Materlik, G., *ABSORPTION OF CIRCULARLY POLARIZED X-RAYS IN IRON*, *Physical Review Letters* **1987**, *58*, 737.

[13]   Gambardella, P.; Rusponi, S.; Veronese, M.; Dhesi, S. S.; Grazioli, C.; Dallmeyer, A.; Cabria, I.; Zeller, R.; Dederichs, P. H.; Kern, K.; Carbone, C.; Brune, H., *GIANT MAGNETIC ANISOTROPY OF SINGLE COBALT ATOMS AND NANOPARTICLES*, *Science* **2003**, *300*, 1130.

[14]   Gambardella, P.; Dallmeyer, A.; Maiti, K.; Malagoli, M. C.; Eberhardt, W.; Kern, K.; Carbone, C., *FERROMAGNETISM IN ONE-DIMENSIONAL MONATOMIC METAL CHAINS*, *Nature* **2002**, *416*, 301.

[15]   Lau, J. T.; Fohlisch, A.; Nietubyc, R.; Reif, M.; Wurth, W., *SIZE-DEPENDENT MAGNETISM OF DEPOSITED SMALL IRON CLUSTERS STUDIED BY X-RAY MAGNETIC CIRCULAR DICHROISM*, *Physical Review Letters* **2002**, *89*, 057201/1.

[16]   Lau, J. T.; Fohlisch, A.; Martins, M.; Nietubyc, R.; Reif, M.; Wurth, W., *SPIN AND ORBITAL MAGNETIC MOMENTS OF DEPOSITED SMALL IRON CLUSTERS STUDIED BY X-RAY MAGNETIC CIRCULAR DICHROISM SPECTROSCOPY*, *New Journal of Physics* **2002**, *4*.

[17]   Mannini, M.; Sainctavit, P.; Sessoli, R.; Moulin, C. C. D.; Pineider, F.; Arrio, M. A.; Cornia, A.; Gatteschi, D., *XAS AND XMCD INVESTIGATION OF MN-12 MONOLAYERS ON GOLD*, *Chemistry-a European Journal* **2008**, *14*, 7530.

[18]   Moro, F.; Biagi, R.; Corradini, V.; Evangelisti, M.; Gambardella, A.; De Renzi, V.; del Pennino, U.; Coronado, E.; Forment-Aliaga, A.; Romero, F. M., *ELECTRONIC AND MAGNETIC PROPERTIES OF MN-12 MOLECULAR MAGNETS ON SULFONATE AND CARBOXYLIC ACID PREFUNCTIONALIZED GOLD SURFACES*, *Journal of Physical Chemistry C* **2012**, *116*, 14936.

[19] Mannini, M.; Pineider, F.; Sainctavit, P.; Moulin, C. C. D.; Arrio, M. A.; Cornia, A.; Gatteschi, D.; Sessoli, R., *XMCD OF A SINGLE LAYER OF SINGLE MOLECULE MAGNETS*, *European Physical Journal-Special Topics* **2009**, *169*, 167.

[20] Fauth, K.; Ballentine, G. E.; Praetorius, C.; Kleibert, A.; Wilken, N.; Voitkans, A.; Meiwes-Broer, K.-H., *MAGNETIC PROPERTIES OF FE NANOCLUSTERS ON CU(111) STUDIED WITH X-RAY MAGNETIC CIRCULAR DICHROISM*, *Physica Status Solidi B-Basic Solid State Physics* **2010**, *247*, 1170.

[21] Niemeyer, M.; Hirsch, K.; Zamudio-Bayer, V.; Langenberg, A.; Vogel, M.; Kossick, M.; Ebrecht, C.; Egashira, K.; Terasaki, A.; Moller, T.; Issendorff, B. V.; Lau, J. T., *SPIN COUPLING AND ORBITAL ANGULAR MOMENTUM QUENCHING IN FREE IRON CLUSTERS*, *Physical Review Letters* **2012**, *108*, 057201.

[22] Peredkov, S.; Neeb, M.; Eberhardt, W.; Meyer, J.; Tombers, M.; Kampschulte, H.; Niedner-Schatteburg, G., *SPIN AND ORBITAL MAGNETIC MOMENTS OF FREE NANOPARTICLES*, *Physical Review Letters* **2011**, *107*.

[23] Hirsch, K.; Lau, J. T.; Klar, P.; Langenberg, A.; Probst, J.; Rittmann, J.; Vogel, M.; Zamudio-Bayer, V.; Moller, T.; von Issendorff, B., *X-RAY SPECTROSCOPY ON SIZE-SELECTED CLUSTERS IN AN ION TRAP: FROM THE MOLECULAR LIMIT TO BULK PROPERTIES*, *Journal of Physics B-Atomic Molecular and Optical Physics* **2009**, *42*.

[24] Langenberg, A.; Hirsch, K.; Lawicki, A.; Zamudio-Bayer, V.; Niemeyer, M.; Chmiela, P.; Langbehn, B.; Terasaki, A.; Issendorff, B. V.; Lau, J. T., *SPIN AND ORBITAL MAGNETIC MOMENTS OF SIZE-SELECTED IRON, COBALT, AND NICKEL CLUSTERS*, *Physical Review B* **2014**, *90*.

[25] TURBOMOLE V6.5 2013, a. d. o. U. o. K. a.; Forschungszentrum Karlsruhe GmbH, -.; TURBOMOLE GmbH, s. a. f.; http://www.turbomole.com.

[26] Treutler, O.; Ahlrichs, R., *EFFICIENT MOLECULAR NUMERICAL INTEGRATION SCHEMES*, *The Journal of chemical physics* **1995**, *102*, 346.

[27] Becke, A. D., *DENSITY-FUNCTIONAL EXCHANGE-ENERGY APPROXIMATION WITH CORRECT ASYMPTOTIC BEHAVIOR*, *Physical review A* **1988**, *38*, 3098.

[28] Lee, C.; Yang, W.; Parr, R. G., *DEVELOPMENT OF THE COLLE-SALVETTI CORRELATION-ENERGY FORMULA INTO A FUNCTIONAL OF THE ELECTRON DENSITY*, *Physical review B* **1988**, *37*, 785.

[29] Adamo, C.; Barone, V., *TOWARD RELIABLE DENSITY FUNCTIONAL METHODS WITHOUT ADJUSTABLE PARAMETERS: THE PBE0 MODEL*, *The Journal of chemical physics* **1999**, *110*, 6158.

[30] Weigend, F.; Ahlrichs, R., *BALANCED BASIS SETS OF SPLIT VALENCE, TRIPLE ZETA VALENCE AND QUADRUPLE ZETA VALENCE QUALITY FOR H TO RN: DESIGN AND ASSESSMENT OF ACCURACY*, *Physical Chemistry Chemical Physics* **2005**, *7*, 3297.

[31] Weigend, F.; Häser, M.; Patzelt, H.; Ahlrichs, R., *RI-MP2: OPTIMIZED AUXILIARY BASIS SETS AND DEMONSTRATION OF EFFICIENCY*, *Chemical physics letters* **1998**, *294*, 143.

[32] Grimme, S.; Antony, J.; Ehrlich, S.; Krieg, H., *A CONSISTENT AND ACCURATE AB INITIO PARAMETRIZATION OF DENSITY FUNCTIONAL DISPERSION CORRECTION (DFT-D) FOR THE 94 ELEMENTS H-PU*, *The Journal of chemical physics* **2010**, *132*, 154104.

[33] Weigend, F., *ACCURATE COULOMB-FITTING BASIS SETS FOR H TO RN*, *Physical chemistry chemical physics* **2006**, *8*, 1057.

[34] Carra, P.; Thole, B. T.; Altarelli, M.; Wang, X. D., *X-RAY CIRCULAR-DICHROISM AND LOCAL MAGNETIC-FIELDS*, *Physical Review Letters* **1993**, *70*, 694.

[35] Thole, B. T.; Carra, P.; Sette, F.; Vanderlaan, G., *X-RAY CIRCULAR-DICHROISM AS A PROBE OF ORBITAL MAGNETIZATION*, *Physical Review Letters* **1992**, *68*, 1943.

[36] Stefanita, C. G. *Magnetism: Basics and Applications*; Springer, 2012.

[37] Mannini, M.; Sainctavit, P.; Sessoli, R.; Moulin, C. C. d.; Pineider, F.; Arrio, M.-A.; Cornia, A.; Gatteschi, D., *XAS AND XMCD INVESTIGATION OF MN-12 MONOLAYERS ON GOLD*, *Chemistry-a European Journal* **2008**, *14*, 7530.

5.1.8 Supplementary material to "Single molecule magnetism in isolation – X-ray magnetic circular dichroism (XMCD) spectroscopy of gaseous [Mn$_{12}$ac]$^{+}$"
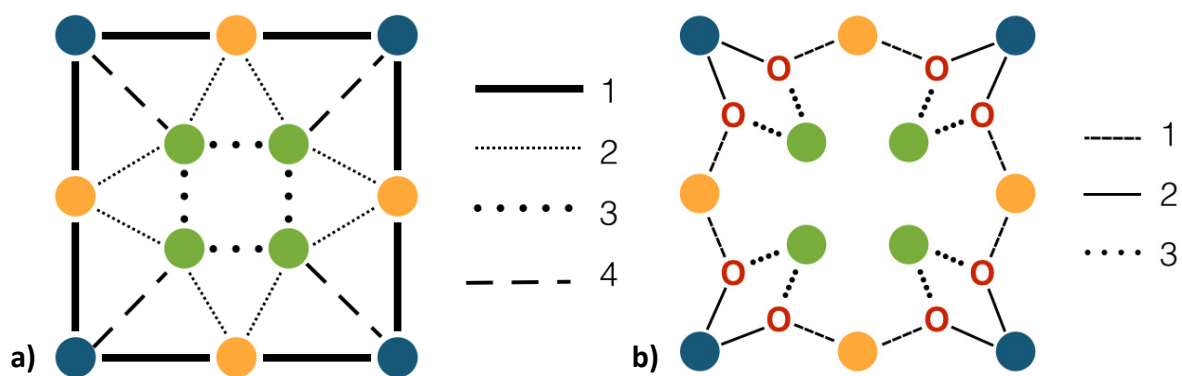

Figure S1 Schematic depiction of the different **(a)** Mn‑Mn (1 – 4, Tab. S1) and **(b)** Mn‑O (1 – 3, Tab. S2) bonds (differently shaped lines) for the three kinds of Mn atoms with different coordination (blue, orange and green spheres) within the [Mn$_{12}$ac] and [Mn$_{12}$ac]$^{+}$ complexes.

5. Spin and orbital magnetic moments of isolated Single Molecule Magnets

Table S1 Bond lengths for the different Mn - Mn distances (cf. Fig. S1a) in the $[Mn_{12}ac]$ (DFT, BLYP, def2-TZVP) and $[Mn_{12}ac]^+$ (DFT, PBE0, def2-TZVP) complexes. The bond lengths involving the Mn atom exhibiting the CH_3CN attachment in the $[Mn_{12}ac]^+$ complex are marked in red.

bond type	complex	bond lengths / Å								average
1	$[Mn_{12}ac]^+$	2.804	2.815	2.830	2.832					2.820
1	$[Mn_{12}ac]$	2.876	2.876	2.876	2.876					2.876
2	$[Mn_{12}ac]^+$	3.421	3.340	3.378	3.359	3.405	3.371	3.380	3.384	3.380
2	$[Mn_{12}ac]$	3.448	3.470	3.448	3.470	3.449	3.471	3.448	3.470	3.459
3	$[Mn_{12}ac]^+$	3.517	3.369	3.098	3.287	3.409	3.327	3.451	3.321	3.347
3	$[Mn_{12}ac]$	3.296	3.404	3.296	3.403	3.295	3.402	3.295	3.403	3.349
4	$[Mn_{12}ac]^+$	2.755	2.774	2.760	2.755					2.761
4	$[Mn_{12}ac]$	2.807	2.807	2.807	2.807					2.807

Table S2 Bond lengths for the different Mn - O distances (cf. Fig. S1b) in the $[Mn_{12}ac]$ (DFT, BLYP, def2-TZVP) and $[Mn_{12}ac]^+$ (DFT, PBE0, def2-TZVP) complexes. The bond lengths involving the Mn atom exhibiting the CH_3CN attachment in the $[Mn_{12}ac]^+$ complex are marked in red.

bond type	complex	bond lengths / Å								average
1	$[Mn_{12}ac]^+$	1.887	1.875	1.859	1.872	1.886	1.860	1.880	1.881	1.875
1	$[Mn_{12}ac]$	1.861	1.888	1.891	1.888	1.892	1.888	1.891	1.888	1.886
2	$[Mn_{12}ac]^+$	1.901	1.888	1.915	1.889	1.893	1.930	1.898	1.925	1.905
2	$[Mn_{12}ac]$	1.942	1.915	1.942	1.915	1.942	1.915	1.942	1.915	1.929
3	$[Mn_{12}ac]^+$	1.845	1.842	1.893	1.879	1.833	1.836	1.833	1.856	1.852
3	$[Mn_{12}ac]$	1.906	1.890	1.906	1.889	1.907	1.889	1.907	1.889	1.898

5.2 Paper draft: "Spin and orbital magnetic moments of isolated $[Fe_4Ln_2]^+$ single molecule magnets by X-ray magnetic circular dichroism"

The following paper draft named "Spin and orbital magnetic moments of isolated $[Fe_4Ln_2]^+$ single molecule magnets by X-ray magnetic circular dichroism" was prepared to be published as a full paper in a slightly modified version. All $[Fe_4Ln_2]$ compounds were synthesized by S. Schmidt in the group of Annie Powell. The experiments were performed by the experimental team consisting of J. Hewer, J. Meyer, A. Lawicki and myself lead by T. Lau at the Helmholtz Zentrum Berlin (BESSY II). The date evaluation was done by myself supported by V. Zamudio - Bayer. The initial paper draft was put together by myself.

Spin and orbital magnetic moments of isolated $[Fe_4Ln_2]^+$ single molecule magnets by X-ray magnetic circular dichroism

Matthias Tombers[a], Jennifer Meyer[a], Joachim Hewer[a], Jonathan Meyer[a], Arkadiusz Lawicki[b], Vicente Zamudio-Bayer[b], Tobias Lau[b], Sebastian Schmidt[c], Annie Powell[c] and Gereon Niedner-Schatteburg[a]

(a) Fachbereich Chemie and Forschungszentrum OPTIMAS, Technische Universität Kaiserslautern, 67663 Kaiserslautern, Germany

(b) Helmholtz-Zentrum für Materialien und Energie, BESSY II, 12489 Berlin, Germany

(c) Institut für Anorganische Chemie, Karlsruhe Institute of Technology, 76131 Karlsruhe, Germany

5.2.1 Abstract

We report spin and orbital magnetic moments of isolated Single Molecule Magnets (SMMs) of the $[Fe_4Ln_2]^+$ (Ln = Gd, Tb) type by gas phase X-ray Magnetic Circular Dichroism (XMCD) spectroscopy. XMCD element selectivity enables us to separate the contributions from the different contained metals to the total magnetic moment of the molecules. Sum rule analysis of the reported XMCD spectra furthermore allows for a separation of these contributions into their spin and orbital part. We check for a predicted antiferromagnetic coupling of the Fe atoms. Furthermore we investigate the influences of structure onto the magnetic moments of the containing Fe and Ln atoms by investigating two different structure types. We find a surprisingly increased orbital contribution for all the lanthanides investigated the magnitude varying. A detailed explanation is pending and it will constitute a challenge for future computational investigations.

5. Spin and orbital magnetic moments of isolated Single Molecule Magnets

5.2.2 Introduction

The element selectivity of resonant X-ray absorption (XA) and associated techniques such as X-ray magnetic circular dichroism (XMCD) allows for a separation of a compound´s properties (e.g. its total magnetic moment) into the contributions from different elements. Sum rule analysis[1,2] of XMCD spectra serves for a further deconstruction of these partial magnetic moments into their spin and orbital contributions. XMCD has proven a valuable tool in the investigations of spin and orbital magnetic moments of samples such as surfaces[3,4], thin films[5-7], deposited nanoparticles[8-14] or clusters[15-20] and adatoms[21-23]. Most recently, this technique has been transferred into the gas phase by the investigation of isolated transition metal clusters[24-28]. Gas phase investigations allow for the determination of a system´s intrinsic properties, i.e. void of any alteration by a supporting substrate or a surrounding environment.

Single molecule magnets (SMMs) are a new class of magnetic materials with highly interesting magnetic properties[29]. They are defined by a high total spin ground state (S) combined with a magnetic anisotropy barrier below a critical temperature. This anisotropy is not based on any long range magnetic ordering as it is the case for most bulk samples showing magnetic anisotropy. It is an intrinsic property of the molecule itself. The combination of the given magnetic properties of the SMMs on a molecular level makes these molecules promising prospects for high capacity data storage devices[30] and for quantum computing[31,32].

In this work we put the possibilities of gas phase XMCD to a test by the first gas phase investigation of isolated iron and lanthanides containing single molecule magnets of the $[Fe_4Ln_2]^+$ type (Ln = Gd, Tb). In addition to the change in the lanthanide metal, we look for structure induced changes of the magnetic moments by investigating two different structure types of the $[Fe_4Ln_2]^+$ compounds. We present X-ray Absorption (XA) and resulting XMCD spectra on the respective Fe $L_{3,2}$ and Ln $M_{5,4}$ absorption edges.

We find very low dichroic signals for the polarization dependent XA spectra on the Fe $L_{3,2}$ absorption edges. These low dichroic signals indicate an antiferromagnetic coupling of the containing iron atoms. We check for changes in the antiferromagnetic coupling by changing the neighboring lanthanide and by changing the system´s structure. The recorded polarization dependent XAS spectra on the lanthanides $M_{5,4}$ absorption edges show significant dichroic effects. Here, we also look for structure induced changes in the magnetizations of the lanthanides.

Despite the well-known limitations of sum rule analysis, especially in the case of the "spin sum rule"[33-35], we gain insight into the fundamental building blocks of a SMMs magnetic properties, by our gas phase X-ray magnetic circular dichroism investigations.

5.2.3 Experimental methods and setup

We used the NanoClusterTrap setup to record the presented polarization dependent gas phase X-ray Absorption (XA) spectra. The NanoClusterTrap is coupled to the UE52-PGM soft X-ray beamline at the BESSY II synchrotron facility of the Helmholtz Zentrum Berlin. The NanoClusterTrap is a custom build mass spectrometer to record Total Ion Yield (TIY) gas phase XA spectra[26-28]. For our experiments we used a custom built ElectroSpray Ionization (ESI) source for ion creation, kindly provided by the group of T. Schlathölter (University of Groningen, The Netherlands). We investigated two different SMMs of the $[Fe_4Ln_2]$ type with Ln being Gd and Tb. The molecular formula of compound **I** is $[Fe_4Ln_2(N_3)_6(N(C_2H_4OH)(C_2H_4O)_2)_4(C(CH_3)_3COO)_4]$. This compound shows a wheel like structure of the Fe and Ln atoms. For compound **II** the molecular formula reads as $[Fe_4Ln_2O_2((CH_3)_3CCOO)_4(NO_3)_2(H_3C_3N(C_2H_4O)_2)_4]$. This compound shows a rectangular arrangement of the Fe atoms with the Ln atoms in the center of this rectangular arrangement.
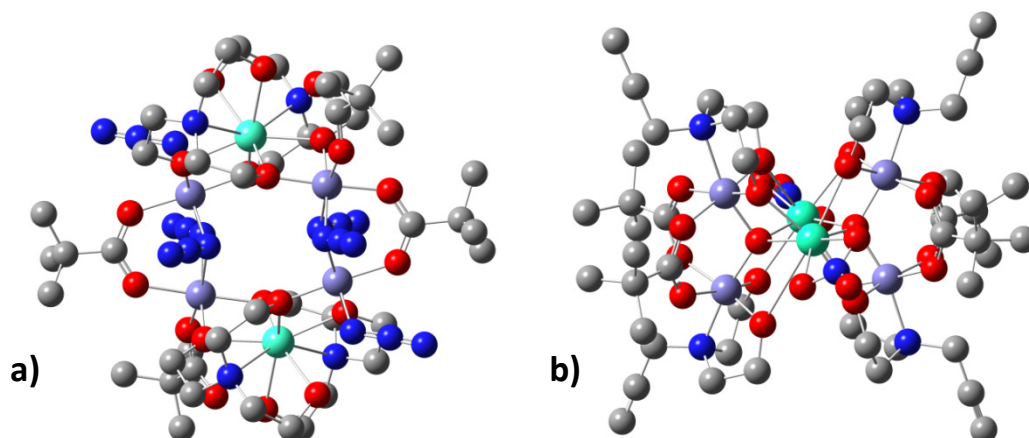
Figure 1 Crystal structures of the $[Fe_4Ln_2]$ complexes for structure type **I** and **II**. Structure **I (a)** presents a cyclic arrangement of the Fe (purple) and Ln (Ln = Gd, Tb, cyan) atoms. Structure **II (b)** presents a rectangular arrangement of the Fe atoms with the Ln atoms in between. Hydrogen atoms are omitted for clarity (C: grey, O: red, N: blue, Fe: purple, Ln: cyan.

All samples were prepared in an acetonitrile (CH_3CN) solution with a concentration of ~ 1 x 10^{-3} mol/l. The investigated cationic species form by replacement of one negatively charged ligand (i.e., CH_3COO^- for $[Fe_4Ln_2]^+$ structure type **I** and NO_3^- for $[Fe_4Ln_2]^+$ structure type **II**) with one neutral acetonitrile solvent molecule during the ESI process.

The ion of interest is mass selected in a linear quadrupole mass filter (Extrel, 40 - 4000 amu). Then, the ions are stored in a linear quadrupole ion trap which is located within the high field region (5 T)

5. Spin and orbital magnetic moments of isolated Single Molecule Magnets

of a superconducting solenoid. The trap is operated at frequencies between 2 and 4 MHz depending on the mass of the investigated ions. Evaporative liquid He cooling cools down the ion trap to temperatures < 4 K. A constant He backing pressure of 5×10^{-7} to 1×10^{-6} mbar within the vacuum chamber cools down the trapped ions by collisional cooling. The ions thermalize at a slightly higher temperature of 10 - 15 K[28] due to "heating" of the ions by the radio frequency of the trap. The ions are constantly injected into the ion trap. From the ion trap the ions are ejected into the reflectron time of flight mass spectrometer with a frequency of about 100 Hz to record mass spectra. For the XA spectra recorded by TIY spectroscopy the ions are irradiated for 10 to 15 s at a set photon energy. A GaAs-diode records the X-ray intensity from the undulator beamline which is used for photon flux normalization of the recorded spectra. Spectra on the Fe absorption edges were taken with an exit slit size of 250 µm and a respective resolution of 500 meV at 711 eV. For spectra recorded at the lanthanide absorption edges the used exit slit width was 500 µm with a respective spectral resolution of ~ 2.5 eV.

For the presented $[Fe_4Ln_2]^+$ - type SMMs, $[FeO]^+$ is the dominating fragment in the TIY mass spectra. The fragment signal intensity only amounts to several percent of the signal intensity of the investigated parent molecule. We recorded spectra for left and right handed circularly polarized light in an alternating manner. The resulting XMCD spectra were analyzed in terms of sum rule analysis[1,2]:

$$m_S^{(z)} = g_S\mu_B \frac{(A - bB)}{c\frac{3}{2}C} n_h - g_S\mu_B \frac{d}{c} \langle T_z \rangle$$

$$m_L^{(z)} = -g_L\mu_B \frac{A + B}{a\frac{3}{2}C} n_h$$

With n_h being the number of holes in the final state, g_S and g_L the g-factors for the electron spin and orbital angular momentum ($g_S = 2.0$, $g_L = 1$), μ_B the Bohr magneton and a, b, c and d are the sum rule related prefactors. We anticipate the containing Fe^{3+} and Ln^{3+} ions to be in a $3d^5$ and $4f^n$ (n = 7, 8 for Gd, Tb) high spin state. Therefore we chose the number of unoccupied valence orbitals n_h to be $n_h = 5$ for Fe^{3+} and $n_h = 7$ and $n_h = 6$ for the Gd^{3+} and Tb^{3+} species. The sum rule related prefactors are 1/2, 2, 2/3 and 7/3 for investigations on the Fe $L_{3,2}$ absorption edges and 1/3, 3/2, 2/3 and 2 for investigations on the Ln $M_{5,4}$ absorption edges[33].
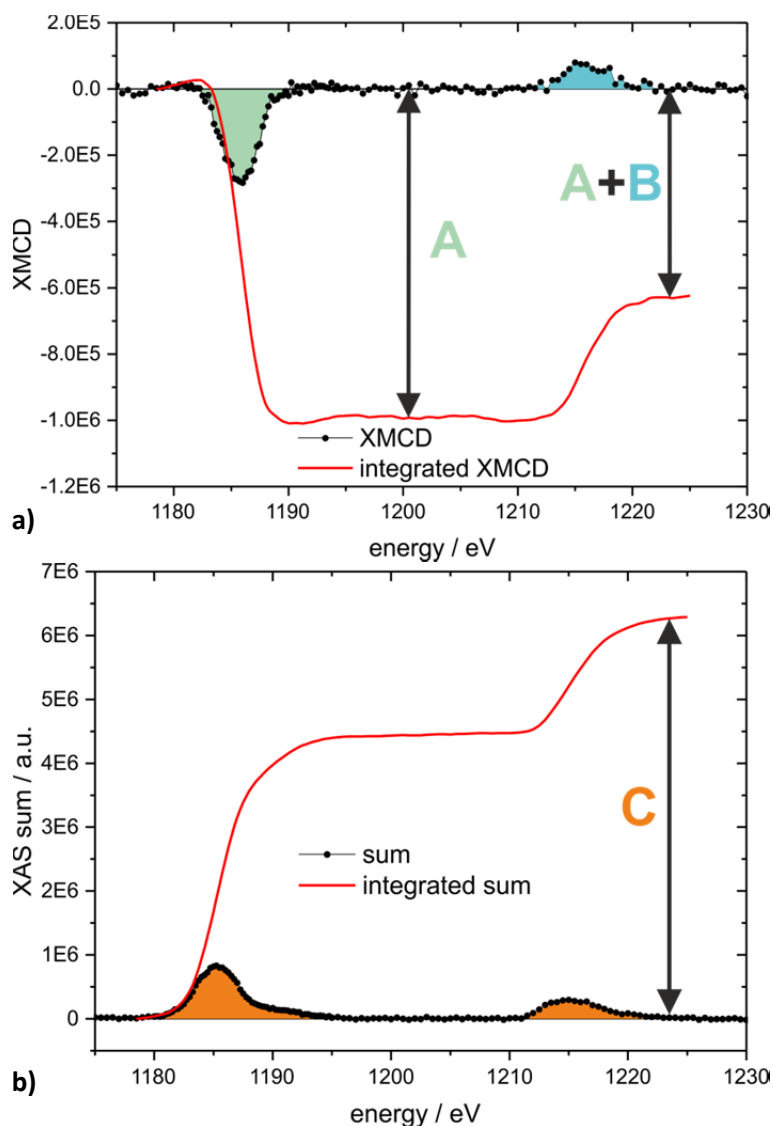
Figure 2 (a) XMCD spectrum and its integral over both ($M_{5,4}$) absorption edges for the $[Fe_4Gd_2]^+$ single molecule magnet of structure type **II.** The integrals over the first and second absorption edge are color coded and named **A** and **B**, respectively.
(b) Integrated sum of both XA spectra for both photon helicities for the $[Fe_4Gd_2]^+$ single molecule magnet of structure type **II**. The integrated area over both absorption edges ($M_{5,4}$) is color coded and labeled **C**.

The color coded elements **A**, **B** and **C** are extracted from the integrals over the XMCD spectra (difference of polarization dependent XA spectra, **A** and **B**) and the respective sum of polarization dependent XA spectra (**C**). We extract the projections ($m_S^{(z)}$ and $m_L^{(z)}$) of the intrinsic spin (m_S) and orbital (m_L) magnetic moments per atom onto the quantization axis by sum rule analysis. The quantization axis coincides with the magnetic field axis of the surrounding solenoid and the X-ray propagation direction. For the presented $[Fe_4Ln_2]^+$ SMMs this was done on the Fe $L_{3,2}$ and the Ln $M_{5,4}$ edges, respectively. The extracted projections of the intrinsic magnetic moments are called magnetizations in the further course of this work. In previous works on transition metal clusters we

scaled these magnetizations to the intrinsic magnetic moments by the Langevin / Brillouin formula[24,28]. Under the given experimental conditions a scaling of the total magnetic moment of the molecule has to be performed[28]. Therefore, knowledge of the exact coupling of all containing magnetic centers is mandatory. This is not known to us. Therefore we omit such a scaling and present magnetizations at the given experimental conditions (B = 5 T, 10 K ≤ T ≤ 15 K).

5.2.4 Results and discussion

The presented polarization dependent XA spectra on the Fe $L_{3,2}$ absorption edges show very small dichroic effects (exemplified in Fig. 3). Within the given ligand field, the containing Fe^{3+} ions are expected to be in a $3d^5$ high spin state[36]. This state contains 5 unpaired electrons which according to Hund´s rules lead to a significant spin magnetic moment per atom (m_S) of 5 μ_B and an orbital magnetic moment per atom of m_L = 0. Such a significant magnetic moment should lead to noticeable dichroic effects on the Fe $L_{3,2}$ absorption edges. This is not the case in our recorded spectra. There are two possible explanations for the found low dichroic effects.
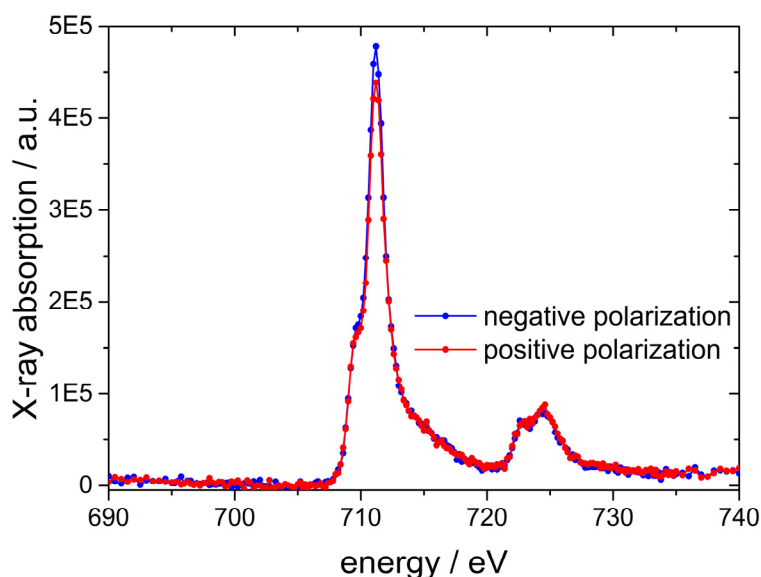
Figure 3 Polarization dependent XAS spectra for negative (blue) and positive (red) circular photon polarization for the $[Fe_4Gd_2]^+$ single molecule magnet of structure type **II.**

At first an insufficient alignment of the magnetic moments of the Fe atoms onto the quantization axis would lead to a decrease in the visible dichroic effect. The found very low dichroic effects would resemble a nearly arbitrary or perpendicular alignment of the Fe magnetic moments. This is highly unlikely under the given experimental conditions (T < 15 K, B = 5 T). Under these conditions, the total magnetic moment should align to the external magnetic field and the X-ray propagation direction, as

the total magnetic moment theoretically only comprises of a spin component, which is highly isotropic.

Another explanation of the found low dichroic effect is an antiferromagnetic coupling of the contained Fe atoms. An antiferromagnetic coupling of 2 Fe atoms at a time would lead to an average magnetic moment equal zero. As the XMCD technique determines the average magnetic moment of all Fe atoms within the molecule, such an average magnetic moment equal zero would lead to a vanishing dichroic effect. Such an antiferromagnetic coupling has already been predicted by earlier magnetic characterizations of similar compounds[36]. Therefore, we conclude on an assignment of an antiferromagnetic coupling. Our gas phase measurements mark this antiferromagnetic coupling as an intrinsic property of the investigated compounds. We find such an antiferromagnetic coupling of the Fe atoms for all investigated compounds ($[Fe_4Gd_2]^+$ I and II, $[Fe_4Tb_2]^+$ I and II; cf. supplementary material, Fig. S1).

The total magnetizations (m_{tot}) extracted by sum rule analysis on the Fe $L_{3,2}$ absorption edges are small (< 0.6 μ_B / atom). The orbital magnetization contributes with ≤ 0.1 μ_B per atom and is constant for all investigated species within experimental uncertainties. The orbital magnetic moment would vanish by a pure $3d^5$ configuration. Instead there are non-zero values overlaping within experimental uncertainties. Possible mixing of excited states with $m_L \neq 0$ with the ground state of Fe^{3+} may introduce some orbital angular momentum.
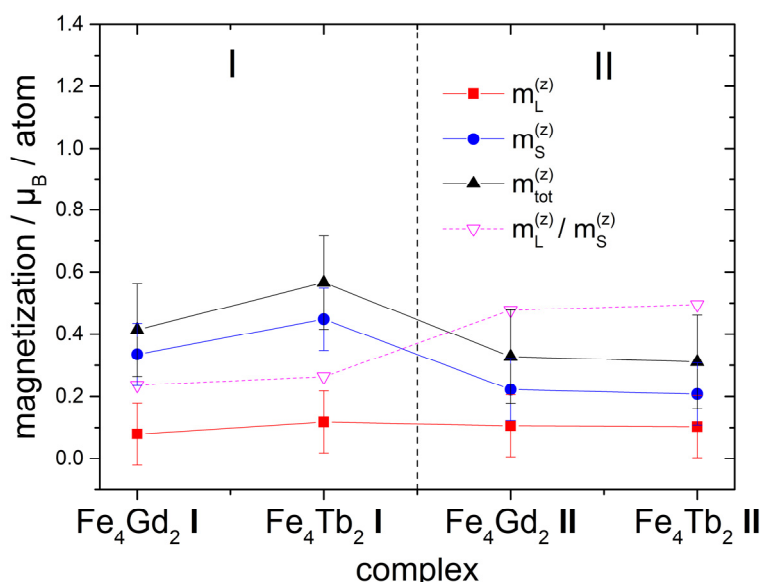
Figure 4 Measured spin ($m_S^{(z)}$, filled blue circles), orbital ($m_L^{(z)}$, filled red squares) and total ($m_{tot}^{(z)}$, filled black triangles) magnetizations and the $m_L^{(z)}$ to $m_S^{(z)}$ ratio (open purple triangles) on the Fe atoms within the investigatd $[Fe_4Ln_2]^+$ single molecule magnets of structure types **I** and **II.**

5. Spin and orbital magnetic moments of isolated Single Molecule Magnets

The recorded spin magnetization is larger than the recorded orbital magnetization (0.2 - 0.4 μ_B / atom). It is considerably lower than the intrinsic spin magnetic moment of an isolated Fe^{3+} ion in a $3d^5$ high spin configuration (m_S = 5 μ_B / atom). This reduction is due to the above described antiferromagnetic coupling. The remaining spin does not change in magnitude by exchange of the Ln atoms, within experimental uncertainties. This is the case for both investigated structures **I** and **II**. The structures themselves of the investigated SMMs show noticeable influences on the detected magnetization. Despite the known enhancement of uncertainties of the spin sum rule in the case of $3d^5$ materials (~ 30 %)[33,34], the recorded differences are considerable. The spin magnetization drops from an average m_s = 0.35 μ_B / atom for structure type **I** to an average 0.2 μ_B / atom for structure type **II**. These changes in the remaining spin magnetization may be due to a structure induced alteration of the antiferromagnetic coupling or a change in alignment of the spin magnetic moment to the external magnetic field. Both reasons are well considerable as of now.

By virtue of our novel technique we deduce that the magnetization on the Fe atoms is less affected by the very nature of the neighboring lanthanides but instead by the species ligand structure. Sum rule analysis allows us to ascribe these changes in magnetization to changes of the magnetization of the spin. The orbital magnetization is not altered at all.

The polarization dependent XA spectra on the Gd and Tb $M_{5,4}$ absorption edges show distinct dichroic effects (exemplified for structure type **II** in Fig. 5, for structure type **I** cf. Fig. S2). These findings in their own lead to the conclusion, that the total magnetization of the investigated molecules is dominated by the contributions from the contained lanthanide atoms. There are noticeable differences in the dichroic effects between the XA spectra for Gd and Tb, especially on the M_4 absorption edge. There is no noticeable difference between the different structure types in the recorded spectra. In contrast to the Fe atoms the structure seems to have little to no influence on the lanthanides´ magnetizations.
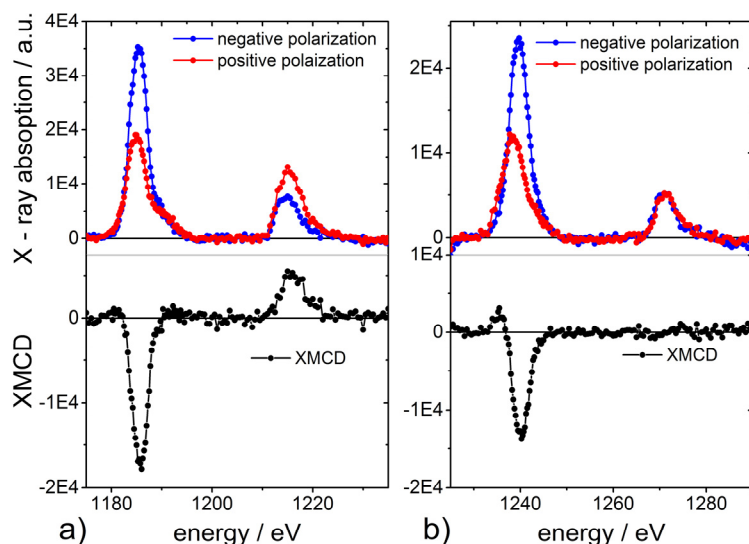
Figure 5 Polarization dependent XA spectra for negative (blue) and positive (red) circular photon polarization and the resulting XMCD spectra (black) on the **a)** Gd $M_{5,4}$ and **b)** Tb $M_{5,4}$ absorption edges for the $[Fe_4Gd_2]^+$ and the $[Fe_4Tb_2]^+$ single molecule magnet of structure type **II.**

Sum rule analysis of the given dichroic effects shows significant differences in the spin and orbital magnetization for the two containing lanthanides. The difference in structure has no influence on the magnetization of the lanthanides. The spin and orbital magnetizations for both structure types compare well within experimental uncertainties. We assumed a high spin state for both lanthanides giving a number of unoccupied valence orbitals (n_h) of $n_h = 7$ for Gd and $n_h = 6$ for Tb for the given spin and orbital magnetizations by sum rule analysis. For both structure types, the spin magnetization drops from about 3.75 μ_B / atom to about 2 μ_B / atom when going from the Gd to the Tb species. The orbital magnetization increases from an average 1.2 μ_B / atom to 2 μ_B / atom. For the high spin state, the electron configuration of the Gd^{3+} ($4f^7$) and Tb^{3+} ($4f^8$) species predict a spin magnetic moment of 7 and 6 μ_B / atom and an orbital magnetic moment of 0 and 3 μ_B / atom. As mentioned above, we omit scaling of our magnetizations as obtained by sum rule analysis to intrinsic magnetic moments. Therefore a direct comparison with the values deduced by Hund´s rule is not possible. An entity that enables indirect comparison is the m_L to m_S ratio. Choosing the m_L to m_S ratio as means of comparison also omits errors by the choice of n_h values.
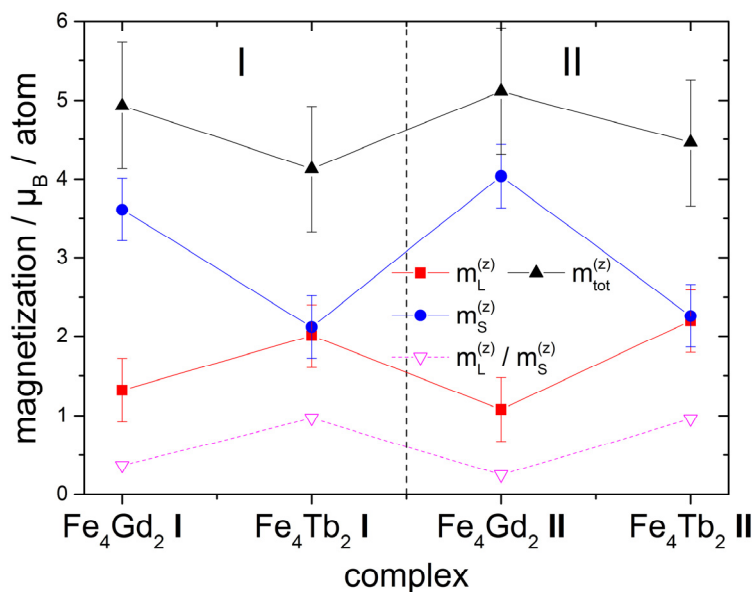
Figure 6 Spin ($m_S^{(z)}$, filled blue circles), orbital ($m_L^{(z)}$, filled red squares) and total ($m_{tot}^{(z)}$, filled black triangles) magnetizations and the $m_L^{(z)}$ to $m_S^{(z)}$ ratio (open purple triangles) on the Ln atoms within the investigatd [Fe$_4$Ln$_2$] single molecule magnets of structure types **I** and **II**.

The predicted m_L to m_S ratio is zero in case of the Gd species. Our measurements reveal m_L / m_S = 0.32. For the Tb species the predicted m_L to m_S ratio is 0.5. We find a value of 1 by our XMCD measurements. In both cases we find enhancement with respect to the predictions by Hund´s rule. There is no obvious explanation for the found increased m_L / m_S ratios as surrounding ligand fields are known to have only little influence on the single atom / ion electron configurations of 4f elements[37]. In the following passages we discuss seven possible explanations and their likelihood for our findings of increased m_L / m_S ratios are discussed.

1.) There might be a spin state different to the predicted high spin state for the investigated lanthanides. In the Gd species for example, pairing 2 of the electrons (unpaired in the high spin case) would lead to a significant reduction of the spin magnetic moment of 2 μ_B. It would give rise to a persistent orbital magnetic moment by an uneven population of different m_l (quantum number) states. This would lift the spherical symmetry of the half-filled 4f orbitals and a non-vanishing orbital magnetic moment would arise. A similar scenario would explain the increase of the m_L to m_S ratio in the case of the Tb species. It is, however, rather unlikely that the ligand field alters the high spin state of the pure ion to form a different spin state. As mentioned above, surrounding ligand fields are known to have only minor effects on the interior 4f orbitals. Furthermore, as complex **I** and **II** show the same magnetizations for both the Gd and Tb species in 2 different ligand fields, it is rather unlikely that similar magnetization occurs by coincidence.

2.) There might be another possible explanation. It is the coexistence of a high and a low spin state within the investigated ions in our ion trap. Our XMCD technique investigates the average over all irradiated molecules. A conceivable coexistence of a low and a high spin state would lead to an average magnetization with a reduced spin magnetic moment. It would, however, lead to an orbital magnetic moment that was increased with respect to the high spin state. An assessment of the possibility of the above described coexistence of a high and a low spin state requires the knowledge of energetic differences between these two states, which might be gained from theoretical investigations. As our experiments are conducted at very low temperatures (~ 15 K), the energy available to populate a configuration different from the ground state is very low (< 1 kJ / mol). This makes a population of two different states rather unlikely.

3.) It is also conceivable that mixing of exited states into the ground state might alter the magnetic moments of this state. Theoretical investigations of the given compounds could serve to clarify the feasibility of such a mixing of states.

4.) A possible reduction or oxidation of the Ln atoms may alter the investigated spin and orbital magnetizations. In the Gd case a reduction and oxidation would lead to a lower spin magnetic moment (either due to spin pairing or due to loss of an unpaired electron). Reduction and oxidation would induce some degree of orbital magnetization due to breaking the spherical symmetry of the 4f orbitals. Such a redox reaction might have taken place during the electrospray ionization process. An unambiguous assignment of the Ln oxidation state in our XAS is not possible due to the insufficient spectral resolution. As the m / z ratio of the investigated ions is known in our mass spectrometric investigations, a general reduction or oxidation of the molecule can be excluded. The assumed redox reaction of the lanthanides has to involve the neighboring atoms. A redox reaction involving the Fe atoms is unlikely, as the XA spectra recorded on the Fe $L_{3,2}$ absorption edges show the distinct features of a Fe^{3+} species. Furthermore a reduced ($3d^6$) or oxidized ($3d^4$) Fe species would maintain distinct orbital magnetic moments which cannot be found in our XMCD investigations. Therefore such a redox reaction would have to involve the surrounding ligands e.g. by a metal to ligand charge transfer (MLCT). Future experiments using higher resolution XAS may serve to elucidate the exact oxidation state of the Ln within the investigated complexes. In general for the Gd^{3+} species a change in the oxidation state seems not preferable as the $4f^7$ configuration with its half-filled 4f shell presents a comparatively stable electron configuration. A change in oxidation state would lead to a significant increase in the internal energy of the molecule.

5.) For the Tb species a reduction (e.g. in the ESI process) would explain the found increase of m_L / m_S ratio with respect to the predicted value of 0.5. An oxidation would form a $4f^7$ ground state similar to the Gd^{3+} ion leading to m_L / m_S = 0. The found m_L / m_S = 1 disproves a possible oxidation in

the ESI process. A reduction of the Tb^{3+} species on the other hand would explain the found increase in m_L / m_S ratio. Adding another electron would lead to further pairing of electrons which results in a reduced spin magnetic moment. This would also lead to a higher anisotropy in the 4f electron distribution and would increase the detectable orbital magnetic moment. A reduction during the ESI process is rather unlikely as the applied spray needle voltage ranges between 3 and 3.5 kV. Such conditions would rather promote oxidation than reduction. Therefore a possible reduction of the lanthanide ions has to be caused by an interplay with the surrounding atoms. As for the Gd species, an unambiguous assignment of the Ln oxidation state in our XAS is not possible due to the insufficient spectral resolution. A redox reaction involving the Fe atoms is unlikely, as the XA spectra recorded on the Fe $L_{3,2}$ absorption edges show the distinct features of a Fe^{3+} species.

6.) Next to a nominal reduction or oxidation of the Ln^{3+} species, partial electron transfer from different negatively charged surrounding ligands into the 4f orbitals might lead to the found increased m_L / m_S ratios as well. In this case the explanation of reduced spin and increased orbital magnetic moments would be analog to the elaborations for a nominal reduction above. Electron transfer from the surrounding ligands into the 4f orbitals is also rather unlikely as the 4f shell is contracted further than e.g. the 6s and p orbitals. If electron transfer from the ligands to the metal is detected the transferred electrons - if anything - would populate the 6s and p orbitals and not the 4f states[38].

7.) Another possible influence on the found spin and orbital contributions to the total magnetic moment is the formation of the cationic species as necessary in the course of mass spectrometric investigations. For all species a negatively charged ligand (($C(CH_3)_3COO)^-$ for structure type **I** and $(NO_3)^-$ for structure type **II**) is swapped for a neutral acetonitrile ligand.

None of the above stated, seven conceivable approaches can unambiguously explain the found increased m_L / m_S ratios. Further investigations e.g. the determination of the exact oxidation state by high resolution XAS spectroscopy and computational investigations on the investigated cationic species in comparison to the neutral SMM would help to find a more definite assignment. A better understanding and validation of our XMCD results could be achieved by theoretical investigations of the presented $[Fe_4Ln_2]^+$ SMMs and the respective spin states of the containing lanthanides, e.g. by a broken symmetry approach[39,40]. Such calculations exceed our area of expertise and have therefore not been performed in the course of this work.

Our measurements in general reproduced the anticipated trends along the row of Gd to Tb species (i.e. stepwise increase of the 4f orbitals occupation). Adding one electron assuming a half occupied $4f^7$ configuration (pure or non-pure high spin state) leads to (initial or additional) pairing of electrons.

This leads to a decreased spin magnetic moment. The orbital magnetic moment increases due to initial or further distortion of the spherical symmetry of the 4f orbitals.

5.2.5 Conclusion

In the presented work, we investigate the intrinsic spin and orbital magnetic moments of isolated single molecule magnets of the $[Fe_4Ln_2]$-type (Ln = Gd, Tb). The element selectivity of the used XMCD technique allows a separation of the total magnetic moments of these compounds into the contributions from the different contained metals. We find that the total magnetic moment is dominated by the contributions from the different lanthanides. Sum rule analysis of the recorded XMCD spectra furthermore allows for a separation of these different contributions into their spin and orbital magnetic moments.

The recorded spectra on the Fe adsorption edges show only very small dichroic effects, which can be attributed to an antiferromagnetic coupling of the Fe atoms. The reported spin and orbital contributions are well in line with the assumed $3d^5$ high spin configuration of the Fe atoms showing a total magnetic moment dominated by the spin magnetic moment. Investigating the influences of neighboring Ln atoms and system structure onto the magnetic moments of the Fe atoms showed little to now influence form the different lanthanides but distinct differences for the two structure types investigated.

The reported XA spectra and respective XMCD spectra on the Ln $M_{5,4}$ absorption edges show much more pronounced dichroic effects. We find distinct differences in these dichroic effects comparing the results on Gd and Tb containing complexes. These differences in the reported spectra certainly reflect in different ratios of the spin and orbital contributions to the total magnetic moment (m_L / m_S = 0.3 for Gd and m_L / m_S = 1 for Tb). The reported m_L / m_S values are not influenced by the different structures of the molecules. Compared to predictions form Hund´s rule, we find significant enhancement of these m_L / m_S ratios. We present possible explanations for such increase m_L / m_S ratios and discuss their feasibility, a detailed explanation pending and presenting a challenge for contemporary computaions.

In summary, we have shown that gas phase XMCD investigations add valuable additional insight into the highly interesting magnetic properties of single molecule magnets.

5.2.6 References

[1]   Carra, P.; Thole, B. T.; Altarelli, M.; Wang, X. D., *X-RAY CIRCULAR-DICHROISM AND LOCAL MAGNETIC-FIELDS*, *Physical Review Letters* **1993**, *70*, 694.

[2]   Thole, B. T.; Carra, P.; Sette, F.; Vanderlaan, G., *X-RAY CIRCULAR-DICHROISM AS A PROBE OF ORBITAL MAGNETIZATION*, *Physical Review Letters* **1992**, *68*, 1943.

[3]   Tischer, M.; Hjortstam, O.; Arvanitis, D.; Hunter Dunn, J.; May, F.; Baberschke, K.; Trygg, J.; Wills, J. M.; Johansson, B.; Eriksson, O., *ENHANCEMENT OF ORBITAL MAGNETISM AT SURFACES: CO ON CU(100)*, *Physical Review Letters* **1995**, *75*, 1602.

[4]   Baberschke, K., *THE MAGNETISM OF NICKEL MONOLAYERS*, *Applied Physics A* **1996**, *62*, 417.

[5]   Chen, C. T.; Idzerda, Y. U.; Lin, H. J.; Smith, N. V.; Meigs, G.; Chaban, E.; Ho, G. H.; Pellegrin, E.; Sette, F., *EXPERIMENTAL CONFIRMATION OF THE X-RAY MAGNETIC CIRCULAR DICHROISM SUM RULES FOR IRON AND COBALT*, *Physical Review Letters* **1995**, *75*, 152.

[6]   Bornemann, S.; Šipr, O.; Mankovsky, S.; Polesya, S.; Staunton, J. B.; Wurth, W.; Ebert, H.; Minár, J., *TRENDS IN THE MAGNETIC PROPERTIES OF FE, CO, AND NI CLUSTERS AND MONOLAYERS ON IR(111), PT(111), AND AU(111)*, *Physical Review B* **2012**, *86*, 104436.

[7]   Dhesi, S. S.; Dudzik, E.; Dürr, H. A.; Brookes, N. B.; van der Laan, G., *CORRELATION BETWEEN L3 ABSORPTION SATELLITE INTENSITY AND SPIN MOMENT IN ULTRATHIN NI FILMS*, *Surface Science* **2000**, *454–456*, 930.

[8]   Baniodeh, A.; Mereacre, V.; Magnani, N.; Lan, Y.; Wolny, J. A.; Schuenemann, V.; Anson, C. E.; Powell, A. K., *PARA VERSUS META LIGAND SUBSTITUENTS AS A MEANS OF DIRECTING MAGNETIC ANISOTROPY IN FE₂DY₂ COORDINATION CLUSTERS*, *Chem. Commun. (Cambridge, U. K.)* **2013**, *49*, 9666.

[9]   Bansmann, J.; Kleibert, A.; Getzlaff, M.; Rodriguez, A. F.; Nolting, F.; Boeglin, C.; Meiwes-Broer, K.-H., *MAGNETISM OF 3D TRANSITION METAL NANOPARTICLES ON SURFACES PROBED WITH SYNCHROTRON RADIATION - FROM ENSEMBLES TOWARDS INDIVIDUAL OBJECTS*, *Physica Status Solidi B-Basic Solid State Physics* **2010**, *247*, 1152.

[10]   Kleibert, A.; Passig, J.; Meiwes-Broer, K. H.; Getzlaff, M.; Bansmann, J., *STRUCTURE AND MAGNETIC MOMENTS OF MASS-FILTERED DEPOSITED NANOPARTICLES*, *Journal of Applied Physics* **2007**, *101*, 114318.

[11]   Gambardella, P.; Rusponi, S.; Veronese, M.; Dhesi, S. S.; Grazioli, C.; Dallmeyer, A.; Cabria, I.; Zeller, R.; Dederichs, P. H.; Kern, K.; Carbone, C.; Brune, H., *GIANT MAGNETIC ANISOTROPY OF SINGLE COBALT ATOMS AND NANOPARTICLES*, *Science* **2003**, *300*, 1130.

[12]   Durr, H. A.; Dhesi, S. S.; Dudzik, E.; Knabben, D.; van der Laan, G.; Goedkoop, J. B.; Hillebrecht, F. U., *SPIN AND ORBITAL MAGNETIZATION IN SELF-ASSEMBLED CO CLUSTERS ON AU(111)*, *Physical Review B* **1999**, *59*, R701.

[13]   Edmonds, K. W.; Binns, C.; Baker, S. H.; Thornton, S. C.; Norris, C.; Goedkoop, J. B.; Finazzi, M.; Brookes, N. B., *DOUBLING OF THE ORBITAL MAGNETIC MOMENT IN NANOSCALE FE CLUSTERS*, *Physical Review B* **1999**, *60*, 472.

[14]   Pietzsch, O.; Kubetzka, A.; Bode, M.; Wiesendanger, R., *SPIN-POLARIZED SCANNING TUNNELING SPECTROSCOPY OF NANOSCALE COBALT ISLANDS ON CU(111)*, *Physical Review Letters* **2004**, *92*, 057202.

[15]   Glaser, L.; Chen, K.; Fiedler, S.; Wellhöfer, M.; Wurth, W.; Martins, M., *MAGNETIC PROPERTIES OF SMALL SIZE-SELECTED CO AND COPT CLUSTERS ON NI*, *Physical Review B* **2012**, *86*, 075435.

[16]   Lau, J. T.; Föhlisch, A.; Martins, M.; Nietubyc, R.; Reif, M.; Wurth, W., *SPIN AND ORBITAL MAGNETIC MOMENTS OF DEPOSITED SMALL IRON CLUSTERS STUDIED BY X-RAY MAGNETIC CIRCULAR DICHROISM SPECTROSCOPY*, *New Journal of Physics* **2002**, *4*, 98.

[17]   Lau, J. T.; Föhlisch, A.; Nietubyc̀, R.; Reif, M.; Wurth, W., *SIZE-DEPENDENT MAGNETISM OF DEPOSITED SMALL IRON CLUSTERS STUDIED BY X-RAY MAGNETIC CIRCULAR DICHROISM*, *Physical Review Letters* **2002**, *89*, 057201.

[18]   Fauth, K.; Hessler, M.; Batchelor, D.; Schutz, G., *STRONG INFLUENCE OF DEFECTS ON THE ELECTRONIC STRUCTURE OF PT ADATOMS AND CLUSTERS ON GRAPHITE*, *Surface Science* **2003**, *529*, 397.

[19]   Ballentine, G.; Heßler, M.; Kinza, M.; Fauth, K., *Superparamagnetism in small Fe clusters on Cu(111)*, *The European Physical Journal D* **2007**, *45*, 535.

[20]   Wurth, W.; Martins, M., *Electronic structure and magnetic properties of small deposited transition metal clusters*, *Chem. Phys. Solid Surf.* **2007**, *12*, 471.

[21]   Eelbo, T.; Waśniowska, M.; Thakur, P.; Gyamfi, M.; Sachs, B.; Wehling, T. O.; Forti, S.; Starke, U.; Tieg, C.; Lichtenstein, A. I.; Wiesendanger, R., *Adatoms and Clusters of 3d Transition Metals on Graphene: Electronic and Magnetic Configurations*, *Physical Review Letters* **2013**, *110*, 136804.

[22]   Gambardella, P.; Dhesi, S. S.; Gardonio, S.; Grazioli, C.; Ohresser, P.; Carbone, C., *Localized magnetic states of Fe, Co, and Ni impurities on alkali metal films*, *Physical Review Letters* **2002**, *88*.

[23]   Brune, H.; Gambardella, P., *Magnetism of individual atoms adsorbed on surfaces*, *Surface Science* **2009**, *603*, 1812.

[24]   Peredkov, S.; Neeb, M.; Eberhardt, W.; Meyer, J.; Tombers, M.; Kampschulte, H.; Niedner-Schatteburg, G., *Spin and Orbital Magnetic Moments of Free Nanoparticles*, *Physical Review Letters* **2011**, *107*.

[25]   Peredkov, S.; Savci, A.; Peters, S.; Neeb, M.; Eberhardt, W.; Kampschulte, H.; Meyer, J.; Tombers, M.; Hofferberth, B.; Menges, F.; Niedner-Schatteburg, G., *X-ray absorption spectroscopy of mass-selected transition metal clusters using a cyclotron ion trap: An experimental setup for measuring XMCD spectra of free clusters*, *Journal of Electron Spectroscopy and Related Phenomena* **2011**, *184*, 113.

[26]   Zamudio-Bayer, V.; Hirsch, K.; Langenberg, A.; Niemeyer, M.; Vogel, M.; Lawicki, A.; Terasaki, A.; Lau, J. T.; von Issendorff, B., *Maximum Spin Polarization in Chromium Dimer Cations as Demonstrated by X-ray Magnetic Circular Dichroism Spectroscopy*, *Angewandte Chemie (International ed. in English)* **2015**, *54*, 4498.

[27]   Hirsch, K.; Zamudio-Bayer, V.; Langenberg, A.; Niemeyer, M.; Langbehn, B.; Moeller, T.; Terasaki, A.; von Issendorff, B.; Lau, J. T., *Magnetic Moments of Chromium-Doped Gold Clusters: The Anderson Impurity Model in Finite Systems*, *Physical Review Letters* **2015**, *114*.

[28]   Langenberg, A.; Hirsch, K.; Lawicki, A.; Zamudio-Bayer, V.; Niemeyer, M.; Chmiela, P.; Langbehn, B.; Terasaki, A.; Issendorff, B. V.; Lau, J. T., *Spin and orbital magnetic moments of size-selected iron, cobalt, and nickel clusters*, *Physical Review B* **2014**, *90*.

[29]   D. Gatteschi, R. S., J. Villain *Molecular Nanomagnets*; Oxford University Press: Oxford, 2006.

[30]   Aromí, G.; Winpenny, R. E. *Single-molecule magnets and related phenomena*; Springer New York, 2006.

[31]   Leuenberger, M. N.; Loss, D., *Quantum computing in molecular magnets*, *Nature* **2001**, *410*, 789.

[32]   Aromí, G.; Aguila, D.; Gamez, P.; Luis, F.; Roubeau, O., *Design of magnetic coordination complexes for quantum computing*, *Chemical Society Reviews* **2012**, *41*, 537.

[33]   Schütz, G.; Goering, E.; Stoll, H., *Synchrotron Radiation Techniques Based on X-ray Magnetic Circular Dichroism*, *Handbook of Magnetism and Advanced Magnetic Materials* **2007**.

[34]   Piamonteze, C.; Miedema, P.; De Groot, F. M., *Accuracy of the spin sum rule in XMCD for the transition-metal L edges from manganese to copper*, *Physical Review B* **2009**, *80*, 184410.

[35]   Jo, T., *The 3d–4f exchange interaction, X-ray second-order optical processes and the magnetic circular dichroism (MCD) spin sum rule in rare earths*, *Journal of electron spectroscopy and related phenomena* **1997**, *86*, 73.

[36]   Schmidt, S.; Prodius, D.; Novitchi, G.; Mereacre, V.; Kostakis, G. E.; Powell, A. K., *Ferromagnetic heteronuclear {Fe-4(Er,Lu)(2)} cyclic coordination clusters based on ferric wheels*, *Chemical Communications* **2012**, *48*, 9825.

[37]   Rinehart, J. D.; Long, J. R., *Exploiting single-ion anisotropy in the design of f-element single-molecule magnets*, *Chemical Science* **2011**, *2*, 2078.

[38]   Baniodeh, A.; Lan, Y. H.; Novitchi, G.; Mereacre, V.; Sukhanov, A.; Ferbinteanu, M.; Voronkova, V.; Anson, C. E.; Powell, A. K., *Magnetic anisotropy and exchange coupling in a family of isostructural Fe(2)(III)Ln(2)(III) complexes*, *Dalton Transactions* **2013**, *42*, 8926.

5.2.7 Supplementary material to "Spin and orbital magnetic moments of isolated [Fe$_4$Ln$_2$]$^+$ single molecule magnets by X-ray magnetic circular dichroism"

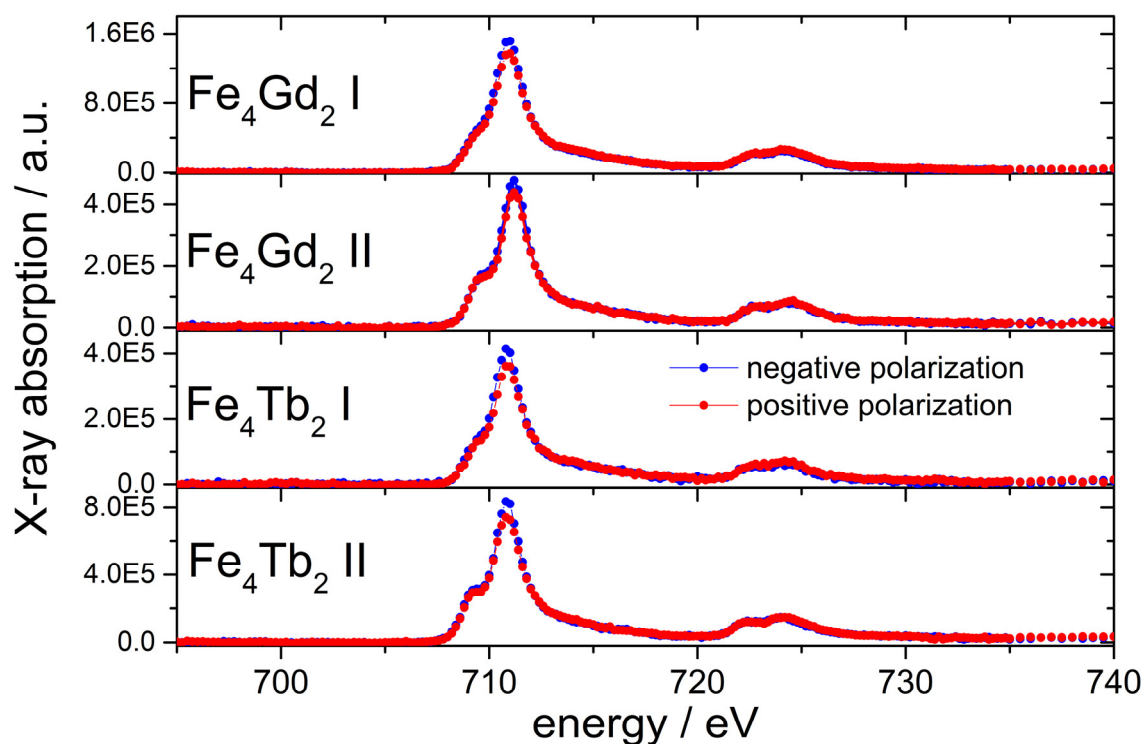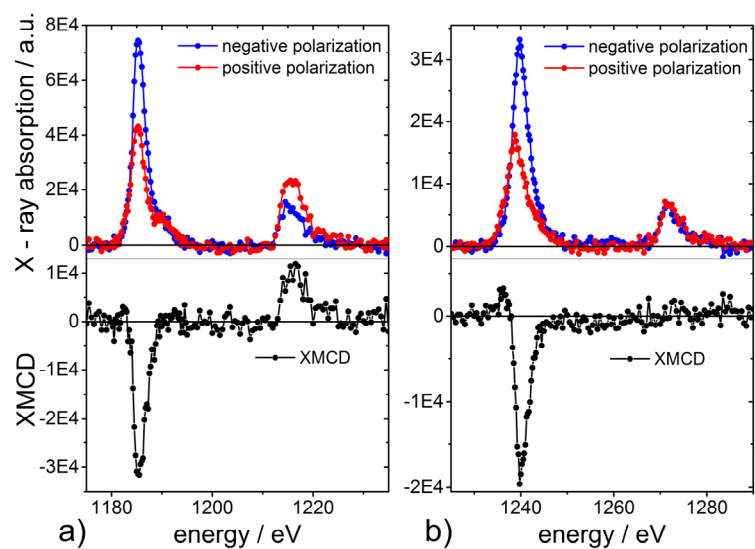**Figure S1** Polarization dependent XA spectra for negative (blue) and positive (red) circular photon polarization for the [Fe$_4$Gd$_2$]$^+$ and [Fe$_4$Tb$_2$]$^+$ single molecule magnets of structure types **I** and **II.**

Figure S2 Polarization dependent XA spectra for negative (blue) and positive (red) circular photon polarization and the resulting XMCD spectra (black) on the **a)** Gd $M_{5,4}$ and **b)** Tb $M_{5,4}$ absorption edges for the $[Fe_4Gd_2]^+$ and the $[Fe_4Tb_2]^+$ single molecule magnet of structure type **I.**

6. SUMMARY AND OUTLOOK

In the present work, magnetic moments of isolated Single Molecule Magnets (SMMs) and transition metal clusters were investigated. Gas phase X-ray Magnetic Circular Dichroism (XMCD) in combination with sum rule analysis served to separate the total magnetic moments of the investigated species into their spin and orbital contributions. Two different mass spectrometry based setups were used for the presented investigations on transition metal clusters (GAMBIT-setup) and on single molecule magnets (NanoClusterTrap). Both experiments were coupled to the UE52-PGM beamline at the BESSY II synchrotron facility (Helmholtz Zentrum Berlin) which provided the necessary polarized X-ray photons. The investigation of the given compounds as isolated molecules in the gas phase enabled a determination of their intrinsic magnetic properties void of any influences of e.g. a surrounding bulk or supporting surface.

The investigation of isolated cationic Fe_n^+ ($7 \leq n \leq 16$ and $n = 18$), Co_n^+ ($8 \leq n \leq 17$ and $n = 19, 22$) and Ni_n^+ ($7 \leq n \leq 17$) transition metal clusters revealed spin and orbital magnetic moments that are enhanced with respect to their respective bulk values and, at the same time, quenched with respect to the magnetic moments of the pure atom. Comparison of the present data to an independent experiment shows only minor deviations. It serves for an independent verification of the spin and orbital contributions of magnetic moments in cationic iron, cobalt and nickel clusters by the XMCD technique. As transition metal clusters bridge the gap between the isolated atom and the bulk, we investigate the applicability of possible scaling laws onto the spin and orbital contributions. In both cases (for the spin and orbital magnetic moments) we found a $n^{-1/3}$ size dependency. In the case of the spin magnetic moment this dependency interpolates between the atom and the bulk value. In the case of the orbital magnetic moment such a scaling law is only applicable when interpolating between the bulk and the diatomic value. This in the first instance unusual choice of reference point is rationalized by recalling the very nature of "primary" atomic orbital moments and "secondary" spin-orbit-coupling induced orbital moments in clusters, the former being quenched in aggregates through loss of symmetry and concomitant loss of orbital degeneracies.

The influence of doping a pure cobalt cluster with a 4d transition metal (Au, Rh) onto the spin and orbital magnetic moments of this pure cobalt clusters was investigated. This was done by recording and comparing the spin and orbital magnetic moments of cationic $[Co_nAu]^+$ and $[Co_nRh]^+$ ($8 \leq n \leq 14$)

6. Summary and outlook

clusters to the spin and orbital magnetic moments of the pure cobalt clusters. This comparison revealed spin and orbital magnetic moments that were increased as well as decreased with respect to the to the pure cluster. There is no general trend. Instead, the recorded values vary strongly by the specific cluster size. Some cluster sizes showed remarkable changes in the recorded spin and orbital magnetic moments. The $[Co_{12}Rh]^+$ cluster, for example, showed an orbital magnetic moment twice as large as the orbital magnetic moment of the pure Co_{13}^+ cluster. A detailed explanation pending, this found increased orbital magnetic moment was attributed to a change in cluster geometry due to Rh doping.

Next to the investigation of isolated transition metal clusters, the present work focuses on the magnetic moments of isolated single molecule magnets in the gas phase. The presented polarization dependent X-ray Absorption (XA) and respective XMCD spectra resemble the first gas phase magnetic characterization of an isolated SMM. As SMMs maintain their highly interesting magnetic properties even as isolated molecules, our gas phase investigation served to record their intrinsic magnetic properties without the interference of a surrounding bulk or supporting substrate.

The first SMM investigated was the archetypal Mn_{12}-acetate ($[Mn_{12}O_{12}(CH_3COO)_{16}(H_2O)_4]$ in short $[Mn_{12}ac]$). The present polarization dependent XA spectra showed distinct dichroic effects on the recorded Mn $L_{3,2}$ absorption edges. We attribute this dichroic effect to a persistent magnetic moment of the $[Mn_{12}ac]$ as an isolated molecule. We did perform a qualitative analysis of spin and orbital magnetic moments in the case of $[Mn_{12}ac]$ due to the limitations of sum rule analysis when applied to early transition metals such as Mn. A comparison of the presented gas phase XMCD spectrum to prior measurements on a $[Mn_{12}ac]$ bulk sample revealed an outermost good agreement between both investigations. This led to the conclusion that the intrinsic magnetic properties of the isolated species are not or only minimally altered by bulk formation. One minor discrepancy between the bulk and the gas phase spectrum was attributed to possible small amounts of radiation damage in the bulk phase experiments. In the presented work, radiation damage was excluded by continuous exchange of molecules in our gas phase experiment. In the presented work we did not investigate the very $[Mn_{12}ac]$ complex but a positively charged derivative ($[Mn_{12}O_{12}(CH_3COO)_{15}CH_3CN]^+$ in short $[Mn_{12}ac]^+$). The issue of possible changes in the magnetic properties of the very $[Mn_{12}ac]^+$ was addressed by Broken Symmetry Density Functional Theory (BS-DFT) calculations. Comparison of the spin density distributions and the internal atomic distances for the energetic minimum structures of $[Mn_{12}ac]$ and $[Mn_{12}ac]^+$ revealed little to no differences in the magnetic structure of both compounds. Therefore the presented magnetic properties of the investigated $[Mn_{12}ac]^+$ could be attributed to the intrinsic properties of the very $[Mn_{12}ac]$.

The second class of investigated SMMs was of a $[Fe_4Ln_2]$ type (Ln = Gd, Tb). Next to the variation of the containing lanthanide two different structure types were investigated (structure type **I**: $[Fe_4Ln_2(N_3)_6(N(C_2H_4OH)(C_2H_4O)_2)_4(C(CH_3)_3COO)_4]$ and structure type **II**: $[Fe_4Ln_2O_2((CH_3)_3CCOO)_4$ $(NO_3)_2(H_3C_3N(C_2H_4O)_2)_4])$. Again, these compounds were investigated as cationic species (structure type **I**: $[Fe_4Ln_2(N_3)_6(N(C_2H_4OH)(C_2H_4O)_2)_4(C(CH_3)_3COO)_3CH_3CN]^+$ and structure type **II**: $[Fe_4Ln_2O_2((CH_3)_3CCOO)_4(NO_3)_1(H_3C_3N(C_2H_4O)_2)_4CH_3CN]^+$). The element selectivity of the XMCD technique allowed for a separation of the total magnetic moment of the molecules into the contributions from the different containing metals. This was done by recording the XAS and respective XMCD spectra on the different element specific absorption edges ($L_{3,2}$ for Fe and $M_{5,4}$ for Gd and Tb).

Despite the assumed $3d^5$ high spin configuration of the Fe atoms, the recorded XA spectra showed very small dichroic effects. This finding was attributed to an antiferromagnetic coupling of the containing Fe atoms. The recorded spin and orbital contributions revealed a total magnetic moment dominated by the spin contribution, the orbital contribution being almost zero. This finding is well in line with a predicted high spin configuration of the Fe atoms. Comparison of the recorded magnetizations for the compounds containing different neighboring lanthanides showed that the investigated lanthanides had little to no effect on the spin and orbital magnetization of the Fe atoms. On the other hand, variation of stabilizing ligands (structures **I** and **II**) induced small but distinct differences in the spin magnetization, the orbital magnetization remaining unaffected.

The dichroic effects on the recorded $M_{5,4}$ Ln absorption edges were much more pronounced than the dichroic effects recorded on the Fe absorption edges. This led to the conclusion that the total magnetic moment of the investigated SMMs is dominated by the contributions of the different lanthanides. The dichroic effects in the respective XA spectra on the Gd and Tb $M_{5,4}$ absorption edges showed distinct differences especially at the M_4 absorption edge. This difference was reflected in the different spin and orbital contributions for the two containing lanthanides. The Gd species revealed a ratio of spin ($m_S^{(z)}$) and orbital ($m_L^{(z)}$) magnetization of $m_L^{(z)} / m_S^{(z)} = 0.3$ whereas the Tb species showed $m_L^{(z)} / m_S^{(z)} = 1$. These values were found for both investigated structure types, leading to the conclusion that the molecules' structure had little to no influence onto the magnetization of the lanthanides. Comparison of the found $m_L^{(z)} / m_S^{(z)}$ ratios to Hund's rule predictions ($m_L^{(z)} / m_S^{(z)} = 0$ for Gd and $m_L^{(z)} / m_S^{(z)} = 0.5$ for Tb) revealed a significant increase in $m_L^{(z)} / m_S^{(z)}$ ratios for the investigated lanthanides. Possible explanations and their feasibility were discussed such as oxidation or reduction of the lanthanides, the (co)existence of a non-pure high spin state as well as partial electron transfer from the surrounding ligands onto the lanthanides and the influence of ion formation a detailed explanation still pending. Contemporary theoretical investigations, e.g. BS-DFT calculations may

serve in the future to determine the magnetic structure. Future high resolution XA spectra may serve to determine the exact oxidation state of the investigated molecules to enable a more distinct assignment of the found increased $m_L^{(z)}$ to $m_S^{(z)}$ ratios.

The present work shows that gas phase XMCD is a valuable technique to investigate the intrinsic spin and orbital magnetic moments of highly relevant magnetic compounds such as transition metal clusters and single molecule magnets.

In future experiments, next to expanding the presented investigations to other SMMs or clusters, one should investigate temperature and / or magnetic field dependent changes in the recorded spin and orbital magnetizations. One intriguing topic is the temperature dependent investigation of the spin and orbital magnetic moments of so called spin crossover complexes[1,2]. These complexes switch from a low spin state at low temperatures to a high spin state after crossing a certain temperature barrier. A proposed temperature dependent investigation could serve for a determination of the intrinsic transition temperature next to the spin and orbital contributions.

In the case of isolated SMMs the presented work focused on recording the spin and orbital contributions to the persistent magnetic moments of these compounds. Such a persistent magnetic moment is one premise for a molecule to be classified as a single molecule magnet. The other one is the presence of a significantly slow relaxation of the magnetization by virtue of a significant magnetic anisotropy barrier. This magnetic anisotropy has not been addressed by the experiments in the presented work so far. Possible magnetic field dependent investigations of the magnetization and concomitant investigation of possible effects of linear dichroism might serve to estimate this anisotropy barrier in our gas phase experiments. Such an investigation might enable the determination of the intrinsic anisotropy barrier of isolated SMMs. In combination with the presented technique this would serve for a comprehensive characterization of the intrinsic properties of SMMs helping in the better understanding of these highly interesting compounds and maybe aid in the development of new and improved SMMs.

[1]   Graf, M.; Wolmershauser, G.; Kelm, H.; Demeschko, S.; Meyer, F.; Kruger, H. J., *TEMPERATURE-INDUCED SPIN-TRANSITION IN A LOW-SPIN COBALT(II) SEMIQUINONATE COMPLEX*, *Angewandte Chemie-International Edition* **2010**, *49*, 950.

[2]   Kruger, H. J., *SPIN TRANSITION IN OCTAHEDRAL METAL COMPLEXES CONTAINING TETRAAZAMACROCYCLIC LIGANDS*, *Coordination Chemistry Reviews* **2009**, *253*, 2450.

7. ZUSAMMENFASSUNG UND AUSBLICK

In der vorgelegten Arbeit wurden die magnetischen Momente von isolierten Einzelmolekülmagneten (SMMs, Single Molecule Magnets) und von Übergangsmetallclustern untersucht. Gasphasen röntgenstrahlinduzierter magnetischer Zirkulardichroismus (XMCD, X-ray Magnetic Circular Dichroism) in Kombination mit der sogenannten Summenregelanalyse diente zur Bestimmung der Anteile der spin- und bahnmagnetischen Momente zum totalen magnetischen Moment der untersuchten Substanzen. Zwei unterschiedliche, auf Massenspektrometrie basierende, Instrumente wurden für die genannten Untersuchungen verwendet. Im Falle der Übergangsmetallcluster war dies das GAMBIT-Setup und im Falle der Einzelmolekülmagnete handelte es sich um die NanoClusterTrap. Beide Instrumente waren an der UE52-PGM Beamline am BESSY II Synchrotron (Helmholtz Zentrum Berlin) angebracht, welche die benötigte zirkular polarisierte Röntgenstrahlung lieferte. Die Untersuchungen der genannten Substanzen als isolierte Moleküle in der Gasphase ermöglichte die Bestimmung ihrer intrinsischer magnetischer Momente ohne den Einfluss etwaiger benachbarter Festkörper- oder tragender Oberflächenmoleküle.

Die Untersuchung kationischer Übergansmetallcluster bestehend aus Fe_n^+ ($7 \leq n \leq 16$ and $n = 18$), Co_n^+ ($8 \leq n \leq 17$ und $n = 19, 22$) und Ni_n^+ ($7 \leq n \leq 17$) zeigten im Vergleich zum jeweiligen Festkörper erhöhte spin- und bahnmagnetische Momente pro atom. Im Vergleich zum jeweiligen isolierten Atom waren diese erniedrigt. Beim Vergleich mit unabhängigen Untersuchungen von spin- und bahnmagnetischen Momenten solcher Übergangsmetallcluster konnten keine bzw. nur geringfügige Unterschiede festgestellt werden. Dies diente zur unabhängigen Bestätigung der gefundenen spin- und bahnmagnetischen Momente mittels XMCD Spektroskopie. Cluster spannen die Brücke zwischen Festkörper und isoliertem Atom. Deshalb wurde in der vorgelegten Arbeit die Anwendbarkeit einzelner Skalierungsgesetze auf die gefundenen spin- und bahnmagnetischen Momente untersucht. In beiden Fällen konnte eine $n^{-1/3}$ Größenabhängigkeit festgestellt werden. Im Falle des spinmagnetischen Momentes interpoliert diese Größenabhängigkeit zwischen dem atomaren und dem Wert des Festkörpers. Im Falle des bahnmagnetischen Momentes trifft eine solche Zuordnung nur bei der Interpolation zwischen dem diatomaren und dem Festkörperwert zu. Diese in erster Linie ungewöhnliche Wahl des Referenzpunktes wurde durch Überlegungen zu „primaren" atomaren und „sekundären" durch Spin-Bahn-Wechselwirkung induzierten bahnmagnetischen Momenten erklärt. Letztere werden in Festkörpern auf Grund von Symmetrieverlust und gleichzeitigem Verlust an orbitaler Entartung gequencht.

7. Zusammenfassung und Ausblick

Der Einfluss des Dotierens mit 4d Übergangsmetallclustern (Au, Rh) auf die spin- und bahnmagnetischen Momente reiner Kobalt Cluster wurde untersucht. Dies geschah durch die Aufnahme und den Vergleich der spin- und bahnmagnetischen Momente kationischer $[Co_nAu]^+$ und $[Co_nRh]^+$ ($8 \leq n \leq 14$) Cluster mit den Werten der reinen Co Cluster. Dieser Vergleich zeigte sowohl erhöhte als auch erniedrigte spin- und bahnmagnetische Momente im Vergleich zu den reinen Clustern ohne einen dedizierten Trend darzulegen. Die gefundenen Änderungen waren im höchsten Grade von der jeweiligen Clustergröße abhängig. Der $[Co_{12}Rh]^+$ Cluster zum Beispiel zeigte ein um mehr als das Zweifache erhöhtes bahnmagnetisches Moment im Vergleich zum reinen Co_{13}^+ Cluster. Mit ausstehender detaillierter Erläuterung des gefundenen erhöhten bahnmagnetischen Momentes, konnte diese nur durch eine Änderung der Geometrie des Clusters erklärt werden.

Neben den Untersuchungen an Übergangsmetallclustern konzentriert sich die vorgelegte Arbeit auf die Untersuchung der magnetischen Momente isolierter Einzelmolekülmagneten. Die vorgelegten Röntgenabsorptions- und die zugehörigen XMCD-Spektren bilden die erste magnetische Charakterisierung isolierter Einzelmolekülmagnete in der Gasphase. Da Einzelmoleküle ihre magnetischen Eigenschaften schon als isolierte Moleküle in der Gasphase ausbilden, dienen unsere Untersuchungen der Bestimmung ihrer intrinsischen magnetischen Momente ohne den Einfluss eines umgebenden Festkörpers oder einer tragenden Oberfläche.

Der erste untersuchte Einzelmolekülmagnet war das archetypische Mn_{12}-Acetat ($[Mn_{12}O_{12}(CH_3COO)_{16}(H_2O)_4]$ abgekürzt $[Mn_{12}ac]$). Die vorgestellten polarisationsabhängigen Röntgenabsorptionsspektren zeigen deutliche dichroitische Effekte auf beiden aufgenommenen Mangan $L_{3,2}$ Absorptionskanten. Dieser gefundene dichroitische Effekt wurde einem permanenten magnetischen Moment des isolierten $[Mn_{12}ac]$ zugeordnet. Die Herleitung der spin- und bahnmagnetischen Momente war aufgrund der Limitierung der Summenregelanalyse für frühe Übergangsmetallcluster wie Mangan nicht möglich. Der Vergleich der vorgestellten Gasphasen-XMCD-Spektren mit früheren Messungen an einer Festkörperprobe zeigte eine herausragende Übereinstimmung beider Spektren. Dies führte zur Schlussfolgerung, dass die Einflüsse der Festkörperbildung auf die magnetischen Momente des isolierten Moleküls nicht vorhanden oder nur sehr gering ausgeprägt sind. Ein gefundener geringfügiger Unterschied zwischen dem Festkörper- und dem Gasphasenspektrum konnte durch mögliche minimale Strahlungsschäden im Falle des aufgenommenen Festkörperspektrums erklärt werden. In den gezeigten Gasphasenmessungen werden mögliche Strahlungsschäden durch permanenten Austausch der Probe verhindert. In den gezeigten Untersuchungen wurde nicht der eigentliche $[Mn_{12}ac]$ Komplex untersucht sondern ein positiv geladenes Derivat ($[Mn_{12}O_{12}(CH_3COO)_{15}CH_3CN]^+$ abgekürzt $[Mn_{12}ac]^+$). Das Problem möglicher Änderungen der Untersuchten magnetischen Momente durch die Bildung des Kations wurde mit

Hilfe von theoretischen Rechnungen (Dichtefunktionaltheorie) unter Verwendung des sogenannten Broken-Symmetry-Ansatzes untersucht. Der Vergleich der Spindichten und der atomaren Abständen in den gefundenen Minimumstrukturen für die untersuchten [Mn$_{12}$ac] und [Mn$_{12}$ac]$^+$ Komplexe zeigte keine oder nur geringfügige Unterschiede zwischen den beiden untersuchten Strukturen. Im Zuge dessen können die präsentierten magnetischen Eigenschaften des untersuchten kationischen [Mn$_{12}$ac]$^+$ als die intrinsischen Eigenschaften des neutralen [Mn$_{12}$ac] angesehen werden.

Bei der zweiten Klassen an untersuchten Einzelmolekülmagneten handelte es sich um Verbindungen des Typs [Fe$_4$Ln$_2$] (Ln = Gd, Tb). Neben der Variation des Lanthanids wurde auch der Einfluss unterschiedlicher Strukturtypen (Strukturtyp **I**: [Fe$_4$Ln$_2$(N$_3$)$_6$(N(C$_2$H$_4$OH)(C$_2$H$_4$O)$_2$)$_4$(C(CH$_3$)$_3$COO)$_4$] und Strukturtyp **II**: [Fe$_4$Ln$_2$O$_2$((CH$_3$)$_3$CCOO)$_4$(NO$_3$)$_2$(H$_3$C$_3$N(C$_2$H$_4$O)$_2$)$_4$]) auf die magnetischen Momente untersucht. Auch hier wurden die genannten Substanzen als kationische Spezies untersucht (Strukturtyp **I**: [Fe$_4$Ln$_2$(N$_3$)$_6$(N(C$_2$H$_4$OH)(C$_2$H$_4$O)$_2$)$_4$(C(CH$_3$)$_3$COO)$_3$CH$_3$CN]$^+$ und Strukturtyp **II**: [Fe$_4$Ln$_2$O$_2$((CH$_3$)$_3$CCOO)$_4$(NO$_3$)$_1$(H$_3$C$_3$N(C$_2$H$_4$O)$_2$)$_4$CH$_3$CN]$^+$). Die Elementselektivität der XMCD-Spektroskopie erlaubt die Separation des totalen magnetischen Momentes in die Beiträge der jeweiligen Metalle. Dies ist möglich durch die Aufnahme von XMCD-Spektren auf den jeweiligen elementspezifischen Absorptionskanten (L$_{3,2}$ für Fe und M$_{5,4}$ für Gd und Tb).

Trotz einer angenommenen 3d^5 Highspinkonfiguration der Eisenatome konnten in den gezeigten Röntgenabsorptionsspektren nur geringe dichroitische Effekte gefunden werden. Diese geringen Effekte wurden einer antiferromagnetischen Kopplung zwischen den Eisenatomen zugeschrieben. Die aufgenommenen spin- und bahnmagnetischen Momente zeigten ein vom Spinmoment dominiertes gesamtmagnetisches Moment, da das bahnmagnetische Moment nahe Null war. Dies zeigte eine sehr gute Übereinstimmung mit der angenommenen Highspinkonfiguration der Eisenatome. Der Vergleich der gezeigten Magnetisierungen für Komplexe mit unterschiedlichen benachbarten Lanthaniden zeigte keinen Einfluss auf die magnetischen Momente der Eisenatome. Eine Änderung der Struktur wiederum (Vergleich von Strukturtyp **I** und **II**) zeigte geringe jedoch signifikante Änderungen im spinmagnetischen Moment. Das bahnmagnetische Moment blieb von der strukturellen Änderung unbeeinflusst.

Die gefundenen dichroitischen Effekte auf den gezeigten M$_{5,4}$ Absorptionskanten der Lanthanide waren deutlich ausgeprägter als die gefundenen Effekte auf den Eisenkanten. Diese Beobachtung alleine führte zu dem Schluss, dass die gesamtmagnetischen Momente der untersuchten Substanzen durch die magnetischen Momente der Lanthanide dominiert werden. Der Vergleich der Röntgenabsorptionsspektren der beiden unterschiedlichen Lanthanide zeigte deutliche Unterschiede in den gefundenen dichroitischen Effekten im Besonderen auf der M$_4$ Absorptionskante. Diese Unterschiede in den gefundenen dichroitischen Effekten spiegeln sich in den unterschiedlichen

Beiträgen von spin- und bahnmagnetischem Moment für die beiden unterschiedlichen Lanthanide wieder. Die Gadolinium Spezies zeigten ein Verhältnis von spin- ($m_S^{(z)}$) und bahnmagnetischem ($m_L^{(z)}$) Moment von $m_L^{(z)} / m_S^{(z)} = 0.3$, wohingegen die Terbium Spezies ein solches Verhältnis von $m_L^{(z)} / m_S^{(z)} = 1$ zeigten. Diese Werte wurden für die beiden untersuchten unterschiedlichen Strukturtypen festgestellt. Dies führte zu der Schlussfolgerung, dass der Strukturtyp nur einen geringen bis keinen Einfluss auf die magnetischen Momente der Lanthanide hat. Der Vergleich der gefundenen $m_L^{(z)} / m_S^{(z)}$ Werte mit Abschätzungen nach der Hund´schen Regel ($m_L^{(z)} / m_S^{(z)} = 0$ für Gd und $m_L^{(z)} / m_S^{(z)} = 0.5$ für Tb) zeigten deutlich erhöhte Werte in den vorgestellten Untersuchungen. Mögliche Erklärungen und deren Wahrscheinlichkeiten wie eine Oxidation oder Reduktion der Lanthanide, die (Co)Existenz eines nicht vollständigen Highspinzustandes sowie partieller Elektronentransfer von den umgebenden Liganden auf die Lanthanide wurden diskutiert. Eine genaue Zuordnung des gefundenen Effektes bleibt ausstehend. Zeitgemäße theoretische Untersuchungen wie z. B. Dichtefunktionalrechnungen nach dem Broken-Symmetry-Ansatz zur Bestimmung der genauen magnetischen Struktur sowie hochaufgelöste Röntgenabsorptionsspektren zur genauen Bestimmung des Oxidationszustandes der Lanthanide werden für eine genauere Zuordnung des gefundenen erhöhten $m_L^{(z)} / m_S^{(z)}$ Verhältnisses benötigt.

Als allgemeine Schlussfolgerung wurde in der vorgelegten Arbeit gezeigt, dass Gashasen-XMCD-Untersuchungen eine nützliche Technik zur Untersuchung der intrinsischen spin- und bahnmagnetischen Momente hoch interessanter magnetischer Substanzen wie Übergangsmetallcluster und Einzelmolekülmagnete darstellt.

In zukünftigen Experimenten wird es interessant sein, neben der Ausweitung der gezeigten Untersuchungen auf weitere Übergansmetallcluster und Einzelmolekülmagnete, die temperatur- und magnetfeldabhängigen Änderungen der spin- und bahnmagnetischen Momente zu untersuchen. Ein interessantes Thema wird die Untersuchung der spin- und bahnmagnetischen Momente sogenannter Spin-Crossover-Komplexe sein. Diese Komplexe wechseln von einem Lowspinzustand bei niedrigen Temperaturen zu einem Highspinzustand nach Überschreitung einer kritischen Temperatur. Die vorgeschlagenen temperaturabhängigen Untersuchungen können neben der Bestimmung der spin- und bahnmagnetischen Momente zur Bestimmung der intrinsischen Übergangstemperatur dienen.

Im Falle der Einzelmolekülmagnete konzentriert sich die vorgelegte Arbeit auf die Untersuchung der Anteile der spin- und bahnmagnetischen Momente zum permanenten totalen magnetischen Moment dieser Substanzen. Dieses permanente magnetische Moment ist eine Voraussetzung für die Charakterisierung einer Substanz als Einzelmolekülmagnet. Die zweite Voraussetzung ist eine ausgeprägt langsame Relaxation der Magnetisierung der Substanz auf Grund einer signifikanten

magnetischen Anisotropiebarriere. Diese magnetische Anisotropie wurde in der vorgelegten Arbeit noch nicht behandelt. Mögliche magnetfeldabhängige Messungen der Magnetisierung und gleichzeitige Untersuchungen eines möglichen linearen Dichroismus könnten zur Abschätzung dieser Anisotropie in unseren Gasphasenmessungen dienen. Solche Messungen könnten dazu dienen die intrinsischen Anisotropiebarrieren von isolierten Einzelmolekülmagneten zu bestimmen. In Kombination mit den bereits gezeigten Messungen könnten solche Untersuchungen zu einer umfassenden magnetischen Charakterisierung der intrinsischen magnetischen Eigenschaften von Einzelmolekülmagneten dienen.

1]   Graf, M.; Wolmershauser, G.; Kelm, H.; Demeschko, S.; Meyer, F.; Kruger, H. J., TEMPERATURE-INDUCED SPIN-TRANSITION IN A LOW-SPIN COBALT(II) SEMIQUINONATE COMPLEX, *Angewandte Chemie-International Edition* **2010**, *49*, 950.

[2]   Kruger, H. J., SPIN TRANSITION IN OCTAHEDRAL METAL COMPLEXES CONTAINING TETRAAZAMACROCYCLIC LIGANDS, *Coordination Chemistry Reviews* **2009**, *253*, 2450.

8. APPENDIX

Next to the primary topic of my thesis about the investigations of spin and orbital magnetic moments of isolated single molecule magnets and transition metal clusters I concluded the work I started during my diploma thesis. In my diploma thesis I worked out a draft on kinetic studies of pure cobalt clusters reacting with benzene in the gas phase. This draft was revised / finalized and accepted for publication at *The Journal of Physical Chemistry A* with the title: *"Inverse H/D Isotope Effects in Benzene Activation by Cationic and Anionic Cobalt Clusters".* This was done during the beginning of my graduate work.

Next to finalizing the paper on pure cobalt clusters with benzene, I worked together with Lars Barzen on his investigations on the gas phase reaction of CoPt-alloy clusters with benzene. The main part of this work on CoPt-alloy clusters was done by Lars Barzen and is part of his doctoral thesis. This work concluded in a publication in *The International Journal of Mass Spectrometry* with the title: *"Benzene activation and H/D isotope effects in reactions of mixed cobalt platinum clusters: The influence of charge and of composition"*. The resulting two publications are reprinted in the following chapter.

Afterwards I focused on the investigations of spin and orbital magnetic moments of transition metal cluster and single molecule magnets. The topic of gas phase activation of benzene by pure cobalt and CoPt-alloyed transition metal clusters will not be addressed in detail in this work. For more detailed information the reader is referred to the doctoral thesis of Lars Barzen[1] and to my diploma thesis[2].

[1]   Barzen, L. *Metal cluster aggregates of the composition Nbn+/-, Con+/- and [ConPtm]+/- as model systems for catalytic C-H activation and structural determination of selected metal peptide complexes of the molecules aspartame (Asp-PheOMe) and Asp-Phe*. Doctoral Thesis, TU Kaiserslautern, **2013**.

[2]   Tombers, M. *Kinetische und magnetische Studien an ionischen Cobalt-Clustern mittels Fourier-Transform Ionen-Zyklotron-Resonanz (FT-ICR) Massenspektrometrie und röntgenstrahlbasiertem magnetischem Zirkulardichroismus (XMCD)*. Diploma Thesis, TU Kaiserslautern, **2011**.

8.1 Publication: Inverse H/D Isotope Effects in Benzene Activation by Cationic and Anionic Cobalt Clusters

The following work has been published in *The Journal of Physical Chemistry A* with the title: *"Inverse H/D Isotope Effects in Benzene Activation by Cationic and Anionic Cobalt Clusters"* within the special issue dedicated to Peter B. Armentrout on the occasion of his 60th birthday. An initial version of the manuscript was written by me on behalf of my diploma thesis revised and finalized during my doctoral studies. Measurements and data evaluation were done by me and Lars Barzen. Structural and energetic calculations were made by Gereon Niedner-Schatteburg.

Full reference to the publication:

M. Tombers, L. Barzen, G. Niedner-Schatteburg, Inverse h/d isotope effects in benzene activation by cationic and anionic cobalt clusters, The journal of physical chemistry. A, 117 (2013) 1197-1203.

Inverse H/D isotope effects in benzene activation by cationic and anionic cobalt clusters

M. Tombers, L. Barzen and G. Niedner-Schatteburg

Fachbereich Chemie and Forschungszentrum OPTIMAS, Technische Universität Kaiserslautern, 67663

Kaiserslautern, Germany

Abstract

Reactions under single collision conditions with benzene C_6H_6 and with benzene-d$_6$ C_6D_6 of size selected cationic cobalt clusters $Co_n{}^+$ and of anionic cobalt clusters $Co_n{}^-$ in the cluster size range of $n = 3 - 28$ revealed that dehydrogenation by cationic clusters is sparse, while it is ubiquitous in reactions by anionic clusters. Kinetic Isotope Effects (KIE) in total reaction rates are inverse and – in part – large. Dehydrogenation Isotope Effects (DIE) are normal. A multistep model of adsorption and stepwise dehydrogenation from the precursor adsorbate unravels a possible origin of the inverse KIE: Single step C-H bond activation is swift (no KIE in forward direction) and largely reversible (normal KIE backwards) while H/D tunneling is likely to contribute (backwards). DFT calculations of the structures and energetics along the reaction path in $[Co_{13}C_6H_6]^+$ lend support to the proposed multistep model. The observed effects on rates and KIEs of cluster charges and of cluster sizes are to elucidate further.

Introduction

Transition metal clusters may serve as model systems for the elucidation of elementary processes in heterogeneous catalysis. Hydrocarbon adsorption and subsequent C-H bond activation are amongst the most important steps in many catalyzed reactions, and either of both is often rate limiting.

Investigations of hydrogen/deuterium (H/D) isotope effects have helped to elucidate the origin of observable phenomena in hydrocarbon activation[1-5]. Cobalt has proven valuable in numerous catalytical applications, in particular as an important metal component in the benzene hydrogenation at low temperatures[6]. Fischer Tropsch conversion of CO by cobalt nano particles showed an inverse H/D kinetic isotope effect with a mechanistic interpretation pending[7]. The significance of H/D atom

tunneling in homogeneous organic transformations was recently highlighted[8]. In the particular case of C-H bond cleavage by oxoiron(IV) complexes it was concluded, however, that multiple spin state surfaces may give rise to possible spin crossover issues that enhance KIEs to such large values that resemble a tunneling like behavior[9]. The investigation of C-H bond reductive elimination of benzene from phenyl metal hydrides revealed a normal kinetic isotope effect (KIE) in the case of molybdenocene and an inverse KIE in the case of tungstenocene[10]. It was concluded that relative barrier heights determine the kinetics and suffice to switch observable KIEs. Similar interpretations arose from the study of temperature dependent alkane reductive elimination from alkyl metal hydrides[11,12]. The lack of H/D isotope effects in the gas phase reactions of neutral zirconium atoms with small olefins was interpreted in terms of a stepwise association – activation mechanism[13].

Prior gas phase studies of benzene adsorption and activation focused on niobium and rhodium clusters[14-16]. Ubiquitous dehydrogenation through niobium cluster cations and anions alike contrast to mere adsorption by $Rh_n^{\pm}$. Little to no observable isotope effects prevailed in either cases. Through methane activation by cobalt cluster cations Armentrout et al.[17] determined their bond energies to D, C, CD, CD_2 and CD_3. Moreover, Armentrout et al. determined the bond energies (BDE) of cobalt-benzene and cobalt-dimer-benzene cations (2.65(11) and 1.73(14) eV, respectively) by meticulous analysis of thermochemical modeling of high precision flow reactor MS experiments[18]. Dissociative nitrogen interaction with cationic cobalt clusters is endoergic[19], nitrogen association to anionic clusters Co_n^- under flow tube conditions only takes place slowly beyond a size threshold of $n \geq 7$[20]. Another flow tube study of photoionization efficiencies of $Co_n(C_6H_6)_m$ clusters focused onto species with multiple benzene adsorbates[21,22]. Negative ion photoelectron spectra of cobalt benzene anions revealed sandwich like structures[23]. Photoionization efficiency (PIE) spectra of cold cobalt clusters ($Co_3, Co_7 - Co_{92}$) revealed vertical ionization potentials (IPs) that decreased rapidly up to n ≈ 20, beyond which IPs evolve more slowly and smoothly. No particular cluster size sticks out significantly[24]. Insight into the electronic structure of cobalt clusters and of cobalt cluster benzene complexes arose from multiple Stern-Gerlach experiments[25-28]. Advanced synchrotron ionization studies of cationic cobalt clusters revealed significant magnetization by spins and by orbital angular moments with little cluster size dependence[29].

Plane wave density functional calculations with PBE exchange correlation functional have revealed a preference of hcp-structures in neutral high spin Co clusters[30] over icosahedral motifs which in turn had been predicted previously by application of the BLYP functional in conjunction with atom centered basis functions of double zeta plus polarization quality[31].

We chose to record the reaction kinetics and H/D isotope effects of size selected cobalt clusters with benzene in the dilute gas phase (under single collision conditions) as enabled by application of

Fourier-Transform Ion-Cyclotron-Resonance (FT-ICR) mass spectrometry[32] in conjunction with the concomitant ion trapping. In this report, we investigated the difference in the reaction of ionic cobalt clusters with benzene (C_6H_6) and benzene-d$_6$ (C_6D_6).

Experimental and theoretical methods

Experimental methods

The experiments were performed with a modified Fourier-Transform Ion-Cyclotron-Resonance (FT-ICR) mass spectrometer (Bruker Apex III). We generated the cobalt clusters with a homebuilt laser vaporization source (LVAP) as described before[16,33]. The second harmonic of a pulsed Continuum Nd-YAG laser is used to evaporate cobalt atoms from a 0.4 – 1.0 mm thick rotating cobalt foil (Alpha Aesar, purity ≥ 99.95%). The emerging metal plasma is cooled and made to yield clusters by a short transverse pulse (40 µs, Helium, 8-15 bar) from a homebuilt piezoelectric valve[34]. Further cooling arises from the subsequent supersonic nozzle expansion through a 20 mm long channel (diameter of 2 mm) into vacuum (10^{-6} mbar). There is no additional ionization step. All investigated ions are generated within the laser induced plasma. Past a 1.4 mm diameter skimmer the cold cluster ions are accelerated, fed into a quadrupole ion bender (90^0) and steered by electrostatic lenses into the high field region of a superconducting magnet (7.05 Tesla, actively shielded) while appropriately decelerated. Eventually, the cluster ions are trapped for reaction and/or detection within the FT-ICR cell of so called "infinity" type[35].

In order to pursue the reactivity studies with benzene (C_6H_6) / benzene-d$_6$ (C_6D_6) we permitted the controlled admission of a reaction gas in order to raise the pressure in the ultrahigh vacuum chamber of the FT-ICR mass spectrometer, where the ICR trapping cell is located, from ~ 3 x 10^{-10} to typically 1-5 x 10^{-9} mbar such that a single bimolecular reactant collision per cluster per second takes place (single collision conditions). A commercial ultrahigh vacuum gauge (cold cathode gas discharge, calibrated for N$_2$) provides for a nominal pressure reading. There is a pressure gradient between the gauge and ICR cell of about a factor of 4, the exact value not being known. Commercially available benzene/benzene-d$_6$ (Sigma-Aldrich, purity ≥ 99.6 %) was applied after degassing by multiple "pump and freeze" cycles. Kinetic curves of reactant and product ions extracted from mass spectra of trapped cluster ions while exposed to the continuously admitted reactant gases and under variation of reaction delays between cluster ion admission and detection. Fits to pseudo-first-order-kinetics arise through a genetic algorithm ("evofit" program[36]).

3.2.2. Theoretical methods

Preliminary density functional calculations were performed by standard programs[37] and by applying the PBE0 exchange correlation functional[38]. Carbon and hydrogen atoms were represented by aug-cc-pVTZ basis sets, cobalt atoms by effective core potentials of double zeta quality[39-40]. The SCF density convergence criterion needed to relax to 10^{-4}. In this way, it became possible to pursue full geometry optimization and subsequent frequency calculations at an approximate level. Found minimum structures revealed either no or a single imaginary frequency that corresponds to some large amplitude motion with a small force constant. Systematic screening for an optimum functional and for usage of advanced basis sets was beyond the scope of this study. Instead, we refer to a recent benchmark study that revealed about equal performance of several DFT functionals (PBE0, B1B95, PW6B95, and TPSS25B95) when computing reactions of late transition metal clusters[41]. The present study focusses on structures, spin states and energetics along the reaction path in $[Co_{13}C_6H_6]^+$. Systematic variation of cluster size and cluster charge remains for further studies.

Kinetic modeling took place by customized code for the *Mathematica 8* program package running on standard PC hardware. In particular the numerical integration of differential rate equations through the *NDSolve* command proved helpful.

Results and discussion

Experimental results
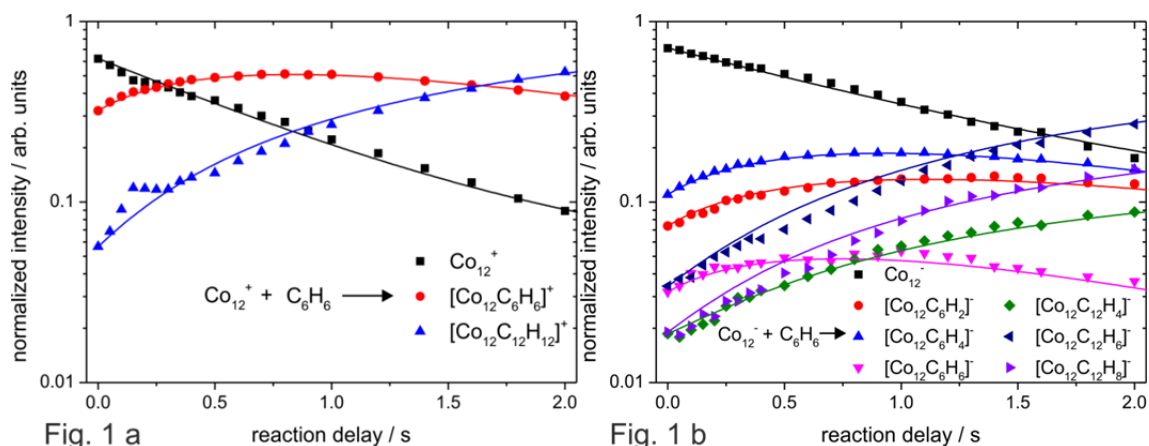
Fig. 1: *Normalized reactant and product intensities in the reactions (a) of cationic cobalt clusters Co_{12}^+ and (b) of anionic cobalt clusters Co_{12}^- with benzene C_6H_6. The temporal evolution of the experimental data points (symbols) is fitted to pseudo first order kinetics (solid lines) which provide for relative partial rate constants.*

The reaction of cationic cobalt clusters Co_n^+ with benzene (C_6H_6) and benzene-d6 (C_6D_6) proceeds towards a single class of primary products (cf. Fig. 1a in the case of $n = 12$):

$$Co_n^+ + C_6(H,D)_6 \rightarrow [Co_nC_6(H,D)_6]^+ \qquad (3.1)$$
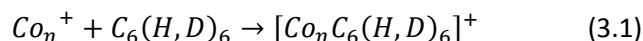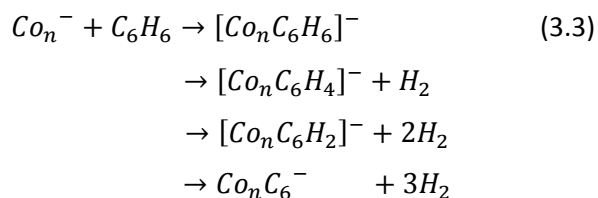
The addition resembles a seemingly intact adsorption of the reactant to the cluster surface. Structural information, however, is not retrieved through this observation. In particular, C-H bond activation with the formation of hydrido-phenylic cobalt clusters $Co_n(H)C_6H_5^+$ is conceivable. In order to account for the concomitant structural ambiguity we designate such observed products with chemical formulas in square brackets as above. Secondary reactions with further C₆H₆ molecules – although well observable (cf. Co₁₂C₁₂H₁₂⁺ and other "C₁₂" products in Figs. 1a and 1b) – are not subject of further inspection as of now. Within the limit of detection the cobalt cluster Co_{13}^+ is the only cationic cluster that proceeds towards a second product channel. It does so through molecular dehydrogenation and much more effectively when reacting with benzene (C_6H_6):

$$\begin{aligned} Co_{13}^+ + C_6H_6 &\rightarrow [Co_{13}C_6H_6]^+ \\ &\rightarrow [Co_{13}C_6H_4]^+ + H_2 \end{aligned} \qquad (3.2)$$
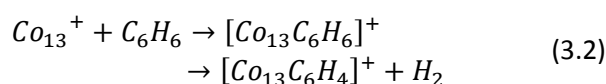
Products from dehydrogenation of perdeuterated benzene (C_6D_6) are barely detectable.

Anionic cobalt clusters such as e.g. Co_{12}^- (cf. Fig. 1b) react efficiently into multiple observable product channels in parallel:

$$\begin{aligned} Co_n^- + C_6H_6 &\rightarrow [Co_nC_6H_6]^- \qquad (3.3) \\ &\rightarrow [Co_nC_6H_4]^- + H_2 \\ &\rightarrow [Co_nC_6H_2]^- + 2H_2 \\ &\rightarrow Co_nC_6^- \quad\;\; + 3H_2 \end{aligned}$$

We label the overall reaction processes as adsorption, dehydrogenation, twofold dehydrogenation and total dehydrogenation, respectively. Once more, the particular structures of the observed products remain ambiguous as of now. The hydrido-phenylic cobalt cluster motif $Co_n(H)C_6H_5^-$ is a conceivable structure in the case of adsorption onto anionic clusters as well. In particular, the observation of strong dehydrogenation lends evidence to a likely C-H bond activation in general.

Kinetic information arises from the temporal evolution of the reactions (Fig. 1a and 1b). The fits of the experimental data (points) to pseudo first order kinetics (curves) determine partial and total relative rate constants and branching ratios amongst competing reaction channels. When assuming the fastest observed reaction to proceed with collision rate the obtained experimental rates would convert into reaction efficiencies per single collision event. In ionic metal cluster molecule collisions,

rates may enhance somewhat through a conducting sphere effect[42]. The provided plots of Fig. 2a and 2b leave the obtained data in the form of relative rate constants, however. Otherwise, there would be exceedingly large uncertainties in the absolute reaction rate values. A quantitative determination of reactant gas densities within the ICR trap is pending.
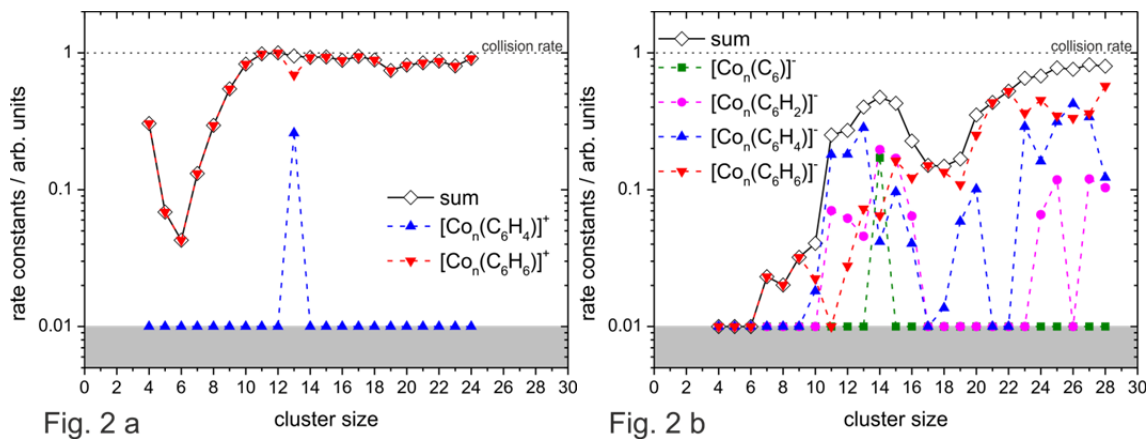

Fig. 2: *Relative partial rate constants for the reaction* ***(a)*** *of Co_n^+ and* ***(b)*** *of Co_n^- with benzene. All values were normalized to the highest rate constant. Total rate constants are provided as well. The shaded areas indicate the background noise level.*

Cationic cobalt clusters Co_n^+ with $n \geq 10$ adsorb benzene with unit efficiency per collision and without dehydrogenation (Fig. 2a). As a sole exemption, Co_{13}^+ does cause some dehydrogenation. This may relate to a conceivable icosahedral structure. At $n = 13$ it would provide for a closed geometric shell (an icosahedron of 12 surface atoms and a single volume atom at the center) with high and equal coordination of all Cobalt surface atoms. Lack of surface defects – adatoms and/or kinks – would allow for high mobility of activated species and possible pairwise recombination of H atoms at the cluster surface. Presence of surface defects might enhance the risk of pinning, reduces mobility on the surface and thereby may suppress H_2 desorption. Seemingly this scenario holds in the case of cationic clusters while it is of less to no importance in anionic clusters (cf. below).

The smaller cationic clusters provide for an adsorption efficiency that is reduced by up to a factor of five resembling a typical behavior of metal cluster reactions under single collision conditions as observed several times before[14,15,16] and attributed to microscopic reversibility within a cluster size dependent, finite heat bath.

Anionic cobalt clusters Co_n^- with $n \leq 6$ do not yield observable products while collisions with benzene inevitably take place at collision rates that are high enough to allow for detection of products down to 1% collision efficiency. The intermediate collision complex $[Co_n C_6 H_6]^-$ may in

principle decay into some charged products that are outside the mass range of detection in the present experiment, e.g. by electron detachment according to:

$$Co_n{}^- + C_6H_6 \rightarrow [Co_nC_6H_6]^{*-} \rightarrow Co_nC_6H_6 + e^- \qquad (3.4)$$
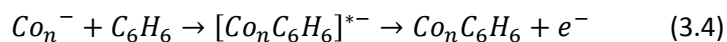
Our recorded data, however, do not provide evidence for a seeming loss of charges such that a "dark" reaction channel by electron detachment is presently ruled out to contribute significantly. Further insight could arise from the inspection of size dependencies in heats of adsorption $\Delta_{ads}H(Co_n{}^- - C_6H_6)$ and in electron detachment enthalpies $\Delta_{detach}H([Co_nC_6H_6]^-)$ of all conceivable isomers, none of which is known as of now.

Instead, basic thermodynamics regards the cluster as a finite heat bath that serves to dissipate the heat of adsorption. The more effective the dissipation the less probable becomes the benzene eventually evaporating off the cluster. With increasing cluster size the total adsorption efficiency rises, as apparent in the rate constants of cationic clusters $Co_n{}^+, n = 6 - 10$, and of anionic clusters $Co_n{}^-, n = 7 - 28$, with some modulation in between.

The size range $n = 11, .., 15$ of anionic clusters is most reactive in terms of dehydrogenation, and it provides for a somewhat larger total reaction efficiency with respect to the general trend. In particular, the cluster anions $Co_n{}^-, n = 10 - 16$, form products of single, double and triple dehydrogenation at enhanced yields as compared to either smaller or larger clusters. These enhanced dehydrogenation reactivities correspond well to the increase of the total rate constant. Other than in the case of cationic clusters (the exceptional $Co_{13}{}^+$) there is no exceptional enhancement or reduction of dehydrogenation efficiency of anionic clusters (an ordinary $Co_{13}{}^-$). This may relate to enthalpic details that are not retrieved at present.

All experiments on benzene reactions with cationic and anionic cobalt clusters have been duplicated with perdeuterated benzene (C_6D_6) as well. Plots of these results are provided in the supplement, Fig. S1a and S1b. The thereby recorded findings are in qualitative agreement with those of benzene (C_6H_6). Differences arise in terms of a quantitative comparison. The many parallel reaction channels of anionic clusters however cause a risk of blurring the overall picture. We therefore introduce some scheme of further data evaluation before commencing with further interpretation.

Data evaluation

In order to take the degree of activation into account and to provide for further data evaluation, we define a so called average degree of dehydrogenation $\langle \chi_n \rangle$ as before[43]

$$\langle \chi_n \rangle = \frac{1}{m} \frac{1}{k_n^{tot}} \sum_{m_i=1}^{m} m_i k_n(m_i) \qquad (3.5)$$

with

$$k_n^{tot} = \sum_i k_n(m_i) \qquad (3.6)$$

Here, m indicates the total amount of hydrogen or deuterium atoms as available from the reactant ($m = 6$ in the present case). The partial reaction rate $k_n(m_i)$ corresponds to the cluster size n and the loss of hydrogen or deuterium atoms m_i in the observed product. $\langle \chi_n \rangle = 1$ indicates complete dehydrogenation, $\langle \chi_n \rangle = 0$ indicates adsorption without any dehydrogenation.
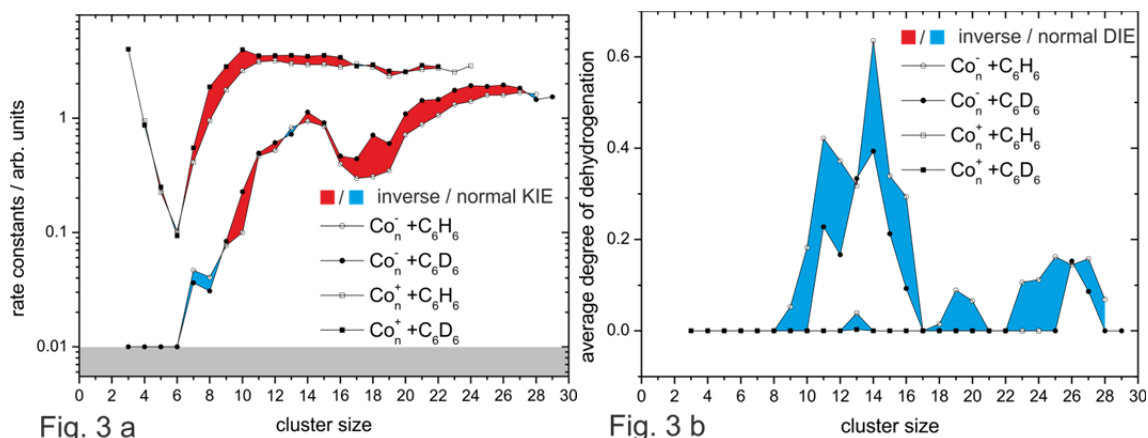
Fig. 3: (a) *Total rate constants of anionic cobalt clusters (circles) and of cationic cobalt clusters (squares) reacting with benzene (open symbols) and benzene-d_6 (filled symbols). Blue and red shadings emphasize normal and inverse kinetic isotope effects KIE(n), respectively. Gray shading indicates the background noise level.* **(b)** *Average degrees of dehydrogenation (see text for definition) of benzene (open symbols) and benzene-d_6 (filled symbols) when reacted by cationic cobalt clusters (squares) and by anionic cobalt clusters (circles). Blue shadings emphasize the prevailing normal Dehydrogenation Isotope Effect (DIE) with no inverse DIE (red) occurring - Co_{13}^- being exempt.*

A convenient way to present the results for further discussion is the combination of total reaction rates with normal benzene and with perdeuterated benzene in a single plot (Fig. 3a) and of average degrees of dehydrogenation of benzene and of perdeuterated benzene in another plot (Fig. 3b). The isotopic effects are indicated by coloring the area between related curves such that a cluster size dependent kinetic isotope effect KIE(n)

$$KIE(n) := \frac{k_{tot}^{(H)}(n)}{k_{tot}^{(D)}(n)} \qquad (3.7)$$

is indicated as normal ($KIE(n) > 1$) by blue shading and as inverse ($KIE(n) < 1$) by red shading (Fig. 3a). The diagram provides a set of data for cationic cobalt clusters and a set of data for anionic cobalt clusters. $KIE(n)$ is inverse in the case of cationic clusters throughout all n values and it is inverse in the case of most anionic clusters. Anionic clusters Co_n^- with either $n \leq 9$ or $n \geq 26$ are exemptions and reveal a normal isotope effect. While we can observe the C_6D_6 rate constants of anionic and cationic clusters revealing all of the gross features as in the C_6H_6 case before, the merging point of anionic and cationic rate constants with C_6D_6 is shifted to lower cluster sizes. The rate constants of Co_{4-8}^+ with C_6D_6 and C_6H_6 diminish by up to one order of magnitude (at $n = 6$) with respect to those of larger clusters where the total reaction rate k_n^{tot} approaches the collision rate k_{coll} . This limiting case, $k_n^{tot} \approx k_{coll}$, corresponds in the terminology of surface science to a sticking probability of unity.

Correspondingly the cluster size dependent dehydrogenation isotope effect $DIE(n)$

$$DIE(n) := \frac{<\chi_n^{(H)}>}{<\chi_n^{(D)}>} \qquad (3.8)$$

is indicated as normal ($DIE(n) > 1$) in blue and as inverse ($DIE(n) < 1$) in red (Fig. 3b). Normal $DIE(n)$ prevails in all cases investigated, namely cationic clusters $3 \leq n \leq 24$ and anionic clusters $4 \leq n \leq 29$. A very small inverse DIE for Co_{13}^- (hardly visible in Fig. 3b) is a possible exemption within combined uncertainties, however. The average degree of dehydrogenation decreases if we exchange C_6H_6 for C_6D_6 to react either with cationic clusters or with anionic clusters. The overall observable activation of C-H/C-D bonds by cationic clusters is negligible and the concomitant DIE vanishes except at Co_{13}^+ where some normal DIE persists. Effective benzene activation and product formation through anionic clusters $Co_n^-, n \geq 9$, leads to considerable dehydrogenation with normal DIE throughout. Dehydrogenation of benzene-d$_6$ takes place by Co_{11-16}^-, (as compared to Co_{9-16}^-, with benzene) and by $Co_{26,27}^-$ (as compared to Co_{18-20}^- and Co_{23-28}^- with benzene). Overall, the dehydrogenation of benzene-d$_6$ by cobalt cluster anions diminishes with respect to the one of benzene.

Numerical values of the KIE(n) derive from the data sets of Fig. 3a through eq. (3.7) and as displayed in Fig 4a and 4b.
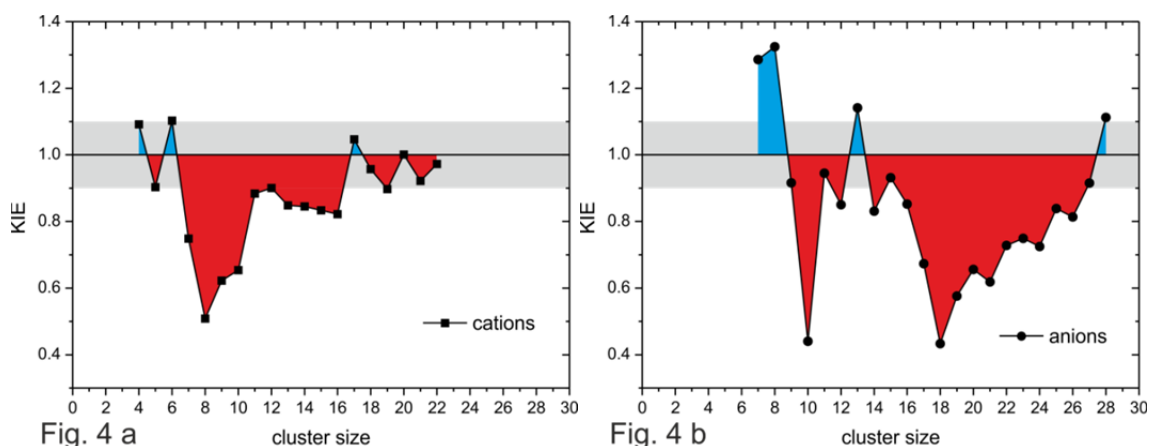
Fig. 4: *Kinetic Isotope Effects (KIE) as function of cluster size in the reactions of C$_6$H$_6$ / C$_6$D$_6$ **(a)** with cationic cobalt clusters and **(b)** with anionic cobalt clusters. Blue shadings indicate normal KIEs and red shadings indicate inverse KIEs. Gray shading indicate the estimated uncertainty.*
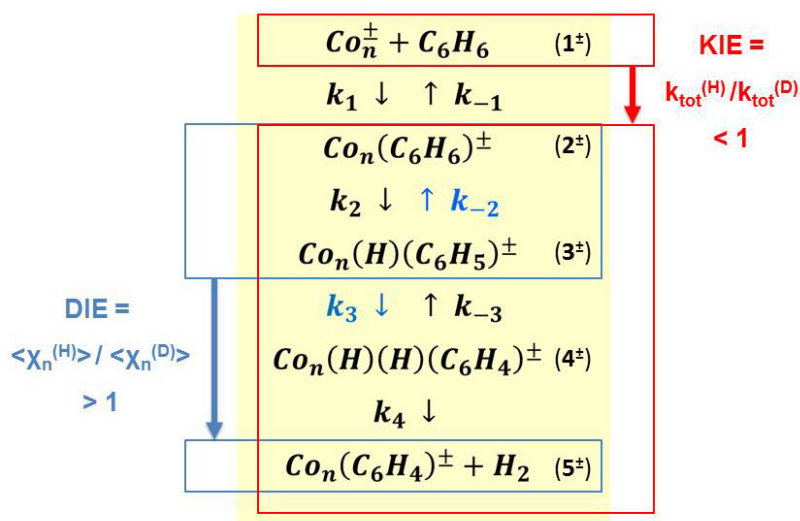
The reaction with benzene-d$_6$ for cationic clusters is up to 5 times faster than the reaction with benzene for e.g. KIE($Co_8{}^+$).

Kinetic interpretation of the inverse Kinetic Isotope Effect (KIE) in terms of consecutive elementary processes

The found isotope effects on rate constants (Kinetic Isotope Effect $KIE(n)$ is inverse) and on the dehydrogenation efficiency (Dehydrogenation Isotope Effect $DIE(n)$ is normal) ask for a kinetic interpretation in terms of a model that comprises of consecutive elementary processes. While it is not possible to obtain definite answers at the present state of investigations, it is mandatory to evaluate possible and likely effects.

The energetics of benzene adsorption and activation through ionic cobalt clusters are largely unknown. Some insight arises from the inspection of atomic cobalt ion complexes and of energetics from cobalt surface studies[18,44-53]. It shows that some independent cluster calculations are mandatory.

We devise a scheme of consecutive elementary processes as follows:

$$\begin{array}{c}
\boxed{Co_n^{\pm} + C_6H_6 \qquad (1^{\pm})} \\[4pt]
k_1 \downarrow \quad \uparrow k_{-1} \\[4pt]
Co_n(C_6H_6)^{\pm} \qquad (2^{\pm}) \\[4pt]
k_2 \downarrow \quad \uparrow k_{-2} \\[4pt]
Co_n(H)(C_6H_5)^{\pm} \qquad (3^{\pm}) \\[4pt]
k_3 \downarrow \quad \uparrow k_{-3} \\[4pt]
Co_n(H)(H)(C_6H_4)^{\pm} \qquad (4^{\pm}) \\[4pt]
k_4 \downarrow \\[4pt]
Co_n(C_6H_4)^{\pm} + H_2 \qquad (5^{\pm})
\end{array}$$

KIE = $k_{tot}^{(H)}/k_{tot}^{(D)}$

< 1

DIE = $\langle \chi_n^{(H)} \rangle / \langle \chi_n^{(D)} \rangle$

> 1

(3.9)

Note, that the magnitude of each rate constant k_i actually depends on the cluster size n, charge state +/-, forward or reverse direction, and isotope H or D, thus $k_i = k_{\pm i}^{\pm,(H/D)}(n)$. The rate constants k_1 and k_{-1} designate the elementary processes of adsorption and desorption, k_2 and k_{-2} those of a C-H bond activation and of its recombination, k_3 and k_{-3} those of a second C-H bond activation and of its recombination, and k_4 designates molecular desorption of H_2. The reverse process (k_{-4}) does not occur because of the experimental conditions of extreme dilution in ultra high vacuum in conjunction with ion cloud trapping at sparse number densities. The kinetic isotope effect KIE on each of these elementary processes is discussed below:

1.   Adsorption of C_6H_6 or of C_6D_6 onto $Co_n^{\pm}$ (rate constant k_1). The initial adsorption of benzene or benzene-d_6 leads to an almost complete loss of its translational entropy. An ideal gas estimate according to Sackur and Tetrode yields a normal KIE ≤ 1.13 . This KIE is independent of cobalt cluster size and holds for cationic and anionic clusters as well.

2.   Desorption of C_6H_6 from $Co_nC_6H_6^{\pm}$ or of C_6D_6 from $Co_nC_6D_6^{\pm}$ (rate constant k_{-1}). The vibrational mode within the complex $2^{\pm}$, that corresponds to the reaction coordinate of desorption, is $\nu(Co_n^{\pm} - C_6H_6)$ or $\nu(Co_n^{\pm} - C_6D_6)$, respectively. Our DFT calculations estimate these frequencies to 324 cm^{-1} and 211 cm^{-1}, respectively. The difference of ~ 0.05 kJ/mol in zero point energy is vanishingly small. The related KIE is negligible.

3.   C-H bond or C-D bond activation (rate constant k_2). When taking place in the course of adsorption or swiftly afterwards, the adsorbate C_6H_6 or C_6D_6 is energized through the released heat of adsorption. The prevailing C-H activation barriers are not known. Most likely they depend on the size, on the net charge and on the spin state of the clusters. In the present case of cobalt clusters the C-H activation k_2 likely is somewhat endoergic (cf. Fig. S3 in the supplement) and it cools the cluster adiabatically. The KIE diminishes because of the hot starting point.

The significance (or insignificance) of tunneling contributions to k_2 was addressed before e.g. in the quantum dynamic modeling of CH_4 dissociation on metal surfaces[54]. It revealed the sensitivity of kinetic isotope effects on the location of the activation barrier. Entrance channel barriers (when the molecule vibrates towards the surface) show little to no KIE by tunneling. Exit channel barriers (when H/D moves away from the C-H or C-D bond) are prone to large tunneling KIEs. For the time being we assume the former case valid in C-H and C-D activation within $Co_nC_6H_6{}^{\pm}$ and $Co_nC_6D_6{}^{\pm}$. Thus KIEs in k_2 may well be small to negligible – and with a tendency towards normal KIE , if any.

4.   Recombination (rate constant k_{-2}), with a significant normal KIE(n)). The reverse exoergic C-H recombination starts from a hydrido-phenylic cluster structure **3$^{\pm}$**. This complex had cooled significantly by having spent the endoergic heat of formation of about 100 kJ/mol in the course of formation from the prior adsorption complex **2$^{\pm}$** . The hydrido-phenylic cluster complex **3$^{\pm}$** is thus cold. Zero point energy of the cobalt hydrid bond is lowered by isotopic substitution and the activation barrier towards recombination accordingly enhanced. Because of the cold conditions at this stage a significant normal KIE results. It is likely that H/D-atom tunneling adds on top and significantly increases the normal KIE. A normal KIE (without tunneling contributions) of up to 7 (by zero point effects ZPE) would not suffice to drive the overall (inverse) KIE below 0.95. It would take much higher values of KIE > 10 in k_{-2} in order to rationalize an overall observable KIE < 0.5. Such high KIE values for k_{-2} are likely caused by H/D tunneling. Taking all elementary process up to here together (k_1, k_{-1}, k_2, and k_{-2}), a significant normal KIE in k_{-2} may occur in backwards direction towards reactants. The other three rate constants reveal no or little KIE. The first part of Scheme (3.9) (up to here) thus predicts an inverse KIE in the total observable rate constant for adsorption $k_{obs}{}^{adsorb}$– as is indeed observed in the recorded experimental data.

5.   Second C-H bond activation (rate constant k_3). It is possible that a second C-H bond is activated without releasing molecular hydrogen from the cluster adsorbate complex. In this case the second activation stays "invisible" as compared to the prior activation k_2 . In the case of clusters that do yield efficient dehydrogenation, however, its presumed normal KIE (both by ZPE and by tunneling) induces a normal KIE in dehydrogenation (next step). The order of magnitude in the normal KIE of $k_3$may be comparable to the normal KIE in k_{-2}.

6.   Recombination (rate constant k_{-3}). Recombination of the second activated C-H bond is conceivable. It is in competition to the presumably swift desorption (next step), however. Therefore, it is assumed to be negligible. Some normal KIE in backwards direction is conceivable, it would add to the previous KIEs in backward direction without altering observable KIE effects.

7.   Molecular desorption of H_2 (rate constant k_4). The molecular desorption is subject of a small normal KIE that adds on top of the larger normal KIE in k_3.

The combination of the first four listed elementary processes is thus expected to describe the product yields of adsorption. When adding the subsequent three processes a qualitative description of the observable dehydrogenation is expected. The KIEs in both processes – inverse KIE in adsorption and normal DIE in dehydrogenation - should emerge.

In order to corroborate this hypothesis we undertook extended kinetic modeling by solving the kinetic differential equations that resemble Scheme (3.9). We proceeded by variation of normal KIEs in the rate constants k_{-2} and k_3 while keeping all other seven rate constants neutral (KIE = 1). It showed that ZPEs in C-H and Co-H bonds are far too small to model overall inverse KIEs of up to 0.4. Instead, the assumption of contributions to k_{-2} and k_3 from hydrogen/deuterium tunneling (large normal KIEs) sufficed to model an inverse KIE in adsorption of up to 0.4 and below, and a normal KIE in dehydrogenation (DIE > 1). Both effects are stable against a wide variation of 10 < KIE < 100 in k_{-2} and k_3 .

In principle successful – the kinetic modeling of Scheme (3.9) falls short to elucidate dependencies on cluster size and on cluster charge of KIEs and DIEs. Such a large scale endeavor takes additional insight into the enthalpies and entropies of the stationary points and barriers along the dehydrogenation reaction path. On a much smaller scale our own computations reveal some energetics of stationary points along the reaction coordinate of a single combination of cluster size and cluster charge assuming icosahedral (though relaxing) cluster geometries (cf. Fig. S3 in the supplementary material). The found values lend support to the kinetic model in general while the lack of reliable transition state information is to acknowledge.

Despite all efforts, it remains an open question why dehydrogenation is strongly sustained by an intermediate size range of anionic clusters while it is sparse by cationic clusters of all sizes – n=13 exempt. Hidden electronic effects seem likely. The anticorrelation of high dehydrogenation yields (with concomitant large DIE) and reduced KIE in total yields is obvious as a phenomenon. It takes further effort to elucidate.

Summary and conclusions

We investigated the reaction with benzene and benzene-d_6 of size selected cationic cobalt clusters $Co_n{}^+$ and of anionic cobalt clusters $Co_n{}^-$ in the size range n = 3 - 28 in extension of prior work on reaction of transition metal clusters with benzene[14,15]. Dehydrogenation by cationic clusters is sparse, it is ubiquitous in reactions by anionic clusters. Kinetic isotope effects KIE(n) in total reaction rates are inverse and – in part - large, dehydrogenation isotope effects DIE(n) are normal. A multistep

model of adsorption and stepwise dehydrogenation from the precursor adsorbate proves suitable to rationalize the found KIEs and DIEs in principle. Some DFT calculations – though preliminary – lend strong support to the otherwise assumed structures and enthalpies. Particular insights into the effects of charge and of cluster size are largely beyond this model. It is mandatory to spend further efforts in experiment, in modeling and in high level ab initio calculations in order to fully elucidate the Cobalt-benzene model system. Comparison to other transition metal clusters would be beneficial. Such experiments are under way.

Acknowledgment

Associated Content

Supporting Information (see chapter 3.6.):

Figures showing relative partial rate constants for the reaction of Co_n^+ and of Co_n^- with perdeutero-benzene. A scheme for energetics of the benzene cobalt interaction as a function of cobalt sample size. A qualitative scheme of the energetics along the reaction coordinate of C-H bond activations in $Co_n^\pm + C_6H_6$ as compared to $Nb_n^\pm + C_6H_6$ and $Rh_n^\pm + C_6H_6$. Figures of calculated structure of $Co_{13}(C_6H_6)^+$, $Co_{13}(H)(C_6H_5)^+$ and $Co_{13}(H)(H)(C_6H_4)^+$. And the full reference to the Gaussian program package.

References

(1)   Anslyn, E. V.; Dougherty, D. A. *Modern Physical Organic Chemistry*; University Science Books: Sausalito, 2006.

(2)   Kohen, A.; Limbach, H.-H. *Isotope Effects in Chemistry and Biology*; CRC Press: Boca Raton, 2006.

(3)   Johnston, H. S. *Gas Phase Reaction State Theory*; The Ronald Press Company: New York, 1966.

(4)   Wiberg, K. B. *Chem. Rev.* **1955**, *55*, 713-743.

(5)   Melander, L.; Saunders Jr., W. A. *Reaction Rates of Isotopic Molecules*; Wiley: New York, 1980.

(6)   Lu, S.; Lonergan, W. W.; Bosco, J. P.; Wang, S.; Zhu, Y.; Xie, Y.; Chen, J. G. *J. Catalysis* **2008**, *259*, 260-268.

(7)   Yang, J.; Tveten, E. Z.; Chen, D.; Holmen, A. *Langmuir* **2010**, *26*, 16558-16567.

(8)   Patureau, F. W. *Angewandte Chemie - Intern. Ed.* **2012**, *51*, 4784-4786.

(9)   Klinker, E. J.; Shaik, S.; Hirao, H.; Que, L. *Angewandte Chemie – Intern. Ed.* **2009**, *48*, 1291-1295.

(10)   Churchill, D. G.; Janak, K. E.; Wittenberg, J. S.; Parkin, G. *J. Am. Chem. Soc.* **2003**, *125*, 1403-1420.

(11)   (a) Northcutt, T. O.; Wick, D. D.; Vetter, A. J.; Jones, W. D. *J. Am. Chem. Soc.* **2001**, *123*, 7257-7270. (b) Jones, W. D. *Acc. Chem. Res.* **2003**, *36*, 140-146.

(12)   (a) Janak, K. E.; Parkin, G. *J. Am. Chem. Soc.* **2003**, *125*, 6889-6891. (b) Janak, K. E.; Churchill, D. G.; Parkin, G. *ACS Symposium Series* **2004**, *885*, 86-104.

(13)   Porembski, M.; Weisshaar, J. C. *J. Phys. Chem. A* **2000**, *104*, 1524-1531.

(14)   Berg, C.; Beyer, M.; Achatz, U.; Joos, S.; Niedner-Schatteburg, G.; Bondybey, V. E. *J. Chem. Phys.* **1998**, *108*, 5398-5403.

(15)   Pfeffer, B.; Jaberg, S.; Niedner-Schatteburg, G. *J. Chem. Phys.* **2009**, *131*, 194305/1-12.

(16)   Berg, C.; Schindler, T.; Niedner-Schatteburg, G.; Bondybey, V. E. *J. Chem. Phys.* **1995**, *102*, 4870-4884.

(17)   Citir, M.; Liu, F.; Armentrout, P. B. *J. Chem. Phys.* **2009**, *130,054309/1-16*.

(18)   Meyer, F.; Khan, F. A.; Armentrout, P. B. *J. Am. Chem. Soc.* **1995**, *117*, 9740-9748.

(19)   Liu, F. Y.; Li, M.; Tan, L.; Armentrout, P. B. *J. Chem. Phys.* **2008**, *128,194313/1-12*.

(20)   Kapiloff, E.; Ervin, K. M. *J. Phys. Chem. A* **1997**, *101*, 8460-8469.

(21)   Kurikawa, T.; Hirano, M.; Takeda, H.; Yagi, K.; Hoshino, K.; Nakajima, A.; Kaya, K. *J. Phys. Chem.* **1995**, *99*, 16248-16252.

(22)   Xiuyun, Z.; Jinlan, W. *J. Phys. Chem. A* **2008**, *112*, 296-304.

(23)   Gerhards, M.; Thomas, O. C.; Nilles, J. M.; Zheng, W. J.; Bowen, K. H. *J. Chem. Phys.* **2002**, *116*, 10247-10253.

(24)   Yang, S.; Knickelbein, M. B. *J. Chem. Phys.* **1990**, *93*, 1533-1540.

(25)   Billas, I. M. L.; Chatelain, A.; De Heer, W. A. *Science* **1994**, *265*, 1682-1684.

(26)   Xu, X.; Yin, S.; Moro, R.; de, H. W. A. *Phys. Rev. Lett.* **2005**, *95*, 237209/1-4.

(27)   Knickelbein, M. B. *J. Chem. Phys.* **2006**, *125,044308/1-7*.

(28)   Payne, F. W.; Jiang, W.; Emmert, J. W.; Deng, J.; Bloomfield, L. A. *Phys. Rev. B: Condens. Matter Mater. Phys.* **2007**, *75*, 094431/1-10.

(29)   Peredkov, S.; Neeb, M.; Eberhardt, W.; Meyer, J.; Tombers, M.; Kampschulte, H.; Niedner-Schatteburg, G. *Phys. Rev. Lett.* **2011**, *107,233401/1-5*.

(30)   Datta, S.; Kabir, M.; Ganguly, S.; Sanyal, B.; Saha-Dasgupta, T.; Mookerjee, A. *Phys. Rev. B: Condens. Matter Mater. Phys.* **2007**, *76*, 014429/1-11.

(31)   Ma, Q. M.; Liu, Y.; Xie, Z.; Wang, J. *J. Phys.: Conf. Ser.* **2006**, *29*, 163-166.

(32)   Marshall, A. G.; Hendrickson, C. L.; Jackson, G. S. *Mass Spectrom. Rev.* **1998**, *17*, 1-35.

(33)   Maruyama, S.; Anderson, L. R.; Smalley, R. E. *Rev. Sci. Instr.* **1990**, *61*, 3686-3693.

(34)   Proch, D.; Trickl, T. *Rev. Sci. Instr.* **1989**, *60*, 713-716.

(35)   Caravatti, P.; Allemann, M. *Org. Mass Spectrom.* **1991**, *26*, 514-518.

(36)   Graf, M., Diploma Thesis, TU Kaiserslautern, 2006 (unpublished).

(37)   Frisch, M. J.; Trucks, G. W.; Schlegel, H. B. ; Scuseria, G.E.; Robb, M. A.; Cheeseman, J. R.; Scalmani, G.; Barone, V.; Mennucci, B.; Petersson, G.A., *et al,* Gaussian 09, Rev. B.01, Gaussian, Inc., Wallingford CT, 2009

(38)   Adamo, C.; Barone, V. *J. Chem. Phys.* **1999**, *110*, 6158-6170.

(39)   Kaupp, M.; Schleyer, P. V.; Stoll, H.; Preuss, H. *J. Chem. Phys.* **1991**, *94*, 1360-1366.

(40)   (a) Bergner, A.; Dolg, M.; Kuchle, W.; Stoll, H.; Preuss, H. *Mol. Phys.* **1993**, *80*, 1431-141. (b) Dolg, M.; Stoll, H.; Preuss, H.; Pitzer, R. M. *J. Phys. Chem.* **1993**, *97*, 5852-5859.

(41)   Quintal, M. M.; Karton, A.; Iron, M. A.; Boese, A. D.; Martin J. M. L. *J. Phys. Chem. A* **2006**, *110*, 709-716.

(42)   Kummerlöwe, G.; Beyer, M. K. *Int. J. Mass Spectrom.* **2005**, *244*, 84-90.

(43)   Niedner-Schatteburg, G., Habilitation Thesis, TU München, 1996.

(44)   Georgiadis, R.; Fisher, E. R.; Armentrout, P. B. *J. Am. Chem. Soc.* **1989**, *111*, 4251-4262.

(45)   Fisher, E. R.; Armentrout, P. B. *J. Phys. Chem.* **1990**, *94*, 1674-1683.

(46)   Sallans, L.; Lane, K. R.; Squires, R. R.; Freiser, B. S. *J. Am. Chem. Soc.* **1985**, *107*, 4379-4385.

(47)   Elkind, J. L.; Armentrout, P. B. *J. Phys. Chem.* **1986**, *90*, 5736-5745.

(48)   Cassady, C. J.; Freiser, B. S. *J. Am. Chem. Soc.* **1985**, *107*, 1566-1573.

(49)   Allison, J.; Ridge, D. P. *J. Am. Chem. Soc.* **1979**, *101*, 4998-5009.

(50)   Kemper, P. R.; Bushnell, J.; von Helden, G.; Bowers, M. T. *J. Phys.Chem.* **1993**, *97*, 52-58.

(51)   Kemper, P. R.; Bushnell, J.; van Koppen, P.; Bowers, M. T. *J. Phys. Chem.* **1993**, *97*, 1810-1817.

(52)   Hettich, R. L.; Jackson, T. C.; Stanko, E. M.; Freiser, B. S. *J. Am. Chem. Soc.* **1986**, *108*, 5086-5093.

(53)   Vankoppen, P. A. M.; Kemper, P. R.; Bowers, M. T. *J. Am. Chem. Soc.* **1993**, *115*, 5616-5623.

(54)   Luntz, A. C.; Harris, J. *Surface Science* **1991**, *258*, 397-426.

Supplementary material

to

Inverse H/D isotope effects in benzene activation by cationic and anionic cobalt clusters

Matthias Tombers, Lars Barzen and Gereon Niedner-Schatteburg

Fachbereich Chemie and Forschungszentrum OPTIMAS, Technische Universität Kaiserslautern, 67663 Kaiserslautern, Germany

Fig. S1: Relative partial rate constants for the reaction **(a)** of Co_n^+ and **(b)** of Co_n^- with perdeutero-benzene.

Fig. S2: Energetics of the benzene cobalt interaction as a function of cobalt sample size.

Fig. S3: Qualitative scheme of the energetics along the reaction coordinate of C-H bond activations in $Co_n^\pm + C_6H_6$ as compared to $Nb_n^\pm + C_6H_6$ and $Rh_n^\pm + C_6H_6$.

Fig. S4(a): Calculated structure of $Co_{13}(C_6H_6)^+$.

Fig. S4(b): Calculated structure of $Co_{13}(H)(C_6H_5)^+$.

Fig. S4(c): Calculated structure of $Co_{13}(H)(H)(C_6H_4)^+$.

Full reference to the Gaussian program package
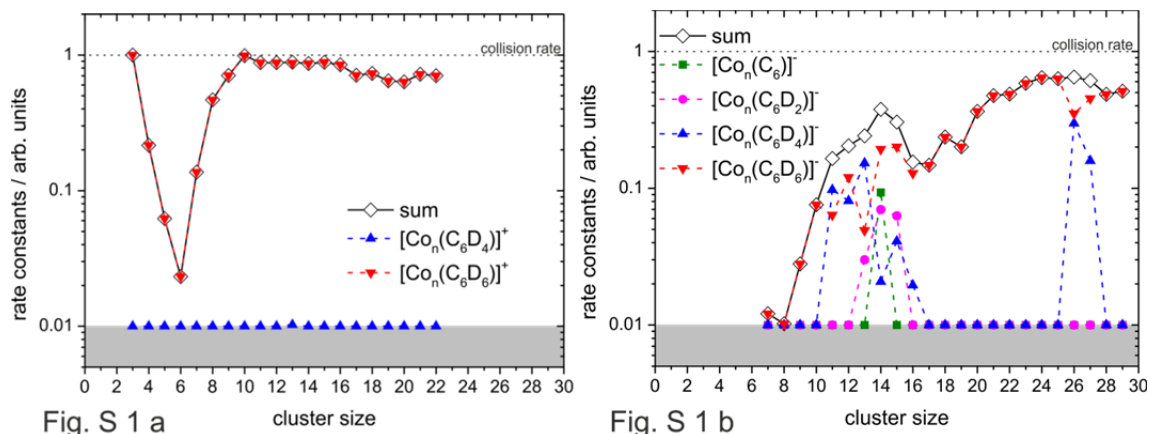
Fig. S1: Relative partial rate constants for the reaction **(a)** of Co_n^+ and **(b)** of Co_n^- with perdeutero-benzene. All values were normalized to the highest rate constant. Total rate constants are provided as well. The shaded areas indicate the background noise level.
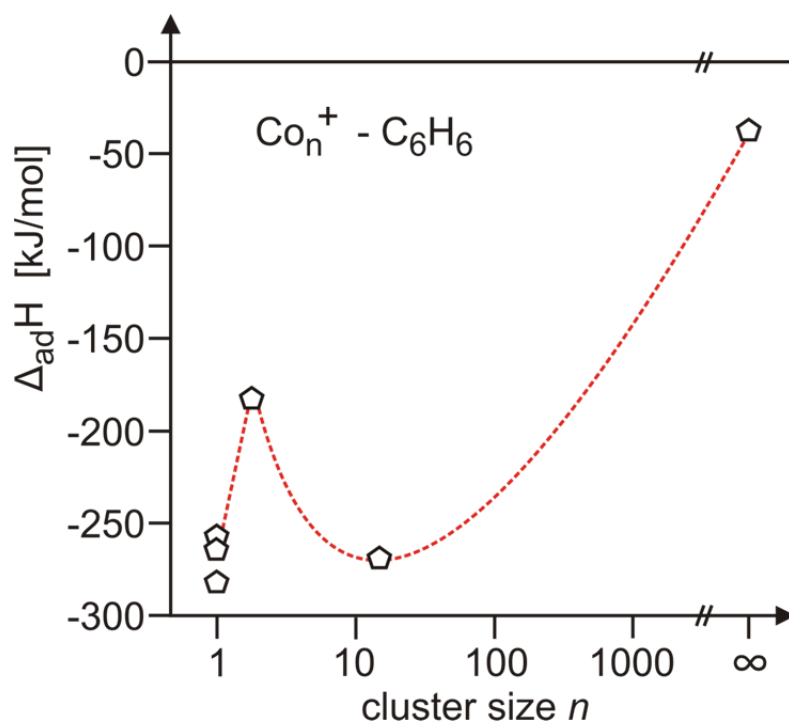
Fig. S2: Energetics of the benzene cobalt interaction as a function of cobalt sample size. Indicated value at n=1 see: B. Freiser: *Organometallic Ion Chemistry*, Kluwer Academic Publishers, Dodrecht 1996; at n = 2: F. Meyer, F. Khan, and P. Armentrout, J. Am. Chem. Soc. **117**, 9740 (1995); at n = 13: this work (DFT calc.) ; at n = ∞ see: S. Lu, C. A. Menning, Y. Zu, and J. G. Chen, Chem. Phys .Chem. **10**, 1763 (2009)
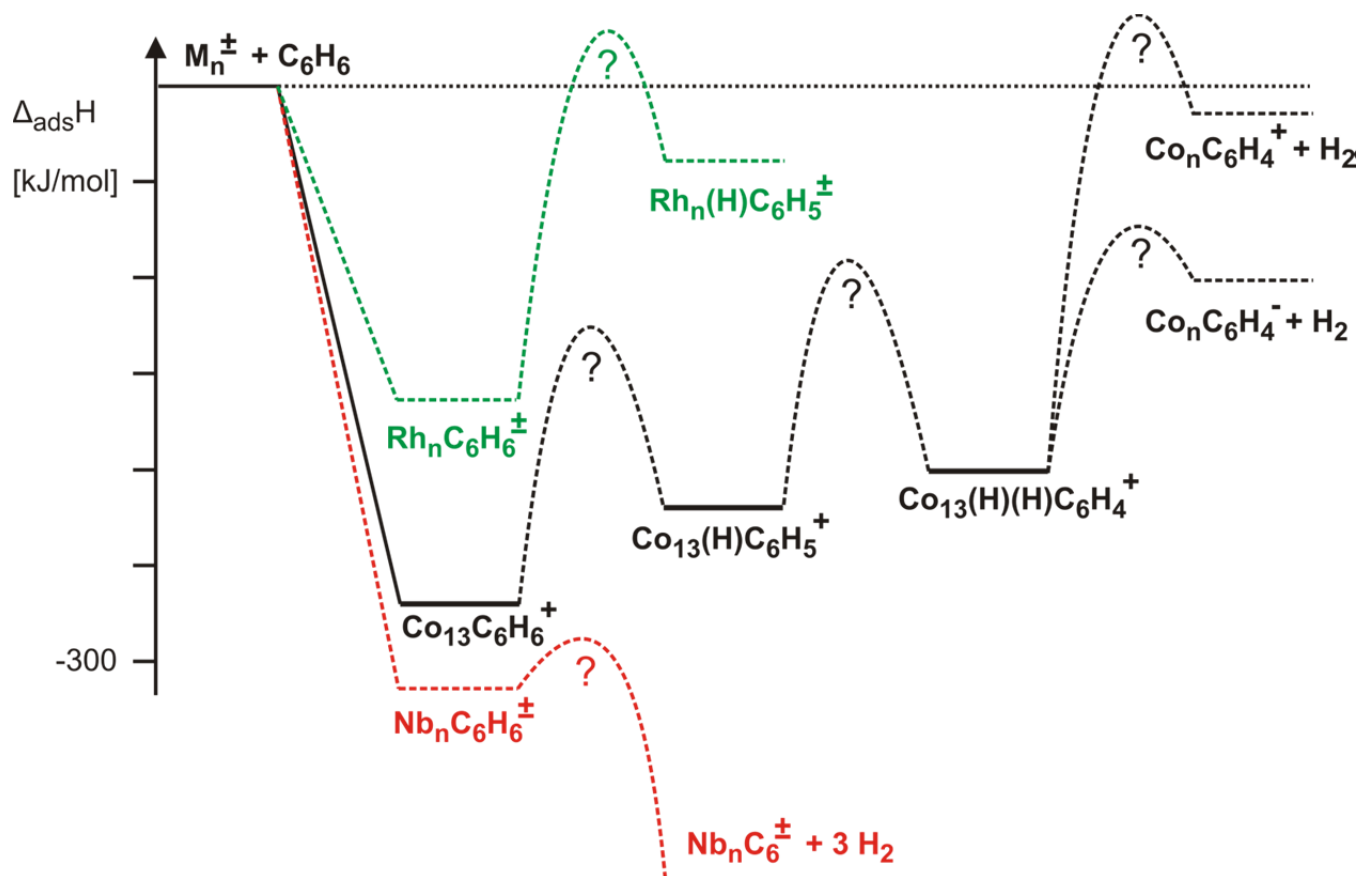
Fig. S3: Qualitative scheme of the energetics along the reaction coordinate of C-H bond activations in $Co_n^\pm + C_6H_6$ (black line) as compared to $Nb_n^\pm + C_6H_6$ (dashed red line) and $Rh_n^\pm + C_6H_6$ (dashed green line). Niobium readily activates benzene while Rhodium adsorbs without activation. Neither of both reveals considerable KIEs – irrespective of charge or cluster size. Benzene activation by Cobalt clusters is in between and gives rise to KIEs – largely independent of charge and across an intermediate range of cluster sizes. Calculated enthalpies of intermediates along the reaction coordinate of dehydrogenation in $[Co_{13}, C_6H_6]^+$ are indicated in bold – no corresponding values known in the cases of Rhodium or Niobium. Other charge states and other cluster sizes of $Co_n^\pm$ may possess shift values of these enthalpies. The Cobalt related part of the diagram closely resembles Scheme (9) within the text body of the publication.
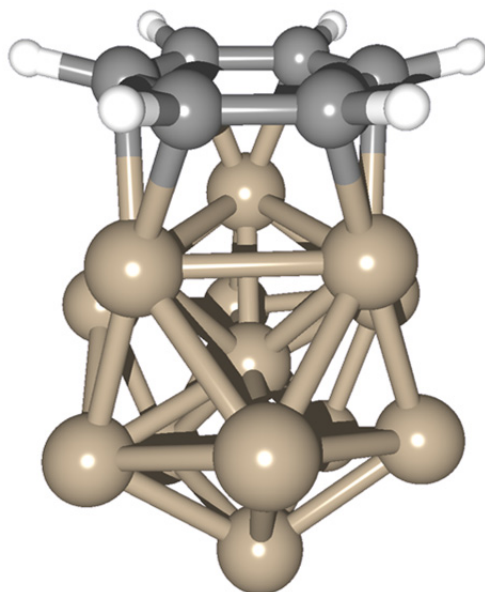
Fig. S4(a): Calculated structure of $Co_{13}(C_6H_6)^+$. All structures are predicted to possess likely high spin ground electronic states that comprise 14 unpaired electrons. Calculations are preliminary, and a systematic verification is pending.
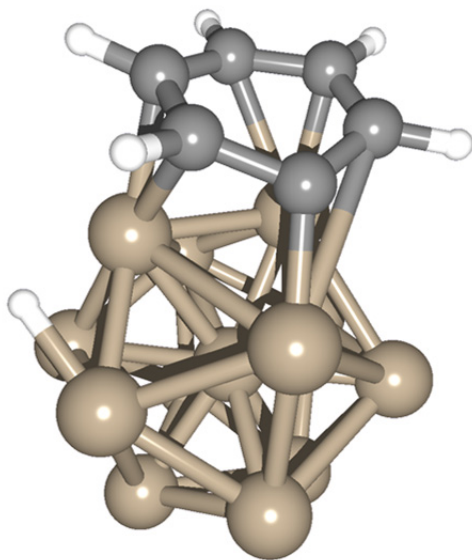
Fig. S4(b): Calculated structure of $Co_{13}(H)(C_6H_5)^+$. All structures are predicted to possess likely high spin ground electronic states that comprise 14 unpaired electrons. Calculations are preliminary, and a systematic verification is pending.
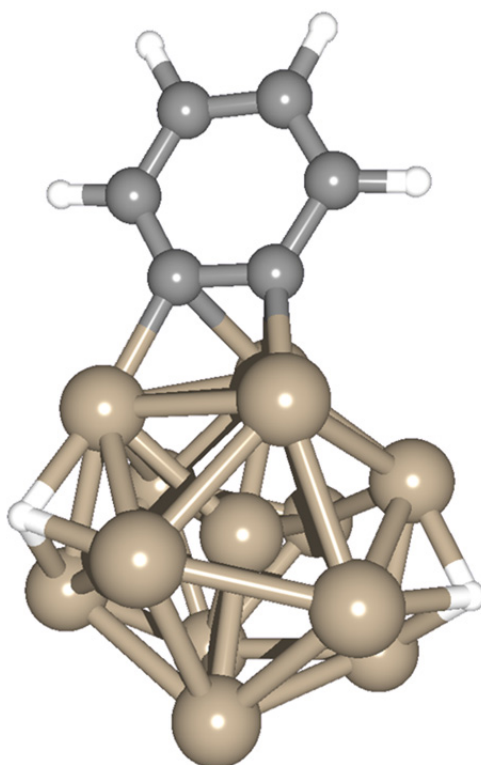
Fig. S4(c): Calculated structure of $Co_{13}(H)(H)(C_6H_4)^+$. All structures are predicted to possess likely high spin ground electronic states that comprise 14 unpaired electrons. Calculations are preliminary, and a systematic verification is pending.

Full reference to the Gaussian program package:

Gaussian 09, Revision **B.01**, Frisch, M. J.; Trucks, G. W.; Schlegel, H. B.; Scuseria, G. E.; Robb, M. A.; Cheeseman, J. R.; Scalmani, G.; Barone, V.; Mennucci, B.; Petersson, G. A.; Nakatsuji, H.; Caricato, M.; Li, X.; Hratchian, H. P.; Izmaylov, A. F.; Bloino, J.; Zheng, G.; Sonnenberg, J. L.; Hada, M.; Ehara, M.; Toyota, K.; Fukuda, R.; Hasegawa, J.; Ishida, M.; Nakajima, T.; Honda, Y.; Kitao, O.; Nakai, H.; Vreven, T.; Montgomery, Jr., J. A.; Peralta, J. E.; Ogliaro, F.; Bearpark, M.; Heyd, J. J.; Brothers, E.; Kudin, K. N.; Staroverov, V. N.; Kobayashi, R.; Normand, J.; Raghavachari, K.; Rendell, A.; Burant, J. C.; Iyengar, S. S.; Tomasi, J.; Cossi, M.; Rega, N.; Millam, J. M.; Klene, M.; Knox, J. E.; Cross, J. B.; Bakken, V.; Adamo, C.; Jaramillo, J.; Gomperts, R.; Stratmann, R. E.; Yazyev, O.; Austin, A. J.; Cammi, R.; Pomelli, C.; Ochterski, J. W.; Martin, R. L.; Morokuma, K.; Zakrzewski, V. G.; Voth, G. A.; Salvador, P.; Dannenberg, J. J.; Dapprich, S.; Daniels, A. D.; Farkas, Ö.; Foresman, J. B.; Ortiz, J. V.; Cioslowski, J.; Fox, D. J. Gaussian, Inc., Wallingford CT, 2009.

8.2 Publication: Benzene activation and H/D isotope effects in reactions of mixed cobalt platinum clusters: The influence of charge and of composition

The following work has been published in *The International Journal of Mass Spectrometry* with the title: *"Benzene activation and H/D isotope effects in reactions of mixed cobalt platinum clusters: The influence of charge and of composition"* within the special issue dedicated to Peter B. Armentrout on the occasion of his 60th birthday. The text of the publication was mainly written by Lars Barzen and is part of his doctoral thesis. Measurements and data evaluation were done by Lars Barzen, Christine Merkert, Joachim Hewer and me. Structural and energetic calculations were made by Gereon Niedner-Schatteburg.

Full reference to the publication:

L. Barzen, M. Tombers, C. Merkert, J. Hewer, G. Niedner-Schatteburg, Benzene activation and H/D isotope effects in reactions of mixed cobalt platinum clusters: The influence of charge and of composition, International Journal of Mass Spectrometry, 330 (2012) 271-276.

Benzene activation and H/D isotope effects in reactions of mixed cobalt platinum clusters: the influence of charge and of composition

Lars Barzen, Matthias Tombers, Christine Merkert, Joachim Hewer and Gereon Niedner-Schatteburg

Fachbereich Chemie and Forschungszentrum OPTIMAS, Technische Universität Kaiserslautern, 67663 Kaiserslautern, Germany

Abstract

A dedicated ion trap served to investigate the reaction with benzene and benzene-d_6 under single collision conditions of size selected bimetallic cobalt platinum clusters $Co_nPt_m^{\pm}$ in the size range n + m ≤ 8. Dehydrogenation by cationic cobalt clusters Co_n^+ is sparse, it is effective in small bimetallic clusters $Co_nPt_m^+$, n + m ≤ 3. Single platinum atoms promote benzene dehydrogenation while further cobalt atoms quench it. Mixed triatomic clusters $Co_2Pt_1^-$ and $Co_1Pt_2^-$ are special in causing effective reactions in a cooperative way. Kinetic Isotope Effects KIE(n) in total reaction rates are inverse and – in part – large, Dehydrogenation Isotope Effects DIE(n) are normal. A multistep model of adsorption and stepwise dehydrogenation from the precursor adsorbate proves suitable to rationalize the found KIEs and DIEs in principle. The pronounced influence of cluster charge and of cluster composition demands for further investigation.

Introduction

Bimetallic transition metal clusters may serve as model systems for the elucidation of elementary processes in heterogeneous catalysis. Hydrocarbon adsorption and subsequent C-H bond activation are amongst the most important steps in many catalyzed reactions, and either is often rate limiting. Cobalt has numerous applications as heterogeneous catalyst based on its redox properties that allow for ease of electron transfer via unstable intermediates [1]. Platinum is well known for its capability to cause catalytic hydrogenation and/or dehydrogenation of many functional groups at low temperature [1]. In batch and flow reactor studies bimetallic PtCo catalysts are more active in benzene hydrogenation than monometallic Co and Pt catalysts [2]. The activity showed to follow the

trend: PtCo >> PdCo > RuCo ~ Pt ~ Co ~ Ru ~ Pd [3]. Cobalt monolayers on bulk platinum exhibited low temperature hydrogenation properties e.g. on cyclohexene [4]. Transition metal cluster alloys have found application as oxygen-reduction catalyst in the polymer electrolyte membrane of fuel-cells to improve and reduce platinum loading [5-7]. Magnetic cobalt platinum nanoparticles are considered suitable media for ultra-high density magnetic recording [8]. An introductory overview over recent work on cobalt platinum nano particles can be found elsewhere [9].

Prior gas phase studies of benzene adsorption and activation focused on niobium and rhodium clusters [10-12]. Vivid dehydrogenation through niobium cluster cations and anions alike contrast to mere adsorption by $Rh_n^\pm$. Little to no observable isotope effects prevailed in either cases. Prior ion trap investigations revealed catalytic dehydrogenation of saturated and aromatic cyclic hydrocarbons by small platinum clusters Pt_n^+ , $n \le 4$ [13]. Methane activation through platinum clusters proved sensitive to their charge states and/or structures with n = 4 behaving special [14], and a normal H/D isotope effect in dehydrogenation was found subsequently [15].

The relative scale of binding strength in complexes of atomic transition metal is established well. Armentrout et al. have conducted multiple guided ion beam studies and found the following trends in binding energies: $[Pt\text{-}CH_3]^+$ > $[Co\text{-}CH_3]^+$ > $[Rh\text{-}CH_3]^+$ and $[Pt\text{-}H]^+$ > $[Co\text{-}H]^+$ > $[Rh\text{-}H]^+$ [16-22]. In a recent study with complexed platinum cations they found the thermal C-H bond activation of benzene reversible [23]. By guided beam studies of cobalt cluster cations Armentrout et al. obtained cluster binding energies [24], deuteride - cluster binding energies [25] and methyl - cluster binding energies [26].

Density functional theory showed capable to allow for structural predictions on small neutral and anionic cobalt clusters $Co_n^{0,-}$,n ≤ 6 [27] and of neutral cobalt-platinum "nanoalloy" clusters Co_nPt_m , n + m ≤ 5 [9]. Triangular, rhombic and trapezoidal structures prevailed.

Our present study serves to investigate the reactions of benzene C_6H_6 and perdeutero benzene C_6D_6 under single collision conditions with isolated bimetallic cobalt platinum clusters $Co_nPt_m^\pm$, n + m ≤ 8, by application of Fourier-Transform Ion-Cyclotron-Resonance (FT-ICR) mass spectrometry.

Material and methods

The experiments were performed with a modified Fourier-Transform Ion-Cyclotron-Resonance (FT-ICR) mass spectrometer (Bruker Apex III). We generated the mixed cobalt platinum clusters with a homebuilt laser vaporization source (LVAP) as described before [12, 28]. The second harmonic of a pulsed Continuum Nd-YAG laser is used to evaporate off atoms from a 0.4 – 1.0 mm thick rotating

Cobalt Platinum alloy target (HMW Hauner, Co:Pt molar ratio of 2:1). The emerging metal plasma is cooled and made to yield clusters by a short transverse pulse (40 µs, Helium, 8-15 bar) from a homebuilt piezoelectric valve [29]. Further cooling arises from the subsequent supersonic nozzle expansion through a 20 mm long channel (diameter of 2 mm) into vacuum (10^{-6} mbar). There is no further ionization step in addition. All investigated ions are generated within the laser induced plasma. Unfortunately, the current ion source yielded neither Pt_2^+ nor Pt_3^+ clusters while utilizing the present mixed metal target. Future experiments with a pure platinum target will help this.

Past a 1.4 mm diameter skimmer the cold cluster ions are accelerated, fed into a cw quadrupole ion bender (90^0) and steered by electrostatic lenses into the high field region of a superconducting magnet (7.05 Tesla, actively shielded) while appropriately decelerated. Eventually, the cluster ions are trapped for reaction and/or detection within the FT-ICR cell of so called "infinity" type [30].

Internal degrees of freedom of the cluster ions are relaxed to sub thermal energies through the supersonic expansion in the cluster source. Kinetic energies of the heavy cluster ions is limited by the storage in the ion trap to $E_{kin,lab}$ < 0.5 eV (laboratory frame value). In collisions with light neutral gases the collision energies in the center of mass frame amount to quasi thermal values $E_{kin,cm}$ ~ 0.1 eV and below.

In order to pursue the reactivity studies with benzene (C_6H_6) / benzene-d$_6$ (C_6D_6) we permitted the controlled admission of a reaction gas in order to raise the pressure in the ultrahigh vacuum chamber of the FT-ICR mass spectrometer, where the ICR trapping cell is located, from ~ 3 x 10^{-10} to typically 1-5 x 10^{-9} mbar such that a single bimolecular reactant collision per cluster per second takes place (single collision conditions). A commercial ultrahigh vacuum gauge (cold cathode gas discharge, calibrated for N_2) provides for a nominal pressure reading. Commercially available benzene/benzene-d$_6$ (Sigma-Aldrich, purity ≥ 99.6 %) was applied after degassing by multiple "pump and freeze" cycles. Kinetic curves of reactant and product ions extract from mass spectra of trapped cluster ions while exposed to the cw admitted reactant gases and under variation of reaction delays between cluster ion admission and detection. Fits to pseudo-first-order-kinetics arise through a genetic algorithm ("evofit" program [31]).

An exact absolute calibration of the reactant gas pressure at the location of the ICR cell is at present not possible. There is a pressure gradient between gauge and ICR cell of about a factor of 4, the exact value not being known, and most likely depending on the chemical nature of the prevailing neutral gas. Gauging against known reactions is conceivable, in principle, and tedious, in practice. There are few absolute rate constants of bimolecular reactions of small molecular ions with neutral benzene published. None of these ions is accessible with the current ICR setup for technical reasons, however.

Reactions of benzene cations with benzene and other hydrocarbon molecules were shown to vary largely depending on the ion precursor [32]. Future attempts in gauging the absolute reactant gas density of the present ICR setup are pending. For the time being we rely on the evaluation of relative rate constants that compare against each other. From studies of large cobalt clusters up to Co_{28}^+ with benzene it may be concluded that the fastest observed reaction rates come close to collision rate. This would relate to a benzene to cobalt surface sticking coefficient of unity, and we have normalized the recorded relative rate constants accordingly. The noise equivalent detection limit of the relative rate constants amounts to k ≈ 0.0025.

We pursued accompanying *ab initio* modeling of clusters and products by density functional theory (DFT). We utilize a level of theory that is similar to our study on pure cobalt clusters. A combination of the Stuttgart relativistic effective core potentials for Co and Pt with cc-pVDZ basis sets for carbon and hydrogen [33-35] proved appropriate in conjunction with the PBE0 hybrid exchange correlation functional [36] as implemented in the Gaussian 09 program suite [37]. No effort was made to cover all cluster sizes. Instead we focused onto stationary points of the $^M[Co_nPt_m, C_6H_6]^+$ potential hypersurfaces with n + m = 3 and variation of the spin state multiplicity M. Full coverage of these investigations remains to a future publication[38] while some preliminary results will be discussed here as needed.

Results and discussion

The recorded kinetics reveal that pure cobalt clusters $Co_nPt_m^\pm$, m = 0, react with benzene to form a single type of products:

$$Co_n^\pm + C_6(H,D)_6 \rightarrow [Co_nC_6(H,D)_6]^\pm \qquad (4.1)$$

This holds for both cationic clusters as well as for anionic clusters, and for reactions with benzene C_6H_6 and perdeutero benzene C_6D_6 alike. Dehydrogenation does not take place up to the limit of sensitivity of this experiment in the range of n = 3 - 10 − with the $Co_{9,10}^- + C_6H_6$ cases exempt, where some additional products form ($[Co_{9,10}C_6H_4]^-$, see eq. 4.2b below). Indication of the product species in (4.1) in square parenthesis shall indicate the ambiguity in its molecular structure. While the sum formula is well determined through the high resolution mass detection its structure, of course, is not. It is well conceivable, that benzene does react beyond mere attachment to the cobalt cluster. It may well have experienced activation of some C-H bond thereby forming a hydrido phenylic complex of the form $Co_n(H)C_6H_5^\pm$. Activation of multiple C-H bonds would induce a subsequent pair wise recombination of the hydridic H-atoms and desorption of molecular H_2. While this is not observed

either the benzene adsorbate cluster complex or the hydrido phenylic complex stabilize radiatively on the long run. Anionic cobalt cluster cations may stabilize by electron detachment, in addition. As of now, we do not have evidence for such processes in the current case.

Mixed cationic and anionic clusters $Co_nPt_m^{\pm}$, n,m ≥ 1, react with benzene C_6H_6 and with perdeutero benzene C_6D_6 either through association (4.2a) or through dehydrogenation (4.2b):

$$Co_nPt_m^{\pm} + C_6(H,D)_6 \rightarrow [Co_nPt_mC_6(H,D)_6]^{\pm} \qquad (4.2a)$$

$$\rightarrow [Co_nPt_mC_6(H,D)_4]^{\pm} + (H,D)_2 \qquad (4.2b)$$
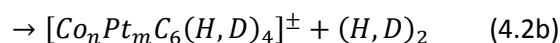
The ratio of both varies with cluster size, with cluster charge and somewhat with the reactant. No products of reactions were observed that would proceed beyond single dehydrogenation (4.2b). In particular, there was no evidence for loss of odd numbers of H-atoms or for loss of more than a single molecule of H_2. It is therefore most likely that a single molecular hydrogen evolves per encounter of cluster and reactant. Seemingly, C-H and C-D bond activation ceases after two instances per benzene molecule at most.
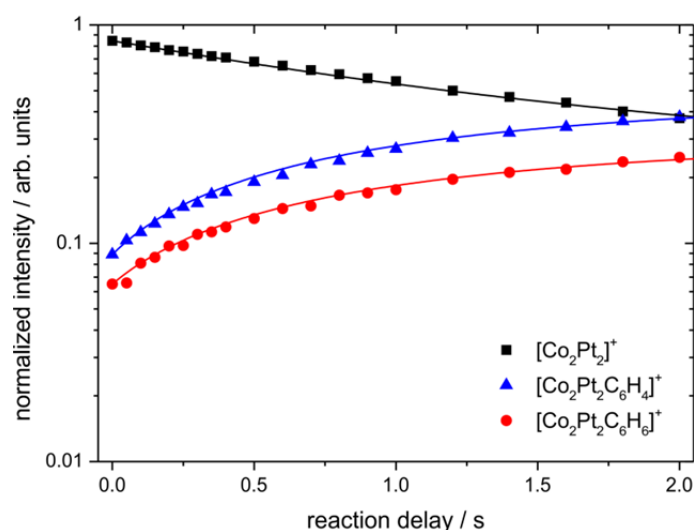
Fig. 1: *An example for the reaction kinetics of $Co_2Pt_2^{+}$ (black, squares) with C_6H_6. Symbols represent experimental data, solid lines represent numerical fits by a genetic algorithm to pseudo first order kinetics. Association (red, circles) and dehydrogenation (blue, triangles) take place in parallel.*

Fitting the recorded kinetics (cf. e.g. in the case of $Co_2Pt_2{}^+$ + C_6H_6 at Fig. 1) yields relative partial rate constants for association and for dehydrogenation, and the relative total rate constants.
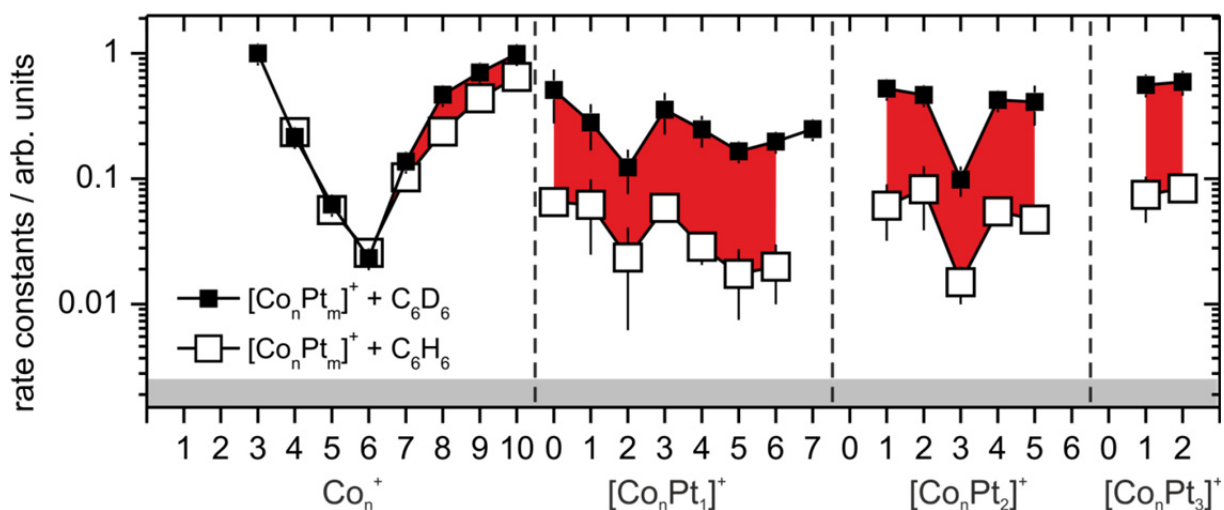
Fig. 2: *Total rate constants for the reaction of $Co_nPt_m{}^+$ with benzene (open symbols) and perdeutero benzene (solid symbols). The observed inverse Kinetic Isotope Effect (KIE) is emphasized by red shading of the areas in between of the corresponding rate constants. The noise equivalent level of the present experiments is indicated by grey shading.*

Total reaction rates with benzene and with perdeutero benzene of pure cationic cobalt clusters $Co_n{}^+$ reveal a pronounced size dependence. The rates of $Co_6{}^+$ diminish by a factor of 40 with respect to larger and smaller clusters. The very cause is unknown while numerous speculations arise. A drop with cluster size in the total association rate of alkanes on small niobium cluster cations was attributed before to an increase of coordinative saturation and a concomitant drop of reactivity [10]. In principle such an argument might hold for the case of cobalt as well. In reactions with benzene the same study found a rise in total reaction rate upon increase of the size of these clusters, possibly due to the rise in heat capacity that helps to dissipate the released heat of adsorption. A combination of both counteracting effects, however, was not observed up to now in the reactions of transition metal clusters.

Notably there is little difference whether reacting benzene C_6H_6 or perdeutero benzene C_6D_6. It is common practice to discuss such differences in terms of a Kinetic Isotope Effect (KIE) defined as the ratio of hydrogenic rate constant $k_{tot}{}^{(H)}(n)$ and perdeutero rate constant $k_{tot}{}^{(D)}(n)$:

$$KIE(n) = \frac{k_{tot}^{(H)}(n)}{k_{tot}^{(D)}(n)} \qquad (4.3)$$

Normal KIE > 1 or inverse KIE < 1 elucidate indirectly the underlying micro kinetics. (Throughout all of this paper blue and red colors code for normal and inverse KIEs). In the present case of Co_n^+ + C_6H_6/C_6D_6 reactions, the KIE is small (< 0.5) and inverse.
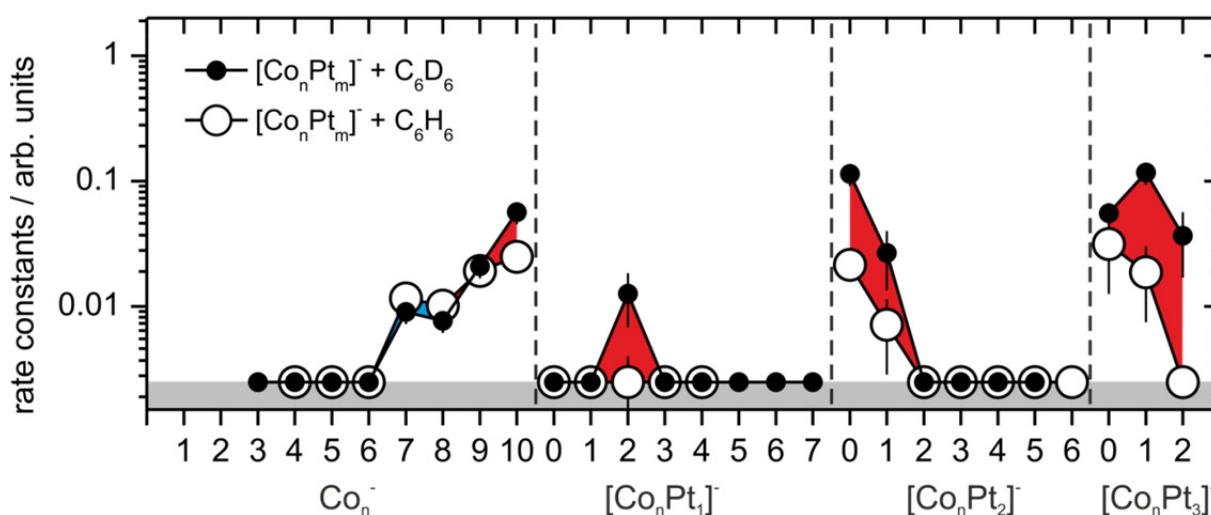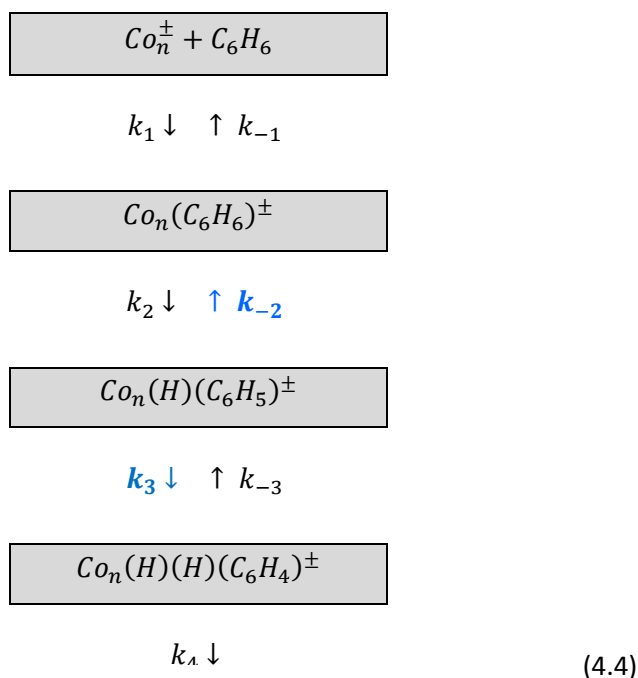

Fig. 3: *Total rate constants for the reaction of $Co_nPt_m^-$ with benzene (open symbols) and perdeutero benzene (solid symbols). The observed inverse Kinetic Isotope Effect (KIE) is emphasized by red shading of the areas in between of the corresponding rate constants. Some normal KIE is signified by blue shading. The noise equivalent level of the present experiments is indicated by grey shading.*

Anionic cobalt clusters Co_n^- with n ≤ 6 do not yield observable products while collisions with benzene inevitably take place at collision rates that are high enough to allow for detection of products down to 1% collision efficiency. Adsorption induced electron detachment is a conceivable reason, while our recorded data do not provide evidence for such a "dark" reaction channel. Further insight could arise from the inspection of size dependencies in heats of adsorption $\Delta_{ads}H(Co_n^- - C_6H_6)$ and in electron detachment enthalpies $\Delta_{detach}H([Co_nC_6H_6]^-)$ of all conceivable isomers, none of which is known as of now. Instead, basic thermodynamics regards the cluster as a finite heat bath that serves to dissipate the heat of adsorption. The more effective the dissipation the less probable becomes the benzene eventually evaporating off the cluster. With increasing cluster size the total adsorption efficiency improves. The rises in adsorption efficiency are apparent in the rate

constants of anionic clusters Co_n^- , n ≥ 7. The according reactions of Co_n^- with C_6D_6 reveal a small inverse KIE (< 0.5) with n = 7,8 exempt (normal KIE).

We have most recently undertaken a systematic evaluation of KIEs in cobalt cluster reactions with benzene and worked out a multi-step reaction model (4.4) that managed to explain this somewhat surprising finding [39]. The argumentation runs – in short – as follows:

$$Co_n^{\pm} + C_6H_6$$

$$k_1 \downarrow \quad \uparrow k_{-1}$$

$$Co_n(C_6H_6)^{\pm}$$

$$k_2 \downarrow \quad \uparrow \mathbf{k_{-2}}$$

$$Co_n(H)(C_6H_5)^{\pm}$$

$$\mathbf{k_3} \downarrow \quad \uparrow k_{-3}$$

$$Co_n(H)(H)(C_6H_4)^{\pm}$$

$$k_4 \downarrow \qquad\qquad (4.4)$$

Scheme (4) equally holds for reactions with C_6D_6. The observable reactions of association and of dehydrogenation comprise the consecutive elementary processes: adsorption and desorption (k_1 and k_{-1}), C-H bond activation and its recombination (k_2 and k_{-2}), second C-H bond activation and its recombination (k_3 and k_{-3}), and molecular desorption of H_2 (k_4). Most of these processes provide for little to no KIE (for more detail see [39]). Merely the C-H recombination (k_{-2}) and the second C-H activation (k_3) provide for a normal KIE, in part due to zero point effects and mostly due to strong mass effects in H/D tunneling. Altogether the combination of KIEs from these seven elementary processes results in an observable inverse KIE for association and in a normal KIE for dehydrogenation – as indeed observed in the experiments with pure cobalt clusters up to n = 27 [39].

When doping cobalt clusters with a single platinum atom or with a few platinum atoms one obtains mixed clusters $Co_nPt_m^{\pm}$, at present with n ≤ 7 and m ≤ 3. These mixed clusters undergo – in principle – the same reactions (4.2a,b) as pure cobalt clusters.

Once more, there is no reaction observed that would go beyond single dehydrogenation (4.2b). Differences with respect to the pure clusters arise as follows: The remarkable size dependence of cationic rates diminishes in the reactions of mixed clusters. The inverse KIE persists in the mixed clusters, and it increases significantly as compared to the inverse KIE of pure cobalt clusters. Anionic mixed clusters are less reactive by more than an order of magnitude (cf. Figs 2 and 3). While pure anionic cobalt clusters set in to react at n = 7 and beyond, only small mixed clusters of five atoms at most react at all. These are namely $Co_2Pt_1{}^-$, $Co_1Pt_2{}^-$, $Co_1Pt_3{}^-$, $Co_2Pt_3{}^-$, and the pure platinum clusters $Pt_2{}^-$ and $Pt_3{}^-$. Inverse KIEs prevail throughout, and they are larger in anionic mixed clusters than in pure cobalt clusters.

It is worthwhile to deliberate on the likely origin of the enhanced inverse KIEs in heterogeneous clusters. As a starting point one may assume the previous micro kinetic model of scheme (4.4) valid for heterogeneous clusters as well. If so then it is once more the recombination of the hydridic hydrogen atom with the phenyl ligand (microscopic rate constant k_{-2} in scheme (4.4)) which is subject to a normal KIE (in backwards direction). The platinum heteroatom would enhance this KIE which implies that platinum would drive hydrogenation more efficiently than cobalt – as is anticipated by prior studies (cf. introduction). Moreover the experiments with pure anionic platinum clusters show efficient dehydrogenation of benzene (4.2b). Namely Pt_2^- reacts efficiently with either benzene or perdeutero benzene as compared to $CoPt^-$ which does not provide for any reaction rate within our experimental uncertainties. Similarly, Pt_3^- readily reacts effectively with either benzene or perdeutero benzene while $CoPt_2^-$ does so slowly if at all. The thus emerging picture of a more efficient hydrogen release from heterogeneous clusters – in conjunction with the inverse KIE in the total overall reaction rates – furthermore implies large tunneling contributions to k_{-2}. This is the major cause of the normal KIE > 7 in k_{-2} which in turn explains the inverse KIE in the overall reaction. $Co_nPt_2^-$ only reacts as long as n ≤ 1. This particular cooperativity of small heterogeneous metal clusters of at most three atoms is noteworthy.

Association (4.2a) and dehydrogenation (4.2b) are competing parallel reactions. The branching ratio amongst both varies with size, charge and composition of clusters, and with the deuteration of benzene. In order to discuss the degree of activation and to provide for some data reduction, we define a so called "average degree of dehydrogenation" $\langle \chi_n \rangle$ as before [40]:

$$\langle \chi_n \rangle = \frac{1}{m} \frac{1}{k_n^{tot}} \sum_{m_i=1}^{m} m_i k_n(m_i) \qquad (4.5)$$

with

$$k_n^{tot} = \sum_i k_n(m_i) \qquad (4.6)$$

Here, m (= 6 in the present case) indicates the total amount of hydrogen or deuterium atoms as available from C_6H_6/C_6D_6. The partial reaction rate $k_n(m_i)$ classifies according to the cluster size n and the loss of hydrogen or deuterium atoms m_i in the observed product. $\langle \chi_n \rangle = 1$ would indicate complete dehydrogenation, $\langle \chi_n \rangle = 0$ would indicate adsorption without any dehydrogenation.
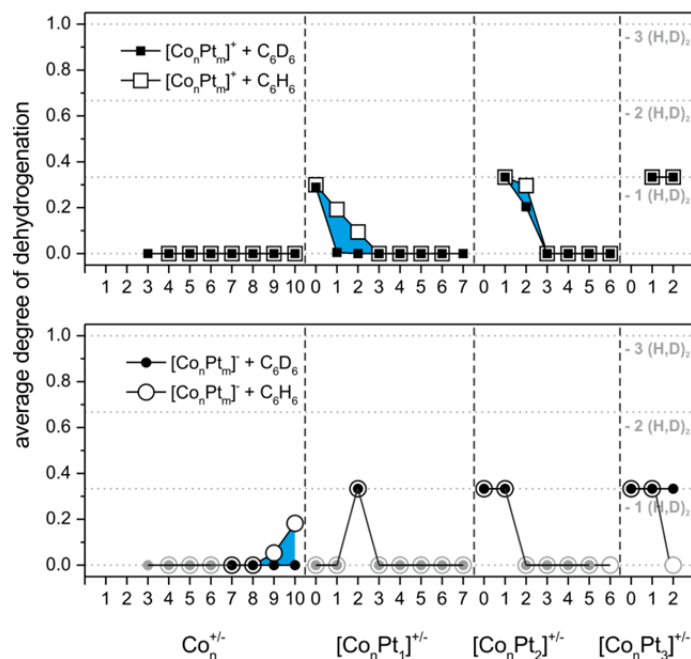

Fig. 4: *Average degree of dehydrogenation $\langle \chi_n \rangle$ (a) by pure and mixed cationic clusters and (b) by pure and mixed anionic clusters. Blue areas indicate a normal Dehydrogenation Isotope Effect (DIE > 1). Those $\langle \chi_n \rangle = 0$ values that are indicated in grey arise from vanishing total reaction rates $k_{tot}(n) = 0$. Solid symbols represent reaction with C_6D_6, open symbols with C_6H_6. Uncertainties are within the size of the symbols.*

The thus obtained values of $\langle \chi_n \rangle$ range between 0 and 1/3. The latter signifies a branching ratio of (4.2a) : (4.2b) of 0 : 1, in other words: single dehydrogenation only. The observable influence of deuteration is small. We label the kinetic isotope effect on $\langle \chi_n \rangle$ as a Dehydrogenation Isotope Effect (DIE):

$$DIE(n) = \frac{\langle \chi_n^{(H)} \rangle}{\langle \chi_n^{(D)} \rangle} \qquad (4.7)$$

The (few) cases where $DIE(n) \neq 1$ are: $Co_1Pt_2^+$, $Co_2Pt_1^+$, $Co_2Pt_2^+$, Co_9^-, and Co_{10}^-. All of these reveal a normal DIE. From our micro kinetic model of consecutive elementary steps (scheme (4.4)) we recall likely tunneling contributions in hydrogen migration steps k_{-2} (C-H recombination) and k_3 (second C-H activation). The former served to rationalize the inverse KIE in the observed total rates, the latter explains the observation of a normal DIE.

The observed isotope effects, both KIEs and DIEs, are thereby well interpreted - the observed effects of cluster size and of composition remain to discuss. The most pronounced size effects are: (1) the quenching of the total reactivity in anionic cobalt clusters through addition of a single or a few platinum atoms (cf. Fig. 3); (2) the quenching of the average degree of dehydrogenation in small mixed cationic clusters $Co_{1,2}Pt_{1,2}^+$ through addition for single further cobalt atoms (cf. Fig. 4a) ; and (3) the almost "magic" size dependence of the average degree of dehydrogenation in mixed anionic clusters with e.g. $Co_2Pt_1^-$ and $Co_1Pt_2^-$ sticking out as compared to others (cf. Fig. 4b). None of these three effects is accessible to an unambiguous interpretation. They challenge further investigations.
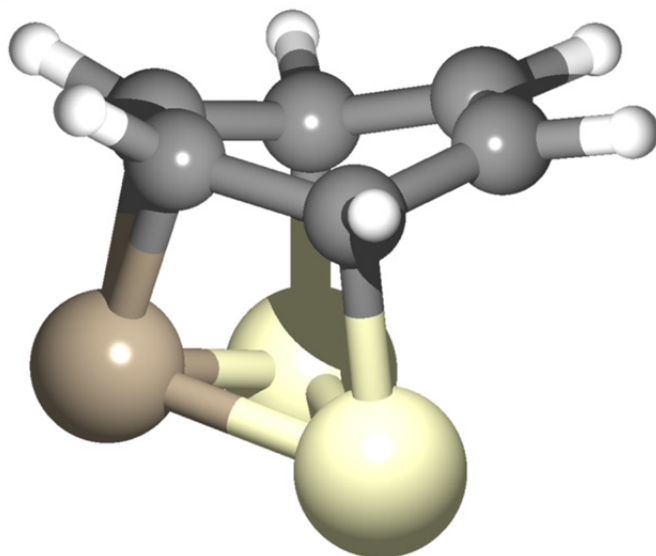
Fig. 5: *A calculated (PBE0/Stuttgart ECP; cc-pVDZ) association complex by example: $Co_1Pt_2(C_6H_6)^-$ in singlet spin state. The cobalt atoms favor η_2 coordination ("on bridge") towards two carbon atoms within the benzene ring. The two platinum atoms favor η_1 coordination ("on top") to single carbon atoms. Some aromaticity is lost by forcing the ring into a non-planar geometry (further discussion see text).*

We have started a systematic *ab initio* approach on structures and energetic of the seemingly "magic" $Co_nPt_m^+$, n + m = 3 case [33-37]. This investigation is still in progress. Some preliminary – yet robust – findings help to elucidate the interaction of these clusters with benzene at this stage: All clusters with cobalt favor high spin states. Cobalt atoms favor η_2 coordination ("on bridge") towards C_2 units in benzene. The coordination and hybridization at the carbon center remains constant before and after coordination, i.e., the C-C π bond is replaced by a metallacycle. Platinum atoms favor η_1 coordination ("on top") to single carbon atoms in benzene. The coordinating C becomes sp^3 hybridized instead of sp^2, which results in the puckering of the ring. This clearly weakens the π bond, creating a radical center at the adjacent carbon atom. The ability to activate a C-H bond in proximity follows. In all cases investigated thus far the side on coordination of a triangular metal cluster with maximum hapticity towards benzene proved most stable (cf. Fig. 5). Single or twofold C-H bond activation with migration of the activated hydrogen onto the metal cluster leads to a tilt of the benzene plane with respect to the metal triangle. It is open as of now whether benzene adsorption induces structural changes of the mixed clusters.

Further support of the experimental findings arise from computed (yet preliminary) enthalpies, confirmation pending. - Benzene dehydrogenation by homogeneous Cobalt cluster cations Co_3^+ seems endoergic, and it is predicted exoergic for mixed cluster cations $Co_2Pt_1^+$ and $Co_1Pt_2^+$:

$$^7Co_3^+ + C_6H_6 \ \rightarrow \ ^7[Co_3C_6H_4]^+ + H_2 \qquad \Delta_rH = +67 \ \frac{kJ}{mol} \qquad (4.8a)$$

$$^6Co_2Pt_1^+ + C_6H_6 \ \rightarrow \ ^6[Co_2Pt_1C_6H_4]^+ + H_2 \qquad \Delta_rH = -6 \ \frac{kJ}{mol} \qquad (4.8b)$$

$$^5Co_1Pt_2^+ + C_6H_6 \ \rightarrow \ ^5[Co_1Pt_2C_6H_4]^+ + H_2 \qquad \Delta_rH = -48 \ \frac{kJ}{mol} \qquad (4.8c)$$
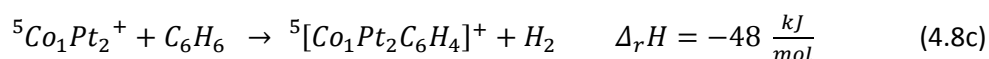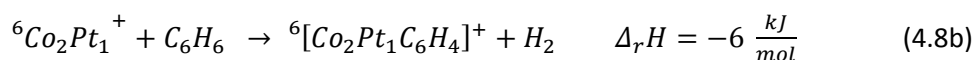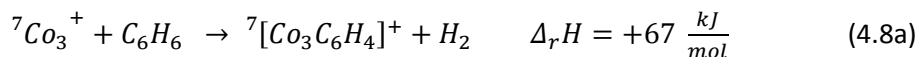
The same high spin multiplicities prevail in reactants and products while other spin states may get involved in the course of the reaction. The influence of spin orbit coupling may be significant in the mixed clusters as induced by the high nuclear charge of platinum. The present level of DFT does not cover this, however. The experimentally observed rise in dehydrogenation efficiency upon replacement of cobalt for platinum is well in agreement with the calculated ergicities at the present – albeit limited – level of theory. A complete documentation and discussion of the ongoing computations remains to a future publication in due time [38].

Summary and conclusions

We investigated the reaction with benzene and benzene-d_6 of size selected bimetallic cobalt platinum clusters $Co_nPt_m^{\pm}$ in the size range n + m ≤ 8 in extension of prior work on reaction of transition metal clusters with benzene [14, 15]. Dehydrogenation by cationic cobalt clusters Co_n^+ is sparse, it is effective in small bimetallic clusters $Co_nPt_m^+$, n + m ≤ 3. Thus single platinum atoms promote benzene dehydrogenation while further cobalt atoms quench it. Mixed triatomic clusters $Co_2Pt_1^-$ and $Co_1Pt_2^-$ are special in causing effective reactions and single dehydrogenation through some kind of cooperativity while $Co_nPt_{1,2}^-$, n ≥ 3 do not react at all.

Kinetic Isotope Effects KIE(n) in total reaction rates are inverse and – in part - large, Dehydrogenation Isotope Effects DIE(n) are normal. A multistep model of adsorption and stepwise dehydrogenation from the precursor adsorbate proves suitable to rationalize the found KIEs and DIEs in principle. Particular insights into the cause of the found effects of charge, size and composition of mixed clusters shall arise from ongoing ab initio modeling of especially the n + m = 3 case. Further experiments are under way as well.

References

[1] B. Cornils, W.A. Hermann, R. Schlögl, C.-H. Wong, Catalysis from A to Z, Wiley-VCH, Weinheim, 2000.

[2] S. Lu, W.W. Lonergan, J.P. Bosco, S. Wang, Y. Zhu, Y. Xie, J.G. Chen, Low temperature hydrogenation of benzene and cyclohexene: A comparative study between γ-Al2O3 supported PtCo and PtNi bimetallic catalysts, Journal of Catalysis, 259 (2008) 260-268.

[3] S. Lu, C.A. Menning, Y. Zhu, J.G. Chen, Correlating Benzene Hydrogenation Activity with Binding Energies of Hydrogen and Benzene on Co-Based Bimetallic Catalysts, Chemphyschem, 10 (2009) 1763-1765.

[4] N.A. Khan, L.E. Murillo, J.G. Chen, Observation of novel low-temperature hydrogenation activity on Co/Pt(III) surfaces, Journal of Physical Chemistry B, 108 (2004) 15748-15754.

[5] V.R. Stamenkovic, B.S. Mun, M. Arenz, K.J.J. Mayrhofer, C.A. Lucas, G. Wang, P.N. Ross, N.M. Markovic, Trends in electrocatalysis on extended and nanoscale Pt-bimetallic alloy surfaces, Nat Mater, 6 (2007) 241-247.

[6] Y. Bing, H. Liu, L. Zhang, D. Ghosh, J. Zhang, Nanostructured Pt-alloy electrocatalysts for PEM fuel cell oxygen reduction reaction, Chemical Society Reviews, 39 (2010) 2184-2202.

[7] S. Mukerjee, S. Srinivasan, Enhanced electrocatalysis of oxygen reduction on platinum alloys in proton-exchange membrane fuel-cells, Journal of Electroanalytical Chemistry, 357 (1993) 201-224.

[8] M.N. Dave, M.L. Wears, J. Michael, C. Desmond, Fabrication and characterization of nano-particulate PtCo media for ultra-high density perpendicular magnetic recording, Nanotechnology, 18 (2007) 205301.

[9] A. Sebetci, Density functional study of small cobalt-platinum nanoalloy clusters, Journal of Magnetism and Magnetic Materials, 324 (2012) 588-594.

[10] C. Berg, M. Beyer, U. Achatz, S. Joos, G. Niedner-Schatteburg, V.E. Bondybey, Effect of charge upon metal cluster chemistry: Reactions of Nb-n and Rh-n anions and cations with benzene, Journal of Chemical Physics, 108 (1998) 5398-5403.

[11] B. Pfeffer, S. Jaberg, G. Niedner-Schatteburg, Reactions of simple aromatic heterocycles with niobium cluster ions (n < 30), Journal of Chemical Physics, 131 (2009).

[12] C. Berg, T. Schindler, G. Niednerschatteburg, V.E. Bondybey, Reactions of simple Hydrocarbons with Nb_n^+ - Chemisorption and Physisorption on Ionized Niobium Clusters, Journal of Chemical Physics, 102 (1995) 4870-4884.

[13] G.S. Jackson, F.M. White, C.L. Hammill, R.J. Clark, A.G. Marshall, Gas-phase dehydrogenation of saturated and aromatic cyclic hydrocarbons by Pt-n(+) (n=1-4), Journal of the American Chemical Society, 119 (1997) 7567-7572.

[14] U. Achatz, C. Berg, S. Joos, B.S. Fox, M.K. Beyer, G. Niedner-Schatteburg, V.E. Bondybey, Methane activation by platinum cluster ions in the gas phase: effects of cluster charge on the Pt-4 tetramer, Chemical Physics Letters, 320 (2000) 53-58.

[15] M.K. Beyer, G. Kummerlowe, I. Balteanu, S. Zheng, O.P. Balaj, V.E. Bondybey, Activation of methane and methane-d 4 by ionic platinum clusters, International Journal of Mass Spectrometry, 254 (2006).

[16] Y.M. Chen, P.B. Armentrout, Activation of C2H6, C3H8, and C-C3H6 by gas-phase Rh+ and the thermochemistry of Rh-ligand complexes, Journal of the American Chemical Society, 117 (1995) 9291-9304.

[17]   Y.M. Chen, J.L. Elkind, P.B. Armentrout, Reactions of Ru+, Rh+, Pd+, and Ag+ with H-2, HD, and D-2, Journal of Physical Chemistry, 99 (1995) 10438-10445.

[18]   R. Georgiadis, E.R. Fisher, P.B. Armentrout, Neutral and ionic metal hydrogen and metal-carbon bond-energies - reactions of Co+, Ni+, and Cu+ with ethane, propane, methylpropane, and dimethylpropane, Journal of the American Chemical Society, 111 (1989) 4251-4262.

[19]   E.R. Fisher, L.S. Sunderlin, P.B. Armentrout, Guided ion-beam studies of the reactions of Co+ and Ni+ with CH3Cl, CH3Br, CH3I - implications for the metal-methyl ion bond-energies, Journal of Physical Chemistry, 93 (1989) 7375-7382.

[20]   Y.M. Chen, D.E. Clemmer, P.B. Armentrout, Conversion of CH4 to CH3OH - reactions of CoO+ WITH CH4 and D-2, Co+ with CH3OD and D2O, and Co+(CH3OD) with Xe, Journal of the American Chemical Society, 116 (1994) 7815-7826.

[21]   X.G. Zhang, R. Liyanage, P.B. Armentrout, Potential energy surface for activation of methane by Pt+: A combined guided ion beam and DFT study, Journal of the American Chemical Society, 123 (2001) 5563-5575.

[22]   J.L. Elkind, P.B. Armentrout, Effect of kinetic and electronic-energy on the reactions of Co+, Ni+, and Cu+ with H-2, HD, and D2, Journal of Physical Chemistry, 90 (1986) 6576-6586.

[23]   B. Butschke, D. Schroeder, H. Schwarz, Thermal C-H Bond Activation of Benzene with Cationic Pt(CX3(L) (+) Complexes in the Gas Phase: A Combined Experimental/Theoretical Study (X = H, D; L=1,10-Phenanthroline, 2,2 '-Bipyrimidine, 2,2 '-Bipyridine, and (o,o '-Cl2C6H3)N=C(CH3)-C(CH3)=N(o,o '-Cl2C6H3)), Organometallics, 28 (2009) 4340-4349.

[24]   S. Goebel, C.L. Haynes, F.A. Khan, P.B. Armentrout, Collision-induced dissociation studies of Co(CO)(X)(+), X=1-5 - sequential bond-energies and the heat of formation of Co(CO)(4), Journal of the American Chemical Society, 117 (1995) 6994-7002.

[25]   F.Y. Liu, P.B. Armentrout, Guided ion-beam studies of the kinetic-energy-dependent reactions of Co-n(+) (n=2-16) with D-2: Cobalt cluster-deuteride bond energies, Journal of Chemical Physics, 122 (2005).

[26]   M. Citir, F. Liu, P.B. Armentrout, Methane activation by cobalt cluster cations, Co-n(+) (n=2-16): Reaction mechanisms and thermochemistry of cluster-CHx (x=0-3) complexes, Journal of Chemical Physics, 130 (2009).

[27]   A. Sebetci, Cobalt clusters (Co(n), n <= 6) and their anions, Chemical Physics, 354 (2008) 196-201.

[28]   S. Maruyama, L.R. Anderson, R.E. Smalley, Direct injection supersonic cluster beam source for FT-ICR studies of clusters, Review of Scientific Instruments, 61 (1990) 3686-3693.

[29]   D. Proch, T. Trickl, A high-intensity multi-purpose piezoelectric pulsed molecular-beam source, Review of Scientific Instruments, 60 (1989) 713-716.

[30]   P. Caravatti, M. Allemann, The infinity cell - a new trapped-ion cell with radiofrequency covered trapping electrodes for Fourier-Transform Ion-Cyclotron Resonance mass-spectrometry, Organic Mass Spectrometry, 26 (1991) 514-518.

[31]   M. Graf, Diploma Thesis, TU Kaiserslautern, Kaiserslautern, 2006

[32]   M.L. Gross, D.H. Russell, R.J. Aerni, S.A. Bronczyk, Ion-molecule reaction chemistry of variousgas-phase C6H6 radical cations, Journal of the American Chemical Society, 99 (1977) 3603-3609.

[33]   M. Kaupp, P.V. Schleyer, H. Stoll, H. Preuss, Pseudopotential approaches to Ca, Sr, and Ba hydrides - why are some alkaline-earth MX2 compounds bent, Journal of Chemical Physics, 94 (1991) 1360-1366.

[34] A. Bergner, M. Dolg, W. Kuchle, H. Stoll, H. Preuss, Ab-initio energy-adjusted pseudopotentials for elements of groups 13-17, Molecular Physics, 80 (1993) 1431-1441.

[35] M. Dolg, H. Stoll, H. Preuss, R.M. Pitzer, Relativistic and correlation-effects for element 105 (Hahnium, Ha) - a comparative-study of M and MO (M=Nb, Ta, Ha) using energy-adjusted abinitio pseudopotentials, Journal of Physical Chemistry, 97 (1993) 5852-5859.

[36] C. Adamo, V. Barone, Toward reliable density functional methods without adjustable parameters: The PBE0 model, Journal of Chemical Physics, 110 (1999) 6158-6170.

[37] M.J. Frisch, G.W. Trucks, H.B. Schlegel, Gaussian 09, in, Gaussian, Inc., Wallingford CT, 2009.

[38] G. Niedner-Schatteburg, unpublished results and work in progress

[39] Tombers, M.; Barzen, L.; Niedner-Schatteburg, G., Inverse H/D isotope effects in benzene activation by cationic and anionic cobalt clusters, Journal of Physical Chemistry A **2013**, 117, 1197.

[40] G. Niedner-Schatteburg, Habilitation Thesis, TU München, Garching, 1996

Danke an meine Freunde für die Unterstützung während der letzten Jahre und die manchmal notwendigen Ablenkungen vom Promotionsstress.

Danke an meine Familie, im Besonderen meinen Eltern, meiner Schwester und meinem Schwager für die Unterstützung und den Rückhalt während meines Studiums und der Promotion.

Lebenslauf

Matthias Tombers

AUSBILDUNG

März 2011 – heute	TU KAISERSLAUTERN, *KAISERSLAUTERN* **Doktorand in Physikalischer Chemie** Titel der Doktorarbeit: „Spin and orbital magnetic moments of isolated single molecule magnets and transition metal clusters"
Sept. 2010 – März 2011	TU KAISERSLAUTERN, *KAISERSLAUTERN* **Diplom in Chemie**, Note 1,1 Titel der Diplomarbeit: „Kinetische und magnetische Studien an ionischen Cobalt-Clustern mittels Fourier-Transform Ionen-Zyklotron-Resonanz (FT-ICR) Massenspektrometrie und röntgenstrahlbasiertem magnetischem Zirkulardichroismus (XMCD)"
Okt. 2005 – Sept. 2010	TU KAISERSLAUTERN, *KAISERSLAUTERN* Studium der Chemie
Aug. 1996 – März 2005	GYMNASIUM KONZ, *KONZ* Abitur (Note 2,1)

WEITERE AKTIVITÄTEN

April 2011 – Jan. 2015	Doktorandenprogramm des Sonderforschungsbereiches 3MET, *KAISERSLAUTERN / KARLSRUHE* **Sprecher und Koordinator**

AUSZEICHNUNGEN

Steinhofer Preis der Prof. Dr. Drs. h.c. A. Steinhofer Stiftung für herausragende Leistungen während der Diplomarbeit

Analyst Poster Prize der 11th FT-MS-Conference, Paris, 2014

VERÖFFENTLICHUNGEN

1. **Tombers, M.**, L. Barzen, and G. Niedner-Schatteburg, *Inverse H/D Isotope Effects in Benzene Activation by Cationic and Anionic Cobalt Clusters.* Journal of Physical Chemistry A, 2013. **117**(6): p. 1197-1203.
http://dx.doi.org/10.1021/jp305281m

2. Barzen, L**.**, **M. Tombers**, C. Merkert, J. Hewer, and G. Niedner-Schatteburg, *Benzene activation and H/D isotope effects in reactions of mixed cobalt platinum clusters: The influence of charge and of composition.* International Journal of Mass Spectrometry, 2012. **330**: p. 271-276.
http://dx.doi.org/10.1016/j.ijms.2012.09.008

3. Peredkov, S., A. Savci, S. Peters, M. Neeb, W. Eberhardt, H. Kampschulte, J. Meyer, **M. Tombers**, B. Hofferberth, F. Menges, and G. Niedner-Schatteburg, *X-ray absorption spectroscopy of mass-selected transition metal clusters using a cyclotron ion trap: An experimental setup for measuring XMCD spectra of free clusters.* Journal of Electron Spectroscopy and Related Phenomena, 2011. **184**(3-6): p. 113-118.
http://dx.doi.org/10.1016/j.elspec.2010.12.031

4. Peredkov, S., M. Neeb, W. Eberhardt, J. Meyer, **M. Tombers**, H. Kampschulte, and G. Niedner-Schatteburg, *Spin and Orbital Magnetic Moments of Free Nanoparticles.* Physical Review Letters, 2011. **107**(23).
http://dx.doi.org/10.1103/PhysRevLett.107.233401

5. Dielemann, D., **M. Tombers**, L. Peters, J. Meyer, S. Peredkov, J. Jalink, M. Neeb, W. Eberhard, T. Rasing, G. Niedner-Schatteburg, A. Kirilyuk, *Orbit and spin resolved magnetic properties of size selected $[Co_nRh]^+$ and $[Co_nAu]^+$ nanoalloy clusters,* ACCEPTED AT PHYSICAL CHEMISTRY CHEMICAL PHYSICS
http://dx.doi.org/10.1039/c5cp01923k

6. Meyer, J., **M. Tombers**, C. v. Wüllen, G. Niedner-Schatteburg, S. Peredkov, W. Eberhard, M. Neeb, S. Palutke, M. Martins, W. Wurth, *The spin and orbital contributions to the total magnetic moments of free Fe, Co and Ni clusters,* SUBMITTED

7. **Tombers, M.**, J. Meyer, T. Lau, B. v. Issendorff, E. Kessler, M. Prosenc, C. v. Wüllen, G. Niedner Schatteburg, *Single molecule magnetism in isolation – X- ray magnetic circular dichroism (XMCD) spectroscopy of gaseous $[Mn_{12}ac]^+$,* IN PREPARATION

8. **Tombers, M.**, J. Meyer, J. Hewer, V. Zamudio-Bayer, A. Lawicki, T. Lau, B. v. Issendorff, G. Niedner Schatteburg, *Spin and orbital magnetic moments of isolated $[Fe_4Ln_2]^+$ single molecule magnets by X-ray magnetic circular dichroism,* IN PREPARATION

Eingeladene Vorträge

5. – 10. Jun. 2015	"Single Molecule Magnets investigated by gas phase X-ray magnetic circular dichroism (XMCD) spectroscopy" GRC "Clusters and Nanostructures", Girona, Spanien (hot topic)
17. – 23. Mai 2013	"Isolated Transition Metal Clusters: Formation and Cold Ion Trap Investigation for their magnetic properties", 5th International Workshop on Electrostatic Storage Devices, Heidelberg

Posterbeiträge:

22. – 27. Feb. 2015	Gordon Research Conference "Gaseous Ions", Galveston, TX, USA
29. – 31. Mai 2014	Bunsentagung der Gesellschaft Deutscher Chemiker (GDCh), Hamburg
26. Apr. – 2. Mai 2014	Gordon Research Conference "Molecular & Ionic Clusters", Lucca, Spanien
22. – 25. Apr. 2014	11th European Fourier Transform Mass Spectrometry Conference, Paris, Frankreich
22. – 25. Sep. 2013	2nd International Conference on Bimetallic Complexes, Karlsruhe
16. – 18. Okt. 2013	Konferenz des Sonderforschungsbereiches SFB/TRR 88 „3MET", Bad Bergzabern

Besuchte Konferenzen ohne Vortrag oder Posterbeitrag

2. – 5. Dez. 2014	User Meeting of the Helmholtz Zentrum Berlin, Berlin, Germany
2. – 4. Jun. 2011	Bunsentagung of the German Chemical Society (GDCh), Berlin, Germany
3. – 4. Sep. 2010	"150th anniversary "Weltkongress der Chemie"", Karlsruhe, Germany
10. – 12. Jun. 2009	EPITOPES conference, Paris, France

Eidesstattliche Erklärung

Hiermit bestätige ich, Matthias Tombers, dass die vorliegende Arbeit gemäß der Promotionsordnung des Fachbereichs Chemie der Technischen Universität Kaiserslautern selbständig und nur unter Verwendung der angegebenen Quellen und Hilfsmittel angefertigt wurde.

Kaiserslautern, im Juli 2015